TECHNISCHE UNIVERSITÄT MÜNCHEN

Institut für astronomische und physikalische Geodäsie
Ingenieurfakultät Bau Geo Umwelt

DOKTORARBEIT

TWANGS - High-Frequency Disturbing Signals in 10 Hz Accelerometer Data of the GRACE Satellites

NADJA PETERSEIM

zur
Erlangung des akademischen Grades des

DOKTOR-INGENIEURS
(Dr.-Ing.)

TECHNISCHE UNIVERSITÄT MÜNCHEN

Institut für Astronomische und Physikalische Geodäsie

TWANGS - High-Frequency Disturbing Signals in 10 Hz Accelerometer Data of the GRACE Satellites

Nadja Peterseim

Vollständiger Abdruck der von der Ingenieurfakultät Bau Geo Umwelt der Technischen Universität München zur Erlangung des akademischen Grades eines

Doktor-Ingenieurs (Dr.-Ing.)

genehmigten Dissertation.

Vorsitzende: Univ.-Prof. Dr.-Ing. Uwe Stilla

Prüfer der Dissertation:

1. Univ.-Prof. Dr.techn. Roland Pail
2. Ass. Prof. Dr. ir. Pieter N.A.M. Visser, Technische Universiteit Delft / Niederlande
3. Univ.-Prof. Dr.phil.nat. Urs Hugentobler

Die Dissertation wurde am 11.03.2014 bei der Technischen Universität München eingereicht und durch die Ingenieurfakultät Bau Geo Umwelt am 07.07.2014 angenommen.

Abstract

The GRACE space mission was launched in 2002 in order to map Earth's gravity field with an unprecedented spatial and temporal resolution. The twin satellites were originally designed for a lifetime of five years, but GRACE is still in orbit and functioning up to this point. However, the results of the gravity field are not matching the accuracy predicted prior to launch. One of the key instruments aboard of the GRACE space mission is the accelerometer, which detects the non-gravitational forces exerted upon the spacecraft, such as atmospheric drag or solar radiation pressure. In this work, we analyze the 10 Hz Level 1A accelerometer data in order to detect disturbing signals that could not be related to any known source. Earlier investigations showed that heater activations and de-activations as well as electric current changes within the magnetic torquer rods yield clearly detectable signals in the accelerometer data. We focused on signals known as 'twangs', which are rapid and short signals with a very high amplitude and can occur as often as 600 times a day per satellite. They occur simultaneously in all three axes of the accelerometer data and are greatest in the radial component, where they can reach an amplitude of up to 50 µm/s^2. A twang consists of two main peaks of opposite orientation and may be followed by an oscillating decay if the ratio of the amplitude of these two peak differs significantly from 1. The duration of the first two peaks is in the order of half a second. Twangs may be separated into two types, negative or positive, depending on the orientation of the first peak. The shape of a twang may alter in a case-by-case scenario by means of amplitude or oscillation, but are in terms of duration and period highly repeatable and can be superimposed. In order to parameterize any given twang, we developed analysis techniques that helped us to detect twangs within 10 Hz Level 1A accelerometer data. Twangs can be detected by using the Gaussian reconstruction filter in order to re-sample the data to 100 Hz, as 10 Hz sampling is too sparse to detect such a short signal. Afterwards we built a model that can match the twangs in accelerometer data by a set of parameters that need to be adjusted by means of least square adjustment. As the period of the oscillation is different from the period of the first two peaks, the model is set together by three different pieces. The first part is the derivative of the Gaussian curve for the first two peaks and a double-damped oscillation for a possible oscillating decay. The connector between the derivative of the Gaussian curve and the damped oscillation is a 3rd degree piecewise polynomial. With this model, we can investigate the behavior of twangs by means of their parameters with respect to the time of occurrence as well as to geographical or orbital locations. Twangs do not occur randomly but follow rather strict patterns that are correlated to geography, season, local time and the solar impact in terms of the β_{prime}-angle, and thus incidence angle onto the surfaces of the spacecraft. Among others, we detected a correlation of the distribution to the terrestrial long wave radiation, i.e. infrared. This correlation appears to be dominating all other detected patterns. Furthermore, we found that the overall number of twangs may decrease or the energy of twangs may become significantly smaller if certain surfaces of the GRACE spacecraft are illuminated, such as, for example, the nadir surface of the satellite. Due to our observations and investigations, we need to reconsider the established hypothesis that twangs are caused by micro-vibrations of the nadir mounted insulation foil. In this work, we state the hypothesis that the origin of twangs may be found in discharging events of the surfaces, which are charged by the spacecraft surrounding. Some of our observations support both hypotheses, but the majority only supports the discharging hypothesis and some may be regarded as a contradictor to the micro-vibration hypothesis. In addition to this, we assume a degradation of the dielectric material used for the outer surface of GRACE due to the impact of highly energetic electrons and dielectric breakdowns due to high potentials. One hint at this may be found in the increase of the overall number of twangs over time and the simultaneous decrease of the amplitude of twangs. Yet, the increasing number of twangs for certain geographical distributions may also be found in the decaying orbital height, as some environmental parameters may be stronger in lower altitudes. Twangs that cannot be sufficiently explained by the discharge hypothesis could be linked to a changing electrical input current of the solar arrays mounted on the zenith surface of the GRACE spacecraft. Moreover, we introduce a possible impact onto the gravity field of Earth as determined by GRACE by an adhoc approach developed in the early state of our works, and conclude with an outlook regarding further works.

Kurzfassung

Die Stallitenschwerefeldmission GRACE ist im Jahre 2002 gestartet um das Erdschwerefeld mit einer bis dato unerreichten Genauigkeit im räumlichen wie auch zeitlichen Sinn zu erfassen. Die GRACE Zwillingssatelliten sind ursprünglich für eine Lebenszeit von fünf Jahren ausgelegt worden, jedoch befinden sie sich nach wie vor funktionierend und arbeitend im Orbit. Die im Vorfeld der Mission durch Simulationen vorhergesagte Genauigkeit der Ergebnisse wurde jedoch noch nicht erreicht. Eines der Schlüsselinstrumente an Bord der GRACE Mission sind die beiden Akzelerometer, welche die nicht-gravitativen Anteile der Kräfte messen, welche auf die Satelliten wirken. Solche Kräfte sind zum Beispiel atmosphärische Reibung oder der Sonnenstrahlungsdruck. Im Rahmen dieser Arbeit wurden von uns die 10 Hz Level 1A Akzelerometerdaten analysiert um bisher unbekannte oder unbestimmbare Störsignale in diesen zu identifizieren. Frühere Untersuchungen der Daten haben gezeigt, dass das An- sowie Ausschalten der Heizer ebenso wie Stromstärkeänderungen für die magnetischen Steuerelemente klar sichtbare Signale in den Akzelerometerdaten hervorrufen. Wir haben uns auf Signale konzentriert, die im Allgemeinen als "Twangs" bekannt sind. Diese sind schnelle und äußerst kurze Signale mit einer verhältnismäßig sehr hohen Amplitude und können bis zu 600-mal pro Tag und Satellit auftreten. Twangs erscheinen gleichzeitig in allen drei Achsen der Akzelerometerdaten, wobei ihre größte Amplitude in der radialen Komponente gemessen werden kann. Hier können Twangs bis zu 50 µm/s² erreichen. Ein Twang besteht aus zwei großen Signalspitzen die entgegengesetzt orientiert sind und je nach Form von einer nachfolgenden Oszillation begleitet werden können. Die geschieht hauptsächlich dann, wenn das Verhältnis der Amplitudenhöhe der ersten beiden Signalspitzen signifikant von 1 abweicht. Die Dauer der ersten beiden Spitzen ist in der Regel eine halbe Sekunde lang. Aufgrund ihrer Orientierung können Twangs in zwei Typen kategorisiert werden, die wir positiv oder negativ benennen, je nach Orientierung der ersten Signalspitze. Die Form eines Twangs kann sich von Szenario zu Szenario verändern, wobei diese Veränderungen hauptsächlich in der Amplitude und Oszillation zu erkennen ist. Die Dauer der Twangs und ihrer einzelnen Signalspitzen ist äußerst stabil und damit können Twangs verschiedener Szenarien übereinander gelagert werden. Um einen Twang zu parametrisieren haben wir eine Analysetechnik entwickelt mit der Twangs in den 10 Hz Akzelerometerdaten erkannt werden können. Dafür werden Twangs mit Hilfe des Gauß'schen Rekonstruktionsfilters auf 100 Hz gesampelt da 10 Hz zu grob für die Kreuzkorrelations-Analysetechnik sind. Anschließend wurde ein Modell für die Twangs entwickelt, welches aus einem Satz verschiedener Parameter besteht. Mit der Methode der kleinsten Quadrate kann dieses Modell für jeden beliebigen Twang angepasst werden. Da die Periode der Oszillation von der Periode der beiden Hauptsignalspitzen abweichen kann, wurden für dieses Signalstück andere Parameter benötigt. Über ein Polynom dritten Grades wurden diese beiden Teilstücke so miteinander verbunden, dass sie stetig differenzierbar bleiben.

Aufbauend auf diesem Modell kann das Verhalten der Twangs aus verschiedenen Blickwinkeln in Abhängigkeit der Modellparameter sowie Zeit und Geographie untersucht werden. Daraus zeigte sich, dass Twangs nicht zufällig erscheinen, sondern streng geographisch korreliert sind. Diese Korrelation kann unter anderem von der Lokalzeit, und somit des β_{prime}-Zyklusses sowie der Jahreszeit abhängen. Darüber hinaus haben wir starke Abhängigkeiten gegenüber der terrestrischen langwelligen Strahlung, bzw. infrarotes Licht, ermitteln können, welche die geographische Verteilung der Twangs zu einem Großteil zu beeinflussen scheint. Darüber hinaus haben wir herausgefunden, dass die Anzahl und auch die Energie der Twangs gemindert wird, wenn bestimmte Oberflächen der GRACE Satelliten dem direkten Sonnenlicht ausgesetzt sind. Dies ist besonders für die Unterseite der Satelliten der Fall.

Aufgrund unserer Untersuchen muss eine neue Hypothese bzgl. der Ursache der Twangs aufgestellt werde. Die bisher bekannte Hypothese, dass Mikrovibrationen der an der Unterseite angebrachten Isolierfolie die Ursache sind kann unsere Beobachten nur ungenügend stützen. Im Rahmen dieser Arbeit wurde deshalb die Hypothese aufgestellt, dass Twangs durch Entladungsvorgänge verursacht werden. Diese kommen durch hohe Aufladungsvorgänge der Außenpanele der Satelliten durch die sie umgebenden Einflüsse zustande. Einige Beobachtungen unterstützen beide Hypothesen, die meisten jedoch nur die der Entladungsvorgänge.

Einige Twangs können auch einer dritten Hypothese zugeordnet werden, demnach einige Twangs durch Veränderungen der Eingangsstromstärke der Solarpanele hervorgerufen werden.

Zusätzlich vermuten wir eine Abnahme der dielektrischen Eigenschaften der Materialien der Außenpanele von GRACE über die Zeit. Dies kann Entladungsvorgänge begünstigen und so zu einer höheren Anzahl von Twangs mit kleinerer Amplitude führen, was unseren Beobachtungen entspricht. Diese Beobachtung kann jedoch auch mit dem Absinken der Orbithöhe über Zeit zusammenhängen, da in niederen Höhen einige Umweltparameter an Stärke gewinnen.

Anschließend zeigen wir mit einem adhoc Ansatz ob Twangs in den 10 Hz Akzelerometerdaten die Eigenschaft besitzen könnten, das durch GRACE bestimmte Schwerefeld der Erde zu beeinflussen.

This work is also published in the DGK Schriftenreihe, Verlag der Bayerischen Akademie der Wissenschaften in Kommission beim Verlag C. H. Beck, Issue Reihe C, Vol. 735, ISSN 0065-5985, ISBN 978-3-7696-5147-8.

Contents

Part I

Introduction

1 Accelerometry and gravity field satellite missions

One of the major characteristics of near planetary space environments is the remaining microgravity due to the mass of the planetary body. As the residual gravity in orbit is far from zero, it should be finely measured and understood as it may affect spacecraft, on-board instruments on spacecraft as well as the biology of any individual traveling into space. Regarding measurements of Earth's gravity from space, there are two main applications that make use of accelerometers. One is to measure the forces that act upon a spacecraft's surfaces for a fine orbit determination. In combination with GPS phase measurements, this may yield to a determination of the Earth's gravitational field. This principle has been made use of at several missions and also the mission we refer to in this work, the GRACE mission (**G**ravity **R**ecovery **A**nd **C**limate **E**xperiment). Furthermore, accelerometers can be used for gradiometry, which yield a better resolution in terms of spherical harmonics (degree and order). A gradiometer consists of several identical accelerometers mounted on a stable structure, measuring among others the gradients of Earth's gravity field (Marque et al. (2008)). For such applications, the resolution of the accelerometer must be approximately better than $1 \cdot 10^{-12} \frac{m}{s^2}$ (Touboul et al. (1998)). In order to obtain these high levels of sensitivity, ordinary accelerometers supporting nominal acceleration levels exerted by Earth's gravitational field on Earth's surfaces cannot be used due to the huge range. Therefore, specific space accelerometers need to be developed, making use of the advantages of the environment existing in Earth's orbits. In case of GRACE they measure the atmospheric drag, solar radiation pressure, albedo, and other non-gravitational forces experienced by the spacecraft. This is necessary in order to rule out these effects of the actual measurements of orbit determination via GPS and range rate measurements carried out by the K-band microwave system.

There is a very limited number of manufacturers that are able to develop accelerometers that can be used for these applications. Most space missions up to date making use of such instruments were equipped with servo-controlled electrostatic accelerometers constructed by ONERA (Office National d'Études et de Recherches Aérospatiales) in France.

In the past two decades evolution of satellite based gravity field recovery missions has advanced majorly. With CHAMP (**CHA**llenging **M**inisatellite **P**ayload), GRACE and GOCE (**G**ravity Field and Steady-State **O**cean **C**irculation **E**xplorer) space and geodetic communities have achieved to launch three highly successful missions that were and are able to determine Earth's gravity field with a very high accuracy. The advantage of determining gravity from space is to recover the gravity field globally, an aspect that neither terrestrial gravity nor airborne based gravity are naturally able to supply, despite their high accuracy. Hence, the distribution of available gravity data is very non-isotropic and yield major data gaps. This is in fact a troublesome issue concerning an Earth covering gravity field, that usually comes in spherical harmonicss, such as EGM96 or earlier. These contain poorly covered areas, which suffer from high standard deviations. While satellite based gravity field missions come with a lesser accuracy due to their higher altitude, they are able to carry out measurements globally, only limited to inclination. The spatial resolution is depending on both sensor accuracies as well as the mean orbit altitude.

The Earth's gravity field describes the gravitational influence evoked by the body mass of planet Earth. As the density distribution on the surface of Earth and also within the Earth's mantle is highly inhomogeneous, gravity is not constant at same heights. Therefore, gravity field recovery is a complex task for which especially satellite missions are beneficial. A good way to describe the he Earth's gravity is by means of spherical harmonics.

Gravity field data from satellites are used by a broad variety of users in different fields of science. Gravity changes can be seen as a direct effect of climate changes and can be measured by means of the decreasing ice shields in Greenland and Antarctica (e.g. Forsberg and Skorup (2005); Morrison et al. (2007); Velicogna and Wahr (2005); Ramillien et al. (2006)). Also smaller and not directly visible impacts of climate changes can be revealed by long term time series of gravity field data (e.g. Peterseim (2009); Steffen et al. (2009)). Its main applications are found within geophysical, i.e. hydrological, investigations (e.g. Steffen et al. (2009)), but also in other fields satellite recovered gravity field data can be valuable, such as the impact of structure related impacts (Wang et al. (2007)).

On July 15 in 2000 CHAMP, the first new generation gravity field satellite mission, planned and designed by Helmholtz Zentrum Potsdam Deutsches GeoForschungsZentrum (GFZ) in cooperation with Deutsches Zentrum für Luft- und Raumfahrt (DLR), has been launched. CHAMP detected the Earth gravity field from July 2000 to September 2010 with approximately 5 nm/s^2, which is roughly equivalent to a height variation on Earth of about 1 mm (GFZ (2013)). Besides collecting valuable information about Earth gravity field, CHAMP also determined the magnetic field of Earth as well as gathered information about the atmosphere, respectively ionosphere, at CHAMP altitudes (GFZ (2013)). GRACE was launched 2 years later, in order to determine temporal variations within the Earth gravity field and derive an even better accuracy than CHAMP (cf. following chapters). GOCE is the latest actually launched gravity field satellite mission and is the first of ESA's (**E**uropean **S**pace **A**gency) living planet program. Having the lowest altitude of all gravity field satellite missions so far, GOCE detects the gravity field with the best accuracy and resolution. The 6 highly sensitive accelerometers of the on-board gradiometer allow a high accuracy for even shorter wavelengths of the gravity field. Other, possibly upcoming, gravity field missions are in planning phase, such as e.motion by TUM or the recently selected GRACE Follow-On Mission by NASA and DLR.

GRACE Mission - A brief overview

The GRACE mission was selected as second of US NASA's (**N**ational **A**eronautics and **S**pace **A**dministration) Earth System Science Pathfinder (ESSP) program. This program shall be a new and innovative approach to detect certain attributes about Earth, such as ice, ocean, gravity and atmosphere, using advanced remote sensing techniques. Many of the missions within the ESSP involve international partnerships. GRACE is a collaboration between NASA and DLR. The ground segment is funded by ESA. A collaboration between the Center for Space Research (CSR) at the University of Texas at Austin (with Prof. Byron Tapley as a principle investigator), the GFZ Potsdam (including Dr. Frank Flechtner as co-principle investigator, formerly Prof. C. Reigber) and the Jet Propulsion Laboratory (JPL) of Caltech, Pasadena regarding the design and construction has been arranged – these institutes have been the proposer of the mission. CSR, GFZ and JPL are furthermore the three main official analysis centers that supply with Level 2 gravity field data made available as a set of spherical harmonics.

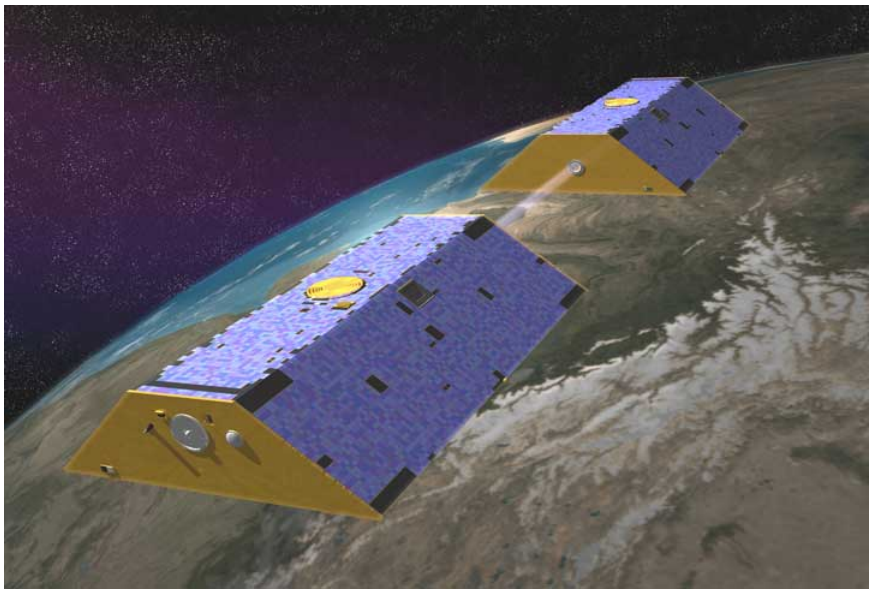

Figure 1.1: Artistic image of GRACE satellites A and B in orbit

GRACE is thought to be successor of the German CHAMP in the field of gravimetric measurements. Besides using a next generation type of highly precise accelerometers, the required dramatic step in accuracy of GRACE is by using two identical satellites following each other in the same orbit. In order to distinguish between the two spacecraft they are named satellite A and B, sometimes ironically referred to as "Tom & Jerry". The Earth's gravity field is being mapped by GRACE by making accurate measurements of the biased inter-satellite range between satellites A and B using the on-board K-band microwave ranging system, which has been an absolute novelty at the time of GRACE's launch. In order to establish the inter-satellite microwave link, the leading satellite needs to be yawed by 180 degrees, so that the panel equipped with the transmitting/ receiving microwave ranging device is pointing at the trailing satellite (see figure 1.2, showing the GRACE mission schematically). Figure 1.1 displays the constellation of the GRACE satellites in orbit in terms of an artistic impression. The target upon GRACE launch was to measure the changing rate of the distance between GRACE A and B with an accuracy of better than 1 μm/sec at the rate of 1 Hz. In fact, one could say that by this the satellites themselves can be pictured as the actual experiment whereas the satellites are small-mass probes (425 kg each, Mazanek et al. (2000)) in the terrestrial gravity field, delivering a snapshot of Earth's gravity field every month (Herman et al. (2004)). The mapping of the variability of the Earth's gravity field is indeed the main target of the GRACE mission. The highly accurate data determined by GRACE allow scientists to weigh various parts of the Earth system as well as determining weight distributions and changes on land as well as in ocean mass, the growth and shrinking of the polar ice sheets and glaciers, and hence the rather direct impacts of global climate changes. Furthermore, the amount of water in underground aquifers, and other possible issues profoundly affecting Earth's climate can be detected. GRACE provides a good perspective on ocean circulation and the time variability of Earth's shape or geoid (Space Systems/ Loral (1998)). For instance, up to 10 cm groundwater storage changes due to heavy rain in tropical forest areas could be detected (Herman et al. (2004)).

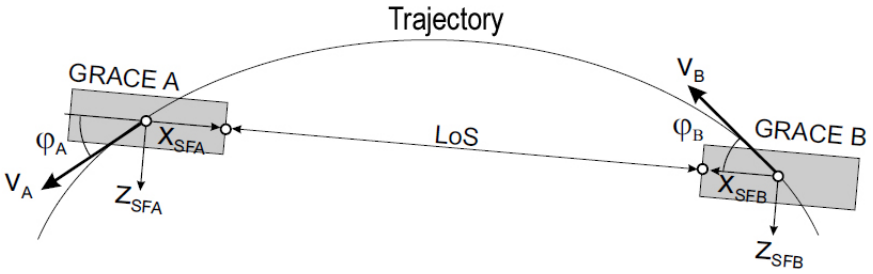

Figure 1.2: Line of Sight (LoS)/ Microwave (K-Band) establishment of GRACE, scheme

Originally, GRACE was planned for a five year lifetime. Being launched March 17, 2002 from Plesetsk Cosmodrome in Russia, GRACE is still in orbit measuring Earth's gravity field up to date, however. The mean inclination of GRACE is 89°, which means that GRACE is flying in a so-called polar orbit, almost covering the Earth's poles. The initial altitude was roughly 500 km, but has decayed by several km over the years to approximately 450 km. Unlike the GRACE's predecessor CHAMP, the GRACE mission consists of two identical twin satellites, which follow each other in the same orbit with a separating distance anywhere between 100 and 400 km. The configuration is optimal at a separation of approximately 230 ± 50 km, however (Frommknecht (2007); Space Systems/ Loral (1998)).

GRACE science data is being made available to the scientific community short time after calibration and validation of the measurements of the on-board instruments. The Level-1 products include the line of sight (LoS) range between the satellites measured by the microwave ranging system, the non-gravitational accelerations detected by the on-board accelerometer, the GPS navigation solution as well as any related ancillary data. Level-2 data includes among others the coefficients in spherical harmonics of the terrestrial geopotential field and the spacecraft position and velocity. The characterization of Earth's geopotential field by coefficients of a spherical harmonic expansion is the baseline of the science mission definition. These coefficients are estimated to a degree and order (d/o) of 160 or more for the long-term static mean part, and to d/o 120 or less for the time variable part, depending on the technique made use of by the individual analysis center.

An additional science objective is to provide several hundred globally distributed daily profiles of the excess delay, or bending angle of the GPS measurements due to the ionosphere and the atmosphere, using GPS limb-sounding. These can be converted to total electron content and/or refractivity in the ionosphere and troposphere, respectively (Stanton (2000)).

2 Definition of task and goals

The accelerometers mounted on-board the GRACE spacecraft are named SuperSTAR and are produced by ONERA in France. They were the first with an accuracy better than 10^{-10} m/s^2 in combination with such a low Earth orbit. This means, that comparing the results of the GRACE accelerometer to the data of earlier missions cannot validate the GRACE accelerometer data. The assessment of quality for the SuperSTAR accelerometers mounted on the GRACE spacecraft is no trivial task to be carried out. There are various rather unspecific indicators of the quality of the accelerometer data for GRACE. For instance, there is the gravity field of GRACE in comparison with any previous gravity field. Concerning satellite missions,the accuracy of temporal variations of the gravity field is unmatched up to date. Furthermore, accelerometer data quality may be to a certain degree verified by means of orbit determination results. However, gravity field accuracy as predicted by simulations prior to launch have not been achieved up to date (Wahr et al. (2006)). Among many error sources, the assessment of quality of the accelerometer data is one of the candidates to be investigated. The advantages are that the raw 10 Hz accelerometer data available for the GRACE mission offer a unique chance to investigate high-frequency effects onto a low Earth orbiter as GRACE. High-frequency signals may include any signals induced by spacecraft on-board instruments as well as external and environmental sources which act upon the whole satellite body.

The frame of this work is loosely based on the schedule of the IMPALA program by Germany's BMBF (Rummel and Gruber (2008)). The program's task was to investigate the signals found in the 10 Hz accelerometer data of GRACE in order to address the source of errors within the data and eliminate them, if possible. This aims at improving the accuracy of the gravity field as determined by GRACE as the results are still not matching the results predicted by simulations prior to launch, however they are unprecedented. In the frame of this work especially twangs shall be addressed in order to investigate their behavior, systematic and origins as well as to predict a possible influence onto the gravity field as determined by GRACE. Twangs are sudden spikes that are discovered within the raw 10 Hz accelerometer data of GRACE, which consist of a sudden peak with several orders of magnitude larger than the average noise level of the accelerometer data, often followed by a decaying oscillation. Prior to this work twangs were believed to be due to a vibration of the nadir insulation of the satellite.

The direct analysis of raw 10 Hz accelerometer data is a rather direct approach in order to describe the constitution and possibly also the quality of the accelerometer data of the GRACE satellite mission. Before we started our investigations we knew that a variety of error sources existed, which were either already investigated and ready to be eliminated or needed some further investigations. Thruster activation events are a known source for increasing the 10 Hz accelerometer signal level, but are believed to be a linear acceleration due to a misalignment of the thrusters. Furthermore, electric current changes occurring in the instruments on-board of the GRACE spacecraft and twangs specifically are expected to increase the noise level of the accelerometer data. In the frame of our work we focused on the twangs as we investigated many highly interesting correlations between twangs and ionospheric and geographic locations, as well as to solar impacts upon satellite surfaces.

Many of the error sources within the 10 Hz accelerometer data are within the order of magnitude of external non-gravitational data and deserve a rather detailed investigation even if believed to be outruled by the low-pass filter in order to retrieve data for gravity field processing. Most of these signals vanish within 10 seconds or less (Flury et al. (2008)). This means that any possible influence onto the gravity field as determined by GRACE depends on whether the high-frequency signal within 10 Hz is too small, i.e. short, in order to be disregarded by the low-pass filter. Also, it is rather important whether these signals are resulting in a net zero acceleration within their short time-frame.

As a further result of investigations carried out concerning the 10 Hz accelerometer data it may be possible to understand the sources of the twangs and possibly also how they may couple into the accelerometer.

2.1 Foreword

Investigating the 10 Hz accelerometer data is a highly complex task and soon exceeded our perception of what can be found and done within a very limited number of work-years. Therefore, a major part of this work is dedicated to the most intriguing subject of the high-frequent signals that we found, which are twangs. And even concerning this topic only we could easily spend a few more years researching twangs and all their attributes. We decided to present the most striking results of our investigations upon twangs in this work and state a hypothesis which could be one possible answer to the question: What is the source of twangs? This is not trivial, indeed, as a real inverse transfer function for the accelerometer has not been available to us. Therefore, we had to estimate and in consequence give evidence for what we suggest the cause for these signals is. However, this hypothesis is very complex and until the end of this study we were unable to state a mathematical model that could give further support for our theory.

It was hard to draw a line to distinguish between an actual twang and noise. The definition of the magnitude of the twang is arbitrary, but in order to keep the amount of found twangs manageable we had to define a threshold. However, there is no reason why signals or noise with a smaller magnitude could not be twangs due to the same or similar causes. The boundaries between certain types of disturbing signals in the 10 Hz accelerometer data may be indistinctly. It is understandable that investigating every single peak in the data, that cannot be directly linked to any known source, is more than unreasonable. Therefore, we limited ourselves to the major amplitudes and referred to them as twangs. This, however, means that this work may not be yet the answer to all unidentified sudden peaks in the accelerometer data exceeding a certain magnitude. Perhaps it just takes a few more years of investigation in order to understand the full range of signals discovered within the accelerometer measurements, or perhaps, they will remain obscure.

2.2 Structure of thesis

The structure of this work may be an unconventional one to the reader. Most theses are written in a way were a hypothesis is backed up by observation and is guided by means of theoretical explanations. This approach did not occur as feasible to us. Therefore, we decided to write the thesis in a way we carried out our investigations: we will state observations and provide with theoretical background information if necessary. However, we will not draw conclusions while describing these observations. This is simply due to the fact that our hypothesis cannot be stated upon single observations, but the observations need to be considered as a sum. In order to guide the reader towards our hypothesis it was therefore easier to introduce all these obersvations first, and then present a physical explanation based upon the whole scheme of the work. In order to keep a neatly arranged structure despite this unconventional approach, we supplied with a short interim résumé between the observation part and the hypothesis part of this work.

We did not intend to be construct a confusing structure. But we felt, that the thesis would be harder to understand if oriented at a conventional set-up.

Part II

GRACE Design and Payloads

This section is to introduce the reader into the design and key instruments of GRACE as well as into any critical system or payload of GRACE that may be affecting the mission itself or have a greater impact onto the results of this work. The signals in the accelerometer data, as described in the task definition, can be due to various origins. Therefore, a rudimentary knowledge of the GRACE spacecraft body and system is helpful in order to understand the conclusions that can be drawn from our investigations carried out.

3 Design of Shape and Material

Understanding the disturbance environment in which the GRACE satellites will operate is critical to the design and analysis of the satellite system as analysts must obtain an accurate estimate of the spacecraft's orbital lifetime, evaluate spacecraft attitude control requirements in terms of control authority and propellant consumption, and estimate station-keeping requirements in terms of maneuver frequency and propellant consumption (Mazanek et al. (2000)). In order to minimize atmospheric drag and to prolong the missions lifetime, an aerodynamic shape of the satellites is necessary. As both GRACE spacecraft are identical, whereas one is flying with a 180 degree yaw, the shape of the satellite must be one which is aerodynamic regardless whether the spacecraft's attitude is 0 or 180 degrees. Also, drag and solar radiation pressure torques experienced by the satellite may be minimized being optimally shaped. In figure 3.1 the shape of the satellites is depicted, the front and zenith panel in the left picture, and the nadir and aft panel in the right picture.

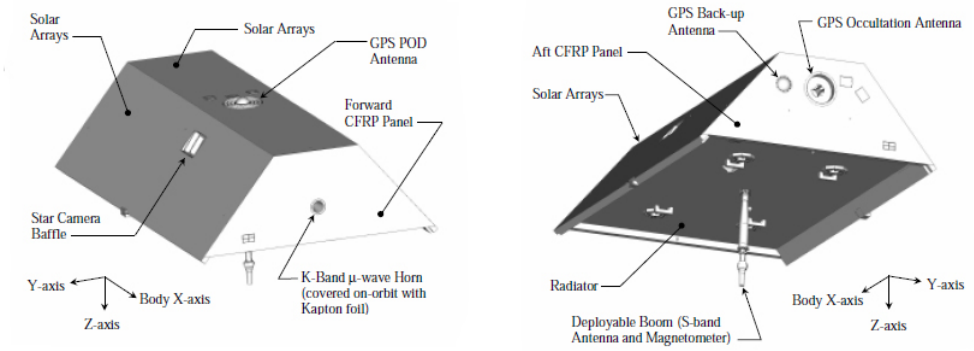

Figure 3.1: Left: Front/ Zenith view, Right: Aft/ Nadir view of the GRACE satellite.

The choice of materials with respect to the panels can be separated into roughly five groups, according to Mazanek et al. (2000). The zenith surface consists mainly of solar arrays, made from fused quartz, a rather reflective surface for residual atmospheric particles, in which the GPS antenna is included. The nadir pointing surface is a radiator, consisting of a Teflon foil coated with aluminum on the inward pointing side. This inward pointing side may be covered with a layer of paint at various parts, but does not cover the whole inward pointing area (Davis (2013)). The front and the aft panels are consisting of Carbon-Fiber Reinforced Plastic (CFRP) and are additionally covered by a protective Kapton foil, as is the K-band horn aperture. The

additional GPS antennas mounted on the aft panel are not covered by that foil, however. Here it is obvious, that there is a small geometrical difference between the front and the aft panel. These surfaces make up major portions of the spacecraft. Any other part of the surfaces of the satellite may be assumed to be made of aluminum. Properties of the main materials used for the outside planes of the GRACE spacecraft are stated in chapter 16.2 on page 133.

The satellites need to be slightly pitched in order to maintain the K-band system establishment by approximately -0.9 deg, which will vary with an alternating separating distance of the two satellites (also cf. 4.1 and 4.2). The greater the distance of the two satellites is, the greater the pitch with respect to the trajectory must be in order to maintain the Line of Sight (LoS, cf. fig. 1.2)(Mazanek et al. (2000)). The GRACE Science Mission Requirements Document (SMRD) states that the ballistic coefficient, ΔB_c, on the satellite is to be kept 0.5% (i.e. 1.05) or smaller in order to ensure a mission lifetime as planned ahead of the mission. The ballistic coefficient describes the ability of a body to overcome air resistance in flight. Due to the inhomogeneous shape of the aft panel, however, this requirement can only be met whenever the separating distance is nominal. Also the different materials used for the zenith and nadir panels contribute to a higher ΔB_c, also the trapezoidal shape of the satellite. Yet, simulations prior to launch have shown, that even the difference in surfaces do not pose a significant problem in terms of the aerodynamic disturbing torques during Science Mode.

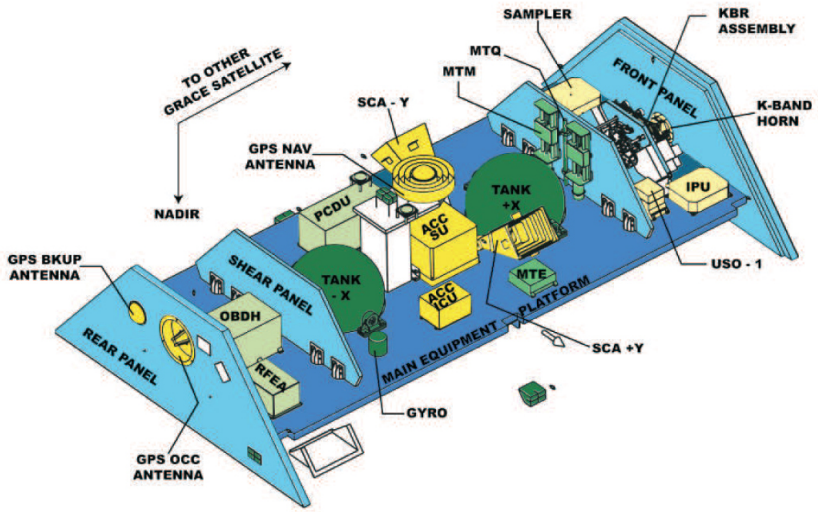

Figure 4.1: Schematic overview over the interior design and instruments of the GRACE spacecraft.

4 Instruments

In order to retrieve accurate information about the Earth's gravity field the collaboration of a broad variety of on-board instruments on GRACE is mandatory. Some actuators and sensors are directly linked to measurements of the Earth's gravity field, while others are to liberate these measurements from biasing signals in order to retrieve the gravity field information solely. The accelerometer is encountered as a key instrument of the GRACE mission. As the accelerometer is also the main objective of this work it will not be introduced in this section, however, but will be intensively discussed in the further process of this work (cf. chapter 5 on page 32). In figure 4.1 a schematic overview of the interior of the GRACE spacecraft and its instruments is given. The abbreviations have the following meaning:

ACC ICU	Accelerometer Interface Control Unit
ACC SU	Accelerometer Sensor Unit
GPS NAV ANTENNA	GPS Navigation Antenna
GPS BKUP ANTENNA	GPS BackUp Antenna
GPS OCC ANTENNA	GPS Occultation Antenna
IPU	Instrument Processing Unit
KBR ASSEMBLY	K-Band Ranging System Assembly
K-BAND HORN	K-Band Transmitter and Receptor
MTE	Center of Mass Trim assembly Electronics
MTM	Center of Mass Trim assembly Mechanism
MTQ	Magnetic Torquers
OBDH	OnBoard Data Handling System
PCDU	Power Control and Distribution Unit
RFEA	Radio Frequency and Electronics Assembly
SCA	Star Camera Assembly sensor
USO	Ultra Stable Oscillator

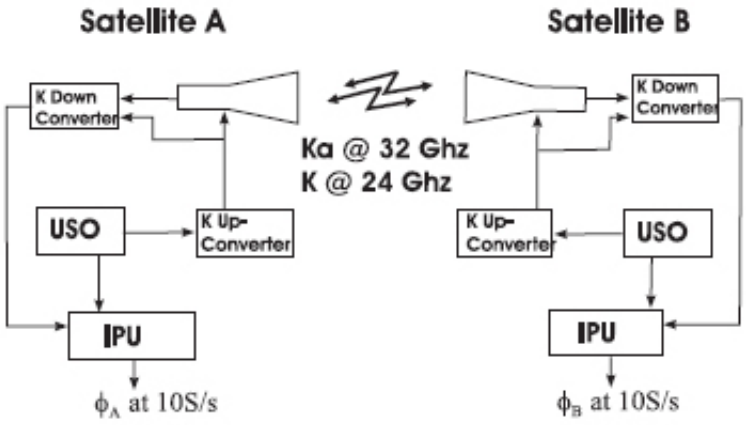

Figure 4.2: Schematic overview over the K-Band-Ranging System (KBR) (Thomas (1999)).

4.1 K-Band-Ranging System (KBR)

As previously mentioned in the introducing chapter, the GRACE satellite mission is equipped with a microwave ranging system, the so-called K-band Ranging System (KBR). Both satellites are equipped with a horn at the front panel (cf. fig. 4.1) with which the microwave signal can be transmitted as well as received. Both satellites transmit a signal at all time, where the signal is a dual µ-wave signal, consisting of a 24 GHz K-Band and a 32 GHz Ka-Band frequency. The wave itself is sinusoidal and is generated by the on-board Ultra Stable Oscillator (USO, cf. fig. 4.2, schematic overview over the KBR). An USO is an electronic oscillator circuit that uses the mechanical resonance of a vibrating crystal of piezoelectric material to create an electrical signal with a very precise frequency, often used for time measurements (Asmar (1997)).

4.2 Attitude and Orbit Control System (AOCS) and its instruments

The Attitude and Orbit Control System (AOCS) is a system consisting of sensors, actuators, electronics and software, which are mandatory in order to acquire adequate knowledge of the satellites attitude and orbit at all times necessary, to generate on-board alarm signals in order to maintain the satellites attitude within strictly set boundaries, and also to supply the spacecraft with control to alter the current attitude or orbit to satisfy the GRACE mission requirements. The establishment of the KBR, and hence the LoS, at any given time is a fundamental aspect for the success of the GRACE mission and the AOCS is to maintain the positive control in order to realize this task. As the satellite is exposed to different environmental forces, the attitude may alter and needs to be restored. Also the constant change in distance makes an attitude control mandatory, as the LoS can only be established when a certain pitch bias of approximately -0.9 degree is kept (also cf. fig 1.2; Herman et al. (2004); Mazanek et al. (2000)). In figure 4.3 a schematic view of the AOCS components as mounted on the GRACE spacecraft is depicted. This chapter shall give a brief introduction of the instruments used by the AOCS and how the AOCS works, i.e. is implemented.

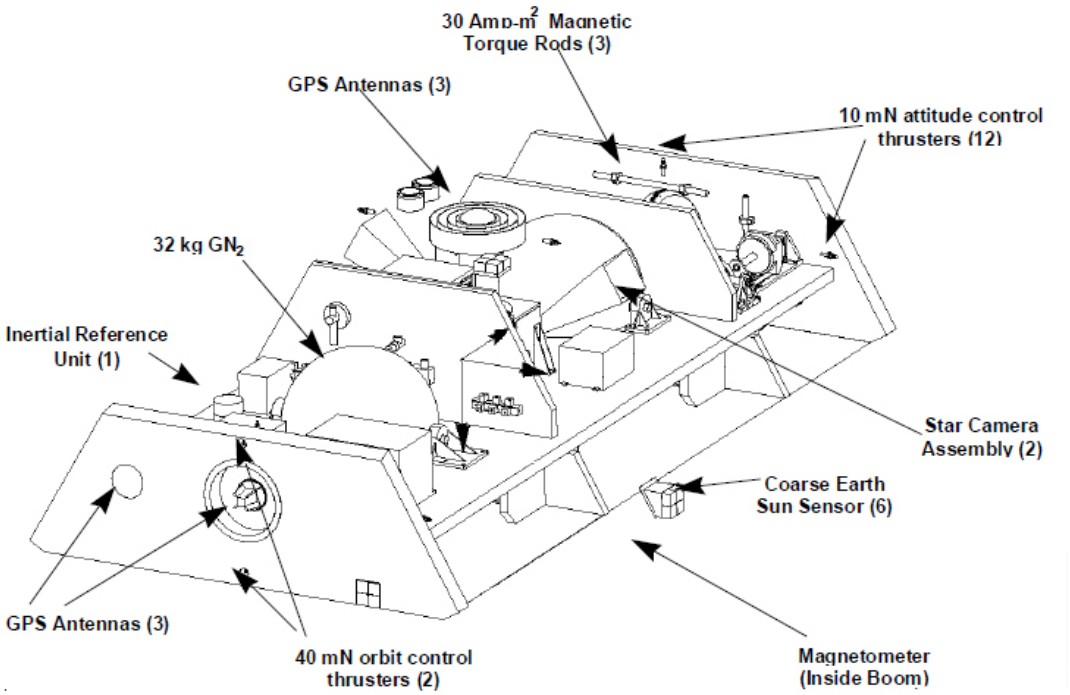

Figure 4.3: Schematic view of the GRACE AOCS components.

The AOCS consists of the following components:

- Cold-Gas-Thruster set using nitrogen as fuel for attitude control as well as for orbit change maneuvers,
- three magnetic torquers (MTQ) for attitude control and maintenance working in combination with Earth's magnetic field, supporting the thrusters,
- the star sensor assembly (Advanced Stellar Compass (ASC)) providing real-time absolute orientation,
- a BlackJack GPS receiver to determine an accurate on-board position in orbit,
- three gyroscopes (Inertial Reference Unit (IRU)) to determine angular rates,
- a coarse earth-sun sensor (CESS) to provide coarse attitude measurements,
- a three axis magnetometer mounted in the S-Band antenna boom, detecting Earth's magnetic field,
- the AOCS software.

The ACC, IRU, CESS, ASC, GPS and the Magnetometer are used for determination of the attitude as well as position of the satellite and are sensors. The thrusters and MTQ are actuators and have the ability to maneuver the satellite. ASC and GPS are hosted on the Instrument Processing Unit (IPU) and are part of the science data system.

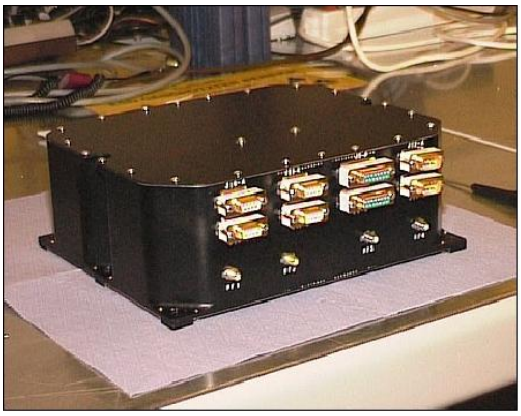

Figure 4.4: Black-Jack GPS Receiver.

GPS Receiver

This chapter is meant to give a brief overview about GPS and the used receiver on-board of GRACE. For more detailed information Seeber (2003) may be consulted. The Global Positioning System (GPS) is a satellite program by the US department of defense, which provides users with an accurate real position with a global coverage. Each GPS satellite is transmitting a signal which can be received by a GPS receiver. Practically, four GPS satellites are needed to retrieve an accurate realtime position and GPS receiver clock correction. In order to provide a global coverage, at least 24 GPS satellites need to be in orbit.

The Black-Jack GPS receiver is a special device developed and manufactured by the Jet Propulsion Laboratory (JPL) in Pasadena in cooperation with NASA and can be seen in figure 4.4. In contrast to commercially available GPS receiver, which come with an accuracy of roughly 20 meters, the Black-Jack receiver can deliver the position with an accuracy of 3.6 cm in an altitude of approximately 700 km and slightly worse at GRACE altitudes (Zumberge et al. (2003)). The Black-Jack receiver is a multifunctional, software driven device, that is not only developed for position measurements, but also for radio occultation and hence is suitable for remote sensing of the atmosphere, respectively the ionosphere.

The GPS device on GRACE is part of the AOCS and delivers precise information about the position and the velocity of the GRACE spacecraft. The retrieved data is forwarded to the IPU/SPU system in order to down-convert and digitize the data. Upon reception at the GPS antenna the accuracy is roughly below 50 m. A new signal is receipted with a rate of 0.1 Hz. The post-processing part at the SPU and IPU take integrated carrier phases into account, and this increases the accuracy of the position and speed vectors of the satellites significantly below 1 m within range and below 1 cm within the phase. If occultation measurements are taken into account at further processing steps, an even better accuracy can be determined.

Advanced Stellar Compass (Star Sensors)

The advanced stellar compass (ASC), also known as star trackers or star sensors, is an instrument to determine the absolute orientation of a body with respect to a given reference frame. This makes the ASC to one of the key instruments for the AOCS of the spacecraft. The ASC usually consists of two parts, where one is a camera head unit (CHU), which consists of a lens, i.e. objective, and a CCD array. The other part is the data processing unit (DPU), which is a powerful micro computing device consisting of a frame-grabber, power conditioning unit and a

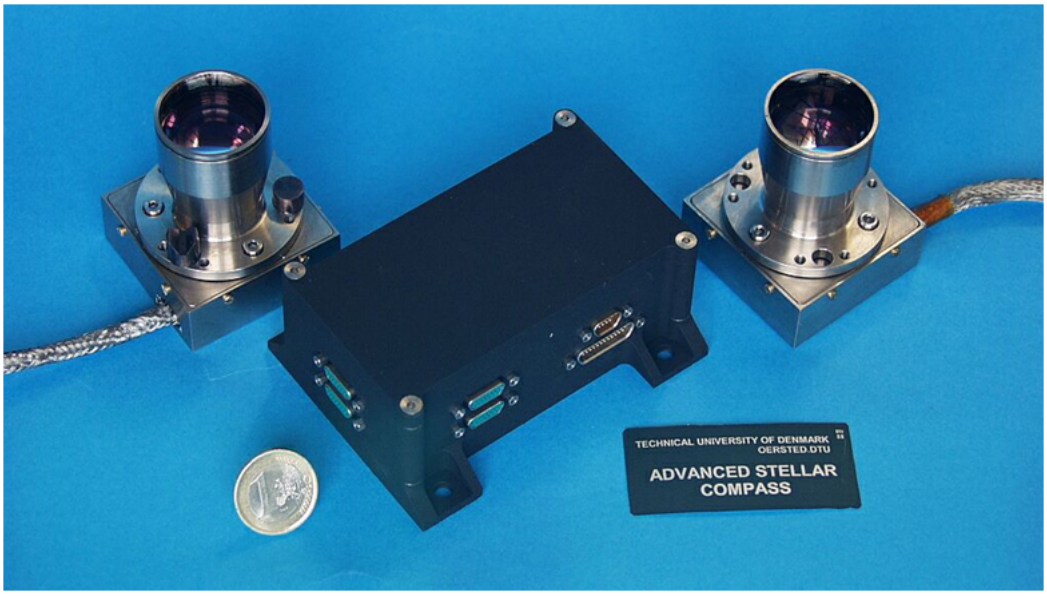

Figure 4.5: 2 CHUs and the DPU as manufactured at Technical University of Denmark.

communication interface to the OBDH. In figure 4.5 two CHUs and one DPU can be seen in accordance with a 1-Euro coin as a reference for its size. GRACE is equipped with 2 CHUs and one DPU, both manufactured at the department of automation at the Technical University of Denmark (DTU) in Copenhagen.

In order to determine the orientation of a satellite, the CHU takes a picture of the starry sky above the satellite. This image is then sent to the DPU, which does the further processing. Bright points in the taken image are considered to be stars, and the constellation of these bright points within the image are compared to a stellar catalogue. Stellar catalogues, such as HIPPARCOS or Tycho, consist of coordinates of up to 118.000 stars with an accuracy of 2-3 milliarcs per semi-annual, and coordinates of more than a million further stars yet less accurate (Perryman et al. (1997)). If the algorithm finds a match, the orientation of the CHU reference frame, which is known as the Star Sensor Reference Frame (SSRF), with respect to the reference frame of the star catalogue, which is usually the International Celestial Reference System (ICRS), can be computed. In case of GRACE, the DPU takes 13.000 of the brightest stars of the HIPPARCOS stellar catalogue into account (Frommknecht (2007)).

The ASC should fulfill the following requirements in order that the AOCS can function properly: The system needs to function fully autonomously, it needs to be able to determine the orientation in real time (means computation should not take longer than 30-50 msec for standard approaches, and at a rate between 1 and 4 Hz), more than 1 CHU is needed and they need to be directed in different/ opposed angles, as one CHU might be blinded by sun or moon (Jørgensen (2000)). Each CHU has a field of view of 18 by 16 degrees, and is providing the attitude with an accuracy of approximately 0.030 mrad (1σ) in the horizontal and vertical and roll about bore-sight of 0.240 mrad (1σ) (Space Systems/ Loral (1998)).

Coarse Earth-Sun Sensor

The Coarse Earth-Sun Sensor (CESS) sensor head, as used on GRACE satellites, consists of a thermistor, which may be black or silver. A sensor head on GRACE has 3 silver and 3 black thermistors, providing a 3/2 redundancy. Each face of the GRACE satellite is equipped with

such a CESS sensor head unit (Space Systems/ Loral (1998)). By the different shade of the color of the thermistor, the irradiated flux by sun and albedo may be determined from the temperature due to absorption. CESS are used for a coarse attitude determination of the spacecraft. The vectors of orientation are derived by combination of all mounted head units, using the fact that the sun is the hottest object in the field of view, and Earth is the second hottest. Apart from the critical early mission phase right after launch, the CESS sensors are mainly used in Fine Pointing Mode (FPM), as an additional check for the ASC performance. In case of a rare occasion when GRACE is flown in Coarse Pointing Mode (CPM), CESS is the main instrument for attitude determination (Herman et al. (2004)).

Inertial Reference Units / Gyroscopes

This unit is purposed to determine the angular rates of the GRACE satellites and its outputs are angular increments. Together with the CESS sensor, the IRU is merely a safe mode sensor, used for the critical start and set-up phase of the mission, or in case of any major failure situations, where the satellite needs to be flown in a CPM. The IRU is a fiber optic gyroscope, utilizing the Sagnac effect, and was not specifically produced for space missions, but is merely a standard product by Litton Guidance and Control. The unit comes with an angular resolution of 0.1967 arcseconds and a measurement range of -17 to 17 degrees per second. The IRU on GRACE A is disfunct since start of mission (Herman et al. (2004)).

Cold-Gas Propulsion System (Thruster)

GRACE spacecraft are equipped with a set of thrusters. These thrusters are needed for maintaining the satellites in a specific orbit and attitude. The thrusters work with a cold-gas system and use nitrogen as a medium. Functionality is given via jet force, a rocket-like force due to Newton's third law, which states that for every action there is an equal and opposite directed reaction. The backward moving exhaust of a fuel, nitrogen in case of GRACE thrusters, pushes the satellite forward.

The fuel for the thrusters is stored in two tanks on-board of each satellite, with a pressure of 350 bars and 16 kg of fuel at the time of launch (Space Systems/ Loral (1998)). Two tanks are necessary for two reasons: on the one hand, center of mass can be balanced out much better this way. The other reason is redundancy. Both branches can therefore be operated individually.

For orbit maintenance purposes each satellite is equipped with two 40 mN thrusters, which are mounted at the anti-flight direction side of the satellite with the force vector pointing through the center of mass of the spacecraft. Orbit corrections are carried out about 2-3 times per year (Herman et al. (2004)).

The attitude control around roll, pitch and yaw is performed by three sets of four cold-gas thrusters, with a nominal thrust-force of 10 mN. The thrusters for attitude control are nominally operated in pairs, which are accommodated such that force free reaction control is achieved (Bettadpur (2007)). In fig. 4.6 the distribution of thrusters on a GRACE satellite is displayed schematically. Thrusters-pairs have been marked in the image, for example A1-1 and A2-1, A1-2 and A2-2.

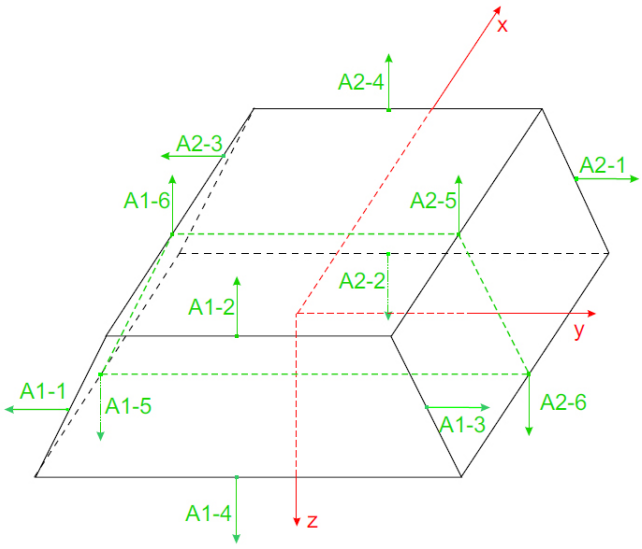

Figure 4.6: Schematic view of the Cold-Gas Propulsion System mounted on the GRACE satellite (Fackler (2005)).

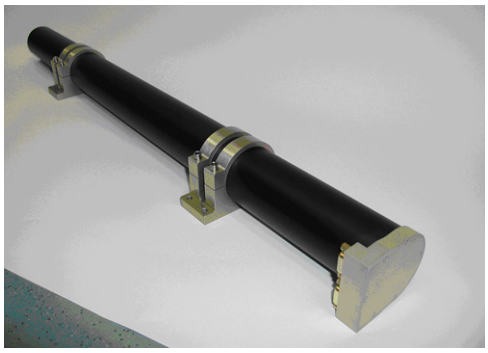

Figure 4.7: Design of a MTQ, manufactured by ZARM.

Magnetometer and Magnetic Torquers

The main target of the magnetometer is to deliver data about the Earth's magnetic flux density at the current position of the GRACE spacecraft to the AOCS in order to adjust the magnetic torquers. Another use of the magnetometer could be to assist determining the momentaneous spacecraft rotation rates. The magnetometer used for GRACE are supplied by the Institute Förster and was in its form already used on GLOBALSTAR and ROSAT. The used electronics for the magnetometer, however, are part of the OBDH of GRACE. The sensor head consists of a three orthogonal axes sensing assembly, and has a measurement range from -50 μT to 50 μT for each axis. The overall resolution of this sensor is 25 nT (Wang (2003)). Since a software update within the AOCS the magnetometer can roughly be used as a coarse attitude determination device in CPM in case both the ASC and the CESS sensors should fail (Herman et al. (2004)).

For the satellite attitude control, magnetic torquers and thrusters are used. Magnetic torquers continuously control the attitude, while the thrusters are activated only in case magnetic torquers alone cannot restore or maintain the satellite's nominal attitude. Both GRACE satellites are equipped with 3 magnetic torquer rods, which are aligned orthogonally within the satellite's body and the axes of the system given by the magnetic torquers are parallel to axes of the

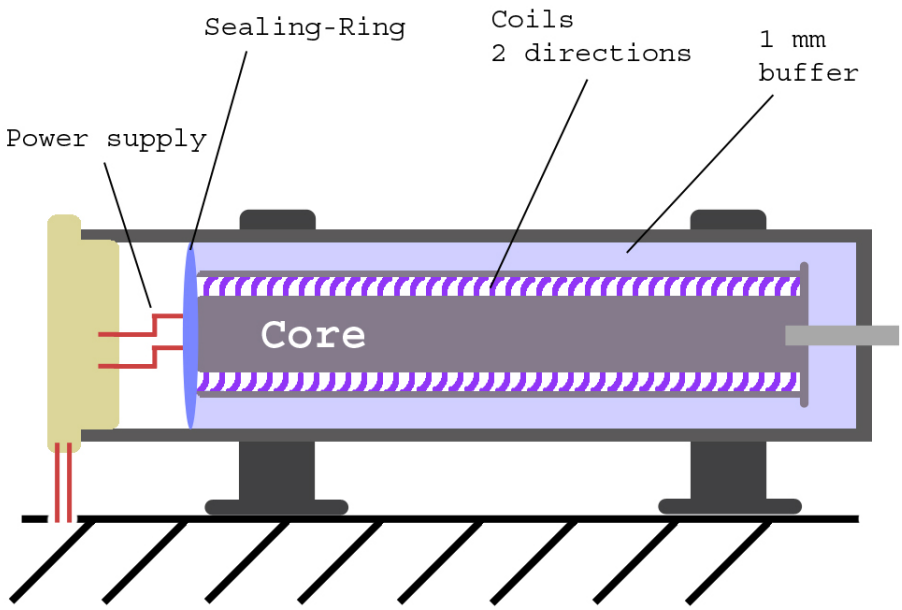

Figure 4.8: Schematic view of a MTQ.

accelerometer. The magnetic torquer rods are electromagnets with the product number MT30-2, which were designed and manufactured by ZARM (Center of Applied Space Technology and Microgravity) at the University of Bremen in Germany. In figure 4.7 a torquer rod, as used in the GRACE satellites, can be seen. A torquer rod is fixed with screws to the satellite body at two points. At both ends of the rod there is a cap screwed on to seal the magnetic torquer. The power supply is connected at the "top" end of the rod (the end pointing at the reader in figure 4.7).

In figure 4.8 the inner construction of the magnetic torquer rod is schematically shown. The material of the core is nickel alloy. The core is encircled by two coils, which have an equal number of twists. In fact, only one coil is actually in use, the other one is for redundancy purpose only. The core amplifies a magnetic dipole which is created by the coil. The ring at the end of the core has the function to keep the core in its nominal place. The core is furthermore tightly screwed to the bottom of the torquer. The space between the core and the inner enclosing walls is filled with an elastomer to stabilize the construction. The power supply is cable-connected to the top of the coil, respectively the magnetic torquer rod.

In order to keep or turn the satellite into its nominal attitude a torque is needed. This torque needs to dominate all other torques acting upon the spacecraft. The magnetic torquers realize a magnetic dipole which interacts with the Earth's magnetic field and so the magnetic torque acting on the spacecraft is produced. The applied torque vector can be derived from the following formula:

$$\overrightarrow{T_M} = \overrightarrow{m} \times \overrightarrow{B} \tag{4.1}$$

with:

B	Earth's magnetic flux density, measured by magnetometers,
m	effective magnetic moment, generated by MTQs.

The magnetic flux density of the Earth is determined with a sample of 4.5 Hz ± 1 Hz by the on-board installed magnetometers (Wang (2003)). In Science Mode (SM, the nominal science flight mode of GRACE), the needed magnetic torque $\overrightarrow{T_M}$ can be computed in accordance with the attitude information provided by the star sensors, and the $\overrightarrow{B}$ provided by magnetometers, and applied.

Systems and Software Design

This section shall give an overview about the different modes that the GRACE spacecraft can be flown in. This can be of interest as the instruments of the AOCS may be acting different from the nominal Science Mode and hence have a greater impact onto the measurements of the accelerometer. Further details may be found in Herman et al. (2004). The operation modes of GRACE can be separated into two main modes: the Fine Pointing Mode (FPM) and the Coarse Pointing Mode (CPM).

- Fine Pointing Mode (FPM)
  - (Backup) Science Mode: The (backup) Science Mode, also referred to as (B)SM, requires that the spacecraft are in the nominal attitude to establish the KBR. As a consequence the leading satellite must be yawed by 180 degrees so that its front panel equipped with the KBR horn is facing the trailing satellite, which is not yawed. The mean distance between the satellites of approximately 230 km implies a slight pitch bias for both satellite with respect to the trajectory of about -0.9 deg, this can also be deduced from figure 1.2, page 16. The pitch angle may range from approximately -0.4 deg for 100 km (minimum separating distance allowed) to -2.1 deg for 500 km (maximum distance allowed)(Mazanek et al. (2000)).
  - (Backup) Attitude Hold Mode: The (backup) Attitude Hold Mode, also referred to as (B)AHM, requires an attitude accuracy of 0.2 degrees, in accordance with the (B)SM. In contrast to the (B)SM any desired attitude in the (B)AHM may be chosen. This attitude, however, is fixed and does not undergo alteration during the period flown in (B)AHM. GRACE is flown in (B)AHM for Orbit Control, i.e. altitude changes which occur 2-3 times a year, Center of Mass (CoM) calibrations and any other special occasions, such as AOCS parameter changes.
- Coarse Pointing Mode (CPM): CPM is a safe mode in which the satellite is flown in early mission phase or at times of any major failures with the requirement to maintain control over critical interfaces, e.g. by thermal means.

Other payloads

There are several other payloads, systems and/ or mechanisms on-board the GRACE spacecraft which shall merely be introduced briefly. More detailed information can be found in Stanton (2000).

- Center-of-Mass Trim Mechanism: This mechanism controls CoM of the spacecraft. Due to fuel consumption as well as a potential deformation of the spacecraft (e.g. due to any environmental impact) the CoM may vary during flight phase (Zheng et al. (2009)). The trim mechanism is to provide a means of adjusting the CoM of the spacecraft during flight. Regular CoM calibration maneuvers are carried out, whereas the satellite is usually flown in AHM. The range of the CoM shift due to the trim mechanism is 2 mm and it has an accuracy of 10 μm (Hudson (2003)).
- S-Band Antenna: The S-Band antenna is the main communication channel with Earth. It is deployed on a short boom in the center of the nadir facing surface (i.e. radiator panel). This device is used for transmission and reception of any commands from and with Earth as well as transferring science data to ground. The Radio Frequency Electronics Assembly (RFEA) is the corresponding unit containing the electronics for the S-Band antenna.
- Power Conditioning and Distribution Unit: The Power Conditioning and Distribution Unit (PCDU) controls the power which is generated by the GRACE solar arrays and is responsible for the power distribution of the entire spacecraft.
- Solar Arrays: GRACE's solar array consists of 4 panels on each of the two spacecraft, where two are body-mounted side panels, and two are mounted on the zenith plane (one forward and one behind the GPS antenna).
- Battery: Each GRACE satellite is equipped with a twenty nickel-hydrogen cell battery that is fully charged prior to launch of the mission. Each battery can deliver 16 A-hr and 28 Volt when fully functional. During the extended phase of the GRACE mission, the batteries arose to a key issue, as on both satellites one or more of the 20 cells of each battery failed. Due to this, the accelerometers are currently switched off during eclipse phase since 2012 (Witkowski and Massmann (2012)).

5 Accelerometer

Accelerometers are devices to measure the proper acceleration of an object. There are several types of principles how an accelerometer can work, according to their target and application in science and industry. In this chapter the servo-controlled electrostatic accelerometer principle, as used for gravimetric space-born missions, is introduced only at first and the mounted SuperSTAR accelerometer is discussed in detail. The data products of the SuperSTAR accelerometer are described in chapter 7.

In cases of CHAMP and GRACE the accelerometer needs to be located in the CoM of the spacecraft in order to detect the non-gravitational forces acting upon the satellite. This is necessary in order to determine the influence of e.g. atmospheric drag, solar radiation pressure, albedo, onto the actual measurements of orbit determination via GPS and range rate measurements carried out by the K-band microwave system in case of GRACE.

5.1 Servo-Controlled electrostatic accelerometer

In brief words, a servo-controlled electrostatic accelerometer works as follows: it carries out the measurement of the electrostatic force that is necessary in order to keep the proof-mass of the accelerometer in its nominal position with respect to its surrounding electrode cage. The electrostatic force is directly proportional to the acceleration exerted upon the instrument. The functionality of a servo-controlled electrostatic accelerometer shall be discussed in theory now, mainly related to the descriptions in the articles Touboul et al. (1998), Touboul (2001), Marque et al. (2008) and Josselin et al. (1999) if not stated otherwise.

5.1.1 Measurement model

The main set-up of an electrostatic accelerometer consists of the proof-mass, whose size and material may differ with respect to its application and specification of accuracy, and its surrounding electrode cage. For gravity field space missions, as introduced, such an accelerometer is usually by default a tri-axial accelerometer with the origin of the Accelerometer Reference Frame (ARF) located in the Center-of-Mass (CoM) of the proof-mass. The proof-mass is fully suspended in all three directions, i.e. levitated within its cage, suppressing any mechanical contact to the benefit of the performance. The materials and the size of the proof-mass and the surrounding cage may vary with respect to the resolution needed, and the gap between the proof-mass and the electrode cage can range from 30 μm to 1 mm.

The main task of a servo-controlled electrostatic accelerometer is to keep the proof-mass at rest by means of creating an electrostatic force that keeps it in the origin of the ARF. Or, as a rather popular description, the electrostatic force necessary in order to restore the nominal position of the proof-mass is measured. This can be expressed by the following equation, where χ^{rel}_{mass} is the relative position of the proof-mass inside its cage with respect to the cage walls:

$$s^2 \cdot \chi^{rel}_{mass} = \Gamma_{s/c}, \tag{5.1}$$

where s is the Laplace derivative variable and $\Gamma_{s/c}$ the actual non-gravitational acceleration of the spacecraft. However, there are several terms that need to be considered, as only for a perfect scenario the spacecraft's acceleration solely would be detected. For this, in addition to equation

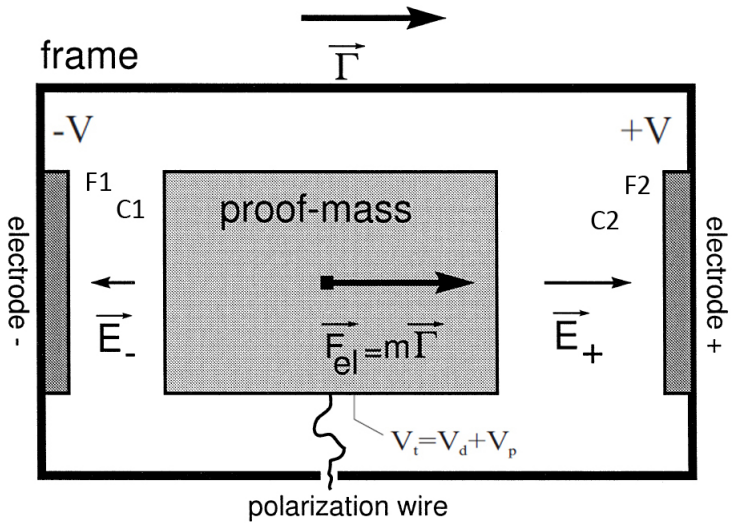

Figure 5.1: Basic schema of one accelerometer axis

5.1 some more factors need to be considered. The accelerometer also measures contributions of g, the gravity field, and ω_p, the angular frequency associated to a parasitic uncontrolled stiffness of the proof-mass. Furthermore, a possible unwanted displacement of the proof-mass with respect to the ARF origin χ_{cage} might occur due to strong vibrations or accelerations, which need to be taken into account. Practically, however, $(\chi^{abs}_{mass} - \chi_{cage})$ is almost zero, when the proof-mass is being optimally servo-controlled. Therefore, equation 5.1 needs to be extended to (measured on ground level)

$$s^2 \cdot \chi^{abs}_{mass} = g + \Gamma_{elec} \pm \omega_p^2 \times (\chi^{abs}_{mass} - \chi_{cage}), \tag{5.2}$$

with Γ_{elec} being the measurement provided by the accelerometer

$$\Gamma_{elec} = \Gamma_{s/c} - \Gamma_{dtb} + (s^2 + \omega_p^2)\chi_n - \frac{m_g}{m_I} g. \tag{5.3}$$

Here, Γ_{dtb} are the disturbances on the measurement due to the environment, such as magnetic, electrical or thermal impacts. The aim is to keep Γ_{dtb} reduced as much as possible and yielding a well identified Γ_{elec}. $\chi_n$describes the position sensor noise. $\frac{m_g}{m_I}$ is the scaling fraction that needs to be multiplied with g in order to regard a residual gravitational influence onto the measurement, if the proof mass is not exactly located in the center of mass of the spacecraft and in the center of the surrounding cage.

The first accelerometers had a spherical proof-mass and showed that a high sensitivity level can be reached, but the level of accuracy is low as the proof-mass may rotate. Therefore, proof-masses are now of cubic shape. The electrode cage is consisting of at least 6 electrodes, where one electrode is facing one side of the cubic proof mass. In figure 5.1 this is schematically shown for one of the three accelerometer axes. Here it is visible that the proof-mass is located between the two electrodes with a nominal gap between the proof-mass and the electrodes. Usually, the

gap is equidistant to either side. The two electrodes are charged with two opposite voltages V_1 and V_2 and are used for both capacitive position sensing as well as electrostatic restoring force generation. The proof-mass itself is also being charged via a very thin connecting gold-wire (usually with a diameter smaller than 15 μm) to the cage with the voltages V_P, a polarization voltage, and V_d, a detection voltage, summing up to the voltage V_t, as can be described by the following equation:

$$V_t = V_P + V_d. \tag{5.4}$$

The detection voltage V_d needs to have a high frequency (100 kHz in case of the GRACE SuperSTAR accelerometer) in order to be high enough to not affect the motion of the proof-mass, and is indeed the detecting signal for the changing capacitance. Both electrodes will attract the proof-mass with the forces F_1 and F_2, proportional to the gradient of the capacitance and the square of the electric potential differences between the proof-mass and the electrodes. The resulting force F on the proof-mass in one axis as depicted in figure 5.1 can be described as follows:

$$F = \frac{1}{2}\left[\nabla C_2(V_2 - V_p)^2 + \nabla C_1(V_1 - V_p)^2\right]. \tag{5.5}$$

In a stable and resting system, i.e. no acceleration experienced, the resulting force F would be 0, with $\Delta C_2 = -\Delta C_1$, respectively $V_1 = -V_2 = V$. If the servo-control is working perfectly in an accelerating system the latter two are valid as well. The resulting force F is proportional to V, and equation 5.3 can also be described as follows, where $H(s)$ is the transfer function of the sensor that transfers the measurement into an actual acceleration V:

$$\Gamma_{elec} = \frac{F}{m} = 2 \cdot \nabla C \cdot V_p \cdot V, \tag{5.6}$$

$$V = H(s) \cdot (\chi_{mass} - \chi_{cage} + \chi_{noise}). \tag{5.7}$$

The transfer function $H(s)$ is depending on the version of the developed accelerometer. In case of the accelerometer used aboard of the GRACE spacecraft (SuperSTAR), $H(s)$ is introduced in chapter 5.2.2.

5.1.2 Parasitic forces acting on accelerometers

According to Karslioglu (2000) there are five main sources for parasitic forces upon space-borne accelerometers. The general understanding of parasitic forces for these types of accelerometers are that the proof-mass encounters interactions with its surrounding environment. The five sources are gravitational nature, thermo-dynamical effects, electrostatic forces, magnetic-static forces and the Lorentz force. These five sources shall be briefly introduced hereafter. The mass of the spacecraft is assumed to be approximately 500 kg, if any of the sources are referring to the mass.

The main cause for the parasitic gravitational force upon the accelerometer measurements are linear deformations of the materials used aboard of spacecraft, resulting in a shift of a center of mass (CoM) of the satellite. This results in an offset between the center of mass of the proof-mass of the accelerometer and the center of mass of the spacecraft. Such an offset can also be caused by general mass shifts (e.g. fuel consumption) or by means of thermal dilation. However, there is no ideal realization of keeping the center of mass of the proof-mass within the center of mass of the satellite, therefore the aim must be to keep the offset within reasonable boundaries. An error of about 1% for CoM shifts may lead to about $10^{-10}m/s^2$, according to the size and mass of the spacecraft.

Thermo-dynamical effects are the next parasitic force. There are two main causes for these effects: thermal motion by means of molecules in the residual gas and radiation pressure due to differential temperatures. The first cause describes a thermal motion between the proof-mass and its surrounding core, which then evokes a force upon the proof-mass' surface, which may be up to $10^{-12}m/s^2$, depending on the accelerometer used. The latter cause is by some magnitudes smaller than the first one, but for some missions it may be considered.

Electrostatic forces upon the accelerometers can be distinguished into two phenomena: the electrification of the proof-mass as it first levitates within its cage, i.e. losing direct contact to the cage, and electrification by means of cosmic particles passing through the spacecraft in low attitudes. These forces may have an impact of up to 10^{-9} to $10^{-13}m/s^2$. ONERA, however, minimizes this effect in its accelerometers by means of a gold-wire used for applying a polarization and detection voltage, which can be additionally used to discharge the proof-mass.

The fourth parasitic force are the magnetic-static forces upon the proof-mass. The impact of this forces is highly depending on the magnetizing abilities of the material of the proof-mass and the magnetic dipole in which the proof-mass is situated. However, this effect is rather small, and is usually not exceeding $10^{-12}m/s^2$.

The last of the parasitic forces is the Lorentz force. This force is encountered when the proof-mass is moving, usually with the same or comparable velocity as the spacecraft in which it is placed, through a magnetic field, for instance Earth's magnetic field. Furthermore, the magnitude of this force is depending on the charge of the proof-mass. When the proof-mass is charged with $2.2 \cdot 10^{-12}$ Coulomb, the resulting effect could be as high as $10^{-13}m/s^2$ in interactions with the Earth's magnetic field and hence rather small. Karslioglu (2000) states that usually the spacecraft itself is charged by the surrounding residual atmosphere and is experiencing the Lorentz force itself, resulting in a smaller impact onto the accelerometer.

5.1.3 Electrostatic accelerometers previously implemented on spacecraft

Three main generations of ultra-sensitive three-axis electrostatic accelerometers were developed by ONERA and mounted on-board of spacecraft prior to the launch of the GRACE mission. The first generation were the DISCOS and CACTUS (**C**apteur **A**ccéléromètrique **C**apacitif **T**riaxial **U**ltra **S**ensible) accelerometers, that were launched in 1972 and 1975, respectively. The previously mentioned spherical proof-mass used for early electrostatic accelerometers was implemented in the accelerometers of this generation. CACTUS, for instance, was designed to measure the surface forces exerted on a satellite by the aerodynamic drag and the solar radiation pressure, which is indeed the main task for the accelerometers on-board of GRACE. The problem with a spherical proof-mass as used here is obvious: the sensitivity of the accelerometer will fluctuate as the proof-mass turns/ spins within the electrode cage, and total spin-stabilization of the proof-mass is not entirely possible.

The next generation of accelerometers of this type can be referred to the ASTRE (**A**ccéléromètre **S**patial **TR**iaxial **E**lectrostatique) accelerometer which was flown in 1996 and 1997 on-board of NASA's space-shuttle Columbia (flights STS-78, STS-81 and STS81R). ASTRE was designed and developed for monitoring the environment of microaccelerometric environment of laboratories in space. It measured the resistance of the shuttle to forward flight due to the residual atmosphere. However, it was highly sensitive to the vibrations caused by the mechanisms and movements of the team in the space lab. Its measurement range is between 1 mg and 1 ng, and the accelerometer collected data covering the whole time-span of these missions. Even though the aim was to reach microgravity level, this goal could not be achieved as the Columbia space-shuttle was maneuvering in orbit too much in order to obtain such a high accuracy. ASTRE had a cubical proof-mass with the dimensions 4 by 4 by 1 cm and the distance of the proof-mass to the surrounding electrode cage was 75 μm.

The last of the three generations worth mentioning in this context is the STAR (**S**pace **T**hree-axis **A**ccelerometer for **R**esearch) accelerometer, which is indeed the predecessor of the SuperSTAR accelerometer mounted on-board of the two GRACE spacecraft. The STAR accelerometer is in its design similar to ASTRE as it is based on the experiences collected from the flights with the ASTRE accelerometer. STAR was defined for the German CHAMP mission, dedicated to Earth observation. STAR came with a resolution of better than $3 \cdot 10^{-9}\mathrm{ms}^{-2}$ for the y- and z-axes (along and cross track), and $3 \cdot 10^{-8}\mathrm{ms}^{-2}$ for the less sensitive x-axis (radial/ nadir pointing). The measurements for STAR were integrated over one second before they were delivered to the data bus of the spacecraft.

Besides these ultra-sensitive three-axis electrostatic accelerometers by ONERA a few other accelerometers flown in space with a levitated proof-mass exist. They shall be merely briefly acknowledged to complete this brief overview. Accelerometer MESA (**M**iniature **E**lectro**s**tatic **A**ccelerometer) was also manufactured by ONERA but consisted of thin-walled cylindrical shaped proof-mass with a thin central flange. Firstly, this type of accelerometer was introduced by Bell Aerospace as a one-axis accelerometer. MESA was one of the sensors of NASA's OARE (**O**rbital **A**cceleration **R**esearch **E**xperiment) program, to measure the space shuttles in-orbit linear accelerations. Two QA3000 accelerometers, which are pendulum accelerometers with a non-levitated proof-mass suspended in all directions, where used in the Quasi-Steady Acceleration Measurement (QSAM) instrument.

5.2 SuperSTAR accelerometer

This section gives the reader an overview about the SuperSTAR accelerometer. The following facts and descriptions are mainly based on Bertin et al. (2000) and ONERA (2013) if not stated otherwise. On both GRACE spacecraft there is a SuperSTAR accelerometer mounted in the center of mass of the satellite. This accelerometer has been designed and constructed by ONERA in France and is in its design and concept the successor of the STAR accelerometer that was built and used onboard of the German CHAMP mission. For a better understanding, it shall be referred to as *the accelerometer*, as the specifications for both accelerometers are identical.

5.2.1 Instrument Concept

The accelerometer is to measure the non-gravitational forces exerted upon the spacecraft. Non-gravitational forces are such as the drag of the residual atmosphere in GRACE orbit altitude, the solar radiation pressure, the albedo, as well as any other non-gravitationally linked impacts. In a perfect system only the non-gravitational forces can be detected, however there are several

disturbing impacts on these measurements. One source of error is the natural offset between the proof-mass position and the position of the center of mass (CoM) of the spacecraft, in which the proof-mass should be located – this leads to unwanted detections of Earth's gravity gradients as well as angular velocities. These need to be determined in the post-processing of the data. Further error sources are described below in this section. Considering this offset, the angular velocities and the gravity gradients, the excitement of the accelerometer sensor may be described by the following equation (Hudson (2003)):

$$\overrightarrow{f}_{exc} = \overrightarrow{f_{ng}} + \ddot{\overrightarrow{b}} + 2\overrightarrow{\omega} \times \dot{\overrightarrow{b}} + \overrightarrow{\omega} \times \left(\overrightarrow{\omega} \times \overrightarrow{b}\right) + \dot{\overrightarrow{\omega}} \times \overrightarrow{b} - \boldsymbol{G}\overrightarrow{b} + \overrightarrow{f_d}, \tag{5.8}$$

with $\overrightarrow{b}$ being the offset of the CoM the proof-mass from the CoM of the spacecraft, $\overrightarrow{\omega}$ is the angular velocity of the satellite and G is a tensor consisting of the gravity gradients experienced by the satellite. $\overrightarrow{f_{ng}}$ is the actual non-gravitational force. Equation 5.8 may be regarded as different approach to describe the excitement with the accelerometer considering equation 5.6. The overall data output can then be represented by

$$\overrightarrow{f_{obs}} = \overrightarrow{\zeta}(t) + \Gamma(t)\overrightarrow{f_{exc}} + \overrightarrow{G}(\overrightarrow{f_{exc}}) + \overrightarrow{n}(t). \tag{5.9}$$

Here, $\overrightarrow{\zeta}$ is a time variable acceleration offset, Γ a scaling factoring-matrix to scale the observed excitement of the proof-mass for each axis along its diagonal, and contributions from the non-orthogonality of the proof-mass and electrode cage in its off-diagonal components. $\overrightarrow{G}(\overrightarrow{f}_{exc})$ is a non-linear response contribution, expressed as a function of the measured accelerations and is not related to G in equation 5.8 above. Furthermore, the system noise is represented as $\overrightarrow{n}$.

Mechanical Set-Up

The SuperSTAR accelerometer consists of four basic elements, as can be seen in figure 5.2. One is the Sensor Unit, consisting of a proof-mass and the surrounding cage. The proof-mass is a metallic cube with the dimensions 4 x 4 x 1cm, a weight of 70 g and consists of a titanium-alloy. It is suspended in all three directions within the surrounding electrode cage, which consists of gold coated silica. As described in the previous section, the proof-mass is servo controlled using capacitive sensors by means of a detection voltage V_d inside the proof-mass in combination with the applied control voltages V_1 and V_2 on the electrodes of the cage and the polarization voltage V_p on the proof-mass. The proof-mass and the electrode cage are the elements of the core of the accelerometer. The core itself is enclosed by a housing of aluminum and soleplate, with vacuum inside that is maintained by means of a getter pump during flight. The proof-mass is fully levitated inside the cage, except for a 5 μm (in diameter) flexible gold wire in order to apply the polarization and detection voltages, V_p and V_d. For the SuperSTAR accelerometer V_p is static, and V_d is a 100 kHz sine voltage. The frequency of V_d is high enough in order to leave the proof-mass motion unaffected.

Another element of the accelerometer is the Electromagnetic Exciter Unit (EEU). This device is only used at start-up problems of the accelerometer. There is an unlikely but given chance that the proof-mass might get stuck. The EEU delivers a 10 mg acceleration evoked by two coils, that will create an electromechanic shock in the Sensor Unit in order to release the proof-mass out of its deadlock position. Upon launch of the GRACE mission this instrument had not to be used.

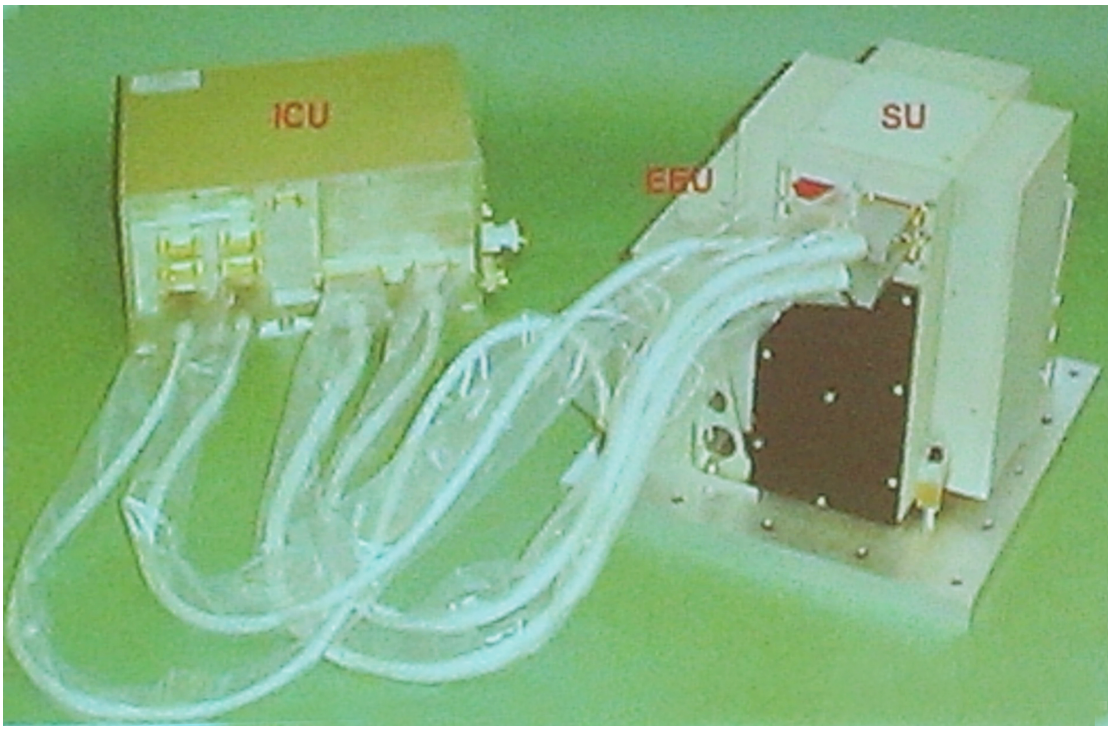

Figure 5.2: The SuperSTAR accelerometer elements before mounted on the GRACE spacecraft platform.

However, now in extended mission phase, with a decaying battery quality, the accelerometers are switched off in eclipse phase (Witkowski and Massmann (2012)). This requires a start-up of the accelerometers as soon as the instruments can be powered by means of the on-board solar arrays.

The third element is the Interface Control Unit (ICU). The ICU supplies power to the Sensor Unit as well as the EEU. In order to perform this task, the ICU handles the power conversion from the Power Control and Distribution Unit (PCDU) of the satellite from primary voltage to secondary voltage, that is used for the accelerometer elements. Furthermore, the ICU is performing the conversion of the analog data to digital science and housekeeping data. Here, a 24-bit $\sigma\Delta$-converter is used for the science data and a 12-bit multiplexed converter for the housekeeping data. The latter data type is interesting for the maintenance of the whole instrument system, as it contains for example the instrument temperature. For further description of the data, please refer to section 7. The ICU is fully redundant.

As a fourth element the connections between the three introduced elements of the accelerometer shall be mentioned. All wires are fixed to the ground in order to remain motionless if the spacecraft is facing turbulences. The wiring from the ICU to the on-board bus is redundant (double independent), and single to the SU and EEU, respectively.

The accelerometer is equipped with several thermistors, and they are located at 6 locations at both the housing and support frame. Within the Sensor Unit a temperature maintenance of 0.1 K is required, for the ICU a range of 0.3 K is acceptable (Hudson (2003)).

The design of the accelerometer units and cases of the single elements yields an exclusion of disturbing forces that could possibly lead to a bias of the measurements. For this, the entire chamber is made of Invar, derived from the term *invariable*. Invar is a nickel-iron alloy and is widely known for a very low thermal expansion coefficient. Furthermore, the material is to shield the instrument from possible magnetic fields induced by the spacecraft itself (e.g. magnetic torquers) or by external sources, such as the Earth's magnetic field. Yet, the power

supply for the Sensing Unit (DC) induces a magnetic field which evokes a magnetic moment on the proof-mass. The magnetic sensitivity of the proof-mass is directly related to the used material of the proof-mass and its magnetic polarizability properties. In case of the SuperSTAR accelerometer, the choice of the titanium-alloy yields matching the mission requirements and also minimizing magnetic effects on the proof-mass. As the magnetic moment naturally cannot be excluded to the full extent due to the necessity of the power supply, a force proportional to that magnetic field gradient is applied by means of a variation of the control voltages V_1 and V_2 of the electrodes. This can be expressed by the following equation, expressed in the capacitance gradient:

$$\Delta C_0 = \alpha(B_{earth} + B_{s/c}) \cdot \nabla B_{s/c}, \tag{5.10}$$

with B being the magnetic moment of the Earth (B_{earth}) and the spacecraft respectively ($B_{s/c}$), $\nabla B_{s/c}$ the total gradient of the magnetic moment of the spacecraft, and α the coefficient of the magnetic polarizability of the material.

If wiring was needed, only copper-zinc alloys have been used. This alloy minimizes corrosion effects and plating is very limited. The life-time of the wiring is beyond the nominal mission duration, including the ongoing extension. While on Earth under normal g conditions outgasing is a critical issue, in space outgasing is minimized to less than 1 % and can be neglected. Furthermore, the eigenfrequency of the whole accelerometer system is known and is beyond a threshold where it could lead to a biasing effect of the measurements. The damping due to the connecting wire between the proof-mass and the surrounding core is indeed producing noise, but tests have shown that this noise level is far below the requirements due to the usage of a very thin wire in diameter. Another requirement yielding sufficient performance of the accelerometer instrument is that the instrument itself is protected against power transients from the bus and other electronic devices mounted on-board the GRACE spacecraft. However, the hypothesis stated in the frame of this work considers a detectable impact due to electrical switching or currents (cf. chapters 7.2 and 13.3).

Mounting and Performance

The SuperSTAR accelerometers on GRACE are mounted in the center of mass of the spacecraft, with the center of the ARF being in the center of the Satellite Reference Frame (SRF). The proof-mass of the accelerometer is to be maintained in the center of the ARF. The axes of the ARF are defined as follows: the z-axis z_{ARF} of the accelerometer is aligned with the pointing vector of the K-band Ranging system (KBR). This axis will be referred to as "along-track" or AT in the frame of this work for an easier comprehension. The y-axis y_{ARF} of the accelerometer is the vector orthogonal to z_{ARF} and is pointing towards Earth – it will be referred to as the "radial" or simply R further on, as this syntax has been used in previous works. The last axis is x_{ARF} and is normal to these to axes and is pointing "cross-track" (CT) to complete the right handed triad. Also confer figure 5.3 for the axes alignments.

The range and resolution values for the SuperSTAR accelerometer on both spacecraft are displayed in table 5.1, according to Hudson (2003) (φ, θ and ψ being the angular accelerations of the spacecraft detected by the accelerometer).

It is visible that one axis is less sensitive than the other two. This is due to the shape of the proof-mass having narrow/ small surfaces in two axes, and one relatively large and square surface. This is necessary for ground testing the accelerometer prior to mission launch as it is mandatory

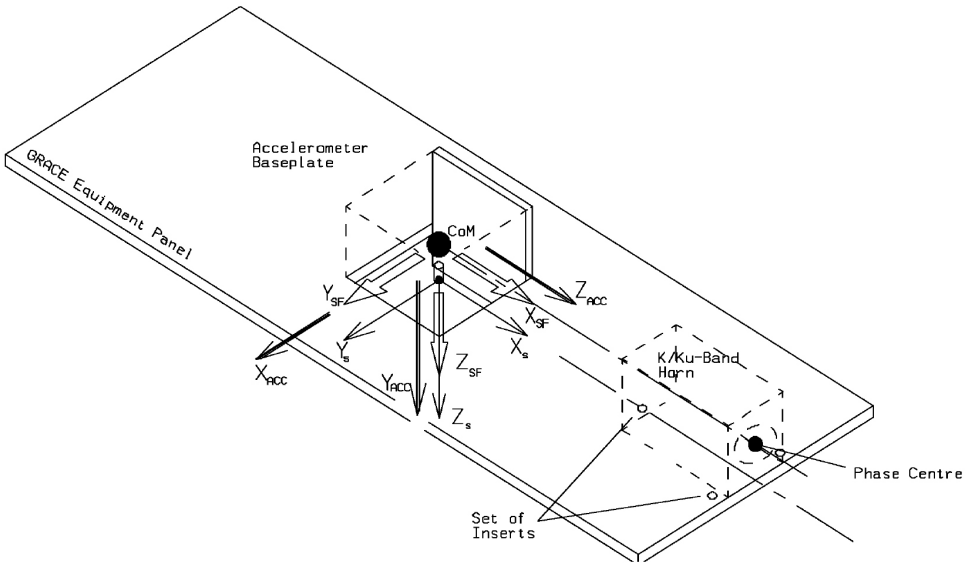

Figure 5.3: Schematic view of the axes alignments, with ACC being the accelerometer and SF the spacecraft.

	Range	Resolution
x_{ARF}	$\pm 5 \cdot 10^{-4} \frac{m}{s^2}$	$10^{-9} \frac{(m/s^2)}{\sqrt{Hz}}$
y_{ARF}	$\pm 5 \cdot 10^{-5} \frac{m}{s^2}$	$10^{-10} \frac{(m/s^2)}{\sqrt{Hz}}$
z_{ARF}	$\pm 5 \cdot 10^{-5} \frac{m}{s^2}$	$10^{-10} \frac{(m/s^2)}{\sqrt{Hz}}$
φ(pitch)	$\pm 10^{-3} \frac{rad}{s^2}$	$2 \cdot 10^{-7} \frac{(rad/s^2)}{\sqrt{Hz}}$
θ (yaw)	$\pm 10^{-2} \frac{rad}{s^2}$	$5 \cdot 10^{-6} \frac{(rad/s^2)}{\sqrt{Hz}}$
ψ (roll)	$\pm 10^{-2} \frac{rad}{s^2}$	$5 \cdot 10^{-6} \frac{(rad/s^2)}{\sqrt{Hz}}$

Table 5.1: SuperSTAR range and resolution performance.

to keep the proof-mass suspended within the electrode cage in all three axes. As the accelerometer is experiencing normal g conditions on Earth, a larger electric field is needed in order to levitate the proof-mass. This can be achieved by creating the cubic test-mass with one surface area larger than the others – however, a larger surface makes the sensitivity of capacitance detection smaller, consequently. For ground testing the less-sensitive axis is nadir pointing, the electrical field in its magnitude directly opposed to Earth's gravity acting upon the proof-mass. When the accelerometer is mounted on-board of the satellite, the accelerometer instrument will be turned with this side pointing cross-track as the measurements of linear accelerations in this direction are expected to be the least critical for the outcome of the GRACE mission as the KBR demands an accuracted measurement in the along-track and radial component.

The accelerometer ground tests are carried out on pendulum benches at the ONERA facilities as well as in the drop tower of ZARM in Bremen, where the accelerometer can be tested under no gravity conditions during free-fall. For the conceptions of the ground testing of electrostatic accelerometers the interested reader shall be referred to Marque et al. (2008) and Willemenot and Touboul (2000).

5.2.2 Transfer function

According to Meyer (2000) a transfer function is a mathematical function, that relates the input to a system to the output or response by means of e.g. a filter circuit. Such a transfer function is commonly used for linear, time-invariant systems (LTI), but can also represent the relation of input and output of systems with slightly non-linear characteristics. In case of the latter, these parameters may not be overdriven, however. As non-linear systems represent the majority of all systems, this approach is feasible for most described systems. The transfer function $H(s)$ is the linear mapping of the Laplace transform for the input or stimulus of the system. The input $x(t)$ may be of analog or digital nature, but usually comes in the time-domain. The system yields the output $y(t)$. In order to compute $y(t)$, the Laplace-transform $X(s)$ of the input $x(t)$ is needed (cf. eq. 5.11). The Laplace-transform of the output $Y(s)$ and its corresponding result in the time-domain $y(t)$ may be obtained by the following relations (Meyer (2000)):

$$X(s) = L\{x(t)\}, \tag{5.11}$$
$$Y(s) = H(s) \cdot X(s), \tag{5.12}$$
$$y(t) = L^{-1}\{Y(s)\}. \tag{5.13}$$

For further information upon transfer functions in general, the interested reader may be referred to Meyer (2000) specifically or any other literature dealing with signal processing and systems.

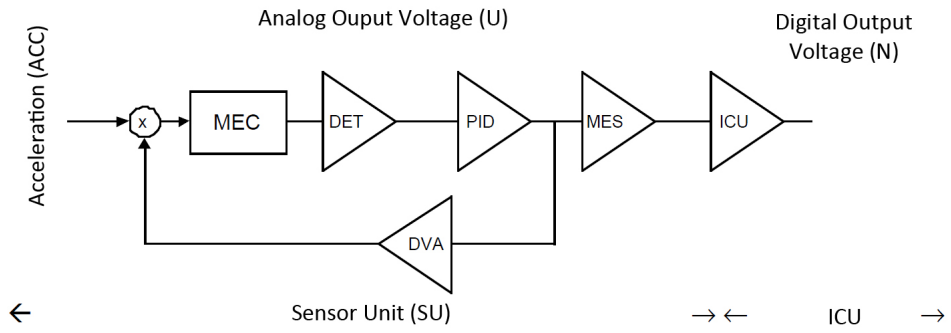

Figure 5.4: Block Diagram of the Sensor Unit w.r.t. the units needed for the transfer function $H(s)$ (Bertin (2000)).

Transfer function in sensitive axes

In this section the transfer function of the SuperSTAR accelerometer mounted upon the GRACE spacecraft for the sensitive axes will be discussed. The following introduced transfer function is based on the linear approach as described by Bertin (2000) and does not take any non-linearities of the instrument into account. However, this approach is feasible for small signals. The number of the parameters is minimal and any other cut-offs do not affect the transfer functions at frequencies below 100 Hz. The described transfer function correspond to the z_{ARF} axis (along-track) when used in the Science Mode (SM, cf. section 4.2). In this case the proof-mass polarization voltage V_p is set to 10 V (cf. eq. 5.4). For in-flight values the actual geometry and characteristics of the Sensor Unit and the electronic boards need to be considered, however, which might result in a slight bias between in-flight results and results obtained with this transfer function.

The accelerometer is, as previously described, an electro-mechanical device to turn an analog acceleration detected by the Sensor Unit of the accelerometer into an electrical signal by means of capacitance measurement. The transfer function will give the relation to this, taking the operations needed by the single parts of the instrument into account, as depicted in figure 5.4. Here, ACC describes the actual analog acceleration, U and the Sensor Unit the analog output voltage, and N and ICU the digital output voltage. Each of the blocks within this block diagram is a electro-mechanical device and performs a unique function needed to obtain the actual output acceleration $y(t)$. Hence, for each of these electro-mechanical devices a unique transfer functions exists, which need to be combined in order to retrieve $y(t)$ from $x(t)$, the actual acceleration. The electro-mechanical devices in the block diagram represent the following:

MEC	proof-mass motion in the electrode cage,
DET	capacitive sensor of proof-mass position,
PID	correcting network,
DVA	actuator, driving the proof-mass back into the center of the electrode cage,
MES	amplifier of the determined acceleration,
ICU	Interface Control Unit, Butterworth filter and A/D conversion.

And the transfer function for any of these devices are stated as follows, according to Bertin (2000): G_{ICU} stands for the digital ICU output converted in μV at the analog input. The order of the transfer functions orients at the set-up of the block diagram, reading from left to right.

$$MEC(s) = \frac{1}{-(2\pi f)^2}, \tag{5.14}$$

$$DET(s) = \frac{G_{det}}{1 + i \cdot \frac{f}{230Hz}}, \ with \ G_{det} = 0.42 \cdot \frac{V}{10^{-6}m}, \tag{5.15}$$

$$PID(s) = G_{corr} \frac{1 + \tau_1(2i\pi f)}{\tau_1(2i\pi f)} \cdot \frac{1 + \tau_2(2i\pi f)}{1 + \tau_3(2i\pi f)} \cdot \frac{1}{1 + \tau_4(2i\pi f)}, \tag{5.16}$$

$$with \quad G_{corr} = 5.247, \ \tau_1 = 0.177s, \ \tau_2 = 0.15s \ \tau_3 = 4.75 \cdot 10^{-4}s, \ , \\ \tau_4 = 3.669 \cdot 10^{-3}s, \tag{5.17}$$

$$DVA(s) = \frac{G_{dva}}{1 + i\frac{f}{170Hz}}, \ with \ G_{dva} = 6.767 \cdot 10^{-5} \frac{\frac{m}{s^2}}{V}, \tag{5.18}$$

$$MES(s) = \frac{G_{mes}}{1 + i\frac{f}{100Hz}}, \ with \ G_{mes} = 2.5 \tag{5.19}$$

$$ICU(s) = \frac{G_{ICU}}{\sum_n c_n (\frac{i \cdot f}{3Hz})^n}, \ with \ G_{ICU} = 10^6 \frac{(10^{-6}V)}{V}. \tag{5.20}$$

For the transfer function $ICU(s)$ for the ICU-block n represent the value $0, \ldots, 4$, and c is a unit-free vector containing the following values: $(1, \ 2.6131, \ 3.4142, \ 2.6131, \ 1)^T$.

From equations 5.14 to 5.18 the open-loop transfer function $OL(s)$ can be derived. This transfer function only takes the devices inside the Sensor Unit into account, and does not supply with any output acceleration $y(t)$.

$$OL(s) = MEC(s) \cdot DET(s) \cdot PID(s) \cdot DVA(s). \tag{5.21}$$

In order to obtain the corresponding closed-loop function $CL(s)$, equation 5.21 needs to be enhanced:

$$CL(s) = \frac{OL(s)}{1 + OL(s)}. \tag{5.22}$$

This still does not supply with the actual acceleration $y(t)$. For this the transfer function for the U-part in figure 5.4, $SU(s)$, and then the overall transfer function for the accelerometer $ACC(s)$, taking equations 5.19, 5.20 and 5.22 into account, need to be derived as follows:

$$SU(s) = CL(s) \frac{MES(s)}{DVA(s)}, \tag{5.23}$$

$$ACC(s) = SU(s) \cdot ICU(s). \tag{5.24}$$

Furthermore, a set of scaling factors ought to be applied to the outputs of $SU(s)$ in equation 5.23 and $ACC(s)$ in equation 5.24, in order to obtain realistic values. The scaling factors are $2.707 \cdot 10^{-5} + 1.115 \cdot 10^{-11} i \ \frac{m/s^2}{V}$ for the analog $SU(s)$ voltage output, and $2.707 \cdot 10^{-11} + 2.369 \cdot 10^{-15} i \ \frac{m/s^2}{10^{-6} V}$ for the digital output at $ICU(s)$ (Bertin (2000)).

Now, the digital output $y(t)$ of the input acceleration $x(t)$ can be determined under consideration of equations 5.11 to 5.13, with

$$y(t) = L^{-1}\{ACC(s) \cdot L\{x(t)\}\}. \tag{5.25}$$

Simplified transfer function

For the introduced transfer function $ACC(s)$ in equation 5.24 an approximation represented by a set of polynomials may be used, according to Bettadpur (2000). This substitution shall be referred to as $G_{ACC}(s)$. The advantage of replacing the nominal transfer function with a polynomial approximation is that pre-existing computer programs may use this set of polynomials in order to turn an arbitrary time series, as represented by $x(t)$, into the approximated acceleration output $y(t)$. This is very useful for testing purposes, in order to trace back signals being investigated in the frame of this work. The proposed set of polynomials used for $G_{ACC}(s)$ are the following:

$$G_{ACC}(s) = \frac{\sum_{n=0}^{2} a_n s^n}{\sum_{n=0}^{9} b_n s^n}, \tag{5.26}$$

$$a = \begin{Bmatrix} 6.05355 \cdot 10^{13} \\ 1.97951 \cdot 10^{13} \\ 1.60722 \cdot 10^{12} \end{Bmatrix}, \tag{5.27}$$

$$b = \begin{Bmatrix} 6.05355 \cdot 10^{13} \\ 2.81871 \cdot 10^{13} \\ 4.93309 \cdot 10^{12} \\ 5.08491 \cdot 10^{11} \\ 3.39074 \cdot 10^{10} \\ 1.15601 \cdot 10^{9} \\ 4.36642 \cdot 10^{7} \\ 687369 \\ 2424.86 \\ 1 \end{Bmatrix}. \tag{5.28}$$

For this work, this set has been used to derive approximate accelerations using the internal SIMULINK function LSIM inside MATLAB, a mathematical program by The Mathworks, Inc. A comparison to the transfer function stated by Bertin (2000) showed that the overall agreement is very good, except for very small deviations near 10 Hz, in the order of a fraction of a degree (Bettadpur (2000)).

Part III

Data

There are generally two types of data products: science data, which is made available for the scientific community, and housekeeping data, consisting of internal satellite data and/ or telemetry data, that is needed for a sufficient maintenance of the spacecraft instruments or its attitude and altitude. The science data products are divided into the raw science data, so called Level 1A data, and their derived Level 1B data, which are used for the actual determination of the gravity field by GRACE. Level 1A data may be considered as the result of the transformation and scaling of the measurements of the specific instruments into physical units. The process for deriving Level 1B data products is a necessary one, as all Level 1A data products are given in the nominal reference frame of the specific instruments and need to be transferred into the Satellite Reference Frame (SRF) in order to make them comparable. Furthermore, many Level 1A data products have a sampling or biases and scales that are not feasible for further processing to the gravity field and hence need to undergo further processes. Also, Level 1A data may contain gaps and errors that need to be filled or corrected.

In this section the accelerometer data as well as previous investigations concerning the accelerometer data are introduced in detail as they are indeed the main objective of this work. Other data products shall merely be briefly introduced, if they have a role within the frame of this work.

6 Science data and Housekeeping/ Telemetry data

6.1 Thruster data (THR1B)

The thruster data files THR1B contain all thruster firing events of the concerning GRACE spacecraft. For each thruster mounted on the satellite the exact time of activation is given in GPS time. Furthermore, the time the thruster was active is given in milliseconds. In addition to this, the file gives information about the total number of cycles and total on time a thruster has been active until the point of the referred activation. There are typically about 600 thruster firings per day, mainly carried out by the thrusters used for attitude maintenance.

6.2 Magnetic Torquer data (MAG1B)

In the MAG1B files the measurements of the magnetometer of the GRACE spacecraft as well as the electric current used for the on-board magnetic torquers used for attitude control are given. Since 2007 the MAG1B is given with a sampling rate of 1 second, and the time-tag is given in GPS time. The magnetic field is given by means of the three axes, which are given in µTesla and in the satellite reference frame (SRF). Six values containing the electric current given in mA for the magnetic torquers are also stored in this file. Each torquer has a set of two values. This is due to the fact that each torquer has two channels, i.e. two ways in which the current could flow. Therefore, it is mandatory that one of the channels always contains the value 0 mA as the current cannot flow both ways simultaneously. Furthermore, the MAG1B data supplies magnetometer and magnetic torquer calibration factors.

6.3 Navigation Solutions

6.3.1 GPS-Solution (GNV1B)

The GNV1B data contains the navigation solution for the GRACE spacecraft. It is available to all users at the data distribution centers ISDC of GFZ and PO.DAAC of JPL. The data is sampled with a rate of 60 seconds and the coordinates consisting in the data files are given in an Earth-fixed reference frame. The coordinates themselves are the GPS coordinates in this reference frame, reflecting the x, y and z axes, referring to the WGS84 ellipsoid. Furthermore, the files consist of the formal error of this position as well as the velocity in all three directions and the corresponding formal velocity error.

6.3.2 Geographical latitude and longitude

Geographical coordinates in terms of longitude λ and geodetic latitude φ are means to describe the location at every point on Earth's surface. Earth is being divided in 360 longitudinal and 180 latitudinal degrees, where the longitude of any point on the surface is the angle east or west of the Greenwich meridian (which is the reference meridian) to another meridian passing through that point. The longitudes converge at the north and south poles and are halves of great circles, i.e. ellipse in case of Earth. The latitude of a point on Earth's surface is the angle north or south of the equatorial plane. The latitude is the angle between this plane and straight line towards the point and its normal. As we intend to describe the geographical correlation of signals in accelerometer data it is feasible to express them in geographical coordinates as they are broadly used and easiest to be interpreted.

In order to derive the ellipsoidal coordinates the GPS data given as x, y and z values in the Earth-fixed reference frame need to be processed. Ellipsoidal coordinates are consisting of the longitude λ and latitude ϕ in which most global maps are displayed. In order to compute the ellipsoidal coordinate for the position i, following equations were used:

$$s_i = \sqrt{x_i^2 + y_i^2}, \tag{6.1}$$

$$\Phi_i = \arctan\left(\frac{z_i \cdot a_E}{s_i \cdot b_E}\right). \tag{6.2}$$

Here, s_i is the distance taking only coordinates x_i and y_i into account. Φ_i is the latitude at i. a_E is the semi-major axis of the Earth ellipsoidal and is 6378137 m, and b_E is the semi-minor axis with 6356152.31 m. With Φ_i the ellipsoidal coordinates ϕ_i and λ_i , which can be derived from the positions x_i and y_i solely, can be computed:

$$\phi_i = \arctan\left(\frac{z_i + e' \cdot b_E \cdot \sin(\Phi)^3}{s_i - e_q \cdot a_E \cdot \cos(\Phi)^3}\right), \tag{6.3}$$

$$\lambda_i = \arctan\left(\frac{y_i}{x_i}\right). \tag{6.4}$$

For any data point needed the specific location can be obtained by means of a spline interpolation between the different locations derived via GPS every 60 seconds.

6.3.3 Attitude - Star Camera data (SCA1B)

The SCA1B data files contain the data for both ASC of the regarded GRACE satellite. The information about the absolute orientation of the spacecraft is given by a set of quaternions for each ASC device, which supplies the relation between the SRF and the ITRF. In addition to this, the formal error for each individual quaternion is supplied.

6.4 Telemetry Housekeeping Power Control data

Telemetry Housekeeping Power Control data, short THPC, is a set of data which consists of the power data for each payload and subsystem mounted aboard the GRACE spacecraft. THPC are either binary, for on/off of a system, or may contain an actual voltage and other units or value. The time interval for THPC data is 3 seconds. In our study we used THPC data in order to estimate a starting and ending input current of the solar arrays and possible jumps within that current. The activation and de-activation time of the on-board heater-circuits can also be found within the THPC data files. In addition to this, the THPC contains many other data and values, such as the BUS voltage, the OBDH voltage, the charging currents, and basically any consumption of each individual payload of the GRACE space systems. The THPC data has been made available to us for the year 2008 with courtesy to the CSR of the University of Texas at Austin.

7 Accelerometer Data

7.1 Data products and processes

There are two types of science data products for the accelerometer data. The derivation of data by the accelerometer Sensor Unit and its corresponding Interface Control Unit (ICU) have been introduced in section 5.2.2 on page 41. The output of the raw 10 Hz accelerometer data is referred to as ACC1A data and are the Level 1A data products as mentioned in the introduction to part III of this thesis. ACC1A data comes in the Accelerometer Reference Frame (ARF) whose axes are parallel to the one of the SRF. The relation of the axes is as follows:

$$\begin{aligned} x_{ARF} &= y_{SRF} \\ y_{ARF} &= z_{SRF} \\ z_{ARF} &= x_{SRF} \end{aligned}$$

Data name	Description
rcvtime_intg	Time in integer seconds past 12:00:00 noon on Jan 1, 2000,
rcvtime_frac	Microseconds part of the time,
time_ref	Time reference frame (R = ARF, G = GPS),
GRACE_id	GRACE spacecraft, A or B,
qualflg	Data quality flag (bits 0 to 7),
prod_flag	Product flag to indicate presence of data type,
lin_accl_x	Linear Acceleration in m/s^2 along x_{ARF},
lin_accl_y	Linear Acceleration in m/s^2 along y_{ARF},
lin_accl_z	Linear Acceleration in m/s^2 along z_{ARF},
ang_accl_x	Ang. Acceleration in rad/s^2 about x_{ARF},
ang_accl_y	Ang. Acceleration in rad/s^2 about y_{ARF},
ang_accl_z	Ang. Acceleration in rad/s^2 about z_{ARF},
icu_blk_nr	ICU block number,
Tenhz_count	10 Hz clock count,
Mhz_count	MHz clock count.

Table 7.1: Contents of ACC1A data product files (JPL (2006)).

In addition to the regular ACC1A file-types, a housekeeping file named ACC1A_t exists, which furthermore contains among others the displacement of each capacitive sensor, the temperature of the individual units and the ICU and SU voltages.

However classified as 10 Hz sampled data, GRACE ACC1A data actually has a slightly odd sampling of 10.034 Hz, which is due to internal processes by means of retrieving the measurements as accelerations. We will keep referring to 10 Hz sampling for an easier comprehension. The sampling furthermore may suffer from slight deviations making the samples not equidistant throughout time. The ACC1A is being produced on a daily base and consists of the data displayed in table 7.1. The 10 Hz sampling solely applies for the linear accelerations, the angular accelerations are given with a rate of 1 Hz. The product flag is the indicator for each new row within a single dataset if linear only or both linear and angular accelerations are given. For ACC1A files only bits 0 to 5 should be used, whereas 0-2 are linear and 3-5 are angular acceleration data, and bits 26-28, which contain ICU block numbers, 10 Hz clock count and MHz clock count.

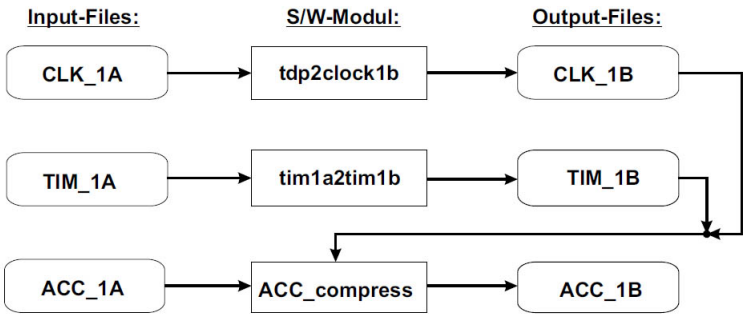

Figure 7.1: Schematic view of ACC1B Processing (Fackler (2005)).

In contrast to ACC1A, Level 1B data format ACC1B comes with strictly 1 Hz sampled data and is a derivation of the ACC1A data. Just like ACC1A, ACC1B has a time tag, which is only given in integer GPS seconds, however. Along with an identifying GRACE ID, 1 Hz linear and angular accelerations are given, as well as linear acceleration fit residuals for each axis describing the difference between the low-pass filtered, i.e. compressed, and uncompressed accelerometer data. The process of how Level 1B data is derived from Level 1A shall be described hereafter.

Level 1B processing

The process-chain to obtain ACC1B data from ACC1A may be roughly divided into 5 steps. These steps include ACC1A data analysis and preparation, derivation of the accurate GPS time, retrieval of the equidistant sampling, filtering and re-sampling, and also the transformation into the SRF.

The input files are, despite the ACC1A file, the data from the CLK1B files, which define the offset between the accelerometer sensor time as computed by the ICU and the GPS time, and, if needed, the TIM1B file, which contains data to convert the OBDH-time (OnBoard Data Handling) to the receiver time. The CLK1B file contains the satellite clock offset between the receiver time t_{rcv} and the GPS time t_{GPS} with a 300 second sampling. The GPS time is determined as follows:

$$t_{GPS} = t_{rcv} + \Delta t_{clk}. \tag{7.1}$$

As Δt_{clk} may vary with respect to time, the needed Δt_{clk} may have to be interpolated in order to retrieve the correct value probably located between the 300 second sampled data points. The overall chain of processes in terms of input and output files is displayed in figure 7.1.

The first step is to eliminate erroneous data within the ACC1A, such as outliers. In order to identify erroneous data the quality flag in the ACC1A data is considered (cf. table 7.1), which indicates erroneous behaviour of the instrument. For example, the flags may indicate a missing synchronization between the OBDH and the IPU clock, or that the time tag itself is defective. Furthermore, data gaps are being identified. Any data gap being larger than 0.2 seconds will be extended by 1 second to either side in order to make sure that no erroneous data will affect the further process. If needed, the OBDH time will be converted into the receiver time at this point. Existing data gaps are filled by a cubic polynomial interpolation, if they are shorter than 100 seconds. 200 data points to each side are considered to retrieve the exact interpolation.

As a second step, the GPS time for the measurements is derived. The satellite clock offsets Δt_{clk}, as introduced above with the CLK1B data product, are being determined for every acceleration measurement by a cubic interpolation. In case of an existing data gap within the CLK1B data, Δt_{clk}will be derived by inter- or extrapolation, and the ACC1B data will be given a quality flag as an indicator at the corresponding times. In addition, a constant value of 0.14 seconds needs to be subtracted, which is due to the Butterworth-filter delay in the process of the instrumental data determination, which extends the equation 7.1:

$$t_{GPS,ACC} = t_{rcv} + \Delta t_{clk} - 0.14s. \tag{7.2}$$

In the third step the linear and angular accelerations will be re-sampled to full integer multiples of 0.1s by means of a quadratic Lagrange interpolation. At this point, the uncompressed accelerometer data is obtained, and is now feasible for filtering as the sampling is equidistant. Afterwards, the angular acceleration data will be re-sampled to full integers of 1 second.

Now the linear accelerations can be filtered. This is carried out with the digital low-pass CRN-filter of order 7 and a bandwidth of 35 mHz, covering a time-span of 140.7 seconds around the sampled data point. The results is now the compressed 0.1 s sampled linear accelerometer data. The data will be re-sampled to full integers of 1 second afterwards. If the residuals between the compressed and uncompressed data points are exceeding the threshold of $1 \cdot 10^{-8}$m/s^2, a quality flag will be set within the ACC1B data corresponding to these data. As a final step the linear and angular accelerations will be transformed from the ARF into the SRF.

7.2 Previous investigations on linear accelerometer data

This section shall give an overview of the investigations carried out in the past concerning the linear accelerations of the Science Mode output of the Level 1A accelerometer data, named ACC1A (e.g. by Flury et al. (2008); Fackler (2005); Frommknecht (2007); Hudson (2003)). The focus lies on the 10 Hz Level 1A ACC1A data as our investigations are carried out based on these data. For the scheme of this work, the data products themselves are described in chapter 7. We chose to introduce these works as they may be considered to be milestones concerning the investigations of GRACE ACC1A data. However, we can only discuss their results briefly and the interested reader may be referred to the individual publications of the corresponding investigations. Investigations of the angular accelerometer shall be neglected at this point, as in the frame of this work merely the linear component of the accelerometer is being regarded. This is due to the fact that angular accelerations are only delivered with a sampling of 1 Hz and hence is not feasible for our analysis.

7.2.1 General 10 Hz data quality assessments

Early investigations on the data quality of the accelerometer intended to verify that the accelerometers are detecting the spacecraft environment such as air drag of the residual atmosphere, solar radiation pressure or albedo to a satisfying level. In order to verify the accelerometer data in this regard, the data may, for instance, be compared to several more or less accurate models describing the satellite's environment. The air drag has the major contribution of the three introduced environmental impacts onto the satellite, with its major impact on the along-track component of the data and with a magnitude of several $1 \cdot 10^{-7}$ m/s^2 and one order of magnitude

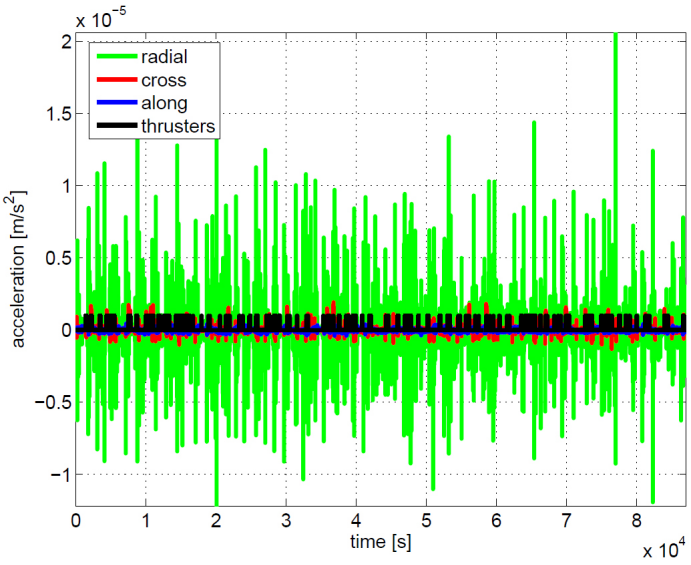

Figure 7.2: 10 Hz ACC1A linear data of GRACE A. Radial component is by far largest, followed by cross-track and along-track (Frommknecht (2007)).

less for the other two axes (Frommknecht (2007)). Hence, the expectations that the data in the along track component is strongest are legitimized. However, Frommknecht (2007) shows in his work, that for both satellites, GR-A and GR-B respectively, the along track Level 1A data component shows to have the smallest magnitude of all three axes (cf. fig. 7.2). In accordance to this result, it is stated that the cross-track axis shows to have a greater impact by firing events of the on-board cold-gas thruster system. Furthermore, the radial component is by far the largest. Here, twangs are found to be the dominating effect - they will be discussed in section 7.2.5 and furthermore in the grander scheme of this work.

For the performance determination of the accelerometers, however, only data without peaks caused by thrusters can be used. Also, the effects due to other instruments should be either non-existent or as small as possible (see following sections for these effects). According to the investigations carried out by Frommknecht (2007) the performance of the sensitive axes, along-track and radial, is about 5 times worse than predicted by the instrument specifications, where the performance for the less-sensitive cross track axis appears to agree with the specifications. For determination of the gravity field only the differential accelerations are considered, which is the acceleration of one satellite subtracted from the acceleration of the other. In this regard, the level for the sensitive axes are about 2 times worse than the specifications with regard to the 5 second sampling used in Level 1B data, or 3 times worse with respect to 1 second sampling, according to Hudson (2003) and Frommknecht (2007). Newer investigations carried out by Flury et al. (2008) could show, that in less noisy periods, with the heater circuits on-board of the satellite being inactive, the accelerometer quality is indeed matching the pre-launch specifications (cf. section 7.2.3 for further information). The general noise level for ACC1A data and their standard deviations σ may be deduced from table 7.2 and are provided as PSD (Fackler (2005)).

Axis/ Satellite	in $\frac{(m/s^2)}{\sqrt{Hz}}$	Along Track	Cross Track	Radial
GRACE A	noise level	$3.6 \cdot 10^{-9}$	$9.9 \cdot 10^{-9}$	$2.2 \cdot 10^{-8}$
	σ	$8 \cdot 10^{-10}$	$2 \cdot 10^{-9}$	$8 \cdot 10^{-10}$
GRACE B	noise level	$3.6 \cdot 10^{-9}$	$1.4 \cdot 10^{-8}$	$3.1 \cdot 10^{-8}$
	σ	$8 \cdot 10^{-10}$	$2 \cdot 10^{-9}$	$8 \cdot 10^{-10}$

Table 7.2: Noise level of the axes of the accelerometer of GR-A and GR-B (Fackler (2005)).

The main causes for the high noise level are found to be the thruster activation, heater activation and de-activation as well as the so-called twangs (for all these effects, cf. the next sections). According to Fackler (2005) twangs are the main reason for the high noise level of the radial component for both spacecraft, and they make up to 30 % of the data, and the main contributions to the noise in along-track and cross-track are thruster activations. Heater activations and de-activations affect most of the data in all axes, disregarding the amplitude and only referring to the time aspect.

7.2.2 Cold-gas thruster system impact

The set-up of the cold-gas thruster system on the GRACE spacecraft is to control the attitude of the spacecraft. For a perfect system this should exclude any impact onto the linear accelerometer data. However, as depicted in figure 7.3, the impact of cold-gas thruster activations is clearly visible in the 10 Hz Level 1A accelerometer data on both spacecraft (Frommknecht (2007)). There may be two reasons as to why thruster events are able to map into linear accelerometer data: the first is describing an offset of the center of mass of the accelerometer proof-mass with respect to the center of mass of the satellite. If this is the case, the accelerometer is in fact not experiencing a real linear acceleration. The mass trim assembly of the GRACE mission reconfigures the center of mass - these maneuvers are carried out regularly to maintain the proof-mass within a range of 100 micrometers to the actual center of mass of the satellite. Except for the two orbit maintenance thrusters, all thrusters should enforce a torque upon the spacecraft and should hence not be a linear acceleration, but only angular accelerations. If the proof-mass is not within very strict boundaries in the center of mass of the spacecraft, the accelerometer will detect a linear acceleration, however. The second reason is actual linear accelerations due to an angle misalignment between the pairs of thrusters, or differences in the thrusting force or thrusting time. These actual linear accelerations are more likely to occur than an impact due to an unbalanced spacecraft mass. The knowledge of whether this is an actual linear acceleration or not may be of importance as it may be contained within the K-band measurements as well in the 10 Hz Level 1A accelerometer data. The spikes may have magnitudes of up to $2 \cdot 10^{-6}$ m/s^2 for the cross-track component, $4 \cdot 10^{-7}$ m/s^2 for the radial and $4 \cdot 10^{-8}$ m/s^2 for the along-track axis (Frommknecht (2007)).

Roesset (2003) could show that thruster firings are not only strongly visible within raw 10 Hz accelerometer data, but by means of the filtering process in order to obtain Level 1B data from Level 1A data the impact of the thruster firings are visible in accelerometer data with a more sparse sampling. In fig 7.4 on the left, this effect is clearly visible. In the 0.1 second sampled data, the thruster firing events are clearly observable as a sudden, downward pointing spike. The lines with the solid black dots, and white squares respectively, represent filtered data to 1 s and 10 s sampling. As the thruster firings do translate into lower sampled accelerometer data, such as Level 1B, there is a possibility of these signals translating into the gravity field based on GRACE data, as in the process for deriving the gravity field the Level 1B accelerometer is considered to

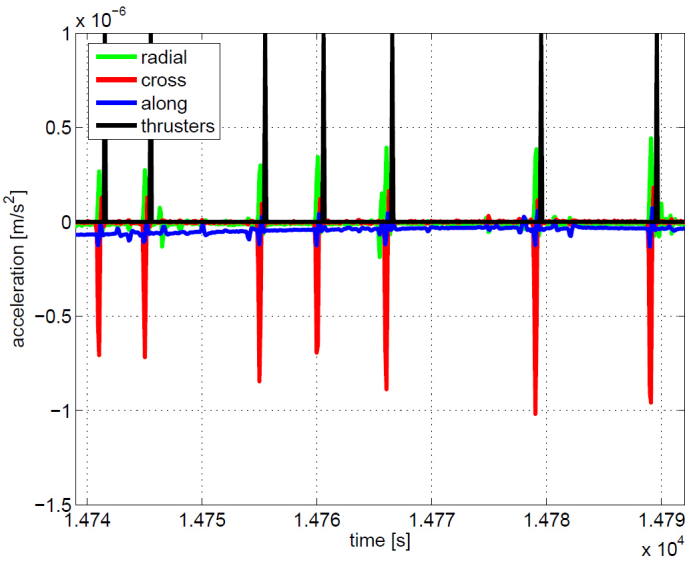

Figure 7.3: Cold-gas thruster events in time domain of linear ACC1A data of GRACE B (Frommknecht (2007)).

reduce non-gravitational effects within the KBR measurements. In a simulation study Roesset (2003) showed an impact of the thruster firings by comparing a simulated gravity field with degree and order of 50 to the EGM96 gravity field in terms of geoid differences. In figure 7.4 (right) the differences of a perfect 7-day based gravity field where no thrusts are needed to the EGM96 are displayed, as well as the differences of a simulation where thrusts were included. The result of this simulation showed, that the differences to the EGM96 gravity field are by one order of magnitude larger, giving evidence for a theoretical impact of the thruster firings into the gravity field mapped by GRACE, considering the EGM96 as a more accurate gravity field representation.

7.2.3 Heater influences

Detailed investigations concerning the influences of heater and heater circuit activations and de-activations on the raw 10 Hz accelerometer data, ACC1A, have been carried out by Flury et al. (2008). Driven by the fact that a lot of data is affected by high-frequency peaks, which may occur as regularly as once per second with alternating amplitudes, investigations regarding their cause were carried out. Led by the investigations of Grunwald and Bock (2000), who investigated the presence of spikes caused by heater activations and de-activations within the CHAMP accelerometer data, the cause for these peaks within the GRACE accelerometer data could be safely linked to heater switching events on-board of the GRACE spacecraft. However, prior to mission this was believed to be impossible, because based on the CHAMP experiences the cause was believed to be of mechanical origin and hence the GRACE platform was made from very stiff carbon fiber reinforced plastic (CFRP) material.

Since May 2007 GRACE thermal control data is being delivered with a 1 Hz sampling in the THPC format within the housekeeping data. This data is strictly binary showing an activated or deactivated status of the corresponding heater circuit. There are 64 heater circuits on each GRACE spacecraft, consisting of one or more heaters, and their activation and duration is autonomously determined as well as commanded by the on-board thermal control system. Information delivered from the thermal sensors to the thermal control system are the key driver

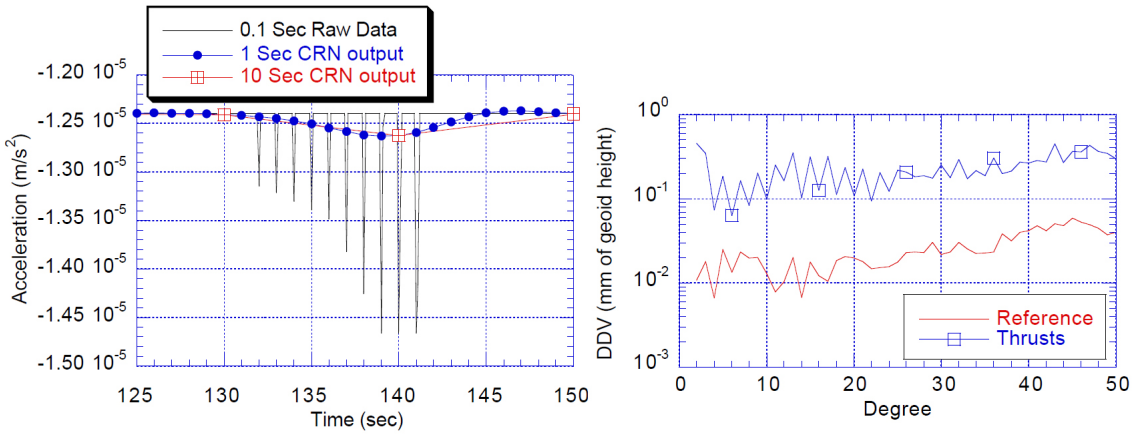

Figure 7.4: Left: Raw 10 Hz accelerometer data including thruster firings (sudden spikes) compared to filtered data to 1s and 10s sampling by means of a CRN-filter. Right: Differences of a simulated gravity field up to d/o of 50. Both lines describe the differences between a simulated gravity field and the EGM96.The blue line includes simulated thrust spikes, and these differences are by one order of magnitude larger than simulations with no thrusting spikes. (Roesset (2003))

for these commands. A thermal sensor is mounted aside of each individual heater, as some instruments require a very strict thermal stability and thus a detailed information about the temperature at different parts of the spacecraft is needed. The active periods of a circuit may last up to 40 seconds, and the periods between activations may range from 1 to several thousand seconds. Taking into account all heaters on-board of a single GRACE spacecraft, the overall switching events per day is typically as high as 120,000.

Combining the time-tagged heater data with the corresponding times of the ACC1A data a large number of spikes can be found, strictly corresponding to the switching events of the heater circuits, cf figure 7.5 (left). They appear simultaneously in all three axes, and every heater can be distinguished in the ACC1A due to the timing of the event and the characteristics of the spike in the ACC1A data by means of shape, amplitude and duration. The following results are shown for one satellite only, as both GRACE satellites appear to have very similar characteristics with respect to the heater issue.

By extracting a few seconds of ACC1A data corresponding to the switching events for individual heaters and the following superposition of that ACC1A data referenced to the time of the switching event of that heater given in the THPC dataset, spikes for every individual heater in all three axes are clearly resolved, as depicted in fig. 7.5 (right). As the ACC1A is not exactly 10 Hz sampled, but has a slightly odd sampling of 10.034 Hz, the shape can be clearly resolved.

The standard deviation of the scatter of a spike may be ranging from 1 nm/s^2 for the along track axis to 3 nm/s^2 for the cross track axis. At the extrema of the spike this scatter may reach values of up to 15 nm/s^2 and is corresponding to the systematic voltage variations of the spacecraft battery (Flury (2011)).

Furthermore, from figure 7.5 (right) it can be deduced that each spike occurs with a delay to the actual switching epoch at 0s, which is given in the THPC data. This delay is very constant, as visible by the clearly resolved spike. The delay has at least three causes: One is that the heater switching time gates are not exactly at the given time-tag of the heater data. The second would be a delay within the accelerometer sensor and its control unit, and the last reason is the internal butterworth filter applied for digitizing the accelerometer measurements, which would also explain why the delay is not the same for the three axes of the accelerometer.

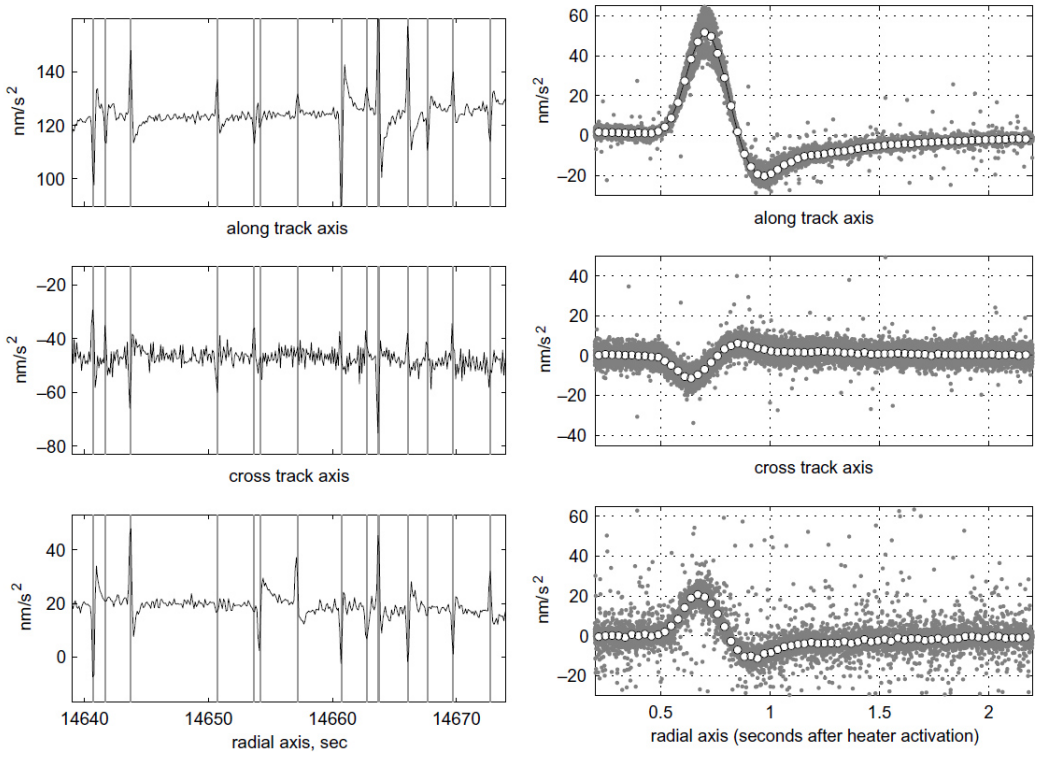

Figure 7.5: Left: Typical spikes in ACC1A data due to heater activations and de-activations, highlighted by the vertical lines. Right: superposition of ACC1A data referenced to de-activation events (1414 single events) for a specific heater (THHA0113) on GRACE A - the dotted lines are representing the average spike model (Flury et al. (2008)).

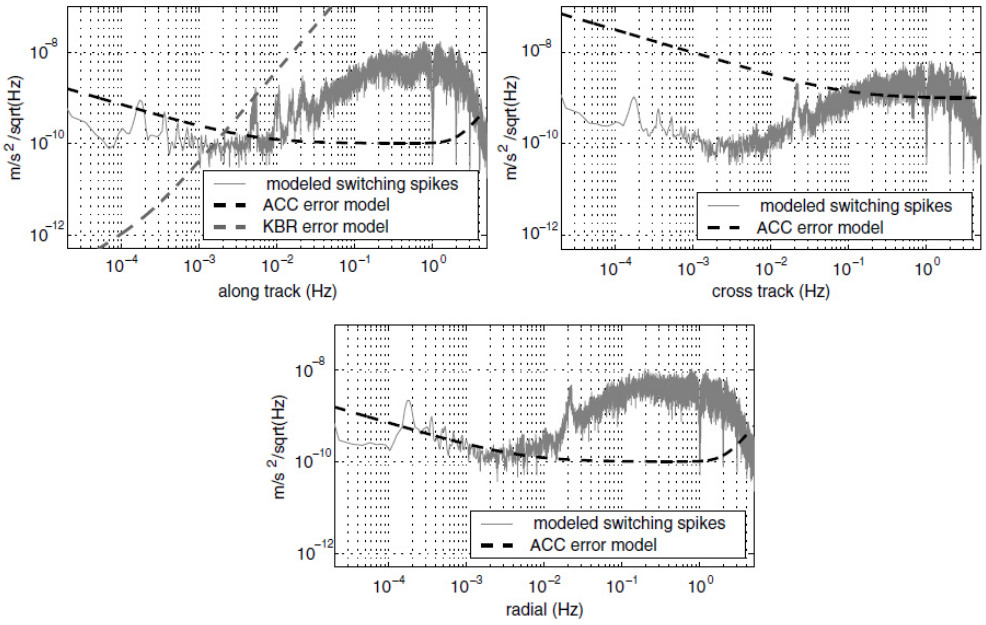

Figure 7.6: PSD of the time-series of heater-spikes for one day in 10 Hz, compared to the specific error model curve for the corresponding accelerometer axis on GRACE A (Flury et al. (2008)).

The amplitudes of the spikes are ranging from 10 to 70 nm/s^2 for 8 groups of heaters located near the accelerometer and from 0.5 to 10 nm/s^2 for 18 other groups of heaters. Other impacts of other heater circuits show either no detectable impact on the ACC1A data or could not be fully understood up to now.

Furthermore, the investigation by Flury et al. (2008) showed that the mounting direction of the heater does not affect the orientation or amplitude of the spikes observable in the accelerometer data. This may be regarded as a hint that not the mechanical effect of the heater itself may cause the spike, but that it is rather of electro-mechanical nature. Also, the investigation could show, that the accelerations of the spikes are generally tending to be a net zero acceleration and hence may not be regarded as an actual linear acceleration.

Beyond these investigations, Flury et al. (2008) were able to build models of the spikes for all three axes of the accelerometer data with respect to any individual heater found to have an impact onto the ACC1A data. With these models time series of heater spikes can be computed, from which Power Spectral Densities (PSD) may be derived. In figure 7.6 PSDs for a day of time series of heater spikes in 10 Hz are shown. There are high amplitudes between 0.1 and 3 Hz, furthermore distinct peaks at 0.1 Hz and 4 mHz, which can be associated with regular switches of the heater circuits. In comparison with the error model specifications it is notable that a slight influence upon the gravity field determined by GRACE might be possible in theory, but is believed to be unlikely.

7.2.4 Magnetic Torquer influences

In Peterseim et al. (2012), and in more detail in Peterseim (2010), we showed that the change of the electric current used for the magnetic torquers used for attitude maintenance has a detectable influence onto the raw 10 Hz accelerometer ACC1A data. The investigations carried out concerning this issue are indeed similar to those carried out by Flury et al. (2008) as described in the previous section.

The data for the electric current strength used for the magnetic torquers are provided by the GRACE data distribution centers ISDC and PO.DAAC and are part of the MAG1B data product (cf. chapter 6.2). As the electric current may alter with a frequency of 1 Hz and is given in accordance with a time-tag for any of the three magnetic torquers for each spacecraft, this effect can be well observed by investigating the corresponding ACC1A for each event. As the signal within the ACC1A data due to magnetic torquers is significantly smaller than the amplitudes due to other impacts, the effects of other sources need to be either avoided in the frame of this study or diminished. In order to investigate the influence of the magnetic torquers, modeled time series with spikes due to heater activations and de-activations provided by Flury et al. (2008) were subtracted and any data affected by thruster firings or twangs neglected. Furthermore, we applied a 35 mHz high-pass filter to avoid the dominating effects of the non-gravitational forces acting upon the GRACE spacecraft. The 35 mHz high-pass filter is in fact the inversed CRN-Filter used for Level 1B derivations.

The study was based upon the assumption that a spike should always be visible at the same fraction of the integer second of the electric current change provided by the MAG1B data. We could prove that a spike occurs simultaneously in all three accelerometer data components, where the largest signal was found in the axis with the same orientation as the corresponding magnetic torquer. As GRACE A and GRACE B showed very similar results, the following results hereafter apply for both spacecraft. A spike due to electric current changes in the magnetic torquers usually is consisting of two peaks with opposite orientation (cf. fig. 7.7, left). Also, we could show that the amplitude and duration of spikes were the same for electric current changes from the same initial current I_1 to the desired current I_2. Hence, it was feasible to extract the 10 Hz high-pass filtered accelerometer data points for a specific current change magnitude and magnetic torquer rod with a time span of a few seconds before and after the actual current change. Then the extracted accelerometer data was referenced to the epoch of the current change given in the MAG1B data and furthermore superimposed in order to obtain a well resolved spike, as is depicted in figure 7.7 (left). Here, a spike due to an electric current change from 0 mA to 48 ± 3 mA in the along-track magnetic torquer is shown, the dots representing the extracted and superimposed accelerometer data in the along track component for a large number of corresponding events, and the solid line an average of the spike. The spike visible approximately one second past the spike occurring at approximately 0s is due to a following current change and shall not be regarded. The slightly odd sampling of 10.034 Hz for the ACC1A data helps to resolve the spikes more smoothly.

By means of this superposition, average spike models could be determined. The results show that the spikes due to electric current change processes within the magnetic torquer rods are a regular and well observable signal for larger electric current changes, with respect to timing, amplitude as well as the shape. An interesting phenomenon occurs when investigating the behavior of an accelerometer data component due to electric current change of the magnetic torquer rod of the same orientation, after that magnetic torquer has undergone a change of the magnetic dipole, i.e. a change of the direction of the electric current. In these cases the amplitude is significantly greater than compared to those spikes due to the same electric current change where the current flow direction did not change (cf. fig. 7.7, right). Here, more than two spikes in the same duration as the normal spike occur.

The amplitudes of the spikes do not increase linearly with an increasing current change, but rather exponentially, as can be seen in fig. 7.8 (upper left). In this picture, the average amplitudes for each step in the along track accelerometer component due to current changes with the initial current of $I_1 = 0$ mA in the along track magnetic torquer are displayed. The upper line represents the average amplitudes of the positive peak of the spike, and the lower line the amplitudes for the negative peak. They are derived by means of a cubic regression.

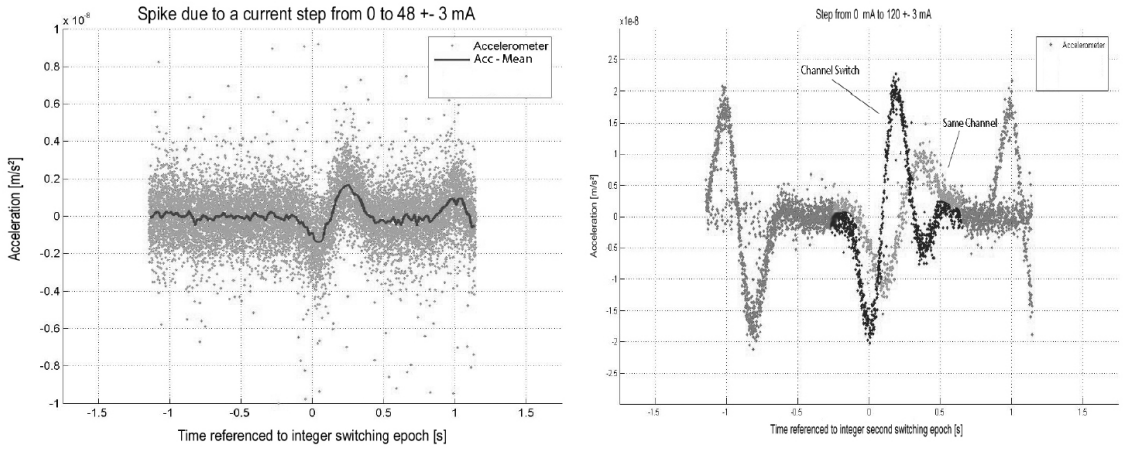

Figure 7.7: Left: Spike in along-track accelerometer data due to a current change from 0 to 48 ± 3 mA in the along-track magnetic torquer - the dots represent the superimposed accelerometer data and the solid line the average spike. Right: Two different types of spikes for a current change of the same magnitude from $I_1 = 0$ to $I_2 = 120$ mA. The spike with the greater amplitude (dark gray) occurs when the channel has changed the second before the actual current change. The spikes at approximately ± 1 s are due to current changes prior or after the investigated current change and the magnitude of these steps may vary (Peterseim et al. (2012)).

For the maximum electric current change magnitude of ± 120 mA the largest impact was usually within the order of 10 nm/s^2 if no change of the dipole direction occurred in the previous second. If the latter was the case, the spike could reach amplitudes twice as large (up to 20 nm/s^2).

In accordance with the heater spike modeled time series by Flury et al. (2008) we were able to derive mean models by the well-resolved spikes due to the superposition, with which we were able to compute modeled time-series consisting of spikes evoked by electric current changes in the torquers. From the modeled spike time series, PSDs due to the spike signals could be derived. These are displayed in fig. 7.8 for all axes and compared to the noise models of the corresponding accelerometer axis. It is obvious, that for regular science mode hardly any low frequencies exceed the accelerometer model, and that a significant impact on the gravity field determined by GRACE is rather unlikely, however hypothetically possible.

7.2.5 Early investigations on twangs

Twangs probably remain the most mysterious signal concerning high-frequency signals to be found within the raw 10 Hz accelerometer data prior to this work. Few investigations are directly dedicated to twangs. A twang itself is a sudden spike in the accelerometer data that is consisting of two peaks, and often followed by an oscillating decay. Twangs can have a duration of several seconds. The name twang derives from its general shape, reminding of the characteristic shape of the signal in the oscilloscope occurring to the sound of a vibrating string, for instance by a bow or a musical instrument, like the string of a modern guitar.

The source of twangs is not yet fully resolved, but in early works it was believed to be due to a vibration of the radial insulation of the GRACE spacecraft (i.e. Hudson (2003), Flury et al. (2008), or Davis (2013)). For further information about the hypotheses of the cause of twangs, part V of this work may be consulted.

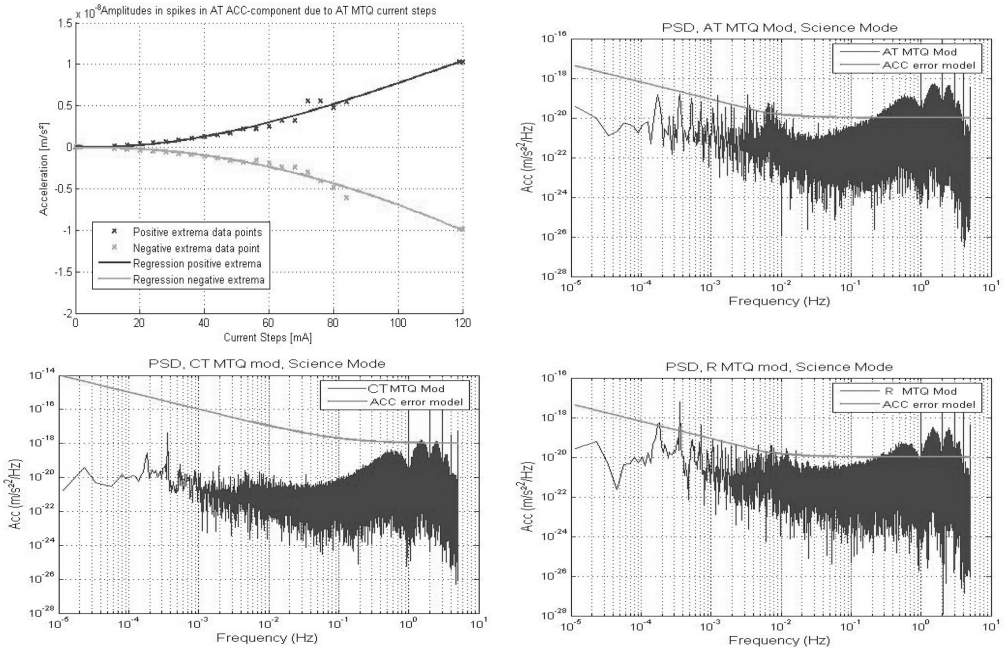

Figure 7.8: Upper left: Amplitudes of spikes in along-track accelerometer component due to positive current change from $I_1 = 0$ mA to any current value I_2 up to 120 mA in along-track magnetic torquer. The upper line is a cubic regression for the positive peak of the spike, the lower line for the negative peak. Other figures: Spectral signal content (PSD) of modeled magnetic torquer current step spikes for one day in heater-free Science Mode data, compared to the expected accelerometer error model. (Peterseim et al. (2012))

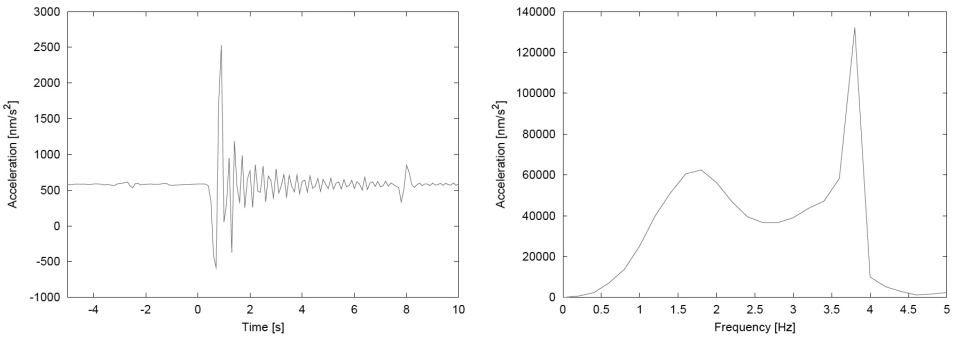

Figure 7.9: Sample of a twang in the radial component with its corresponding spectrum (Hudson (2003)).

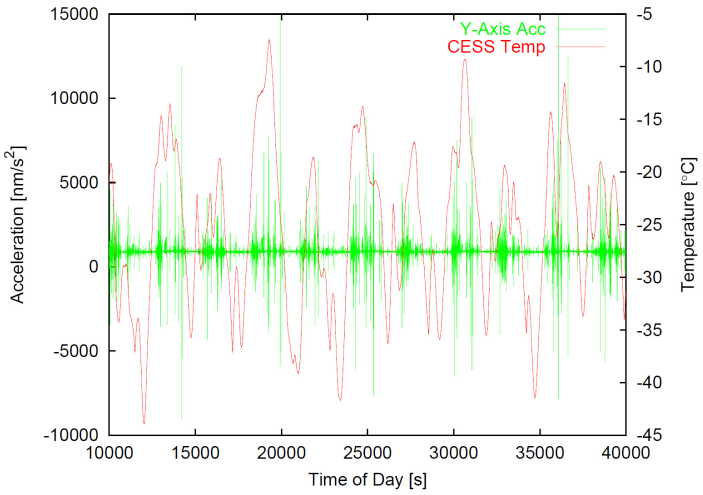

Figure 7.10: Radial component of raw 10 Hz accelerometer data and CESS temperature values (Hudson (2003)).

Hudson (2003) investigated the signal of twangs in more detail and described twangs as a type of signal coming in a variety of shapes and sizes, with amplitudes typically of a few thousand nm/s^2, sometimes reaching up to $20,000\ nm/s^2$ in the radial component. The duration varies from a single oscillation to a slower decay of almost 10 seconds, where the oscillation may have a consistent frequency between 3.5 to 4 Hz. Twangs have their biggest impact in the radial component of the accelerometer data and are by several orders of magnitude smaller in the other axes. They often appear simultaneously in all three axes. A sample twang and its corresponding PSD is displayed in figure 7.9. About 30% of the radial accelerations, about 3% of the cross-track accelerations and approximately 1 % of the along-track accelerations in the 10 Hz accelerometer data are affected by twangs (Frommknecht (2007)). According to Fackler (2005) and Frommknecht (2007) the twangs are the main reason as to why the noise level in the radial accelerometry observations are exceeding the expected noise level, being 5 times higher than specified prior to launch of GRACE.

Furthermore, Hudson (2003) discovered geographical dependencies as for the global distribution of twangs in the accelerometer data. These dependencies correspond mainly to latitudinal trends in combination with seasonal variations. The majority of twangs is strongly restricted to patterns in latitudes near the equator. Also, it was stated, that more than 99% of the twangs appear to have a net acceleration of less than 8.4 nm/s^2, and a vast majority of these even less than 2.8 nm/s^2. This hints at twangs being of net zero accelerating nature, meaning that they are not contributing to actual linear accelerations. The actual acceleration can be determined by means of integrating the corresponding acceleration signal. If acceleration and deceleration due to one signal are of a net acceleration close to zero, no actual acceleration is expected.

In the work of Hudson (2003) it is moreover stated, that the activity of twangs in the radial accelerometer data component is most likely to pick up at higher temperatures. In figure 7.10 this correlation is displayed by means of the temperature of the CESS device being in accordance with the raw 10 Hz accelerometer data in radial direction.

In the following chapter we will address the phenomenon of twangs within the 10 Hz accelerometer data in detail. We will introduce alternating ways of looking at this specific problem and will present a way of building a model for twangs by means of a set of parameters, which can be analyzed themselves.

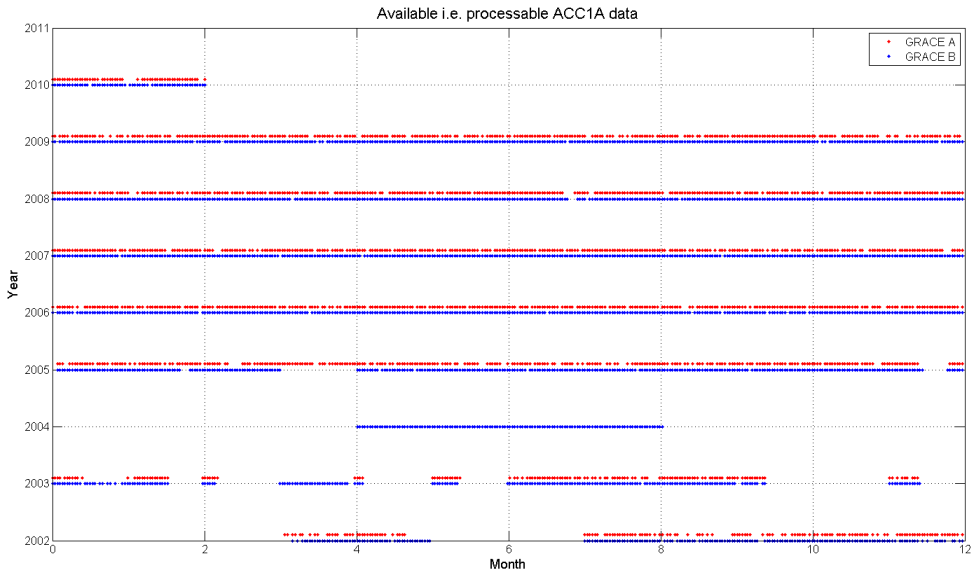

Figure 8.1: ACC1A data available and used for twang investigation.

8 Twangs in ACC1A data

In this part of the study we will describe how twangs can be characterized with respect to their expected frequency as well as their shapes. Also, we will give a description of the approaches we made use of in order to detect twangs within the Level 1A accelerometer data (ACC1A), and which techniques were employed to model, i.e. reconstruct, the twangs. Derived from these processes a time-series of modeled twangs can be obtained, which can be used for deriving Power Spectral Densities (PSD) in order to reveal possible periodical influences. Also, brief discussions concerning the propagation of twangs from 10 Hz Level 1A to 1 Hz Level 1B accelerometer data as well as possible influences onto the gravity field as determined by GRACE are given.

Our investigations on twangs cover a time-span from the start of the mission in March 2002 until February 2010. There are data gaps as not all the data was available to us during the time of investigation. Also, some files were corrupt or not feasible for the investigation of twangs. Figure 8.1 displays the data this study is based upon. If not stated otherwise, the results describe the average results of this data.

8.1 Brief description of twangs

This section is an introduction into twangs. It shall give an overview of what twangs may look like and in which components of the ACC1A data they appear. A more detailed discussion of the parameters that describe a twang in terms of shape, amplitude, duration and oscillation can be found in section 8.3.2.

In the ACC1A data of GRACE twangs can be spotted visually by observing the radial component of the data. This is due to the fact that the amplitude of an average twang exceeds the noise level of the radial component by a factor of 3 or more. Figure 7.10 on page 60 already gives an impression of the magnitude of a twang compared to the noise level of the accelerometer, which can be derived from the calm periods in between the twangs. Twangs are the largest

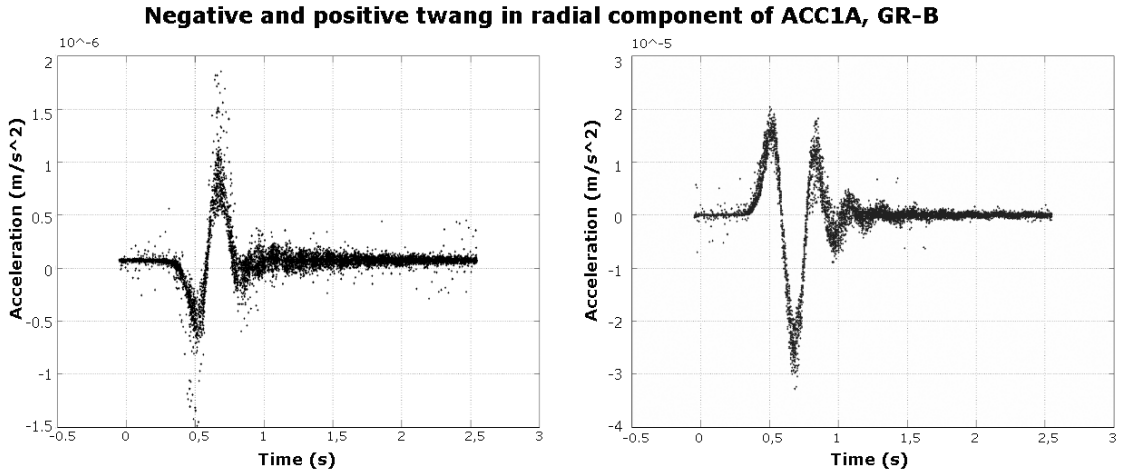

Figure 8.2: The two main types of twangs occurring in ACC1A data - negative (left) and positive (right) type. The visible third major peak in the positive twang is due to the asymmetry of the amplitude of the first two peaks.

high-frequency signals found within the ACC1A data, and the average absolute amplitude in the radial is usually $(1.07 \pm 0.05) \cdot 10^{-7}$ m/s^2, but for some cases a twang may exceed an amplitude of $2 - 3 \cdot 10^{-5}$m/s^2. Figure 8.2 displays two types of twangs most likely to be found within the radial component.

We assume that most twangs can be related to these two types. For an easier comprehension we will refer these two types of twangs from now as to 'negative' and 'positive' twangs. A negative twang describes a twang where the first major peak, between seconds 0.35 to 0.6, is oriented negatively, and its counterpart the positive twang has this peak oriented in the opposite direction. Both types of twangs are characterized by two major peaks, where the first peak ranges from 0.35 to approximately 0.6 seconds, and the other major peak is directly following the first peak, from approximately 0.6 to 0.8 seconds. From the start to the end of the second peak this results in an average duration of 0.4 to 0.5 seconds for any twang found in the radial component of the accelerometer data. While some twangs may decay below noise level right after the second major peak, other twangs are followed by a visible oscillating decay, sometimes covering a time-span of up to 2-3 seconds after the second peak. Our studies state that the length as well as the amplitudes of this damped oscillation is depending on the imbalance of the amplitudes of the two foregone major peaks. If the ratio between these two peaks is one, or relatively close to one, no oscillating decay may be observed. On the right side in figure 8.2 the starting oscillation can be seen at approximately 0.8 seconds.

Twangs occur simultaneously in all three components of the ACC1A data. However, while twangs can be easily observed in the radial component, detection in the other two components is significantly harder, as they are 1-2 order of magnitudes smaller in the along-track component and one order of magnitude smaller in the cross-track component on an average. This leads to an average amplitude of $(3.95 \pm 0.78) \cdot 10^{-9}$ m/s^2 for the along-track component, and $(1.8 \pm 0.61) \cdot 10^{-8}$ m/s^2 for the cross-track component, respectively. Yet, knowing that a twang occurs in all three axes allows detecting a twang via the radial component. The average duration of the twang (excluding the oscillating part) is the same in all three axes. In along-track and cross-track components the ratio between the two major peaks of the twang hardly ever deviates from one, resulting in a non-existing or not observable oscillation following the actual twang. A rather interesting effect is that the twangs in the three components show no consistency regarding their

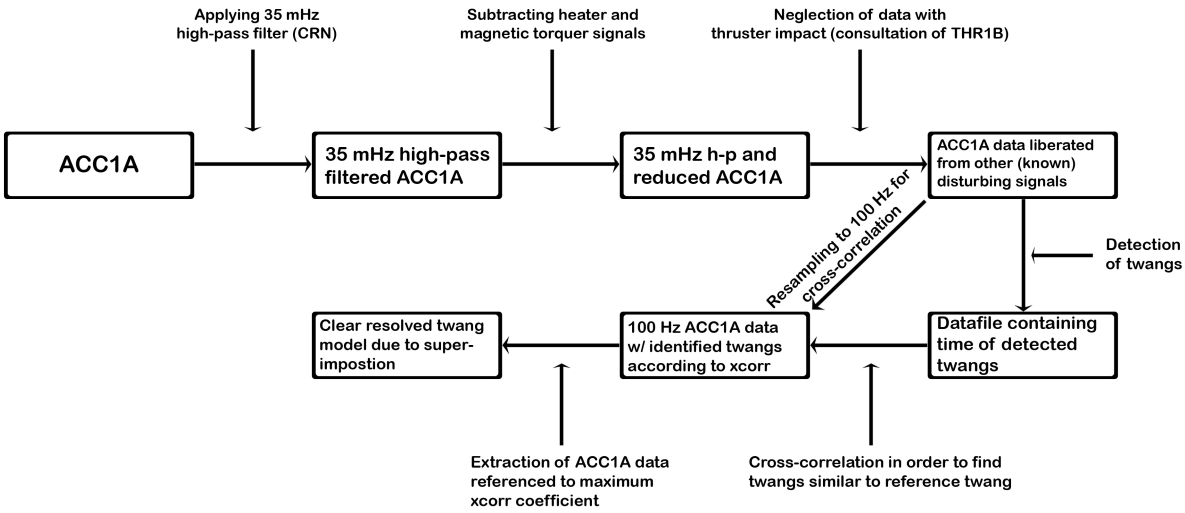

Figure 8.3: Schematic view of the steps necessary prior to detection and investigation of twangs.

orientation. This means that for example negative twangs in the radial direction do not result in twangs of one fixed orientation in the other axes, but are merely subject to change for each case (also cf. part IV of this work). In fact, 57.5 per cent of the along-track twangs and 57 per cent of the cross-track twangs show the same orientation as the radial twangs in case of GRACE B. This is in contrast to any other signal and effect in the ACC1A data previously introduced in section 7.2. Furthermore, even if for most detected twangs a simultaneous signal could be observed in the other two axes, this was not the case for every twang. For approximately 11 per cent only in two axes a twang could be safely detected, and slightly less than 5 per cent only in the radial component a twang could be detected. Yet, many of the non-found or non-regarded twangs were neglected due to uncertainties, such as overlaying noise or other signals, and do not imply that a twang does not always occur in all three axes.

8.2 Identification

In this study we apply two approaches in order to investigate twangs in ACC1A data of GRACE, where one is the actual detection method, and the other one is to classify the twang. Both are used in order to guarantee that a twang is properly detected as an outstanding signal within the ACC1A data and can be assigned to a special group of twangs in order to determine its parameters (cf. following section, 8.3.2). Whereas the first approach computes the ratio of each RMS of two successive intervals in ACC1A data, the second approach is more analytical and makes use of cross-correlation. The first approach is a necessary step in order to avoid noise to be identified as a twang by means of the shape.

8.2.1 Preliminary Steps

Before twangs within ACC1A data can be detected, certain steps need to be carried out in order to avoid any possible influences due to other sources. Figure 8.3 displays a scheme of the preliminary steps.

In addition to high-frequency signals due to on-board instruments or other sources the ACC1A data contains also the low-frequency signals due to atmospheric (thermospheric) drag, solar radiation pressure as well as albedo. For an analysis of signals with a high-frequency nature it is necessary to remove any low-frequency signal. This was realized by means of a 35 mHz high-pass filter. We made use of the official CRN-filter, which is indeed a 35 mHz low-pass filter and used in order to derive ACC1B data products. However, a 35 mHz high-pass filtered ACC1A signal can be retrieved by subtracting the 35 mHz low-pass filtered ACC1A signal. The CRN-filter is explained in detail by Wu et al. (2006).

In order to avoid known third-party induced signals as well as other possible disturbing effects the ACC1A need to be pre-processed before a successful identification of the twangs may be carried out. Known signals that may impact the results of the identification process are due to thruster activations and de-activations, heater switch events as well as current changes within the magnetic torquer rods. These signals were discussed in the previous chapter (cf. chapter 7.2, p. 50). For the signals related to magnetic torquer electric current changes model spike time-series for ACC1A per day were produced by us and were hereinafter subtracted from the ACC1A data. Analogously to this approach, model spike time series due to heater switching events corresponding to the ACC1A data computed by Jakob Flury's group of the Institut für Erdmessung (IfE) at the Leibniz Universität Hannover were subtracted from ACC1A data. This yields ACC1A data which is free from heater and magnetic torquer induced signals.

Furthermore, thruster firing events may result in signals of large amplitude within the ACC1A data. As thruster events are indeed an actual angular or linear acceleration, no time series for a subtraction of thruster spikes from ACC1A data exist. However, due to the availability of the THR1B data files, that contain the exact time stamps for thruster activations and de-activations, the corresponding ACC1A can be neglected and hence are not regarded in the further investigation and analysis process of twangs. As the implementation of the CRN-filter consequently extends the signal due to the thruster activation-deactivation processes to an unknown extent we decided to disregard ± 30 s of the ACC1A data with respect to the thruster events. This time-span was regarded as a safe amount of time in order to avoid a possible thruster induced impact. Due to the enormous amount of twangs per day and the broad availability of ACC1A data covering several years, we are left with a sufficient amount of twangs in order to carry out a successful investigation, so that this time saving approach is justified.

8.2.2 RMS-ratio detection approach

This approach was already used by Hudson (2003) in order to implement a fast tool to detect twangs within ACC1A data. The RMS-ratio detection is an automated process in order to detect a wide sample of twangs within the radial component of the ACC1A data. In principle, the RMS_1 of one second interval is computed and then compared to the RMS_2 of the following one second interval, described by the following equation:

$$\frac{RMS_2}{RMS_1} = \alpha, \tag{8.1}$$

$$\alpha > \alpha_{RMS}. \tag{8.2}$$

α_{RMS} is a previously arbitrary defined threshold. If α exceeds α_{RMS} we flag a twang within the ACC1A data. The higher the ratio, the more likely a twang is identified by the this approach. The threshold in our case was chosen to be 1.17. If this threshold was exceeded, the corresponding

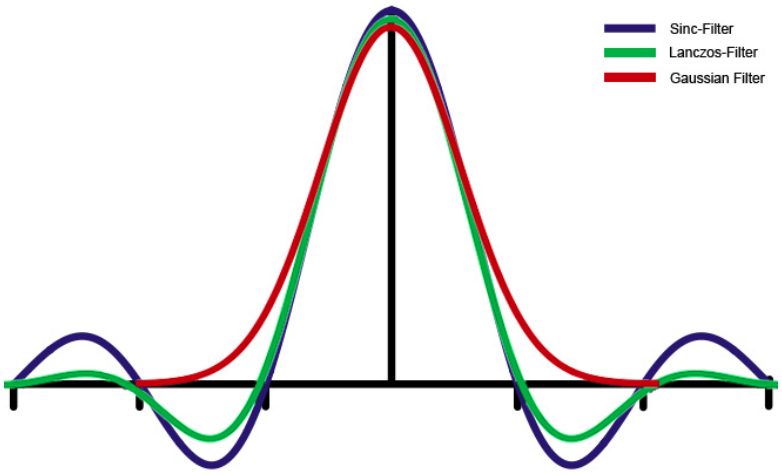

Figure 8.4: Introduction of the reconstruction filter (sinc, Lanczos and Gaussian).

time of α_{RMS} was considered to be the start of a twang. The threshold of 1.17 was validated, as the detected signal was still clearly above noise level. If the preliminary steps described in the previous section are not carried out, however, this ratio-threshold needs to be considerably higher (approx. 1.4) in order to avoid signals due to other sources, yielding falsely detected twangs or noticeably less twangs detected. With this approach averagely 420 twangs per day could be securely identified for GRACE A, and about 270 twangs per day for GRACE B.

8.2.3 Classification with cross-correlation

After having identified a significant number of representative twangs from ACC1A data by means of the RMS-ratio approach described above it is necessary to distinguish between different types of twangs. The two main types the following studies are based upon, 'positive' and 'negative' twangs, have been previously introduced. A reliable and feasible approach in order to give evidence for the existence of two main types is using normalized cross-correlation. A normalized cross-correlation does not only detect signals with the same orientation and similar shape, but also puts emphasis onto the ratios of the different amplitudes of peaks within a twang. This means that a twang needs to be very similar in shape (such as the peak ratio), duration and amplitude in order to be found by means of a normalized cross-correlation with our model. Any twang or twang-like signal, that has been previously chosen, may serve as a model used for this approach. Naturally, it is proficient to start with a signal that might represent the majority of the twangs. The previously introduced figure 8.2 shows superimposed twangs of the same orientation, i.e. type, respectively. The time in this figure is related to the time of the reference twang and the superimposed data has been shifted in time according to the highest cross-correlation coefficient.

However, in order to determine this maximum effectively it is necessary to re-sample the signal as the nominal 10 Hz sampling of ACC1A data is too sparse. We found a re-sampling of the signal to 100 Hz to be sufficient in order to carry out the cross-correlation approach. Not only the model twang that one is intending to detect within ACC1A data needs to be reconstructed to such a higher sampling, but in fact the whole ACC1A data itself needs to be reconstructed, yielding temporary but very large volume of data. There is a range of reconstruction filters that may be applied in order to re-sample a given signal – figure 8.4 represents the three most commonly used filters in this regard, which are the sinc filter, the Lanczos filter and the Gaussian filter. Based on the experience of the heater and magnetic torquer investigations, we expect that

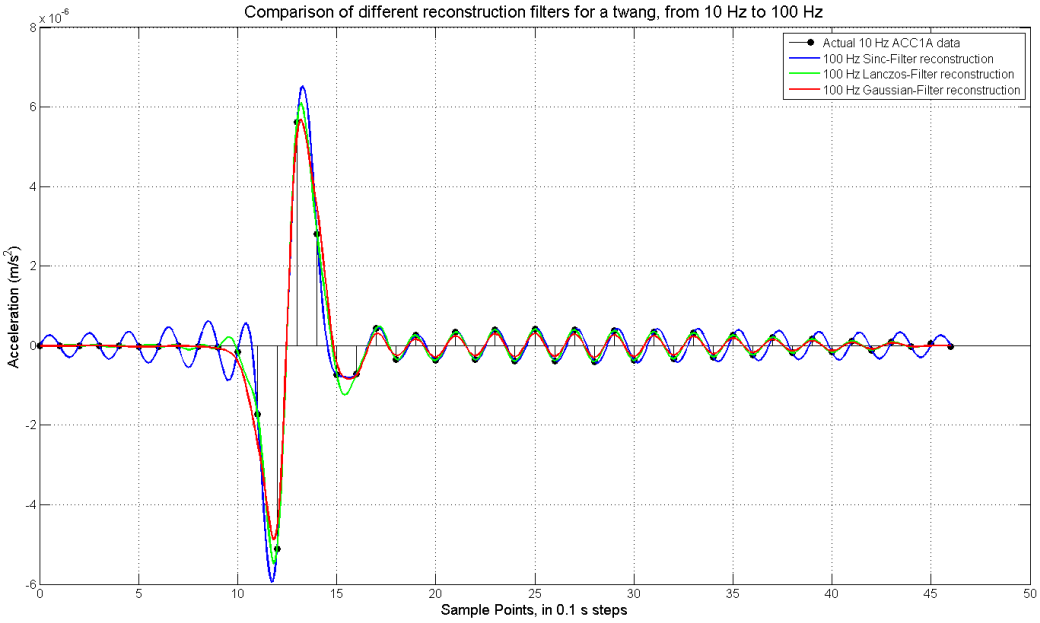

Figure 8.5: Reconstruction-filter applied to a negative twang found in radial of ACC1A of GRACE B on April 1, 2008.

a twang consists of the two main peaks as described before and that these three reconstruction filters should be sufficient to match the underlaying physics. Figure 8.5 displays these three filters applied to a twang found in the 10 Hz sampled ACC1A data. It is obvious that the sinc filter intends to restore the actual amplitude of the twang most accurately. However, the sinc filter does also enhance the 100 Hz signal with artifacts prior and post the visible twang in 10 Hz data, for which there is indeed no evidence of an actual signal within ACC1A data. The Lanczos filter is a more moderate approach, with less artifacts and a slightly under-represented amplitude considering the sinc reconstruction. We chose the Gaussian filter as a reconstruction filter, as it does not enhance the reconstructed signal with any artifacts outside the actual twang. However, it does not fully resolve the amplitude of the twang. Yet, as we are needing the signal for a normalized cross-correlation, the absolute amplitude is not of importance, but only the restoration of the ratio of the amplitudes of the different peak of one twang. Artifacts post and prior to the signal, as they would be present by the application of the sinc and Lanczos filters, might affect the results of the cross-correlation approach and are hence less suitable to access this problem.

Figures 8.2 already made it obvious that the period of the spikes of the twangs is identical and only the amplitudes are varying. This behavior applies for both positive and negative twangs. Approximately 90 per cent of all twangs previously detected with the RMS-ratio approach could be related to any of these two types. As for the remaining twangs, we believe that a majority of these signals may be impacted by other signals or noise, or simply appeared at a time that the sampling of the accelerometer made it impossible to represent the shape of the twang to a sufficient level.

8.3 Modeling and characterization

In this chapter we describe how a model for a twang can be built, how it may be parametrized, and how these parameters can be adjusted to a real scenario. For the parameters we will discuss their influences and behavior over time. For all identified twangs, a model based upon these parameters can be computed and used for deriving twang time-series corresponding to the ACC1A data. This allows to compute the spectral influences of the detected twangs onto the ACC1A data, to reduce these twangs from ACC1A and to compute new ACC1B afterwards. Table 8.1 on page 80 gives an overview of the mean values for the parameters derived during the investigations of twangs in ACC1A data. Most parameters are introduced in terms of the GRACE B ACC1A data and the radial component, as twangs are easiest detected, modeled and isolated in this data component and satellite. If necessary for the rudimentary understanding, we will give references and explanations about the other axes as well.

8.3.1 Introduction of parameter based model and adjustment

As displayed in figure 8.2 the shape of a twang can be clearly resolved if a sufficient number of twangs can be extracted and their corresponding ACC1A data superimposed, referenced to an exact time epoch determined by means of cross-correlation. By such a superposition a mean model can be computed, representing an average twang for each of the two types. However, it only describes the mean of all superimposed twangs. In order to characterize any given twang with a set of parameters other approaches need to be found. In chapter 7.2 we introduced a few signals that can be found in the ACC1A data and are already investigated. In these cases, however, a reference data such as the magnetic torquer (MAG1B) or the heater data exist and signals in ACC1A can be referenced to these time tagged events. In case of the twangs no reference data exist, neither is the exact cause known and hence no information about the time of occurrence nor the twang signal strength is existing prior to our investigations. This results in a model based on a limited set of parameters that can dynamically and automatically be adjusted to any given twang found within ACC1A data. However, the amount of parameters used should be minimized in order to be able to represent only significant deviations from the average twang model.

We found that twangs can be best modeled by a model consisting of three pieces. This is due to the fact that the period of the oscillation showed up to be of different lengths from the period for the first two peaks of the twang, which means that a twang is no oscillation as a whole. The first two peaks of a positive twang can easily be represented by the derivative of the Gaussian curve. This also applies for the negative twang, when the derivative of the Gaussian curve is being multiplied with -1, i.e. when the sign is changed. This derivative needs to be either up- or down-scaled and its width adjusted in order to fit to any given twang. In figure 8.6 an example for a negative twang is displayed, represented by the blue dots which are actual ACC1A data points. The ACC1A data is referenced to the time of the greatest cross-correlation coefficient for this type of reference twang. The solid line that runs approximately in the mean of the dots is in fact the derived model, based on the set of parameters mentioned above. The red part of the solid line is solely based upon the derivative of the Gaussian curve, which is described by the following equation:

$$f(t) = \left(-\frac{a}{\sigma^3} (t - \mu) \cdot e^{-\frac{1}{2}\left(\frac{t-\mu}{\sigma}\right)^2} \right) \cdot \vartheta(t), \tag{8.3}$$

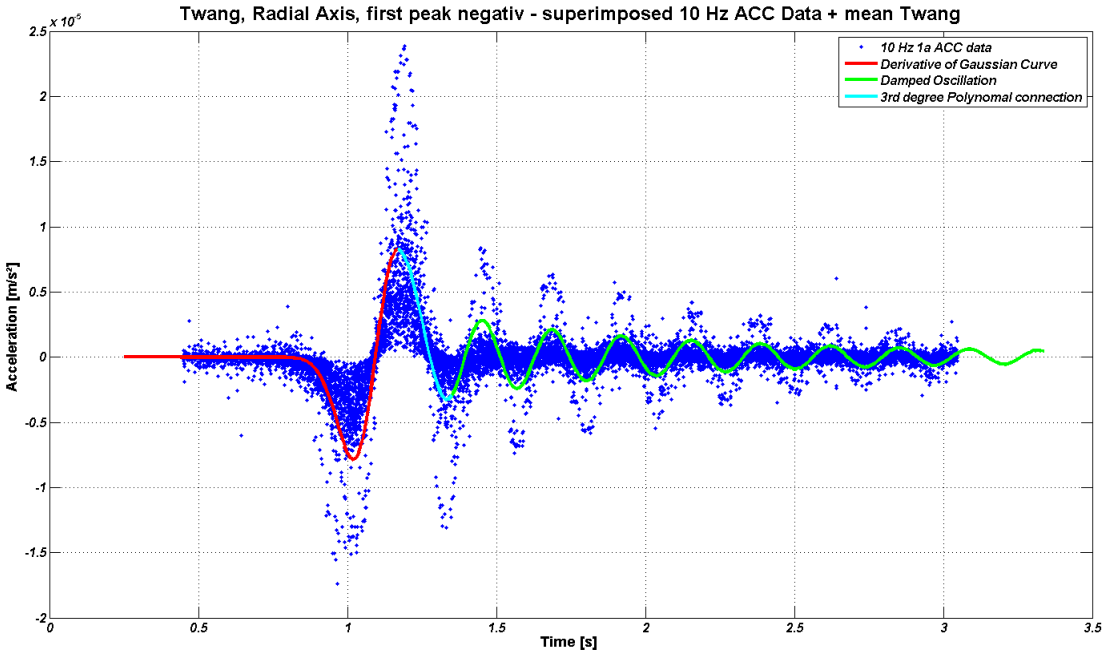

Figure 8.6: Twang in radial of ACC1A and adjusted mean parameter based model. The blue dots are superimposed 10 Hz accelerometer data.

where a is the amplitude, i.e. scaling factor, σ is the width of the derivative of the Gaussian curve, μ the center along the x-axis, which is time t in this case. In order to represent the differences in the peak amplitude we introduce the scalar function $\vartheta(t)$,which is depending on the time. $\vartheta(t)$ is derived by a linear regression of the two peaks of the twang we want to represent, and each value within this function is an individual scaling factor for each dot of the model. $\vartheta(t)$ is based on two parameters of a linear regression. In order to keep the whole system continuously differentiable, the vector is strictly linear. The green part of the solid line in figure 8.6 is describing the possible oscillating part of the twang. The oscillation is described as

$$g(t) = a_2 \cdot \left(e^{d_1 t} + s \cdot e^{d_2 t}\right) \cdot \cos\left(\frac{2\pi}{T} t\right). \tag{8.4}$$

Where a_2 defines the starting amplitude of the oscillation, whose value is depending on the amplitude and orientation of the very first peak of the whole twang and also on the asymmetry defined in equation 8.3. d_1 and d_2 describe two damping factors for oscillations, where one is being controlled by the scaling factor s. During our investigations it has turned out, that a single oscillation damping factor is insufficient for describing the oscillating decay of a twang, as either the oscillation was damped too soon or was extended beyond the actual signal. Hence, we added a second damping factor d_2 being strictly regulated by s. T is describing the period of the oscillation.

The third section of the solid line, depicted in light blue, is a connector between the derivative of the Gaussian curve in red and the oscillating decay in green. The connector is derived by a third degree piecewise polynomial, starting and ending at two extreme points, namely the top of the second peak of the red section and the beginning part of the oscillating decay. This connector

supplies us with a model that is continuously differentiable if combined, which could be realized by additional conditions in the adjustment model. The polynomial connector is described as follows:

$$h(t) = b_0 + b_1 t + b_2 t^2 + b_3 t^3. \tag{8.5}$$

Here, $b_{0...3}$ are the polynomial coefficients. All three sections of the model are generally constructed with a sampling rate of 100 Hz.

In order to adjust this model successfully to any given twang found within the ACC1A data, the introduced parameters need to be fitted to the given situation. There are nine parameters that undergo the fitting procedure. This is realized by a least squares approach. From equation 8.3 the parameters σ, μ and a are derived by means of the LSA (least-square adjustment). $\vartheta(t)$ is also derived by means of LSA, but should not be determined within the same LSA approach in order to avoid ambiguities between the scaling factors, and needs to be computed separately. d_1,d_2, s and T of equation 8.4 are derived by means of LSA afterwards, which is necessary as a_2 is depending on the results of the derived a before. The two damping factors should be adjusted successively in order to avoid ambiguities in this part, as they are correlated too strongly. The piecewise third degree polynomial connector is being computed after these two LSA steps are being carried out.

8.3.2 Discussion of twangs and their parameters

Here, we will give a description of what the average parameters may look like, in what ranges their magnitudes and standard deviations are and how they may behave and/ or change with respect to time. Table 8.1 (p. 80) gives an overview of all parameters and will serve as a reference throughout chapter 8.3.2.

Amount of twangs

Previously, we stated that the average number of twangs detected with the RMS-ratio approach introduced in chapter 8.2.2 is roughly about 420 per day for GRACE A and about 270 for GRACE B, respectively. With a lower threshold in the RMS approach we can detect a higher number of twangs, which appear to be rather noise or of different nature as they cannot be superimposed. However, this amount only reflects the mean number of twangs occurring. The overall number of twangs per day is subject to change and strongly depends on a seasonal impact. Furthermore, a linear trend can be observed, causing the overall number of twangs to increase steadily over time. Also notable is the fact, that GRACE A appears to have significantly more twangs in ACC1A data than GRACE B.

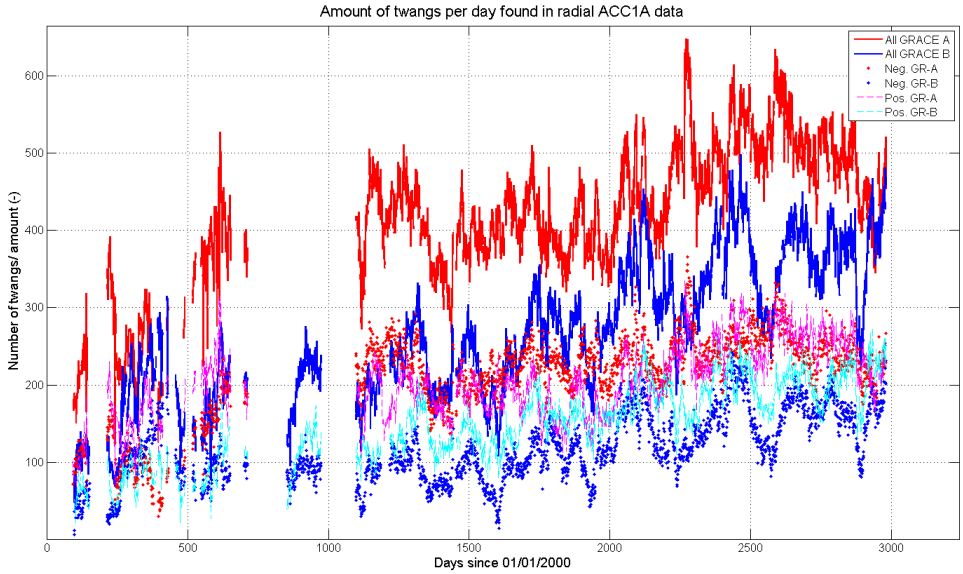

Figure 8.7: Total amount of twangs found per day in radial ACC1A data component since launch of GRACE. The red shaded colors represent GRACE A (GR-A) and the blue shaded colors GRACE B (GR-B). The solid lines display the overall amount of twangs, the dotted and the dashed lines the negative and positive types separately.

Figure 8.7 displays the amount of twangs per day for both satellites, where the solid lines reflect the overall amount of twangs, not distinguishing between positive or negative types. The dotted and the dashed lines represent negative and positive twangs. The gaps in data were explained in the beginning of chapter 8. It is clearly visible that for both GRACE spacecraft the overall amount of twangs is increasing steadily throughout the years since the launch of GRACE in March of 2002, especially visible for the twangs found in the ACC1A data of GRACE B. For both spacecraft the total amount of twangs per day is relatively low at the start of the GRACE mission, between 200 and 250 for GRACE A and half that amount for GRACE B. During GRACE's lifetime until 2010 this number has increased and may exceed a total of approximately 650 twangs per day for GRACE A, and almost 500 for GRACE B.

Moreover, it is deductible from the image that there is a certain periodicity forming the shape of the graphs. Especially the solid blue graph, reflecting the amount of both types of twangs for GRACE B, appears to be steadily increasing while influenced by a periodical behavior. Figure 8.8 shows a corresponding PSD for this dataset. The two marks indicate the highest amplitude visible in the PSD, which correspond to 376.8 and 313.97 days. This means that the dominant period for this dataset is most likely to be found within this range. The two major periods corresponding to that range that may have a greater impact onto GRACE spacecraft are seasonal impacts and hence an annual period of 365.25 days, and the full solar β_{prime}-cycle of 322.3 days as the GRACE orbit plane precesses at -1.117 degrees/day relative to the sun. The β_{prime}-angle is the measurement used mainly in spaceflight and describes the amount of time a satellite spends in direct sunlight. Hence, this angle is especially of importance for the usage of the solar arrays of a spacecraft in order to charge the on-board batteries. Corresponding to these periods we compute the contribution of these periods by means of a regression analysis, shown in figure 8.9. The black line represents the original dataset, the red line the contribution if the major period is due to an annual impact, and the blue line is the contribution if this periodicity is due to the full β_{prime}-cycle. Derived form this picture, the overall residuals are smaller if the β_{prime}-cycle contribution is subtracted, which hints at a solar impact onto the amount of twangs per day

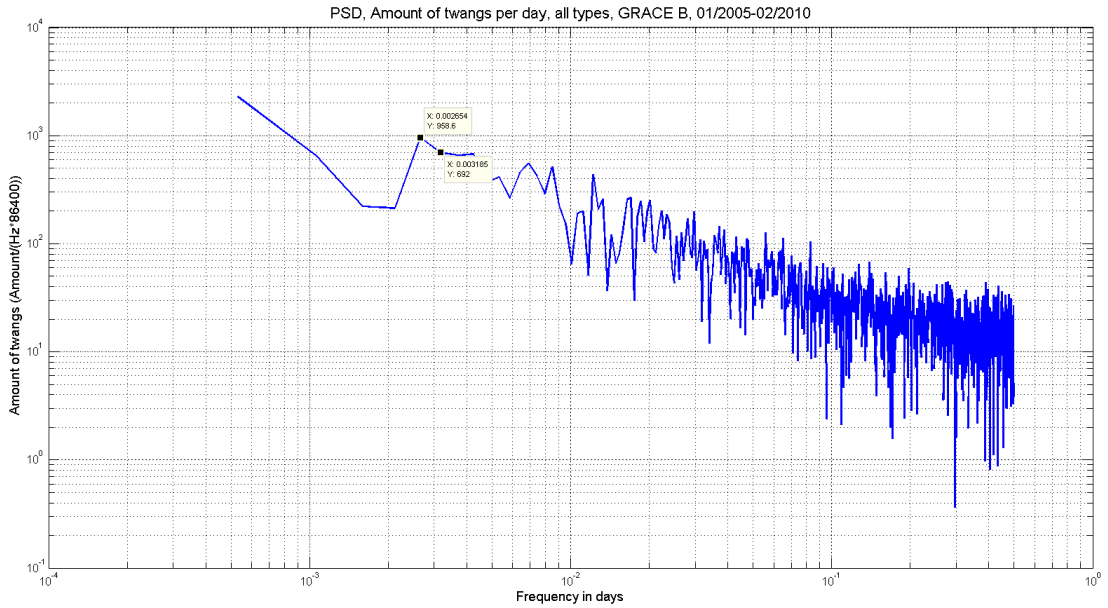

Figure 8.8: Power spectrum density corresponding to the amount of twangs per day found in GRACE B dataset, ranging from 01/01/2005 to 28/02/2010, shown in frequencies per day (Hz · 86400). The two marks indicate the range of the highest amplitude, at 0.002654 ($\triangleq$ 376.8 d) on the left (lower frequency) and 0.003185 ($\triangleq$ 313.97d) on the higher frequency side. The lowest frequencies have a significant amplitude as most of the signal may not be traced back to any period.

within ACC1A data rather than a seasonal impact. Furthermore, the regression analysis revealed that the amount of twangs is increasing by 38.93 twangs per day per year for GRACE B and by 26.94 for GRACE A. As the dataset for GRACE B is a lot smoother and appears to be less noisy as for the occurrence of twangs (cf. chapter IV) it is acceptable to assume that the value for GRACE B is reflecting the situation different from GRACE A.

Amplitudes (a)

Figure 8.10 shows the behavior of the mean amplitude of twangs per day for both GRACE spacecraft (A on the left side and B on the right side). Obviously, the average amplitudes per day are depending on some temporal variations. This behavior applies simultaneously for negative and positive twangs. For most days the mean amplitude of the negative twangs seems to be smaller for both satellites, which is especially visible towards the end of the observed data spectrum. Their mean amplitudes mainly range from $0.95 \cdot 10^{-7}$ to $1.25 \cdot 10^{-7}$m/s^2, and this range is hardly exceeded. However, both negative and positive twangs follow a certain temporal variation. Similar behavior was found for the other two axes, along-track and cross-track, for both GRACE spacecraft - for the cross-track axis of GRACE B and the along-track axis of GRACE A we found that the positive twangs have smaller amplitudes in average. However, the distinct offset in the mean amplitude between these two twang types prevails in any axis.

The power spectrum densities for the datasets for both types of twangs combined for each satellite are displayed in figure 8.11. Here, some major amplitudes are detectable, but they are not significantly greater than any other amplitude corresponding to other frequencies in the PSDs. Both PSDs reveal a possible impact due to the frequency corresponding to 171.3 days at 0.005836 Hz · 86400, which is near the 161-day cycle due to the β_{prime} -angle. Other larger amplitudes can be associated with a frequency indicating 376.8 days, which is near the annual period. A regression analysis for GRACE B showed no correlation between the behavior of the

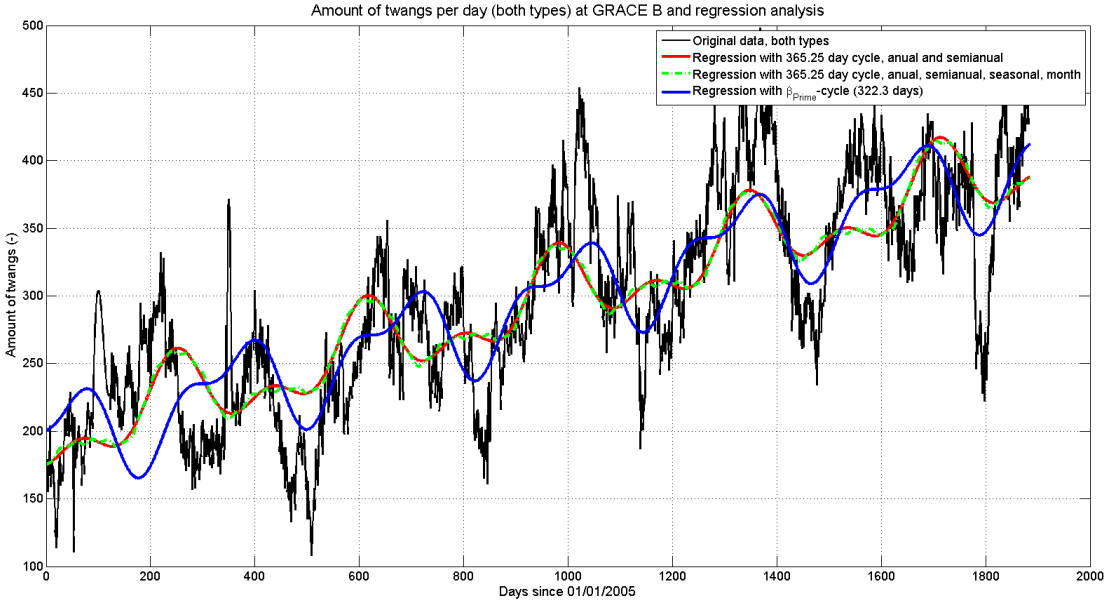

Figure 8.9: Amount of twangs per day for GRACE B from 01/01/2005 to 28/02/2010 and contributions of annual period (anual and semianual in red, including seasons and month in green) and the β_{Prime}-cycle in blue, derived by means of a regression analysis.

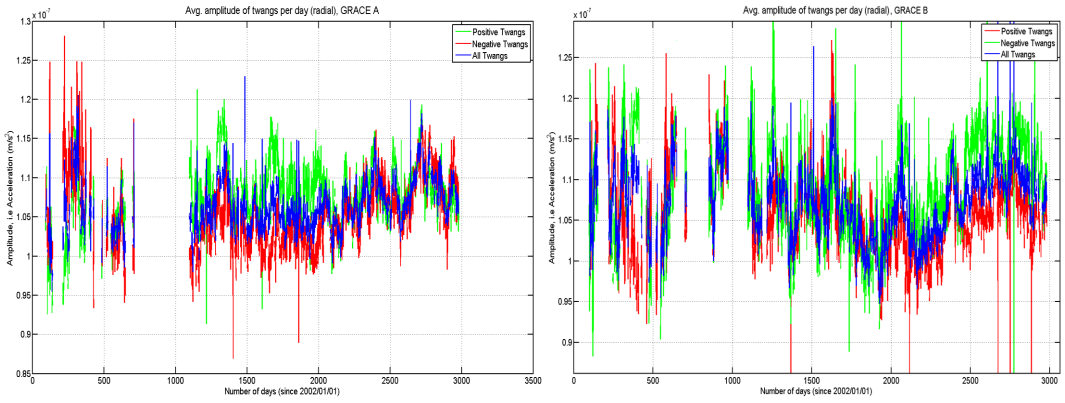

Figure 8.10: Behavior of average amplitudes per day for the radial component of ACC1A for both GRACE spacecraft (A on left side, B on right side). The blue line is the mean amplitude for both negative and positive twangs, the red line represents the average amplitudes for only the negative twangs, and the green line analogously represents the positive twangs.

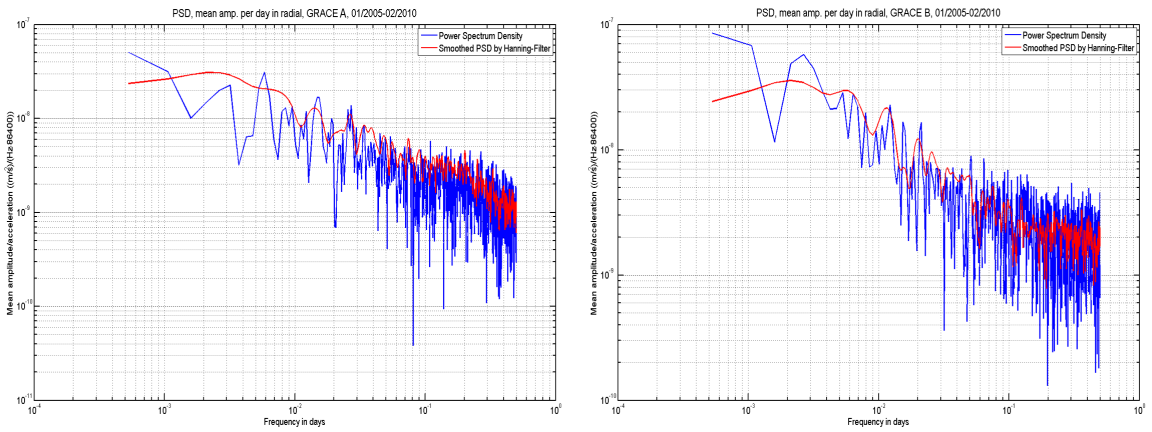

Figure 8.11: Power spectrum densities corresponding to the average amplitudes from figure 8.10 (solely both types combined). The blue line represents a regular computed PSD, whereas the red line is due to a smoothed PSD by a Hanning-Filter with 4 intervals with a quarter length of the actual dataset each.

average amplitude per day over the years to either an annual contribution nor a β_{prime}-cycle contribution. However, for GRACE A we found a similarity to the behavior of the annual period (cf. figure 8.12). The regression analysis revealed a slightly positive trend for the amplitudes of both spacecraft ACC1A data twangs, where the average amplitudes per day for GRACE A is increasing by $6.7 \cdot 10^{-10}$ $\frac{\text{m/s}^2}{\text{yr}}$ and the amplitudes for GRACE B by $7.4 \cdot 10^{-10}$ $\frac{\text{m/s}^2}{\text{yr}}$.

Width (σ)

Similar to the amplitude of the derivative of the Gaussian curve model adjustment, the width σ used to adjust a model to any given twang averaged over the day show temporal dependencies. σ has second as a unit and describes the width of the Gaussian figure (i.e. first two peaks of the twang) with respect to time. Figure 8.13 shows the behavior of the mean width σ per day for both GRACE satellites for the radial component. The majority of the σ-values can be found in a range from .074s and 0.08s, whereas the overall range is somewhat smaller for GRACE A. It is obvious, that the dependencies of σ appear to be very similar to those of the amplitude discussed above. In fact, the cross-correlation coefficients reveal a correlation between those two parameters (a and σ) for the mean value per day of 86.82 per cent for GRACE A and even as high as 93.18 per cent for the GRACE B data. We conclude, that these correlations are due to the fact, that the width of a twang can be a lot better determined whenever the twang is consisting of a greater amplitude as the twang will not decay into the noise level of the accelerometer as fast as it would with a lower amplitude. This results in a width which appears to be broader whenever the amplitude is higher. As σ's standard deviations are very small ($8.396 \cdot 10^{-4}$s for GRACE A and $1.3 \cdot 10^{-3}$s for GRACE B) and the twangs are able to be superimposed very successfully even when using the majority of the twangs of one type (cf. fig. 8.2), we assume that the accuracy of the determination of σ is depending on the scale of the twang. The width can be estimated more accurately with a larger amplitude of the twang as the start and end of the twang are better detectable with respect to the noise level of the accelerometer. Whenever the signal to noise ratio is relatively high, the width is also increasing.

Analogously to the amplitudes we could detect a positive linear trend for both σ-values from Jan 2005 to Feb 2010 for the data for both satellites. For GRACE A we identified a trend of $1.66 \cdot 10^{-4}$s and a slightly bigger one for GRACE B, with $2.03 \cdot 10^{-4}$s.

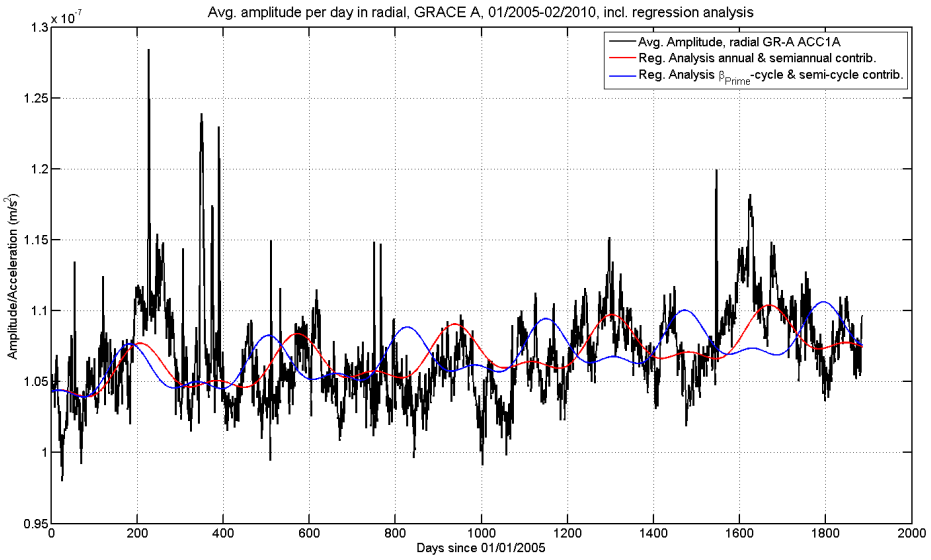

Figure 8.12: Average amplitudes per day for the radial component of ACC1A for GRACE A, both types of twangs (in black). Red and blue are contributions revealed by a regression analysis, where red represents the annual period contribution, and blue represents the β_{Prime}-cycle of 322.3 days contribution.

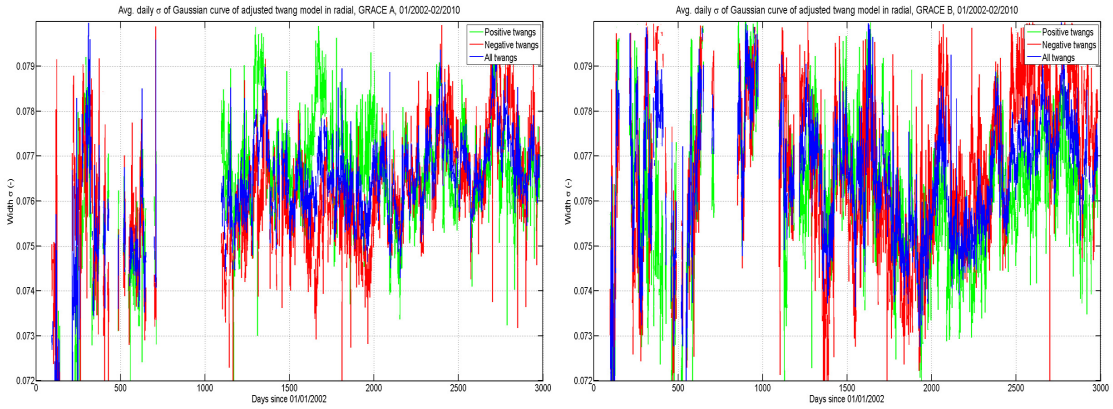

Figure 8.13: Average daily width σ of Gaussian curve of adjusted twang models in the radial ACC1A data axis of both GRACE satellites (A left, B right).

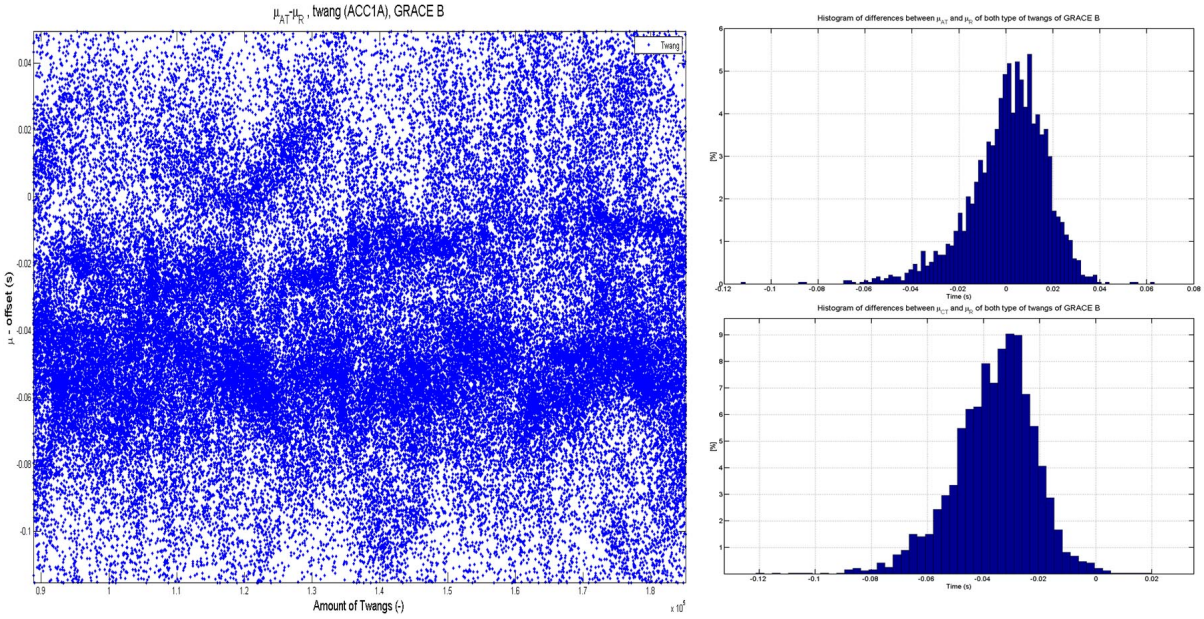

Figure 8.14: Left image: Difference of time of Gaussian curve derivative center point ($\mu_{AT} - \mu_R$, adjusted model to twang) of simultaneous twangs (along-track and radial, GRACE B). Upper right: Histogram of the time difference $\mu_{AT} - \mu_R$ of all detected twangs in ACC1A data of GRACE B. Lower right: cf. upper right image - same scenario but $\mu_{CT} - \mu_R$.

σ in the other axes may vary significantly from the values identified for the radial component of the twangs. We detected a mean value and its standard deviation of $0.093 \pm 0.004s$ for the along-track axis and a mean value of $0.095 \pm 0.008s$ for the cross-track axis for GRACE A. The corresponding GRACE B values are $0.093 \pm 0.003s$ and $0.08 \pm 0.003s$. The cross-track σ-values are hence the only values that reveal a significant difference between the GRACE spacecraft.

Time tag inconsistencies between the accelerometer axes

Despite the fact, that a twang could be successfully detected in all three axes simultaneously for a majority of the cases, slight differences between the center point of the twangs, μ-value, could be detected. The main part of the twang, the derivative of the Gaussian curve, is strictly centered around μ. μ is given in the GRACE reference time (GPS) and is hence identical for all three axes. The difference in these differences is not a constant offset but is merely subject to change from twang to twang. Figure 8.14 displays the differences of μ between the twang model in the radial component and the adjusted model in the other components of GRACE B. The left side of this picture shows the difference in μ case by case between the radial and the along-track adjusted twang model. It displays a representative number of twangs as they appear in the ACC1A data with respect to time. It is notable, that the difference has a mean value of approximately -0.05 seconds, which may be an offset between these two axes, possibly due to a physical cause. Clusters of twangs forming patterns of a certain μ-value difference are visible, but they are not strictly limited and the stray level is rather high so that no clear systematics are revealed. The right side of figure 8.14 displays the histogram for the differences in μ for along-track and cross-track axes relative to the radial axis. In case for $\mu_{AT} - \mu_R$ we can see that the mean difference of $6.202 \cdot 10^{-4}$ seconds is rather close to 0, the standard deviation is 0.017 seconds. $\mu_{CT} - \mu_R$ reveals more of a relatively fixed offset with a mean difference of -0.0362 seconds and a standard deviation of 0.016 seconds. The shape of the histograms is

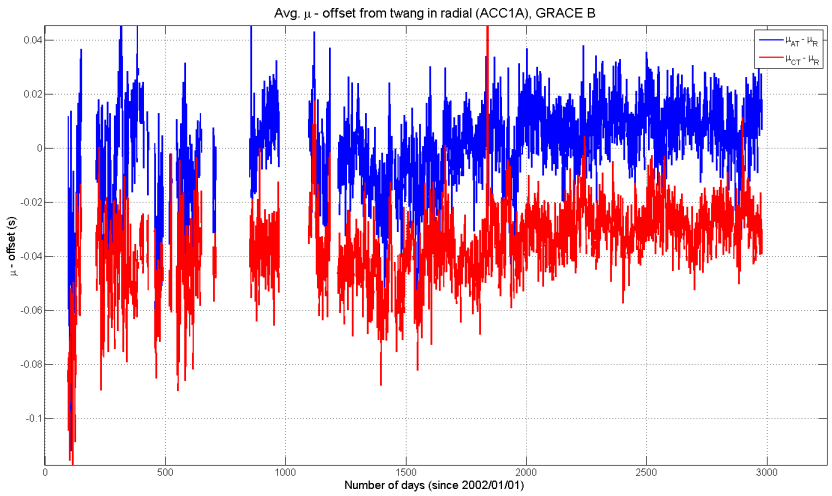

Figure 8.15: Average μ-value per day between the along-track and radial axes (blue), and the cross-track and radial axes (red), respectively. All detected twangs, since 01/2002 to 02/2010, GRACE B.

similar for both cases, with a tendency to a rather negative difference revealing that μ is most likely occurring a little earlier on along- and cross-track relative to radial. The shape might resembles a normal distribution.

Figure 8.15 reveals that the mean μ differences between the adjusted twangs in the radial and those of the other two components are rather stable - apparently there is a flexible mean offset between the appearance of rather simultaneously occurring twangs in the radial and the other ACC1A axes. This offset remains relatively stable between the axes. However, the actual mean μ-difference per day may differ on a daily base, but is showing temporal dependencies, for example between days 1800 and 2000, where a peak can be observed covering approximately 200 days. Here it is notable, that the relative offset between the axes in time is not stable, but is shifted in opposite directions. A clear systematic for the μ-differences could not be derived based on these numbers. However, the time inconsistencies between the time tag of the different axes may be directly linked to the geographical location of the individual twangs (cf. section 11.6).

Asymmetry

The asymmetry of a twang describes the differences of the amplitude of the first two peaks of a twang. In our model, the first two peaks are based upon the derivative of the Gaussian curve and are hence of same amplitude. For almost any case this does not reflect the nature of a twang found in ACC1A data in radial component. In the investigations we will present in this part of our study the numbers will represent the ratio between the two peaks as follows:

$$\alpha_{Asym} = \frac{|a_{p2}|}{|a_{p1}|} = \frac{|\vartheta(t_{p2})|}{|\vartheta(t_{p1})|}. \tag{8.6}$$

Here, a_{p2} is the actual amplitude detected after reconstruction and re-sampling the actual ACC1A data to 100 Hz by means of the Gaussian reconstruction filter of the second peak, and a_{p1} the actual amplitude of the first peak. The ratio is represented by α_{Asym}. α_{Asym} in fact is the scaling factor with which the first peak ought to be multiplied in order to obtain the same value as the amplitude of the second peak. $\vartheta(t_p)$ is corresponding to equation 8.3, which is a scalar function based on a linear regression, and hence on two parameters, derived from the actual amplitudes of the first two peaks of the reconstructed twang.

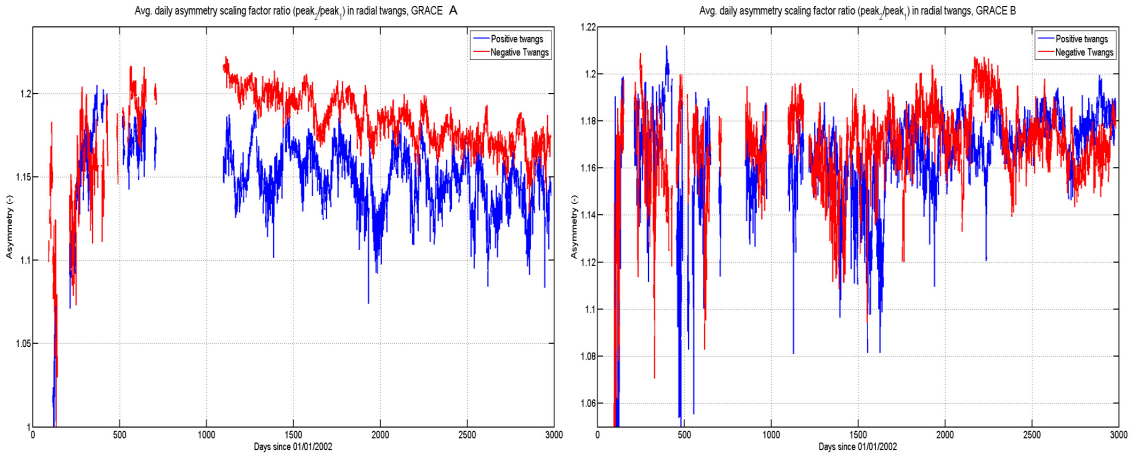

Figure 8.16: Average daily asymmetry ratio between first and second peak. Value 1 means that there is no asymmetry, and value larger than 1 indicates that the second peak is greater in amplitude than the first one.

We found that the average value α_{Asym} for both types of twangs, all axes and both spacecraft is larger than 1, which means that the second peak is usually greater in absolute amplitude than the first peak. Figure 8.16 show the average daily α_{Asym} value for the radial twangs of both satellites. The values for GRACE B (right side) show no significant differences between the positive and negative twangs except for very limited time-spans, for example between days 2200 and 2350. For the radial twangs of GRACE B the overall average values for α_{Asym} are comparable for negative and positive twangs, with 1.17 and 1.165, respectively. In contrast, GRACE A (left) shows a clear distinction in the asymmetry ratio value α_{Asym} for negative and positive twangs throughout the investigated time-frame, where the asymmetry between the peaks for the negative twangs with an overall average value of 1.18 is greater than for positive twangs, with 1.14. For both satellites a time depending behavior of the asymmetry is notable. No significant correlation can be found for GRACE B radial twang data between the two types, which was determined to be 8.8%. GRACE A radial twang asymmetry as in fig. 8.16, however, reveals a correlation between the negative and positive data of 42.9 %, which states the visual indication of the time depending behavior for GRACE A. A PSD of this dataset, however, could not lead to any clear frequency, but in fact to a range of possible influences, where an annual or full β_{Prime}-cycle influence could be a possible reason.

α_{Asym} for the along- and cross-track axes of the twangs found in ACC1A data of GRACE A and B are generally smaller than those found in the radial axes. Especially along-track axis twangs showed a smaller asymmetry with an average α_{Asym}-value of 1.09 for GRACE A for both types and 1.08 and 1.12 for negative and positive twangs for GRACE B. Cross-track axis asymmetries are slightly greater with 1.13 and 1.11 for GRACE A and 1.15 and 1.14 for GRACE B, for negative and positive twangs. No significant correlations for negative and positive twangs could be detected for those two axes, ranging from -4.6 to 23.6%. According to these numbers, the average asymmetries throughout the axis is slightly greater for the twangs found in the GRACE B ACC1A data.

A further interesting characteristic about these data is that trends in the behavior of asymmetry could be detected in some of the axes. For GRACE B positive trends were determined for both types of twangs for the radial and along-track axis, with 0.0015 and 0.0065 α_{Asym}/yr for the negative and 0.012 and 0.002 α_{Asym}/yr for the positive type. Negative trends of -0.004 α_{Asym}/yr

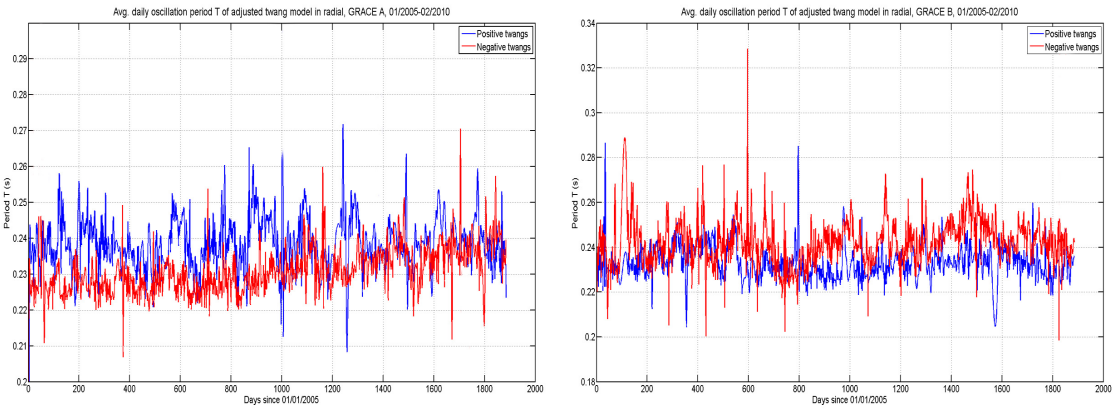

Figure 8.17: Average daily adjusted oscillation period T (interpolated) for radial twangs in GRACE A (left) and B (right). Not for all twangs an oscillation period could be detected or adjusted succesfully, as the oscillation often decayed into noise too early.

for each type for cross-track of GRACE B was found. Trends found in the asymmetry data of GRACE A differ clearly from GRACE B, as the asymmetry in the radial twangs appears to become smaller, revealing trends of -0.0083 and -0.005 α_{Asym}/yr for negative and positive types - both are visually detectable in fig. 8.16 after day 1000. Cross-track here also has negative trends again with the same value for both types, with -0.001 α_{Asym}/yr. Along-track reveal diverse trends for GRACE A, with -0.002 α_{Asym}/yr for the negative twangs and 0.011 α_{Asym}/yr for the positive type.

Oscillation

For some twangs in the radial axis an oscillation can be observed in ACC1A data after the first two main peaks of the actual twang. We assume that oscillations occur due to the difference in the amplitude of the first two main peaks of the twang and hence base our model upon this detected asymmetry (see section above). Furthermore, we believe that oscillations may occur throughout all axes. Yet, due to the smaller amplitude and asymmetry they are not observable in the along and cross-track axes as the oscillation would be smaller than the sensor noise level. In case of the radial axis only those oscillations could be considered which are clearly detectable. This means that no further disturbing signal may be occurring within the next seconds after the actual twang and the asymmetry as well as amplitude of the twang need to be of significant magnitude.

Figure 8.17 displays the daily mean period T of oscillation for both types of twangs in the radial axis for both GRACE satellites. The overall average values for T are 0.231 s for negative twangs for GRACE A and 0.242 s for negative twangs for GRACE B. A temporal behavior is observable for both satellites, especially for the time prior to day 600 for GRACE A. However, we could not clearly associate this behavior to any other parameter, but the shape might resemble the graphs of the amplitude vaguely (cf. fig. 8.10). This could be an indicator, that T can be determined with a better accuracy in case of a higher amplitude. An actual variation of T appears to be rather unlikely with regard to the digital converting filter applied within the accelerometer sensor. However, we are unsure about the significance of this discovery.

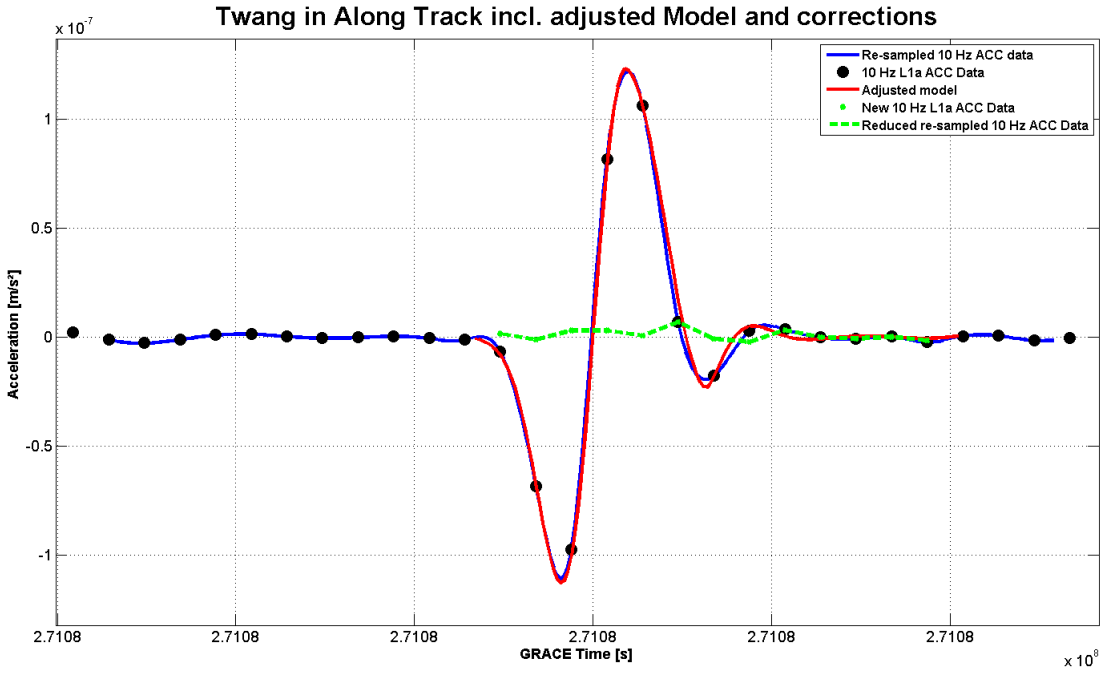

Figure 8.18: Twang in along-track axis of GRACE B and adjusted model. The black dots are the actual 10 Hz ACC1A data, the blue solid line the re-sampled signal onto 100 Hz by means of the Gaussian reconstruction filter. The red solid line is the model adjusted by means of LSA to the reconstructed signal. The green dots represent the residual values of the 10 Hz ACC1A data (ACC1A-TR) after the adjusted model has been substracted at the corresponding times, the dashed green line is the residual of the adjusted model subtracted from the resampled signal.

The damping factors determined are stable throughout all investigated data, yielding time-invariant behavior of the oscillation of twangs. Also, the damping factors are the same for both negative and positive twangs, as well as for GRACE A and B, and have an average value of $-8.71\ \frac{1}{s}$ for the first unscaled damping factor.

8.4 Reduction of twangs and computation of twang time-series

With the adjusted model as introduced in the previous section the actual twang effects may be reduced from the ACC1A data of GRACE. Figure 8.18 displays a single case scenario for a negative twang in the along-track axis of GRACE B. Here the black dots represent the real ACC1A 10 Hz data, and the blue solid line is the reconstructed signal by means of the Gaussian reconstruction filter up to 100 Hz. The red solid line is the model consisting of the previously introduced parameters (cf. eq. 8.3 to 8.5), which has been adjusted to the reconstructed signal. The dashed line represents the residuals in 100 Hz, from which the new 10 Hz data for the time-span of the twang is derived. The residuals are due to the fact that our model can only be approximately adjusted to the actual twang. In the adjustment we weighted the actual 10 Hz data points by a factor of 10 higher than the data of the 100 Hz reconstructed signal, as the reconstructed signal is not the true signal, but only is an approximated signal. As we are unaware whether an actual non-gravitational signal is underneath the twang signal our philosophy is that we rather keep a small amount of residuals than reducing too much of a potential signal. This reduced data may serve as a new, twang reduced ACC1A data, which we shall refer to as ACC1A-TR from now on.

Parameter overview

Average values/ parameter		**GRACE A**		
		R	***AT***	***CT***
Number of twangs/day (radial)		420 (min: 123; max: 648)		
Matched twangs in AT/CR w.r.t. R		-	90.96 %	86.11 %
Same orientation in AT/CT w.r.t. R		-	49.24 %	48.81 %
Linear trend of twangs/year		26.9 (radial)		
Time difference ($\Delta\mu$) w.r.t. radial (s)		-	$6.20 \cdot 10^{-4} \pm 0.017$	-0.036 ± 0.016
Amplitude (m/s^2)	Pos	$10.78 \cdot 10^{-8} \pm 4 \cdot 10^{-9}$	$0.82 \cdot 10^{-8} \pm 0.8 \cdot 10^{-9}$	$1.92 \cdot 10^{-8} \pm 3.1 \cdot 10^{-9}$
	Neg	$-10.52 \cdot 10^{-8} \pm 4.5 \cdot 10^{-9}$	$-0.93 \cdot 10^{-8} \pm 0.3 \cdot 10^{-9}$	$-2.04 \cdot 10^{-8} \pm 13 \cdot 10^{-9}$
Width (σ) of Gaussian curve deriv. (s)		0.077	0.093	0.095
Asymmetry ratio $\left(\frac{\text{Peak}_2}{\text{Peak}_1}\right)$	Pos	1.147	1.09	1.108
	Neg	1.18	1.09	1.129
Oscillation period (s)	Pos	0.238	-	-
	Neg	0.231	-	-
Damping Factor 1 (of Oscillation)(s^{-1})	Pos	-8.689	-	-
	Neg	-8.593	-	-
		GRACE B		
Number of twangs/day (radial)		270 (min: 48; max: 498)		
Matched twangs in AT/CR w.r.t. R		-	91.47 %	89.51 %
Same orientation in AT/CT w.r.t. R		-	57.46 %	56.99 %
Linear trend of twangs/year		38.9 (radial)		
Time difference ($\Delta\mu$) w.r.t. radial (s)		-	$6.20 \cdot 10^{-4} \pm 0.017$	-0.036 ± 0.016
Amplitude (m/s^2)	Pos	$10.54 \cdot 10^{-8} \pm 5.4 \cdot 10^{-9}$	$0.795 \cdot 10^{-8} \pm 1.2 \cdot 10^{-9}$	$1.77 \cdot 10^{-8} \pm 2.3 \cdot 10^{-9}$
	Neg	$-10.87 \cdot 10^{-8} \pm 6.2 \cdot 10^{-9}$	$-0.962 \cdot 10^{-8} \pm 0.8 \cdot 10^{-9}$	$-1.46 \cdot 10^{-8} \pm 5.8 \cdot 10^{-9}$
Width (σ) of Gaussian curve deriv. (s)		0.077	0.093	0.08
Asymmetry ratio $\left(\frac{\text{Peak}_2}{\text{Peak}_1}\right)$	Pos	1.644	1.12	1.137
	Neg	1.697	1.086	1.149
Oscillation period (s)	Pos	0.233	-	-
	Neg	0.242	-	-
Damping Factor 1 (of Oscillation) (s^{-1})	Pos	-8.714	-	-
	Neg	-8.941	-	-

Table 8.1: Overview about the numeric values characterizing the twangs itself, their behavior as well as the parameters of the least square adjusted model.

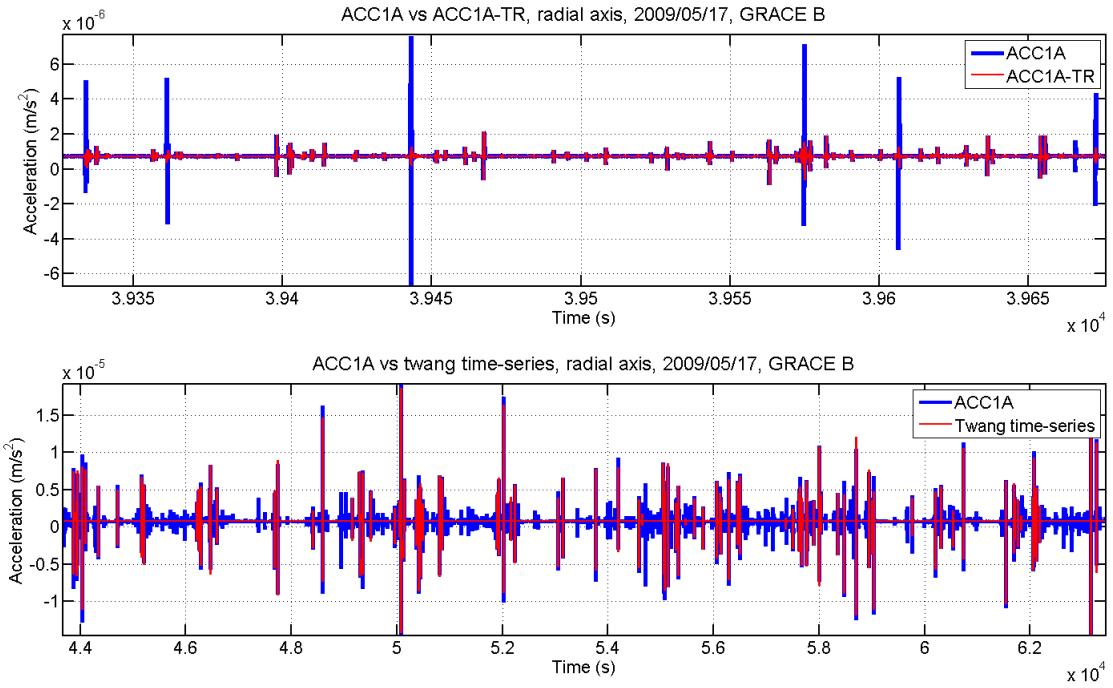

Figure 8.19: ACC1A data in radial axis of GRACE B displaying twangs (blue) for two scenarios. Corresponding signal after twangs have been reduced (ACC1A-TR, upper, red) and the modeled twang time-series (lower, red).

Samples of ACC1A-TR data in comparison to regular ACC1A data are displayed in figures 8.19 to 8.21. Figure 8.19 shows observations for the radial axis of GRACE B, the upper image reveals the actual ACC1A-TR data, where the detected and successfully adjusted twangs were subtracted from ACC1A data. The lower image shows a time-series consisting of adjusted twang models in red compared to the real ACC1A data covering a time-span of about 5.5 hours. This pattern is analogue for figures 8.20 and 8.21 for the along-track axis and cross-track axis, respectively. Those peaks which are not matched by the models are for most parts due to thruster activation events, heater activation and deactivation events, and also due to current changes within the magnetic torquer rods, which have not been reduced from these ACC1A samples displayed in figures 8.19 to 8.21. However, only about 92% of all previously detected twangs (cf. section 8.2.2) could be successfully modeled and then reduced. The remaining twangs could either not be modeled as they were impacted by other sources or the remaining residuals exceeded our threshold. In case of the latter the threshold is defined arbitrary. However, it needs to be chosen carefully as high residuals may have a potential of polluting the ACC1A with an artificial signal. In the lower images it is obvious that the adjusted twang is usually slightly smaller in amplitude than the actual ACC1A data. This is due to the fact that the model has been adjusted to the reconstructed 100 Hz ACC1A signal by the Gaussian reconstruction filter, which underestimates the real amplitude slightly (in contrast to e.g. sinc-filter, cf. chapter 8.2.3). This leaves us with residuals with respect to the assumed original signal. These residuals are usually just slightly beyond noise level and we considered this process as safer than reducing too much or a wrongly adjusted twang due to an improper shape with a different reconstruction filter (cf. discussion in section 8.2.3).

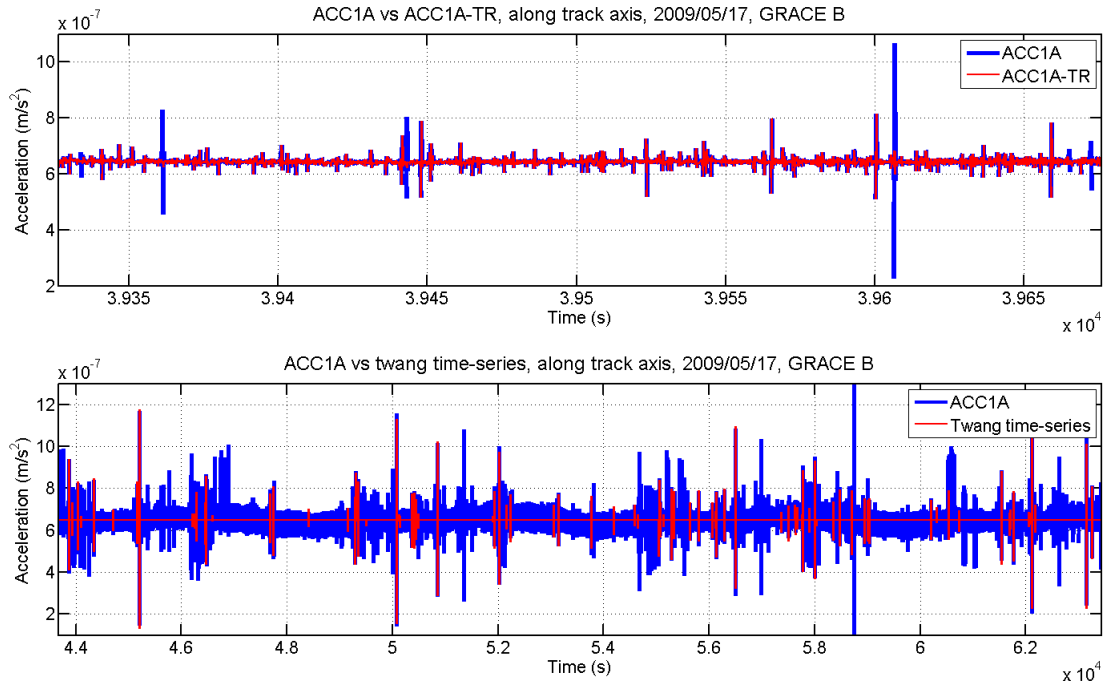

Figure 8.20: ACC1A data in along-track axis of GRACE B displaying twangs (blue) for two scenarios. Corresponding signal after twangs have been reduced (ACC1A-TR, upper, red) and the modeled twang time-series (lower, red).

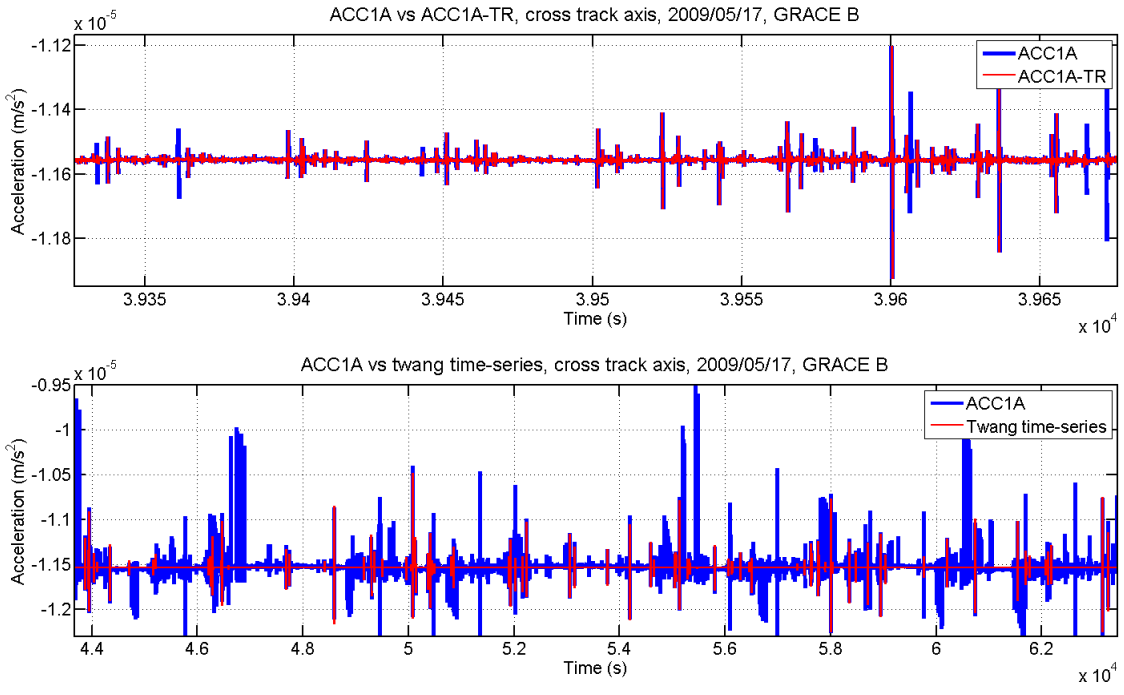

Figure 8.21: ACC1A data in cross-track axis of GRACE B displaying twangs (blue) for two scenarios. Corresponding signal after twangs have been reduced (ACC1A-TR, upper, red) and the modeled twang time-series (lower, red).

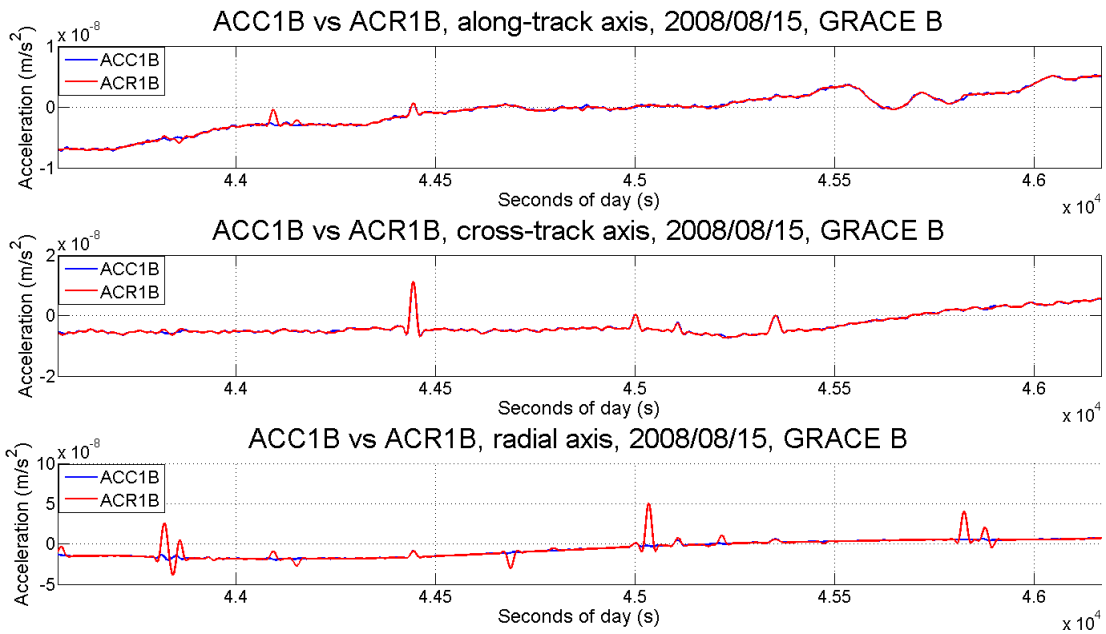

Figure 8.22: ACC1B and reduced ACC1B (ACR1B) data in comparison for all three axes of the data for GRACE B on 2008/08/15.

8.5 Influences in reprocessed ACC1B data

According to the approach described in chapter 7 we reprocessed the ACC1A-TR data to the Level 1b 1 Hz ACC1B data. This allows us to estimate if the twangs may have an actual impact onto further results determined by the GRACE mission. Also, we can deduce the magnitude of the impact of the twangs onto the accelerometer data product itself.

Figure 8.22 displays the difference between the original ACC1B data of GRACE B satellite and the twang reduced reprocessed Level1b 1 Hz data, that we refer to as ACR1B. It is obvious that for the along and cross-track axes the ACR1B data is in accordance with the original ACC1B except for some peaks, where slight differences are notable. These differences occur somewhat more often and are larger for the radial axis. Also, it is visible that twangs as presented in the ACC1A data are not as clearly visible in the ACC1B data, especially regarding the along and cross-track axes.

In the radial axis the reduced ACR1B signal is smoother and the peaks are reduced in amplitude compared to the original data. However, it also is deductible that for numerous occasions the ACR1B signal is polluted by a peak in comparison to ACC1B data. We found that both cases are due to successful reductions of twangs within the ACC1A data. However, due to the only approximate adjustment of the model to the actual twang in the ACC1A data, residuals remain. This is wanted as we have no further knowledge about the residual, underlying signal, which we desire to preserve as accurately as possible. As we considered the two major peaks to be the main issue of the twangs, and as they are furthermore easiest to identify, isolate and model, we focused in our adjustment on these two and neglected modeling the oscillating part if we found it unreasonable to reconstruct this part due to other signals or high noise. In many cases this may yield an overall slightly more asymmetric signal than in the actual ACC1A data, which leaves us with a value slightly deviating from the net-zero acceleration if integrated (e.g. applying trapezoidal approach; Stoer (2005)). If the value of the integrated residuals after the reduction

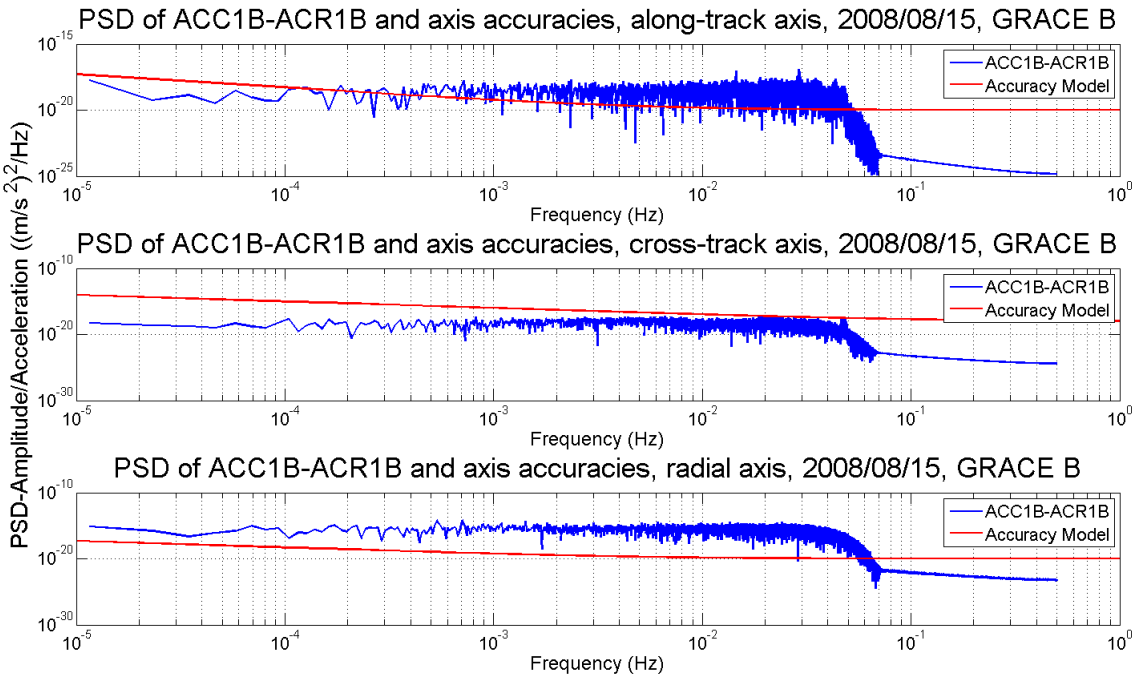

Figure 8.23: PSD of the differences between ACC1B and ACR1B in comparison to the axis specific accuracy model, GRACE B on 2008/08/15.

is in the range of the actual ACC1A or smaller, the peak visible in ACC1B will be reduced in ACR1B data. If this value, however, is significantly larger, the filter applied for reprocessing the ACC1A-TR to ACR1B data will pollute the signal with sharp peaks, visible in figure 8.22.

The difference between ACC1B and ACR1B and the corresponding accuracies for each axis are displayed by means of PSDs for one day of the ACC1B data of GRACE B in figure 8.23. These accuracies are the claimed precision for the accelerometer observations (JPL (2002)). From these PSDs an influence onto the results of the GRACE mission due to twangs in the accelerometer data can be expected, as nearly all lower frequencies of the ACC1B-ACR1B spectrum reveal a larger amplitude than the actual accuracy bar. Up to date, we do not have knowledge about the impact of the unwanted enhanced peaks in ACR1B data. Also, for the along-track axis some lower frequencies between 10^{-3} and 10^{-1} are exceeding the amplitude of the accuracy specification for this axis. Merely for the cross-track axis the difference between these two datasets is below the accuracy specification at all time, and no direct impact due to twangs in this axis is to be expected. For both figures, 8.22 and 8.23, the results for the GRACE A satellite are within the same ranges.

Part IV
Spatial and temporal correlations

One logical step in the analysis of twangs is to have a look into whether they may be distributed according to a rather systematic pattern. In chapter 8 we analyzed the twangs in the ACC1A with respect to the time of occurrence as well as their development over time. This analysis did not reveal any strict evidence for distributions or correlations. However, certain dependencies may be deduced. Another approach is to determine whether twangs are geographically and/or orbitally correlated. Hudson (2003) showed that a geographical correlation is to be expected, but no systematic behavior behind the distribution could be found. The parameters obtained by means of the LSA approach introduced in the previous chapter can be analyzed in terms of geography and support the investigation of twangs.

In the following we will describe how the twangs in both GRACE satellites are distributed, and also how the behavior of the different parameters is with respect to the location of the occurrence of the twang. For each parameter discussed, a rather large amount of figures and cases can be generated. However, it is rather inconvenient to show a large amount of figures within the text of this chapter. Therefore, we will present representative figures only, which we consider to be of help to understand the discussion and to derive the main conclusions. Yet, sometimes it is helpful to consider the complete range of images of a series (e.g. seasonal, temporal) in order to understand the conclusions drawn. In the appendix of this work (cf. page 164) we display a broader range of images and if we feel that it is helpful to confer to it, we will make a reference.

We will restrict ourselves to describe the observations made regarding the distribution of twangs and the behavior of their parameters in terms of geographical correlation. Any further interpretations and hypotheses are stated in the following part of this thesis (V).

This section will deal with the previously introduced parameters and hence all results shown in this section are solely based on information extracted from GRACE ACC1A data. Except for section 10.3 all images presented within this chapter will be examples extracted from GRACE B satellite, as the results are easier to be interpreted here. For the results concerning the GRACE A satellite the corresponding section in the appendix may be consulted (cf. Appendix). Also, we will mainly give explanations based on twangs in the radial component of the accelerometer data. We will introduce the other axes briefly, if significant results were obtained. This is only the case if parameters of twang characteristics are discussed, such as for example amplitude or asymmetry of the twangs. The geographical distribution itself is not changing between the axes, as a twang is occurring simultaneously in all three axes.

The corresponding position over ground is extracted from the GNV1B data (cf. section 6.3.1).

9 Orientation

The most logical approach is to separate the twangs into positive and negative types and determine whether a geographical correlation according to these two types can be detected. Corresponding to the parameters introduced in the previous chapter along with the least squares adjustment of our model, these twangs represent a negative amplitude a for the negative twangs, and a positive amplitude a for the positive twang (cf. equation 8.3, p. 67). Fig. 9.1 shows on the left side the distribution of the two types for GRACE B for the winter in the Northern hemisphere from mid-September to mid-April (period between the equinoxes). Furthermore, the twangs displayed are only occurring at certain times corresponding to the local time (LT)

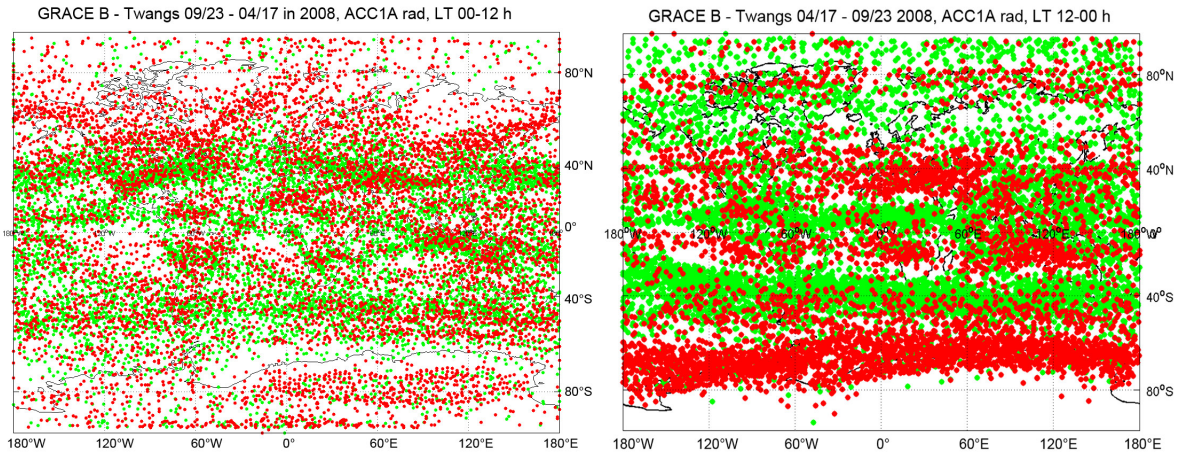

Figure 9.1: Left: Twangs in GRACE B ACC1A radial data component, Sep 23 to Apr 17 of 2008, local time 00-12. Red are negative twangs, green are positive twangs. Right: Twangs in GRACE B ACC1A radial data component, Apr 17 to Sep 23 of 2008, local time 12-00. Red are negative twangs, green are positive twangs.

in orbit between midnight and noon. It becomes obvious, that there are very distinct patterns formed by the distribution of positive and negative twangs. In this figure red represents negative twangs, and green positive twangs. The W-shaped band in the Northern latitudes between 40 and 80 degrees is most striking, as hardly any positive twangs are detected within this band. Also in the Antarctic regions nearly no positive twangs are visible, and the negative twangs form a cloud shaped pattern in the eastern longitudes. Between latitudes 40 North and approximately 60 South a variety of bands can be observed, which seem to be correlated with the geographical location, and also the two types of twangs appear to be systematically arranged with respect to the geography. Some of the bands are consisting of both negative and positive twangs, where others have a clear majority of one of the two types.

Another example for the clearly distinct correlation of positive and negative twangs with respect to the geographical location is displayed in figure 9.1 on the right hand side. This example displays the twangs of GRACE B in 2008 for the time between the equinoxes in the summer of the Northern hemisphere (mid-April to mid-September), and they are limited to orbital LT between 12 (noon) and 24 (midnight). In this case no distinction between ascending and descending node has been made. Also in this picture it is obvious that negative and positive twangs form bands that can be clearly distinguished from one another. Most obvious are the negative twang band, roughly following the coastline of Antarctica, and the positive twang band slightly North of this one at 40 degrees southern latitudes. North of these two bands are further patterns, which appear to be latitudinal bands with a clustering of either negative or positive twangs only.

GRACE A appears to show the same patterns for the same corresponding times in season and LT in orbit, but the patterns are opposed in terms of orientation. This means that patterns, that are consisting of mainly positive twangs in data of GRACE B consist of mainly negative twangs in the data of GRACE A, and vice versa. This may be due to the fact that the leading satellite is yawed by 180 degrees and hence may detect twangs opposed to the trailing spacecraft. However, GRACE A reveals a less strict distinction between positive and negative twangs. GRACE ACC1A data contains a significantly larger number of twangs, that appear less strictly correlated to the geolocation in terms of the orientation (cf. also section 8.3.2).

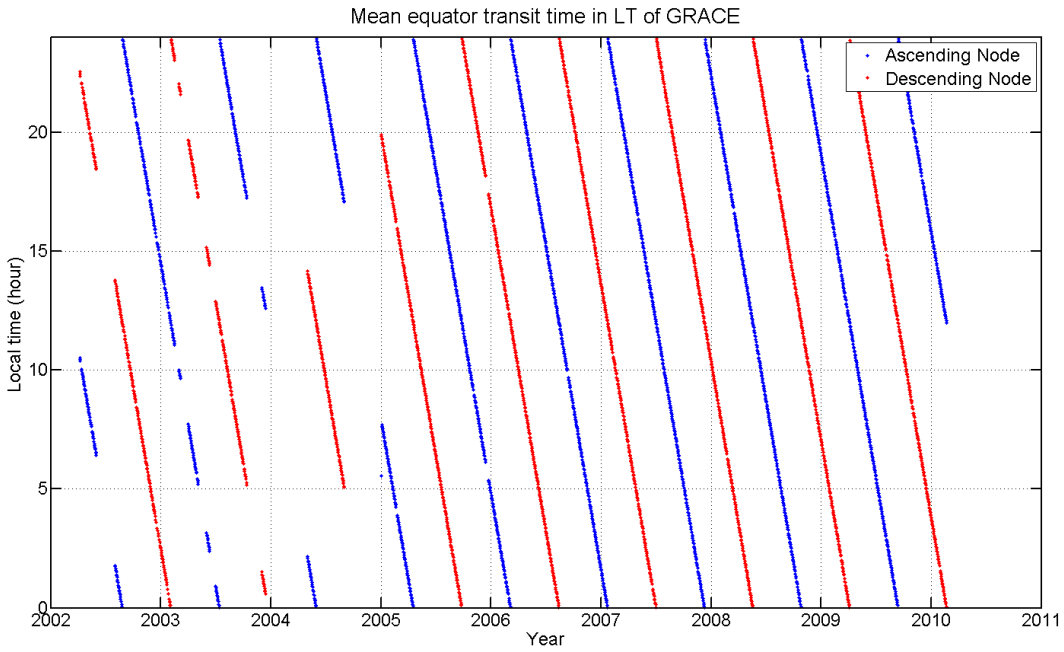

Figure 10.1: Mean local time (LT) in orbit of GRACE spacecraft, passing equatorial latitude. Red is descending orbit, blue is ascending orbit.

10 Season and Local time

10.1 Local time in orbit

In the previous section, where we described the geographical correlation of positive and negative twangs by means of two examples, we limited the occurrence of twangs also by means of local time (LT). This is necessary as we found that the distribution of twangs with respect to the geographical location is strongly depending on the local time. The GRACE spacecraft orbits through all local times once per revolution. However, the more perpendicular they fly with respect to Earth's equator, i.e. the longitudes, the longer the satellites will remain in a specific range of LT. LT 12 means, that they are in noon, having the sun directly above their zenith panel. LT 0, i.e. 24, is midnight, which means the sun is directly below their nadir plane, with the Earth in between, however. Ascending and descending nodes of the satellite are, at the equator, separated by approximately twelve hours LT. As GRACE does not have a sun-synchronous orbit we can determine whether a shifting LT on GRACE may lead to an impact onto the geographical distribution of twangs. The orbit plane of the GRACE satellites shifts at a node of -1.117 degrees/day relative to the sun, which means that it has the same orientation to the sun after 322.3 days, and hence the same LT when in the same node. However, the same LT, but opposed node, is flown after half this time. A critical issue is becoming obvious at this point already: there is up to date not enough GRACE ACC1A data to actually separate influences due to LT, season and ascending and descending nodes, as we have to consider the small amount of twangs during the first one or two years of the mission. We believe that both LT and season have significant influences, but cannot exclude a hypothetical influence due to the node at this time either. Figure 10.1 displays at what LT the GRACE spacecraft passed the equator between 2002 and 2010, based on the available ACC1A data. As the two satellites have slightly different LT a mean value is presented for both ascending and descending node, representative for both spacecraft. For few cases ACC1A data is available for the same season, LT and node. There

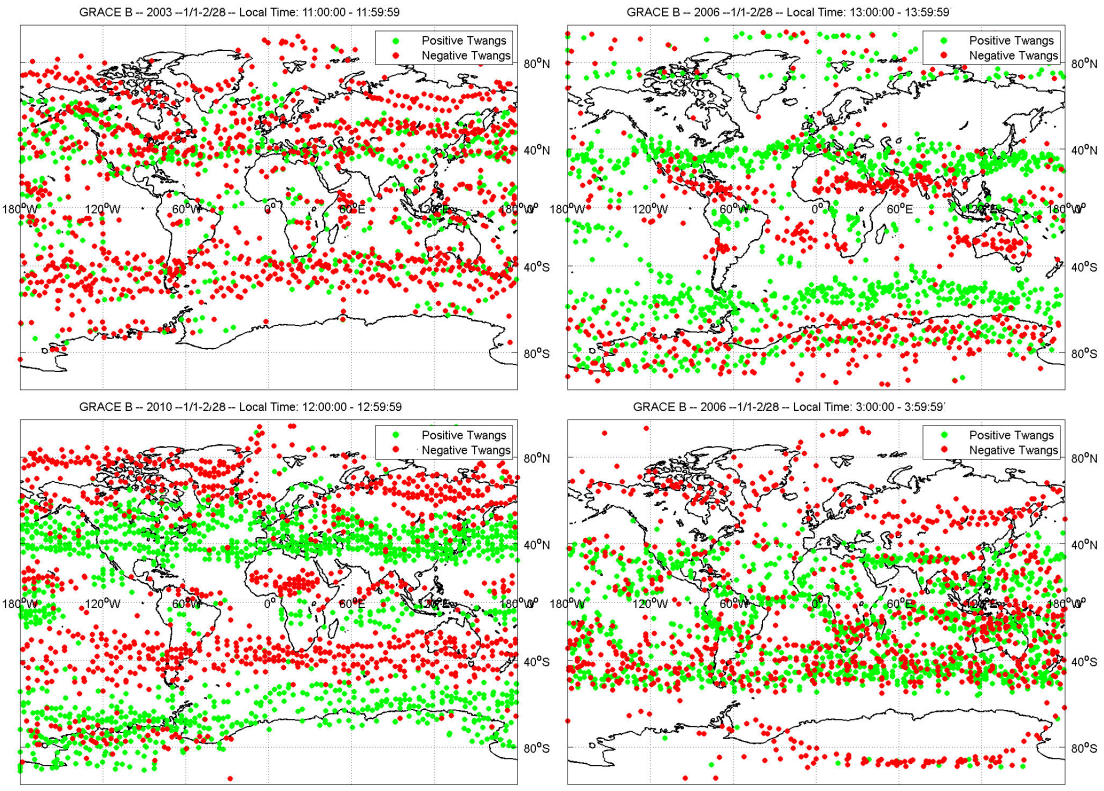

Figure 10.2: Upper Left: GRACE B, twangs in ACC1A rad, Asc Orbit, Jan 1- Feb 28 of 2003 at LT 11-12; Lower Left: GRACE B, twangs in ACC1A rad, Asc Orbit, Jan 1 - Feb 28 of 2010 at LT 12-13; Upper Right: GRACE B, twangs in ACC1A rad, Desc Orbit, Jan 1 - Feb 28 of 2006 at LT 13-14; Lower Right: GRACE B, twangs in ACC1A rad, Asc Orbit, Jan 1 - Feb 28 of 2006 at LT 03-04.

are only very few cases as it takes GRACE approximately 7 years to experience this very same situation. However, in chapter 8.3.2 (p. 69) we already displayed that in the early mission phase (2002 to 2004) significantly less twangs were detected. Yet, a sufficient number of twangs could be extracted in order to analyze their behavior with respect to LT. In the following we will present two different examples for local time behavior. More examples can be found in Appendix B.

In figure 10.2 we show a scenario for January/ February at LT between 11-13 hours in ascending node of 2003 and 2010 on the left side, and descending node for this LT and season of 2006 on the upper right side, as well as ascending node in January/February of 2006 but at LT between 3-4 hours. Although very few twangs for the case of 2003 could be extracted, yet it is observable that the patterns formed by the distribution of twangs are for most parts similar to the case of 2010 concerning the negative twangs. This is especially observable in the slightly W-shaped pattern in the North at about 60° N. Also the band at latitude 40° South is in accordance in both scenarios. In 2003 the majority of the twangs appears to be negative, and only some few positive twangs mix within the patterns formed by the negative twangs. This is different in the scenario of 2010 where very distinct patterns are formed by positive twangs only, especially around latitudes of 40° North and approximately 60° South. Comparing the descending node of 2006 to the scenario of 2003 no similarities can be observed. However, the positive twangs form patterns in the descending node scenario of 2006 that appear to match those of the positive twangs in 2010. Also the narrow band of negative twangs slightly North of the equator is observable in these two cases. The last case of ascending node in 2006 (lower right image) is interesting as it reflects the

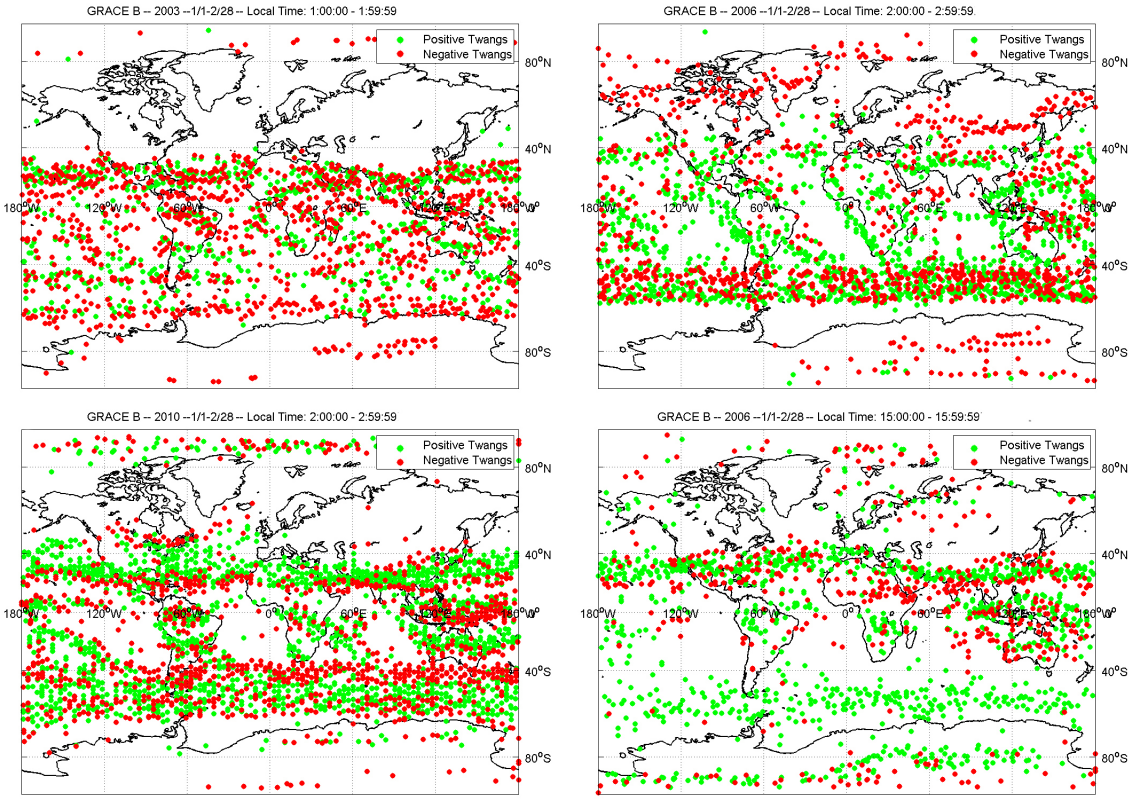

Figure 10.3: Upper Left: GRACE B, twangs in ACC1A rad, Desc Orbit, Jan 1- Feb 28 of 2003 at LT 1-2; Lower Left: GRACE B, twangs in ACC1A rad, Desc Orbit, Jan 1 - Feb 28 of 2010 at LT 2-3; Upper Right: GRACE B, twangs in ACC1A rad, Asc Orbit, Jan 1 - Feb 28 of 2006 at LT 2-3; Lower Right: GRACE B, twangs in ACC1A rad, Desc Orbit, Jan 1 - Feb 28 of 2006 at LT 15-16.

negative patterns at 60° N and 40° S, which are both observable in 2003 and 2010. The positive patterns deduced in the other 2006 scenario as well as in 2010 are not directly visible.

A second example is displayed in figure 10.3. Here we present again examples from 2003 and 2010 on the left side, at the same season as the example described above, however at LT between 1 and 4 hours, with a descending node. On the upper right we have a scenario of 2006 at the same LT and season but with an ascending orbit. The lower right image displays a descending orbit in 2006, at LT 15-16 in the January/ February season. First we compare the two images on the left, namely 2003 and 2010, again with each other. These two cases have in common that the majority of twangs can be seen between latitude of approximately 60° S and South of 40° N. The scenario of 2003, however, mostly presents us negative twangs and only one real observable pattern formed in the very North of this described range of latitudes, forming a horizontally aligned band. The image representing the 2010 situation has a lot more distinct patterns, where positive and negative twangs are clearly separated from each other, both at the Northern part as well as at the Southern end of this particular range. Also near the equator this figure allows to observe more distinctly formed patterns of both positive and negative twangs. The image in the upper right shows very little similarity with either of the two previous described images. Only the majority of twangs, which are mainly positive in this case, are located in the area between latitudes of 40° North and 50° South. Neither a distinct pattern nor the orientation of the twangs appear to match the observations of the previous images. This is similar to the last image, in the lower right of figure 10.2. Only the range of latitudes where the majority of twangs can be

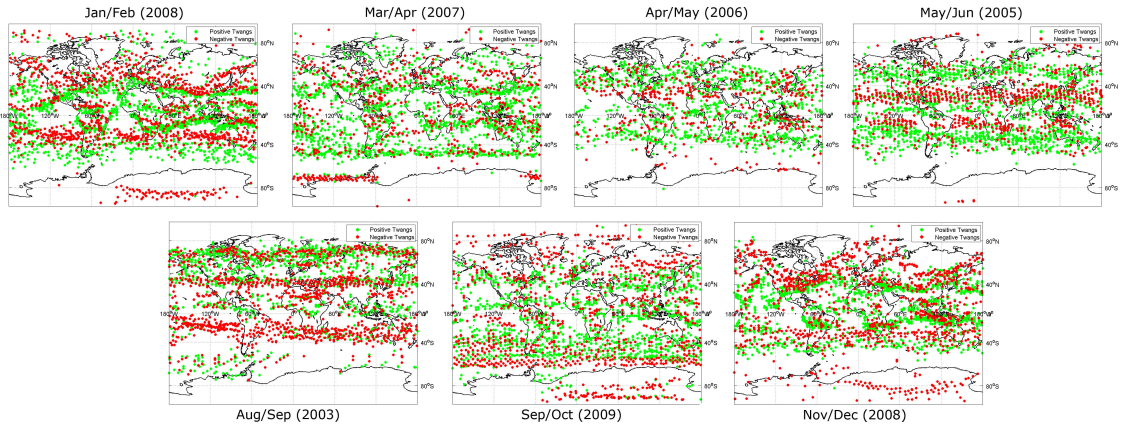

Figure 10.4: Change of twang formed patterns due to season, GRACE B. Red dots represent negative twangs, green dots positive twangs. Each image spans 2 months, all twangs are detected between LT hour 20 and 21 in an ascending orbit. Season progresses from upper left to lower right.

found corresponds to the other images. The patterns, however, show a slightly different behavior and cannot be correlated with the geography. A very significant and slightly W-shaped band is formed by both negative and positive bands near 40°N (cf. fig. 10.3, upper right).

From these observations we conclude, that the main influences appear to be impacted by the same LT and season, and for numerous occasions similar patterns are formed when GRACE spacecraft experiences the same scenario. However, certain patterns, which correlate with geography , also appear to be correlated to LT and season whereas some others, as described in figure 10.2, rather match with the orientation of the node than with LT.

10.2 Seasonal impact

In the last section we mentioned that season (winter, summer, spring and autumn) may have a potential impact onto the geographical distribution of twangs. Therefore we tried to separate season from local time. Now we will try to give an overview about the influence that can be detected due to season by means of selected examples of ACC1A data of GRACE B. Note that for any example a possible influence due to the β_{prime}-cycle of the sun cannot be exactly excluded, as the whole cycle is 322.3 days long in order to have GRACE in the exact same orbital node and same orientation towards the sun. Additionally, it takes about 7 years in order to experience this constellation in the very same season. However, as we previously mentioned, reliable twang distributions are not available prior to 2005 due to gaps in data availability and the lower number of twangs occurring before 2005. Also refer to the figure 10.1 in the previous section to get an overview about the orbital constellation of the GRACE spacecraft. In order to exclude a possible influence due to reversed orbital node we will restrict the node to only one node (either ascending or descending) per example and only will compare to other nodes to observe a potential node influence.

In figure 10.4 a series of figures related to scenarios in ascending node at LT between 20-21 hours is displayed. The seasons vary and are sorted in such a way that the upper left image starts early in the year, January and February, and progresses towards November/ December to the lower right image. Each image is taken from a different epoch from 2003 to 2010, whichever case was available to display the given scenario. The change of the patterns formed by twangs is obvious throughout the seasons, but it is also notable, that seasons that are close to each

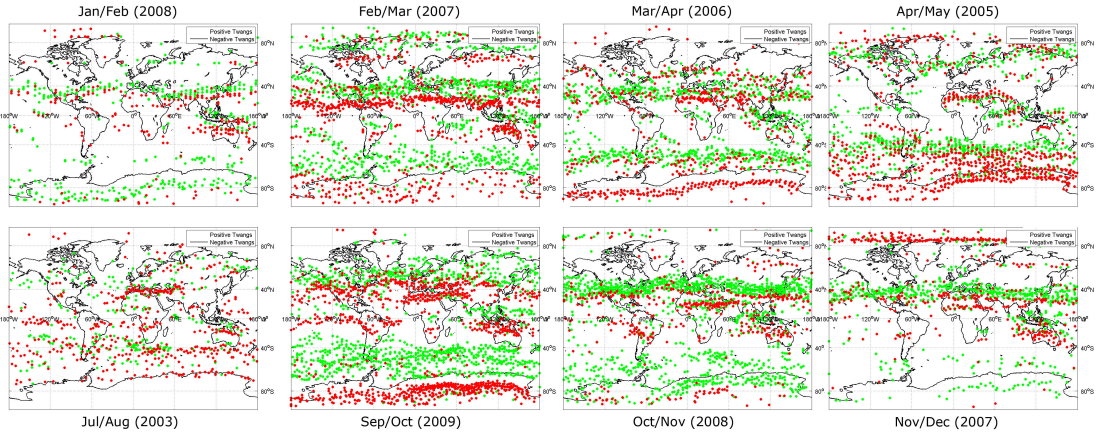

Figure 10.5: Change of twang formed patterns due to season, GRACE B. Red dots represent negative twangs, green dots positive twangs. Each image spans 2 months, all twangs are detected between LT hour 10 and 11 in a descending orbit. Season progresses from upper left to lower right.

other have similarities. For instance, the months in the winter of the Northern hemisphere all appear to show a pattern formed by negative twangs in the far northern latitudes, often forming a W-shaped band. Also it becomes clear that the patterns that can be observed in the months between May and October appear to be de-correlated to a great extent from those observed in the other months of the year, indicating that the patterns may very well depend on the season of the year.

Another example can be seen in figure 10.5, where we compare different patterns of twangs in different months at LT between 10 and 11 hours. These examples are solely extracted from a descending node. A seasonal dependency of the patterns formed by twangs is obvious. This is especially visible for the patterns formed near the Antarctical coast. During months October to February only few and mainly positive twangs can be observed in this region. In the remaining months, however, a band of negative twangs roughly following the shape of the Antarctic coast is being formed, growing broader and more intense towards August/ September. The fifth image (lower left) in figure 10.5 has to be neglected in this regard, as this specific example is from 2003 where very few twangs can be observed and therefore this example may not be able to fully represent the seasonal impact (also. cf. 8.3.2, p. 69). Also the band formed by positive twangs slightly North of the mentioned band of negative twangs at the Antarctical coast appears to be correlated with season in accordance with the months mentioned before, February to September. Furthermore, a certain dependency on the season may be observed somewhat North of the equator with the rather strict separation of positive and negative bands, but this formation is less obvious than the one in southern latitudes.

Many patterns appear to be rather restricted to specific latitudes than longitudes. Therefore, it is more helpful to display how the patterns progress by means of latitude with respect to season or covering a larger time-span of a few years. This can be done by plotting twangs by their appearance in the argument of latitude versus time. The argument of latitude describes the movement of the spacecraft relative to the latitude, starting at 0 degrees, the equator, with an ascending node, until it reaches the North pole at 90 degrees. Then the satellite will enter descending arc, passing the equator again at 180 degrees and reaches the South pole at 270 degrees. This is followed again by an ascending arc until 360 degrees, which corresponds again to the equator.

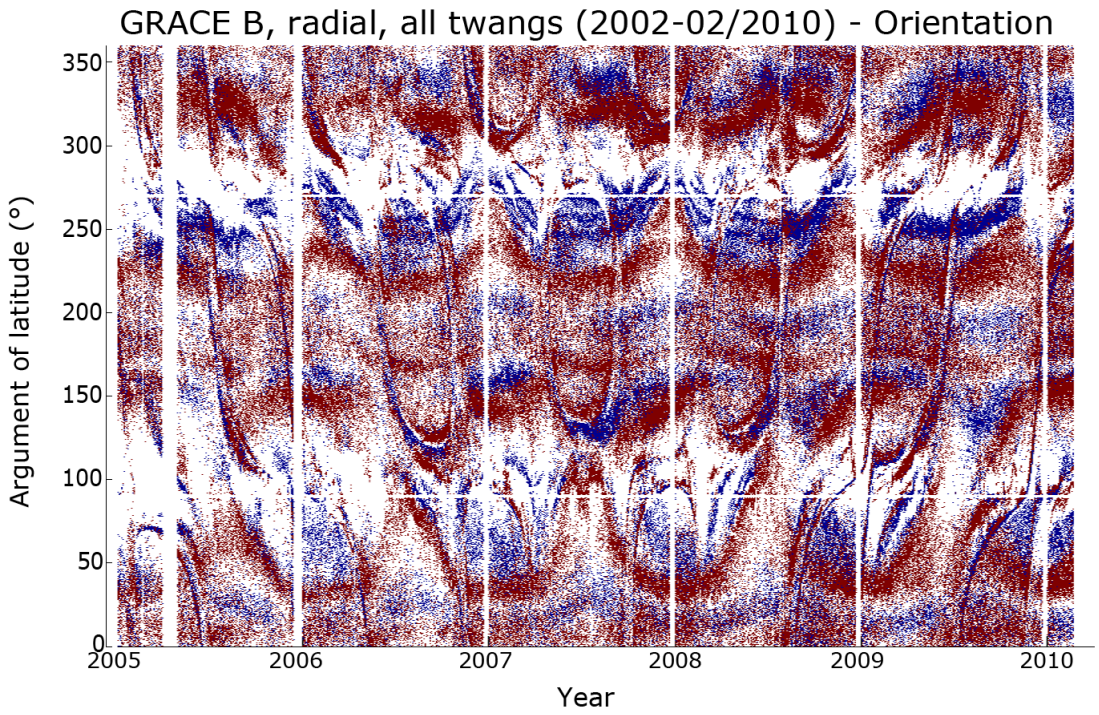

Figure 10.6: Orientation of twang in radial axis. Red dots are negative twangs, blue dots are positive twangs.

Such a scenario is displayed in fig 10.6 where we show all twangs of the available ACC1A data of GRACE B with respect to the argument of latitude. The red dots represent negative twangs and the blue dots are positive twangs. It is obvious that positive and negative bands are formed and shaped very distinctly from each other throughout the years. Also, the latitudinal behavior of the distinct bands appear to be underlying a certain periodicity, this is for example clearly visible at the positive twangs in the argument of latitude range between 150° and 250°. Also visible are the polar gaps at degrees 90 and 270 due to the specific inclination of the GRACE orbit, and the region near the poles where very little to no twang activity can be observed. Also quite obvious are the oval shaped patterns with a majority of negative twangs between 100° and 250°. These are found to be due to a direct solar impact onto the nadir satellite surface (also cf. section 12.2 for more details).

More examples concerning a possible seasonal impact may be found in the Appendix A. By means of the two introduced examples we showed that a seasonal impact onto the geographical distribution of twangs is very likely. This is also supported by cross-correlating the patterns of each months of every year with all other months. In figure 10.7 we show the mean cross-correlation coefficient of every monthly formed pattern of twangs with every other month. These coefficients have been computed as follows:

$$R_{i,j} = \frac{C_{i,j}}{\sqrt{C_{i,i} \cdot C_{j,j}}}, \tag{10.1}$$

where R is a matrix containing the correlation coefficients from input matrices, which is a 180x360 matrix, based on a 1x1 degree grid of the Earth's geodetic coordinates. Every single bin contains the overall number of twangs that occured in the corresponding month. C is the covariance matrix. In order to exclude a possible solar impact we distinguish between such situations where

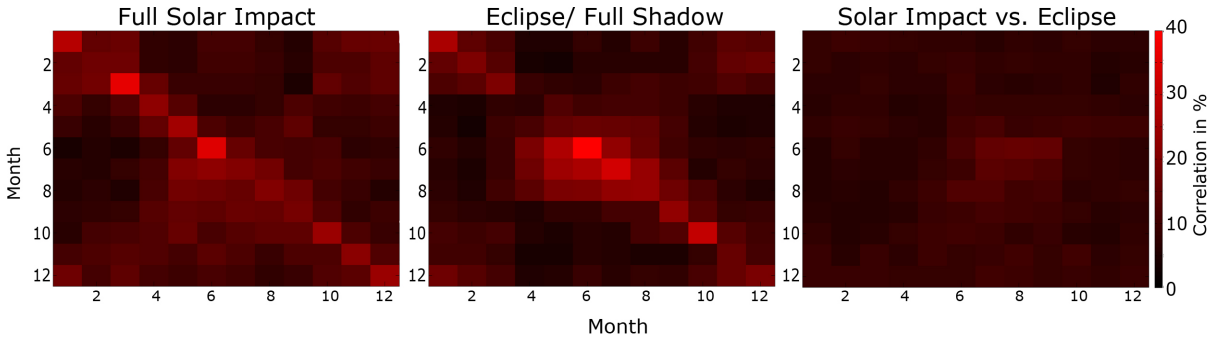

Figure 10.7: Correlation of twang patterns of each month with every other month for which ACC1A data of GRACE B is available for this study. Left image: Only twangs regarded which occurred while GRACE spacecraft were in full sunlight; center image: Only twangs regarded which occured while GRACE spacecraft were in full eclipse; right image: Correlation between patterns detected in full sunlight with those detected in full eclipse.

the GRACE spacecraft are in sunlight and those where GRACE is in eclipse. The highest mean cross-correlation coefficient is always found in the corresponding month, which implies that for example the pattern found in April of 2005 will be most likely showing a higher cross-correlation coefficient in April of any other year than with any other month. This hints at the seasonal impact being larger than a hypothetical β_{prime} impact, as our data covers several years and the cross-correlation coefficients would be less strictly bound to their corresponding months if the solar impact had a larger impact. Yet, by these terms we do not want to exclude a β_{prime} impact at this point. This is necessary as in section 8.3.2 we found that the number of twangs per day appears to be periodical and the corresponding power spectral density revealed that a β_{prime} cycle influence may be as likely as a seasonal, i.e. annual, influence.

10.3 Differences for GRACE A and GRACE B

So far we only showed examples of twangs found in the ACC1A data of the GRACE B satellite. Now we will focus on the similarities and differences of the geographical distribution of twangs detected in both GRACE A and B spacecraft. In order to make the distributions of both satellites comparable the corresponding twangs need to be extracted from the very same epoch in terms of LT, season, orbit and year, i.e. time-tag of GRACE data. We assume that the spatial separation, and hence the time in terms of velocity, can be neglected as both satellites pass the same geographical coordinates in a very short time. In the previous sections we showed that the geographical patterns formed by twangs are subject to change by time, but the change does take a few weeks up to months with respect to season, and 2 to 3 hours or more in terms of local time.

In our example figure 10.8 we display two different scenarios for which the structures formed by twangs are visible for both satellites (upper row represents GRACE A, the lower row displays GRACE B). In order to avoid a possible correlation between the scenarios, the two examples are separated by one year, and also by a few months to display a slightly different season. The most obvious fact about these images is that the patterns formed by twangs are very similar for both satellites in terms of latitude and longitude. However, GRACE A has a significantly larger amount of twangs, and it is visible that for GRACE A often more than one twang occurs in the same orbit in a short time, forming a systematic appearance. Furthermore it is detectable that for various occasions the bands formed by twangs are not as strictly bound to one of the two types, positive or negative twangs, but often are containing a mix of both, where one of the two

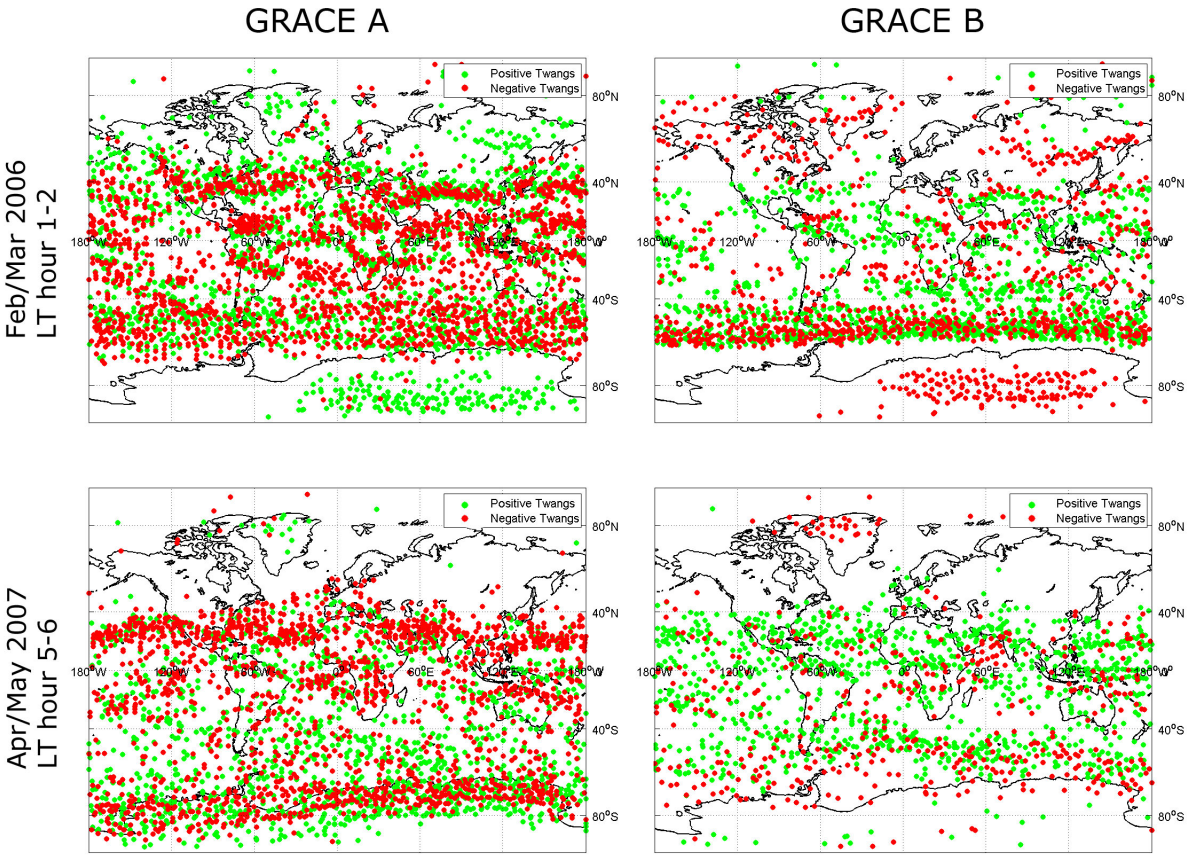

Figure 10.8: Comparison of twang patterns in ACC1A of GRACE A (left column) and GRACE B (right column) for two scenarios. Upper row: scenario for February/ March of 2007 at LT hour between 1 and 2; lower row: scenario for April/ May of 2007 at LT hour between 5 and 6.

types may be holding a majority. For those patterns, where a majority of a type can be clearly detected, it is notable that for GRACE A this type is the opposed type as to the one forming the corresponding pattern for GRACE B.

As the patterns for GRACE A and GRACE B are, apart from the number of twangs and the mixture of types for GRACE A, quite similar, a geographical or geographically associated influence onto the spacecraft is evident. A reason for the reversed type of twang for one satellite compared to the other might be found in the fact that the leading satellite is yawed by 180 degrees in order to establish the inter-satellite ranging system, KBR. This means that the cause for twangs found within the ACC1A data of GRACE has to be found in external sources as prime reason. Further elaboration can be found in part V of this thesis.

11 Temporal and spatial behavior of twang parameters

In this chapter the temporal and spatial behavior of the previously introduced twang parameters shall be described by means of observations. We will not draw further conclusions based on these observations in this chapter. However, many of these observations will be regarded when stating our hypothesis in part V of this thesis. This is necessary as no obervation for itself can give clear evidence for the hypothesis, but they need to be considered summed up.

11.1 Amplitude

In chapter 8.3.2 on page 71 we discussed how the average daily amplitude is behaving over time. This discussion was only addressing the daily behavior and does not reflect the geographical distribution. As we deduced a possible β_{prime} cycle influence, we now will address the question whether the general amplitude a, as introduced in equation (8.3) (p. 67), is correlated to the geolocation. In figure 11.1 we display the amplitudes of positive twangs of GRACE B detected in January and February of the year 2008 between LT 12h and 00h. A clear distinction of amplitudes per band is visible. For this scenario there appear to be two main ranges for amplitudes. The most Northern pattern as well as a pattern that starts at approximate latitude 40° S stretching south, have an amplitude ranging from $2 \cdot 10^{-7}$ to $7 \cdot 10^{-7}$ m/s^2. The other patterns, located in between the just mentioned patterns, running approximately horizontal at approximately 20°N and 20° S latitude, come with an amplitude ranging from $1 \cdot 10^{-6}$ to $1.6 \cdot 10^{-6}$ m/s^2. We chose to display this scenario as a distinction in the amplitudes is very clear in this case, and close to no twangs can be found covering the amplitudes from $7 - 10 \cdot 10^{-7}$ m/s^2. This is a clear indicator for the fact, that not only the distribution of twangs but also their amplitudes are strongly depending on the geographical location of the GRACE satellite.

The next logical step is to address the question whether there is any specific reason for this behavior of the amplitudes of the twangs. In order to examine this issue we chose to display every twang with its corresponding amplitude a with respect to the day of year of 2008 and to the argument of latitude. The argument of latitude is described in section 10.2.

In figure 11.2 this scenario is displayed for positive and negative twangs. We decided to separate these two types, as we found earlier in section 9 that the orientation of twangs is also often subject to be limited to certain latitudes. On the right side the negative twangs are shown, and the positive twangs on the left side. Again it is clearly visible that the amplitude is correlated to specific latitudes throughout the time. This is more clear for the negative twangs than for the positive twangs. In case of the negative twangs, the band formed by twangs that follow a certain range of latitudes appears to be restricted to a very limited range of amplitudes. Also,

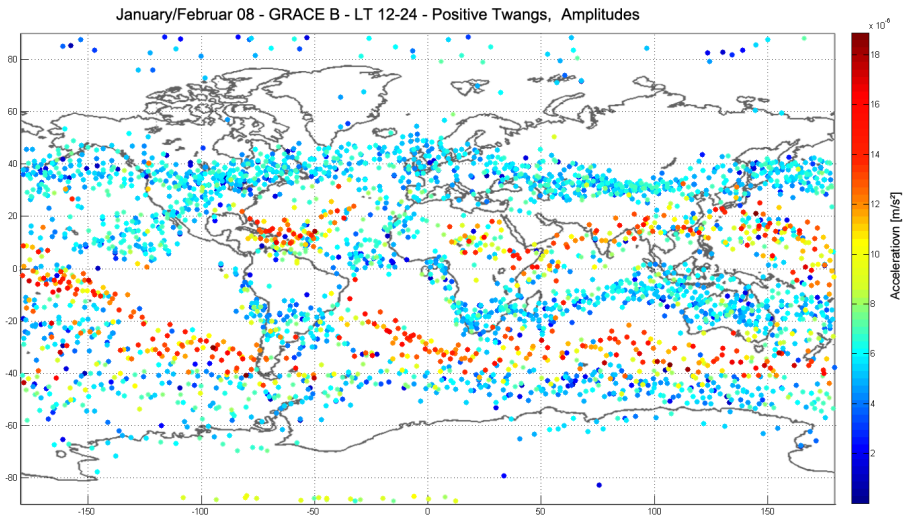

Figure 11.1: Mean amplitude (asymmetry neglected) for each positive twang of ACC1A GRACE B data of January and February 2008 between LT hour 12 and 00.

those patterns that run across a broader bandwidth of latitudes, such as the one visible in the argument of latitude starting at 50° and decaying at approximately 130° from day of year 0 to approximately 200, appear to be very limited to a certain amplitude. This behavior is less obvious in case of the positive twangs. The horizontal patterns of twangs are less strictly correlated to a specific amplitude. Yet, also for the positive twangs dependencies of amplitude values with respect to the latitude are visible. Here, the majority of twangs have an amplitude ranging from approximately $0.9 \cdot 10^{-7}\ m/s^2$ to $1.3 \cdot 10^{-7}\ m/s^2$. The negative twangs appear to have two sets of patterns, where one set is ranging from low $0.6 \cdot 10^{-7}\ m/s^2$ to approximately $0.85 \cdot 10^{-7}\ m/s^2$ and are the blue patterns visible in the left image. Another range for the negative twangs is from approximately $1 - 1.4 \cdot 10^{-7}\ m/s^2$. These two ranges are a lot more separated from each other than the ranges visible for the patterns formed by positive twangs.

Also, in both images we have clusters of twangs in patterns that suddenly have a rather big amplitude. For both types this is the case between day of year 150 to 300 (approximate values) and is especially visible between argument of latitudes 250° to 350°. Especially in the case of the positive twangs this high amplitude starts to appear rather suddenly with respect to the amplitude of the surrounding twangs of the same pattern and those which are located near the described area.

An interesting phenomenon visible for the scenario displayed of the negative twangs can be found around day of year 250 at latitudes 0° to 100°. There are two horizontal bands which start occurring a few days prior to DOY 250 and remain existing towards the end of the year 2008. However, the pattern visible at approximately 250 DOY that runs rather vertically dissects these two bands. The two bands appear to have a slightly but notable larger amplitude after this event than before.

Also for the along-track axis a strong correlation between the magnitude of the amplitude of the twang and the geographical location of the satellite at the time of the occurrence of the twang can be found. In figure 11.3 we present three images, where the left and the center image are displaying the twangs in the along-track component. The left image is showing the positive twangs in the along-track axis, and the center image the negative twangs. Note, that we are separating into these two types now according to along-track appearance and not by means of the

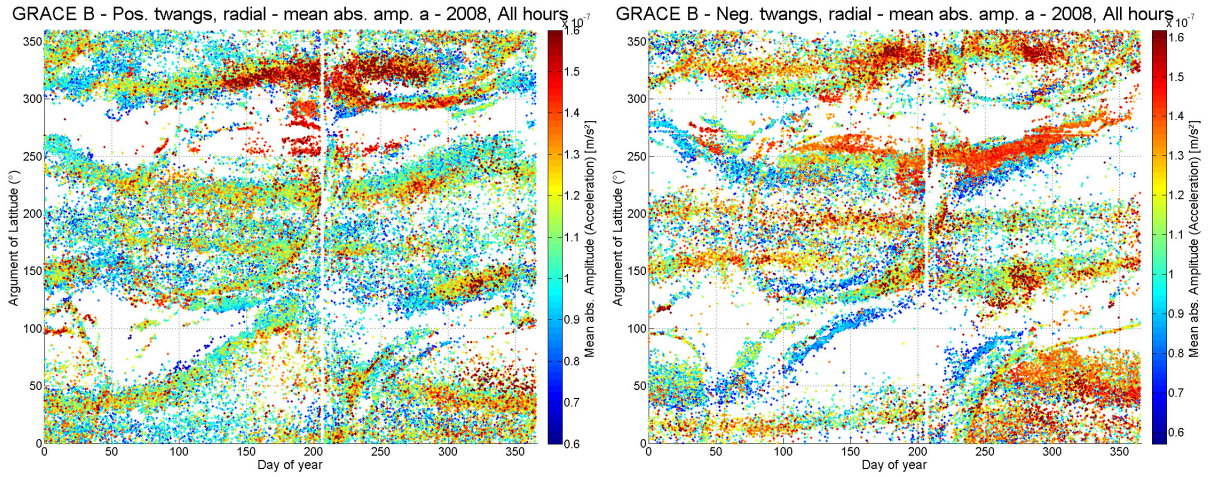

Figure 11.2: Mean amplitude (asymmetry neglected) for positive (left image) and negative twangs (right image) in the radial component of ACC1A data of GRACE B. The x-axis represents the day of year (DOY) of 2008 and the y-axis is the argument of latitude.

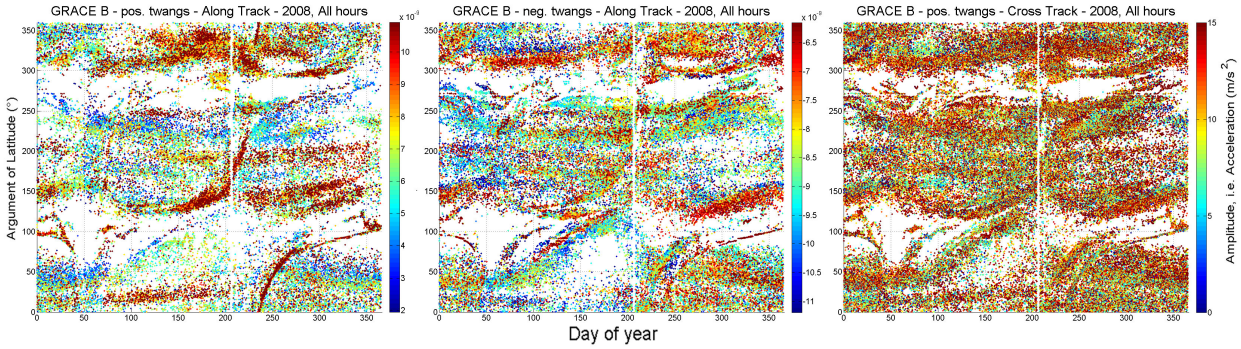

Figure 11.3: Mean amplitude (asymmetry neglected) for positive (left image) and negative twangs (center image) in the along-track component and positive twangs in the cross-track component (right image) of ACC1A data of GRACE B. The x-axis represents the day of year (DOY) of 2008 and the y-axis is the argument of latitude.

radial component. For positive twangs it is notable that twangs forming the oval shape pattern in the center of the picture have a relatively high amplitude of more than $10 \cdot 10^{-9}\ m/s^2$. This also applies to the other areas, where the nadir surface of the satellite is lit by direct sunlight (cf. section 12.2). This strict correlation to those areas is not detectable for the negative twangs, where other correlations are dominating the image, such as the rather horizontal band slightly above degree 300°. In both figures also other areas and patterns are limited in their range of amplitude.

The very right image of figure 11.3 is an example for the geographical appearance for the amplitude of the twangs in the cross-track axis of the ACC1A data. In contrast to the radial and along-track data of the same dataset, no clear correlation to the geographical location can be detected. Throughout the whole year 2008 the amplitude appears to be rather non-systematic with respect to the geographical occurrence of the twang in this axis. Only vague correlations can be observed, as for example, twangs with a higher amplitude appear to have a majority in the oval shaped pattern in the center of the image. This phenomenon is surprising as for the other two axes a very clear and distinct correlation could be detected and the natural

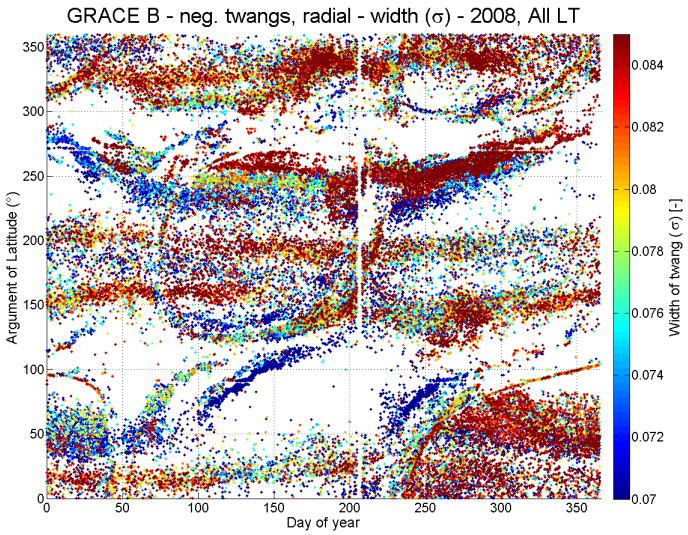

Figure 11.4: Width (σ) of the negative twangs in the radial component of ACC1A data of GRACE B. The x-axis represents the day of year (DOY) of 2008 and the y-axis is the argument of latitude.

expectation would be, that this phenomenon also applies for the third axis. Despite the rather direct assumption, that this may be a typical and yet unexplainable behavior for the cross-track axis, also other hypotheses need to be taken into account, for example that the transfer function for the less-sensitive cross-track axis is different from the other two axes and might influence the amplitude of the twangs. Which could also lead to the hypothesis, that due to the fact that the cross-track axis is a less-sensitive one the noise level in this axis, is by several magnitudes higher than those of the other two axes and the amplitude is hence harder to be accurately modeled by our approach.

11.2 Width (σ)

As already stated in chapter 8.3.2, we assume that all twangs have the very same width in terms of the Gaussian derivative. However, in the referred chapter we also introduced a time-depending behavior of the width, which is highly correlated to the behavior of the daily average amplitude of the twangs with respect to time. In this section we are able to validate the correlation between the width σ of the modeled twangs by means of a Gaussian derivative and the amplitude a of the twang in the very same model.

Figure 11.4 shows σ for all negative twangs in the radial component of ACC1A data of GRACE B for the year of 2008, displayed by means of the day of year on the x-axis and the argument of latitude on the y-axis. It is observable, that the magnitude of σ is linearly depending on the value of a as depicted in figure 11.2 in the previous chapter 11.1. The description of the figure itself is hence congruent to the description of figure 11.2.

This observable correlation between these two parameters is presumably due to the fact that a higher amplitude leads to an improved accuracy of the estimation of the width σ, as due to the higher amplitude the signal is more notable by our approach with respect to the surrounding sensor noise. However, a real and direct correlation between amplitude and width is less likely.

For this phenomenon the other two axes give direct evidence, as this applies to both the along and the cross-track axis as well (cf. Appendix C). The correlation between the width of a twang and the geographical location of the GRACE spacecraft at the time of the event of the twang is

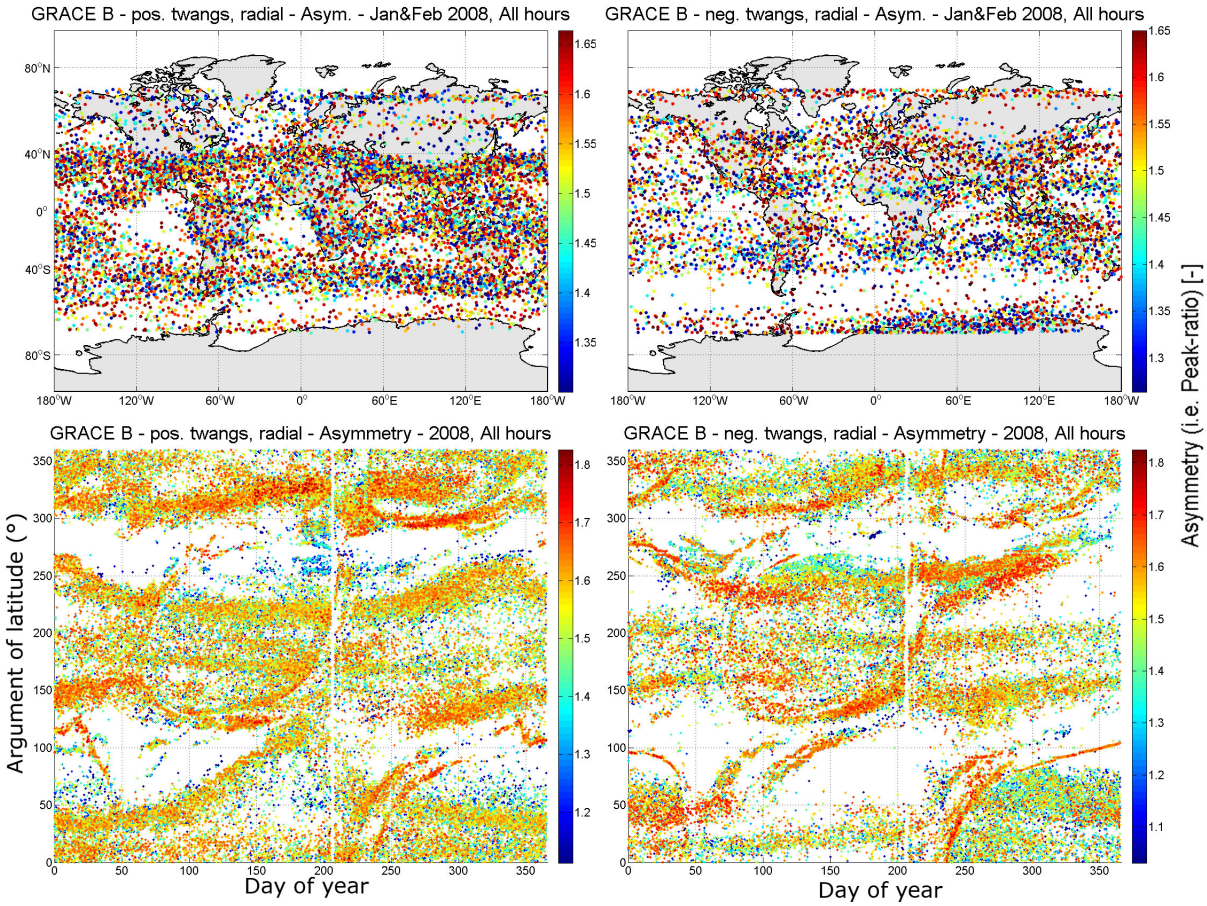

Figure 11.5: Asymmetry of twangs in the radial component of ACC1A data of GRACE B. Upper row: Positive (left image) and negative twangs (right image) in January and February of 2008 including all LT hours, displayed in geographical coordinates. Lower row: Positive (left image) and negative twangs (right image) of all twangs in 2008, displayed by day of year 2008 appearence on the x-axis and the argument of latitude on the y-axis. The scale represents the asymmetry, which represents the ratio of the two peaks - an asymmetry >1 indicates the second peak being greater in amplitude than the first peak.

very clear, which is in contrast to the correlation observed for the amplitude (cf. section 11.1). This correlation between amplitude and width of a twang might help to build more advanced models of twangs in the less-sensitive axis in the future.

11.3 Asymmetry

Concerning the amplitude we want to address the question whether the asymmetry of the twang, as introduced in chapter 8.3, is linked to the geographical occurrence of the twang in orbit. Again we chose to display a scenario for January and February of the year 2008, which is depicted in figure 11.5, upper row. On the left side the positive twangs can be seen, and the negative twangs are shown on the right side. The values of the asymmetry are derived by equation 8.6 on page 76. No particular order of the asymmetry values can be observed according to these two images. The asymmetry rather appears to be unlinked to the geography, and all asymmetry ratios ranging from 1.3 to 1.65 can be observed in all formed patterns by twangs.

This impression is deceiving as figure 11.5 (lower row) reveals. Here the twangs in the radial direction are displayed by the day of year of 2008 with respect to the argument of latitude on

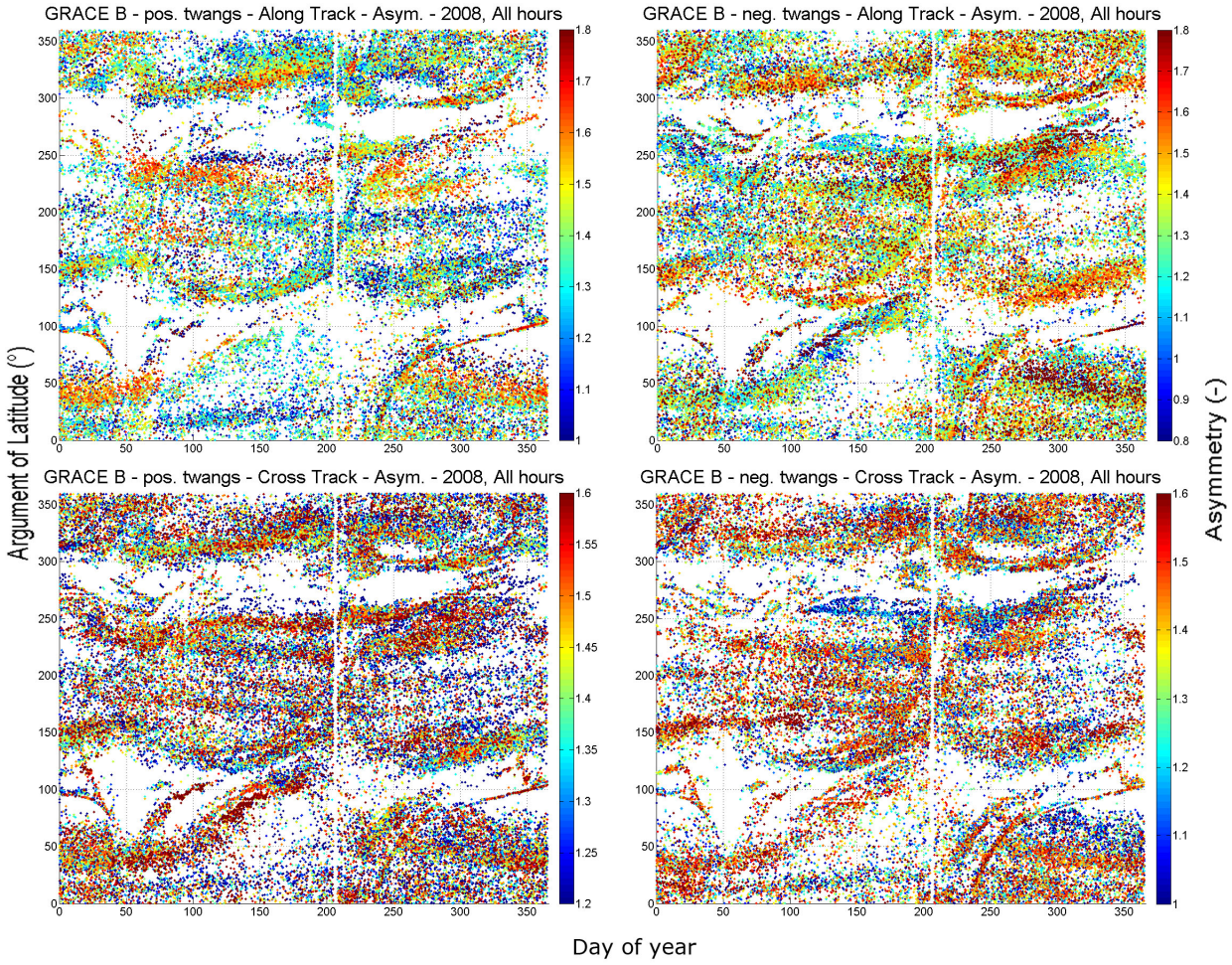

Figure 11.6: Asymmetry of twangs in the along and cross-track component of ACC1A data of GRACE B. Upper row: Twangs in along-track, positive twangs in left image, negative twangs in right image. Upper row: Twangs in cross-track, positive twangs in left image, negative twangs in right image. All twangs of 2008, displayed by day of year 2008 appearance on the x-axis and the argument of latitude on the y-axis. The scale represents the asymmetry, which represents the ratio of the two peaks - an asymmetry >1 indicates the second peak being greater in amplitude than the first peak.

the y-axis, negative and positive twangs are corresponding to the previous figure (11.2). Now, a systematic behavior in the value-distribution of the asymmetry of the twangs becomes observable. This becomes clear for some latitudinal bands between 150° to approximately 250°. But also very obvious is that the oval shaped pattern in the center of the figure appears to be strongly associated with a higher asymmetry of the twangs. This behavior is also notable at other patterns which are not directly linked to a latitude alone, such as the curved pattern between day of year 230 to 350 in the lower range of degrees. These patterns are directly linked to a solar impact onto the nadir surface of the satellite - a phenomenon for which we will give evidence in chapter 12.2.

In the band-pattern of the nadir-plane being sun-lit also a correlation with respect to the asymmetry of the twangs can be observed in the along-track axis. Figure 11.6 shows the twangs of the along (top) and cross-track (bottom) axes with the positive twangs on the left side and the negative twangs on the right side. The separation into each kind has been made by analyzing the amplitude in the corresponding axis. The images reveal that hardly any twangs can be found within the mentioned band for the scenario of the negative twangs in the along-track axis. The

edges to this band, however, reveal a relatively high asymmetry of the twangs in average of 1.4 or higher when compared to the other twangs in the same image. The image displaying the positive twangs for the along-track axis shows, that this band is consisting of mainly positive twangs which have a considerably low asymmetry factor of about 1, which means that these twangs are close to being symmetric. Also at other areas a clear geographical correlation between the appearance of twangs and their corresponding asymmetry can be detected, especially in the horizontally/ latitudinal aligned patterns.

In this figure (11.6), also the cross-track scenarios are displayed. These scenarios do not reveal as much of a strict and distinct separation of the asymmetry of the twangs by means of the location of the GRACE spacecraft in orbit. Certain dependencies can be observed, for example in the higher degrees of the oval shaped pattern due to the nadir surface being in sunlight for the image of the negative twangs, where mainly twangs of a rather symmetric shape are detected, yielding an asymmetry factor of approximately 1. In this approximate region very asymmetric twangs can be found for the case of positive twangs in the cross-track axis. This is also the case in lower degrees (about 45° to 100° at DOY 50 to 150), where many twangs with an asymmetry of larger than 1.6 are found. Also other correlations than the described regions are obvious in case of the cross-track axis, but are less distinct than the introduced ones.

11.4 Oscillation period

In chapter 8.3.2 we already stated the assumption that the observed dependency of the daily averaged oscillation period T on time is correlated to the behavior of the amplitude. By means of figure 11.7 we are able to give evidence for this assumption. On the left image we display the amplitude of the negative twangs of GRACE B of the year 2008 for each day of the year with respect to the argument of latitude. The amplitude is correlated with the value of the oscillation period T on the right image, which displays the very same scenario, except for the values, which is now indeed T. According to those images the oscillation period T is greater if the amplitude is greater as well. This again yields the assumption stated in chapter 8.3.2 that there is a certain possibility that T can be better determined if the amplitude is great, as the signal is more likely larger than the surrounding sensor noise and the oscillation may be observed for a longer time yielding more data points for the determination of T. However, the really high values for T at the approximate degrees 180° to 280° in the argument of latitude at the corresponding day of year 100 to about 330 are in a major contrast to the observed mean value of 0.242 s (cf. chapter 8.3.2). As we expect a rather short and sharp signal being processed by the accelerometer transfer function, yielding our twang structure in ACC1A data, the expectation would be, that the period T of the oscillation is invariant of time, regardless of the amplitude of the actual twang. The rather stiff width σ, being only linked to the amplitude in its geographical distribution, already gave evidence for this fact. However, the values of the described area appear somewhat larger than expectations would allow for such a scenario.

Furthermore, it is interesting that the geographical distribution of the values of T is more depending on the amplitude than on the asymmetry (cf. figure 11.5), as a higher asymmetry yields a longer oscillation with a great starting amplitude a_2 (cf. equation 8.4). The expectations here would be, that such a longer and possibly larger oscillating decay would be better observable than others and hence a certain correlation would become visible. A slight, but uncertain correlation, is observable for small asymmetry, which may be coupled to a higher accuracy of the oscillation period T. But with respect to the dependency detected between a and T, this dependency remains mere speculation. T is expected to be stable and invariant for all cases due to the unalterable transfer function of the SuperSTAR accelerometer. This is in accordance with the width σ of the twangs.

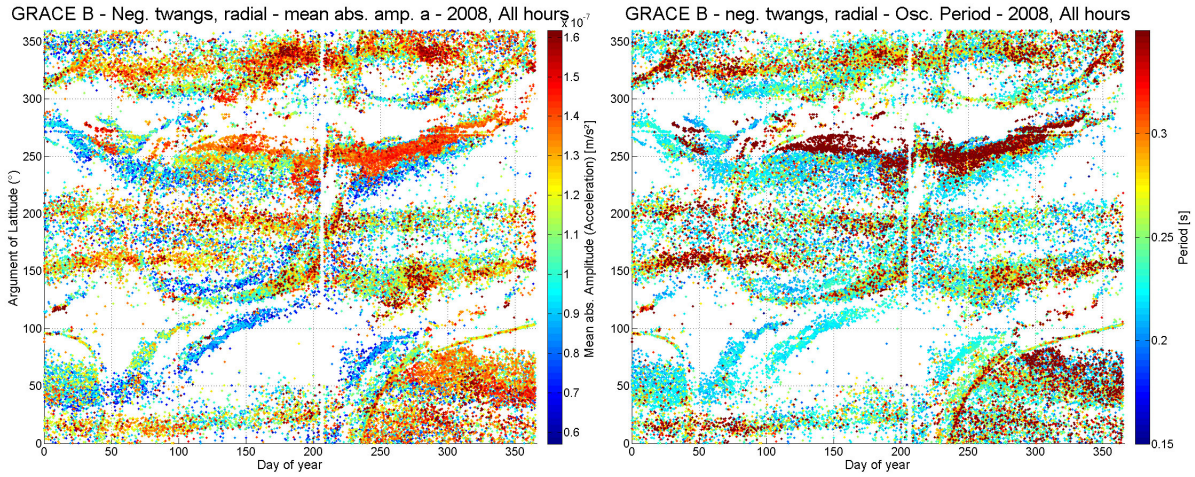

Figure 11.7: Amplitude a (left image) and oscilation period T (right image) of negative twangs in the radial component of ACC1A data of GRACE B. All twangs are occurring in 2008 and are displayed by the day of year as they occur and the argument of latitude on the y-axis.

As the signal in the other two axes is relatively small, hardly any oscillation could be detected (cf. chapter 8.3.2), as the signal decays too rapidly into the noise level of those axes. Therefore, no description for the period T of the oscillation can be given for the along and cross-track axis.

11.5 Energy

The energy of a twang is a combination of both the amplitude of the first two main peaks of the twang and the oscillating decay, if detected. It can only be positive and is defined as follows:

$$E_{TW} = \sum_{t=1}^{n} a(t)^2. \tag{11.1}$$

Here, E_{TW} is the energy of the twang, in $\frac{\mathrm{m}^2}{\mathrm{s}^4}$. t is the data point of the extracted twang in time, and n is the number of extracted data points, which is depending on the length of the twang, including a possible oscillating decay. a is the actual acceleration value of the extracted data point.

In figure 11.8 in the upper row we show the equivalent scenario for the energy value distribution of the twangs of GRACE B in 2008 with respect to the argument of latitude. It is becoming clear that the overall energy of the twang rather orients at the asymmetry (cf. fig. 11.5). This is due to the fact that a twang is extending up to several seconds if the twangs is asymmetric as it is enhanced by an oscillating decay, which contributes to the energy content (cf. fig. 11.2). If only the first two peaks were regarded, the energy of twangs with a great amplitude a are expected to have more energy than highly asymmetric twangs. This is especially clearly visible in the oval shaped area between day of year 50 to 200 and degrees ranging from approximately 120° to 300°. In this pattern the energy is comparably small for the twangs which are not inside this oval band. Twangs with a small energy may also be found outside this band, but close to none with a high energy can be found within.

This is less obvious for the case of the negative twangs. Also here the majority of twangs within the oval-shaped band come with a rather small energy, but the magnitude of the energy of a twang is not as strictly linked to the asymmetry of the twang. For instance, the band with a

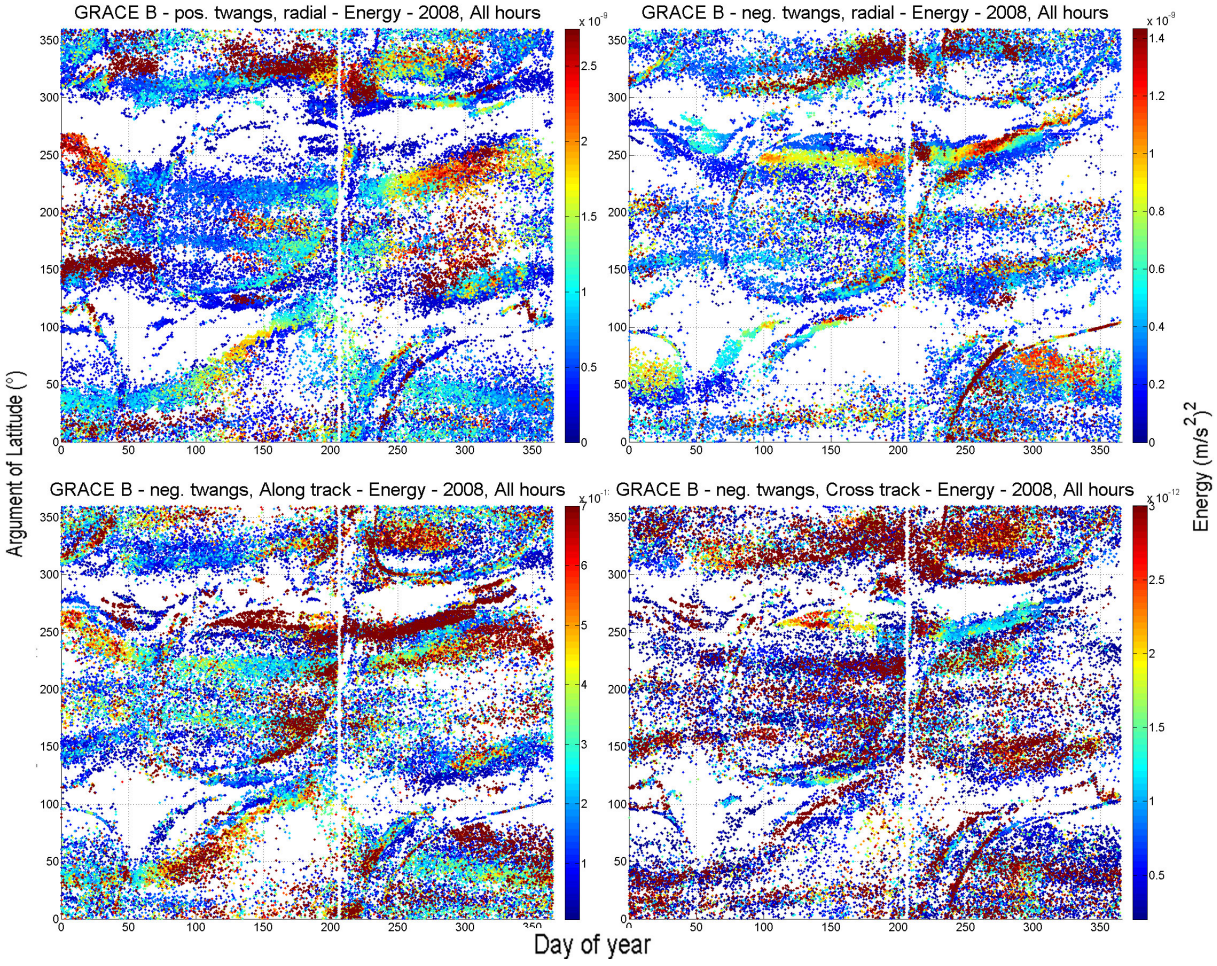

Figure 11.8: Energy of twangs, which are detected in 2008 in ACC1A data of GRACE B. Upper row: Energy of twangs in radial component, displaying positive twangs (left) and negative twangs (right). Lower row: Energy of negative twangs for along-track (left) and cross-track (right). On the x-axis is the day of year of 2008 and on the y-axis the argument of latitude.

really great energy ranging between degrees from 180° to 270° may also be detected in the image for the asymmetry twangs, but the image for the asymmetry twangs also display another band of twangs with more asymmetric twangs joining the just described one from lower degrees around day of year 250 to 320. This band is only vaguely indicated in case of the energy value image, but cannot clearly be correlated to the behavior of asymmetry in this case of negative twangs.

However, for both types of twangs the energy is more depending on the asymmetry of a twang, as an oscillating decay is most likely detected for these cases, which may increase the energy significantly. This is especially reflected in the oval-shaped band as described, where most twangs are more symmetric and hence have only a small oscillation and as for this, a small energy content.

In the other two axes, along and cross-track, the local restriction of certain energy value ranges to a specific area by means of argument of latitude and day of year is also clearly visible. However, due to the lack of modeled oscillations, this distribution is not as easily explainable. We display examples for along-track (negative twangs, lower row left) and cross-track (negative twangs, lower row right) in figure 11.8. Along-track also appears to have low energy content in terms of twangs in the oval shaped pattern just mentioned, a behavior which may be explainable by the rather symmetric twangs in the along-track component. However, the twangs with the very high energy content at the higher degrees near this oval shaped pattern are not entirely agreeing with an asymmetric shape of the twang, as for almost no twang in the along-track component an oscillation could be detected or even modeled. Hence, the oscillation cannot be the explanation for the high energy in this case but need to be found in other sources, such as the height of the amplitude or the 10 Hz sampling. The amplitude does reflect a relatively high value in those regions, but is not as distinctly separated in terms of the value by their surrounding twangs.

The cross-track axis (cf. figure 11.8, lower row right) is, as in most cases so far, rather vague when trying to detect a clear distinct geographical/ temporal behavior of the values of the twangs. However, also the cross-track component show a certain dependency on the latitude and days of the year, which is becoming very obvious at the higher degree range near the oval shaped pattern, where many twangs have an energy content limited to almost exactly $2 - 2.5\ m^2/s^4$, which is a strong indicator for a geographical, i.e. orbital, influence on the energy content of a twang. The corresponding values of these twangs show a relatively high energy and a low asymmetry, which indicates the amplitude being the driving factor in this case, in accordance to our scenarios detected in the along-track component.

11.6 Time-Shift between the axes

In chapter 8.3.2 we also discussed if any dependencies due to the offset in the occurrence of the same twang in the different axes with respect to time could be found. We detected a certain behavior in the average daily offset throughout the days, but could not link this fact to any specific factor. If we plot the value of the offset geographically a more systematic behavior of the difference of the occurrence of the twang becomes clear. We display an example for the difference with respect to time for the twangs. This difference is based on μ, the center point of the Gaussian curve derivative. In our example in figure 11.9 we display this difference by means of $\mu_{radial} - \mu_{AT}$ for positive twangs according to along-track. This means, that any negative value reflects a twang, that is occurring earlier in the along-track component than radial, and other way round for positive values. On the left side the μ-differences for positive twangs in the radial are shown, and on the right side the differences for negative twangs in the radial.

A very strong link between the geographical location of the twangs and the μ-difference can be seen in lower degrees in the argument of latitude between 0 and approximately 100 at the left

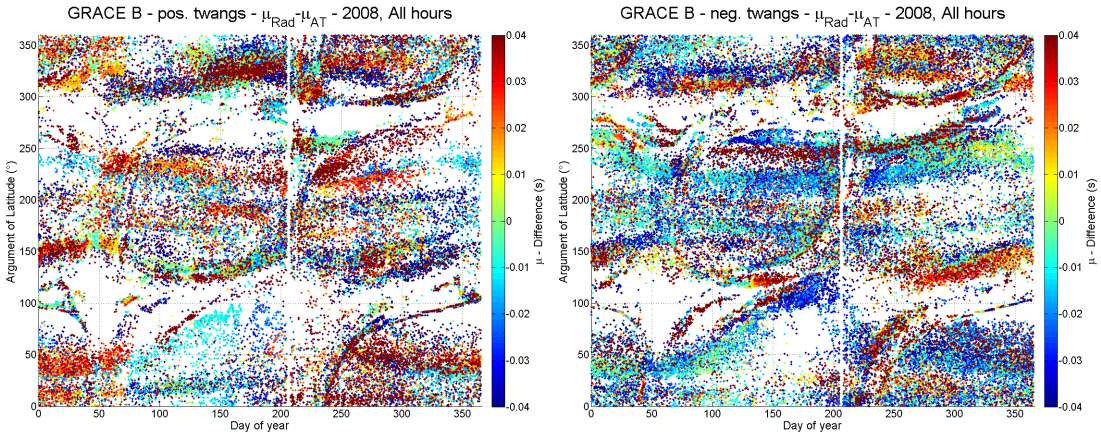

Figure 11.9: Difference of the center in time μ of the Gaussian derivative of the twang model between radial and along-track component for positive (left) and negative twangs (right, according to along-track).

image for the positive twangs in the radial. Between day of year (DOY) 2008 0 to approximately 75 we have a majority of twangs with a μ-difference between 0.02 and 0.03 seconds, followed by twangs with a slightly negative μ-difference of approximately -0.01 seconds between DOY 75 to 160. From DOY approximately 240 to 320 we find twangs with a difference of 0.04 seconds and higher for this range of degrees. Also, underneath these majorities of obvious twangs there are some patterns with a negative difference of -0.03 seconds and lower. Also other latitudinal regions in this image show regional dependencies with respect to the μ-difference, but they may be not as clear as the just described ones. However, certain horizontal bands consist of a majority of twangs with a μ-difference in a very limited range, such as the band at latitudes between 230° and 250° with a difference of 0.01 to 0.025 seconds.

A very interesting scenario can be found in the right image for the negative twangs in the radial. In contrast to the left image, most twangs here appear earlier in the along-track axis than in the radial, which is reflected by the negative values of the dots in the image. Also for the negative twangs local correlations between the geographic location, i.e. latitude, and the μ-difference can be observed. For example, most twangs with a μ-difference higher than 0.02 seconds are within a certain pattern which consists mainly of twangs with a difference of a similar or higher value. Another interesting area is the rather horizontal band running through all days of the year, starting between 240° and 270° at DOY 0 and describe a slightly U-shaped curve towards DOY 360. This band appears to start and end with a μ-difference value of 0 or higher, but the value appears to get smaller and drop down to roughly -0.03 seconds towards the middle of the year around DOY 170.

Similar behavior of the time-offset between the radial and the cross-track component could be observed.

12 Twangs related to solar impact and terrestrial radiation

In this section we attempt to classify twangs according to their geographical distribution. This shall lead the reader towards chapter V, where we will discuss the hypotheses. The classification aims at a separation of twangs according to their origin, which may be of different sources. In the previous chapters we found that twangs may not be strictly correlated to either seasonal impact or the β_{prime}-cycle. Furthermore, we saw dependencies of the twangs with respect to the

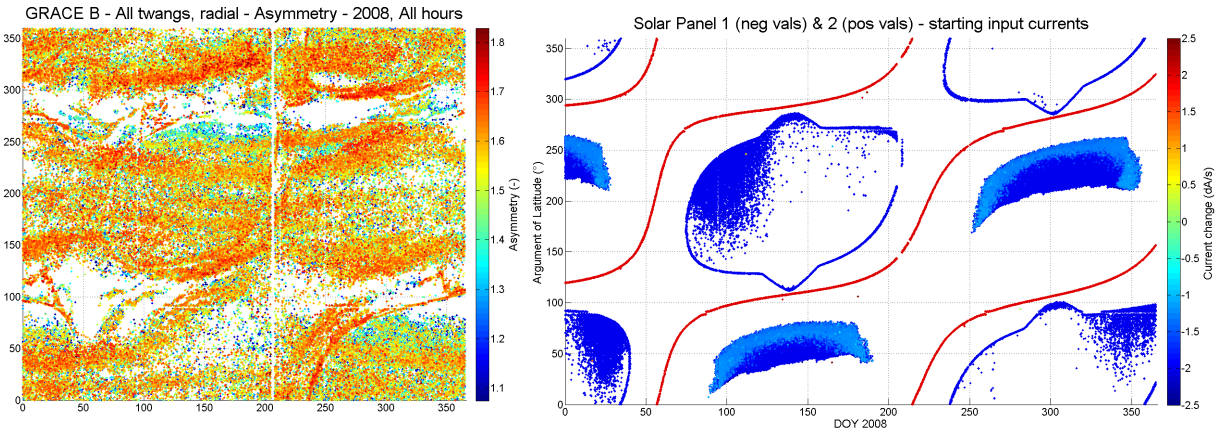

Figure 12.1: Comparison of twang patterns with a starting input current of the solar arrays. For solar array 1 the value 2 has been subtracted, and for solar array 2 the value 2 had been added. The values in the right image represent the current changes whenever the current in the solar array changed from 0 to a positive current.

parameters introduced in the analysis and modeling process. Now, we want to classify twangs by means of the geographical distribution in terms of latitude and time of appearance. The groups we will introduce now will be a reference for the hypotheses in the following chapters.

12.1 Group 1 - Narrow bands, i.e. entering and leaving shadow

One of the best observable patterns formed by twangs are the very distinct pattern of twangs starting in argument of latitude 0° at DOY 230 and will end at DOY 366 and argument of latitude 105°, which are visible in the left subplot of figure 12.1. This distinct pattern resembles a clear and narrow band, which appears to be correlating to the entering and leaving of the shadow areas of the satellite. The corresponding areas are displayed in the right figure of figure 12.1. The lines in this figure have been computed by means of the activation and deactivation of the solar arrays. The red lines are due to solar array 2 of the spacecraft, which is mounted on the zenith surface of the satellite, and the blue dots are the solar array 1, which are in fact two separate arrays mounted on the sides of the satellite. The dots in the figure represent the electric current whenever it changes from or to zero Ampere. The clear lines visible correspond to the clear lines in the left image. However, the lines visible in the left image are not due to activations or de-activations of the solar arrays itself. This becomes obvious in figures 12.2 and 12.3, where it is visible that the patterns resembling these distinct and narrow bands are becoming more and more clear since the launch of GRACE and are consequently due to an aging process within the satellite. Activations and de-activations, on the other hand, evoke the same electrical impulse within the spacecraft and should couple into the accelerometer data uniformly throughout time.

12.2 Group 2 - β_{prime} impact

During our investigations of the twangs in the ACC1A data of the GRACE spacecraft we detected a significant influence onto the spatial distribution and shape of the twangs due to direct solar impacts, which shall now be referred to as group 2. As the GRACE satellite orbit is not sun-synchronous, the spacecraft go through a variety of phases with respect to eclipse and illuminated phases, where different planes of the spacecraft may be directly impacted by

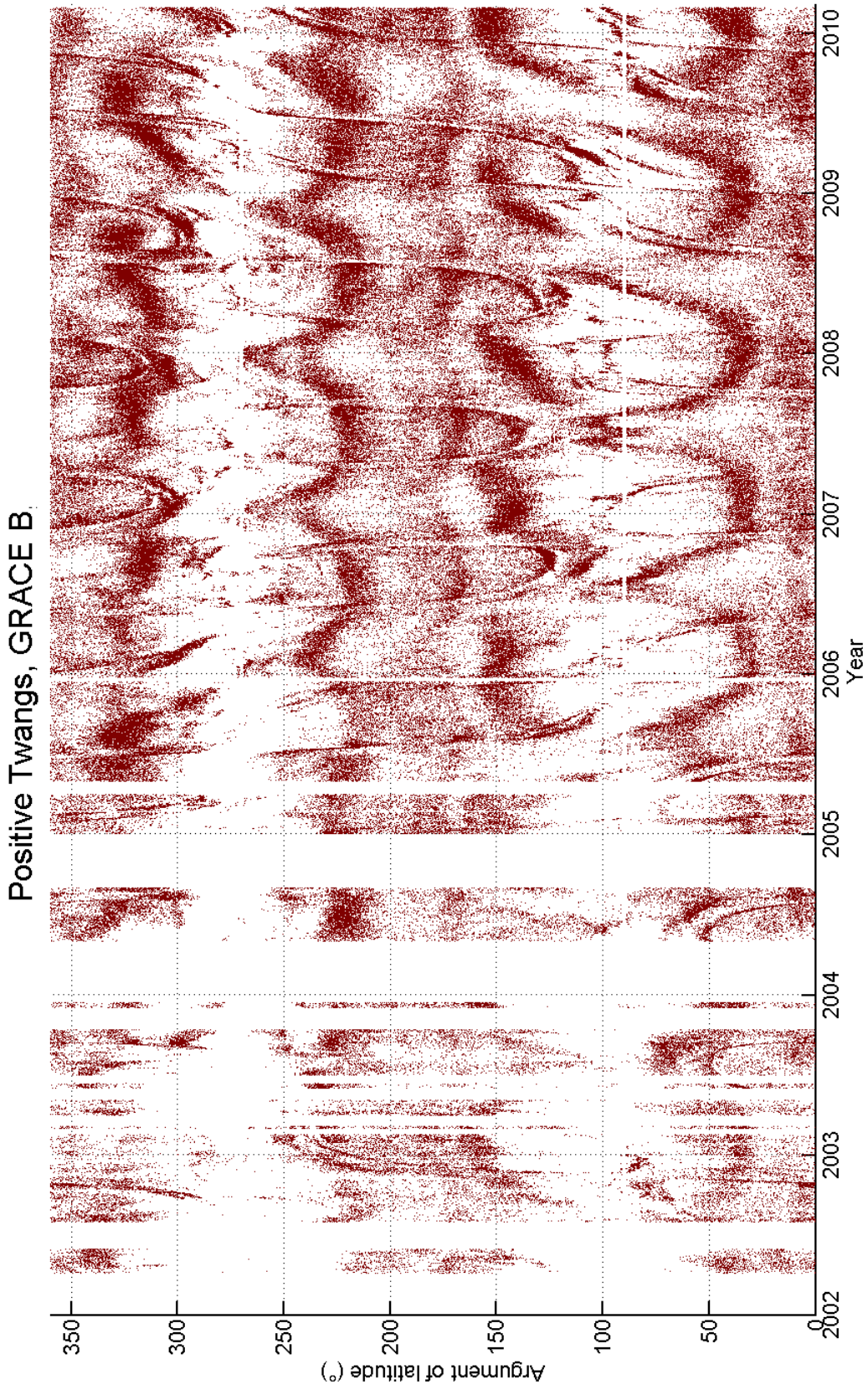

Figure 12.2: Positive Twangs, GRACE B, 2002-2010.

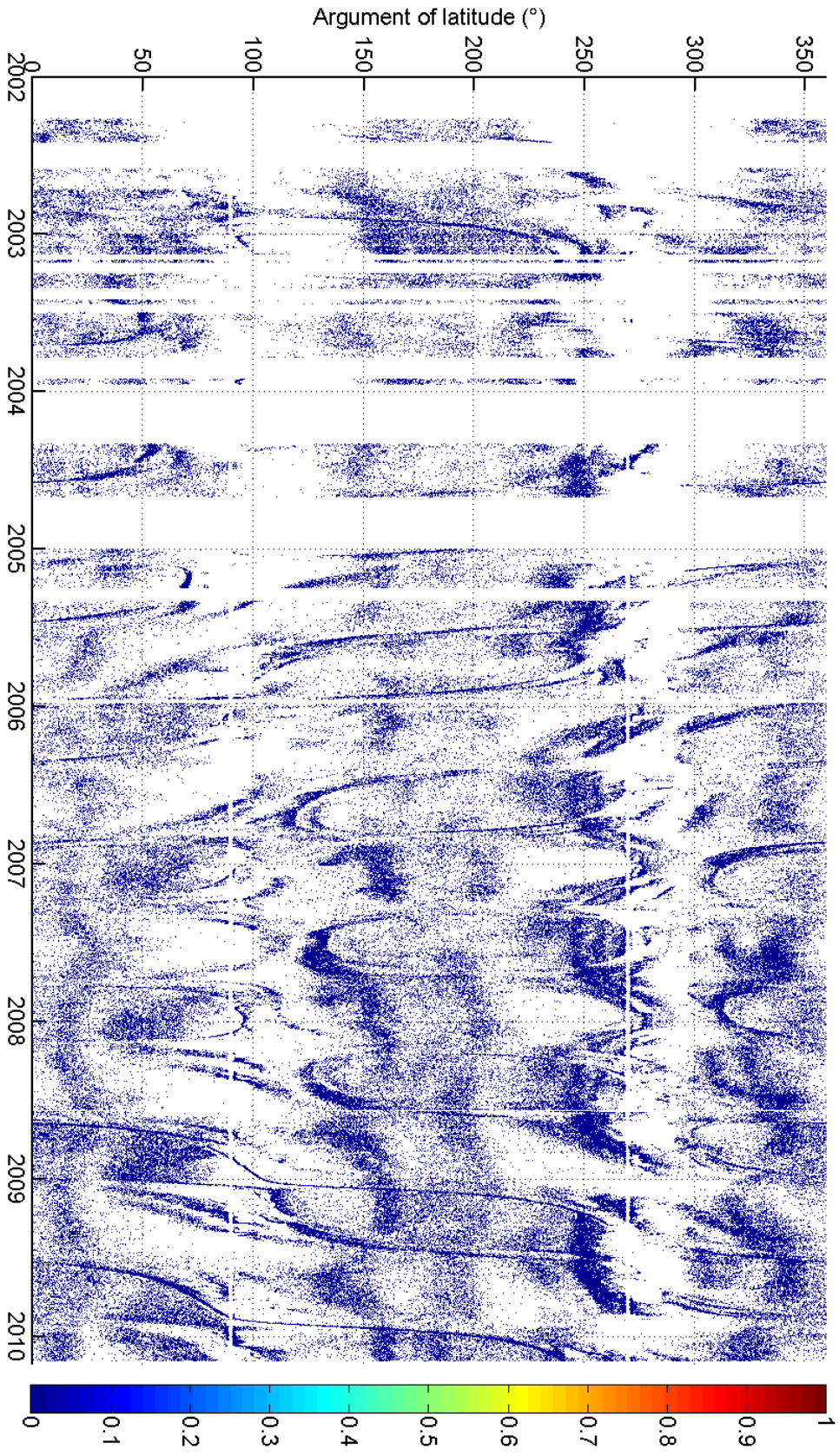

Figure 12.3: Negative Twangs, GRACE B, 2002-2010.

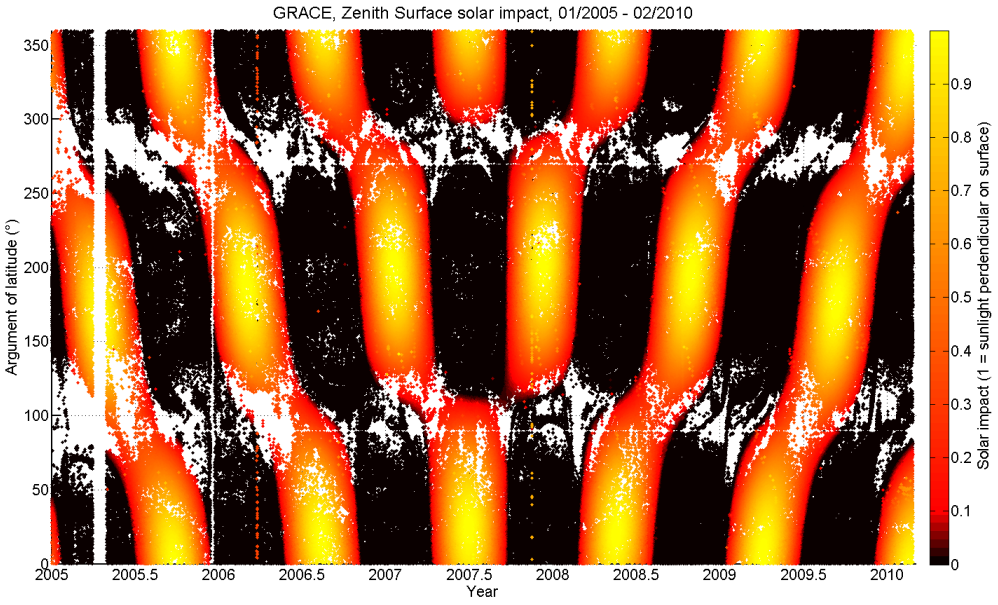

Figure 12.4: Solar impact onto the zenith surface of the GRACE spacecraft by means of twangs of GRACE B.

the sunlight. The cycle of GRACE's position and attitude with respect to the sun is known as the β_{prime}-cycle and is with 322.3 days shorter than the annual period of approximately 365.25 days. As these two periods are nonetheless rather close to each other a long time-span of data needs to be considered in order to distinguish between the annual, i.e. seasonal, impact and the β_{prime}-cycle influence. In figure 12.4 the twangs and the according solar impact onto the zenith surface of the GRACE B spacecraft are displayed. The β_{prime}-cycle can be observed by the orange-red colored patterns that lean towards left or right with approximately 2007.5 as a center point. Here, the shift with respect to the season, and thus an annual period, can be observed.

There are several patterns of twangs that can be correlated to the β_{prime}-cycle. For instance, the structures formed by twangs that are located near and around the poles (corresponding latitudes 90 and 270 degrees). When the spacecraft are approaching the polar area, this structure resembles a W-shaped pattern (as visible in figures 12.2 and 12.3), and is slightly less distinct when the satellite leaves this area. The orientation of this pattern is reversed for GRACE A and B. This pattern, however, is independent of a direct solar impact onto the GRACE spacecraft but does shift according to the β_{prime}-angle. Beyond this, there are other cloud-like patterns at top and bottom of the rather oval shaped areas in the center latitudes of the figure that correspond to the solar impact cycle. These are only observable when the GRACE spacecraft are in direct sunlight.

In this chapter we want to address the question when which surfaces of the spacecraft are illuminated by the sun, and how this may affect the spatial distribution of the twangs and their behavior by means of shape and duration. In the previous chapter (cf. IV) we already stated that the oval pattern detected in the figures displaying the twangs for every day of the year with respect to the argument of latitude of the satellites orbits are caused by a direct solar impact onto the nadir surface of the satellite.

First we will show which outer surfaces of the satellites are illuminated at which parts of the orbit, and then we will emphasize in which of these cases the twangs are corresponding to the direct solar impact. A broader selection of figures concerning the illuminated satellite surfaces as

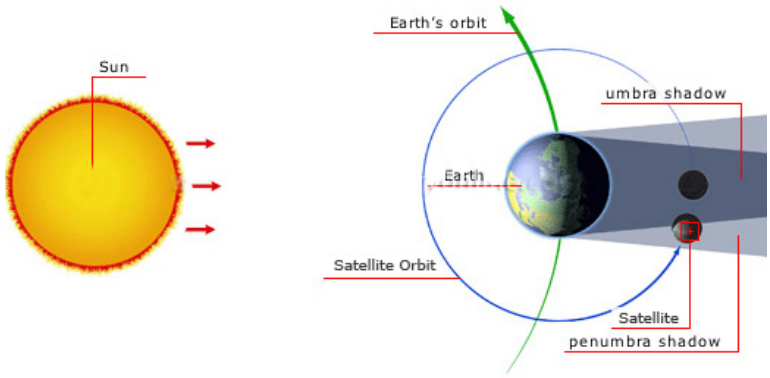

Figure 12.5: Schematic view of how Earth's shadow is eclipsing the satellite (full shadow) and penumbra (semi-shadow).

contained within this chapter is provided in the Appendix D of this thesis. To aim at a better comprehension most images in this chapter will display twangs and scenarios of the year 2008, as most results in chapter IV have been a reference to this year as well.

Determination of solar impact on spacecraft surfaces

In order to determine which parts of the satellite are exposed to direct sunlight several facts need to be known. One parameter is the position of the satellite in orbit, which can be derived from the GNV1B data solution, provided by the major data distribution centers (cf. 6.3.1). This file contains the navigation solution for each satellite, derived by the on-board GPS assembly. Another important parameter that needs to be known is the attitude of the spacecraft in orbit. For this, the orientation provided by the star camera assembly of the GRACE spacecraft can be used, which is contained in the SCA1B data solution (cf. 6.3.3). With these two pieces of information the incidence solar angle upon the surfaces can be computed. This angle describes the orientation of the surfaces towards the sun, where 1 (if given as a cosine), 90° or 100% means that the normal of the surface is directly pointing towards the sun.

This approach, however, only applies for the center of the satellite's reference system, for which those two data sets are given. As we already stated in the introduction to this chapter, twangs may behave differently if a special surface of the satellite is illuminated. Each surface of the satellite has a different incidence angle, depending on the direction in which the normal vector of the surface is pointing. In order to compute the incidence angle for each panel an exact model of the shape of the GRACE spacecraft needs to be taken into account. A description of the planes and the design of the GRACE spacecraft is given in chapter 3.

Further information that needs to be taken into account is the position of the Earth and Moon relative to the vector of the satellite to the sun. This is necessary as both objects may eclipse the satellite from sunlight or put it into a penumbra shadow, which is a part of the shadow where the light source is only partially blocked. A schematic view of how the Earth is blocking the light from the sun is given in figure 12.5. The computation of the solar impact onto the GRACE satellite planes has been carried out by Dr. ir. Eelco Doornbos of TU Delft in the Netherlands (Doornbos (2012)).

In figure 12.6 on the left side we display the direct solar impact onto the nadir surface of the GRACE spacecraft for each twang. The image displays each twang in the corresponding day it

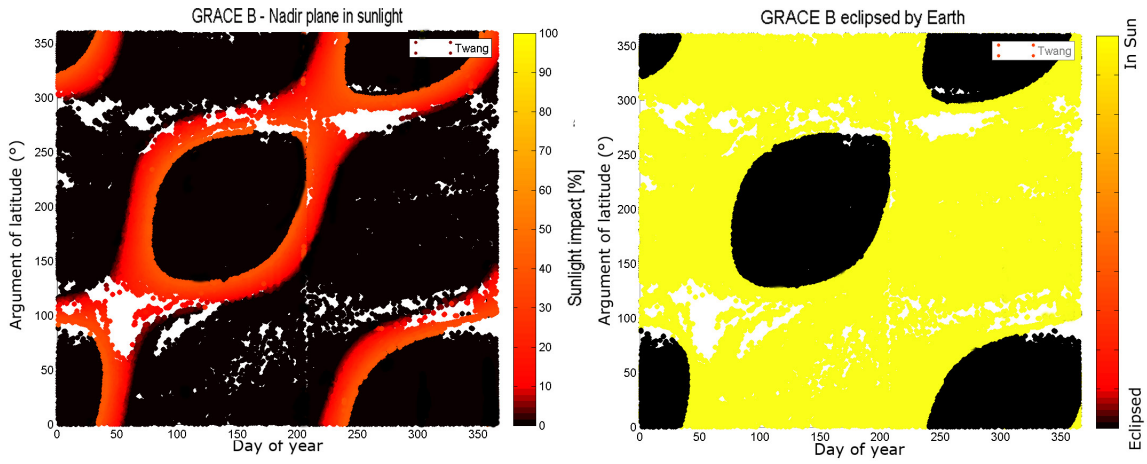

Figure 12.6: Solar impacts on GRACE B satellite (due to the small separation distance between the GRACE spacecraft also valid as a reference for GRACE A). Each dot represents a twang which is colored correspondingly. Left image: Solar impact onto the nadir surface of the satellite only - the scale displays the impact onto the plane, where at 100 per cent the sunrays are perpendicular to the plane. Right image: Solar impact and eclipse onto satellite as a two color schematic.

occurred in the year 2008, and the argument of latitude. Black means that the nadir surface of the satellite was not exposed to any direct sunlight at the time and position of the twang, the other colors indicate the impact, where 100 per cent indicates a cosine incidence angle of 1, which means that the sun rays are impacting the surface perpendicularly. It is obvious that the pattern created in this image by the area in which the nadir surface of the satellite is exposed to direct sun rays is a strict correlation to the pattern previously introduced in most figures of the chapter 11, for example figure 11.5 on page 99. The areas within the oval shaped regions are a total eclipse phase, which can be deduced from the right image of figure 12.6. The left image of figure 12.6 is giving evidence for the fact that the nadir surface is influencing the asymmetry and shape of the twang significantly when it is exposed to direct sunlight (cf. chapter 11). This becomes more obvious when comparing this figure to figure 11.5, as the change of values for the asymmetry is more distinct towards the inner boundary, where the satellite is entering a complete eclipse phase, than towards the outer boundary. Corresponding to this, the eclipse phase is entered very suddenly in terms of solar impact onto the nadir plane, whilst towards the outer boundary the impact value is decaying. Also for other areas the boundary between total eclipse of the satellite and an illuminated nadir surface of the satellite is very obvious. For example the curve described by the solar impact onto the nadir surface in figure 12.6 (left) between DOY 220 and 365 between argument of latitude degrees 0° to approximately 150°. Especially the inner boundary is represented by a very distinct line of twangs with rather distinct values for most parameters.

Another indicator for a direct solar impact onto the GRACE spacecraft can be deduced from the behavior of the amplitude of the twangs in the radial component when a comparison is made between those twangs, which are detected in sunlight and those, which were detected in total eclipse phase (cf. figure 11.2, page 97). Here, it appears that the amplitude for the twangs is slightly greater when the twang is occurring while the spacecraft is in total eclipse phase than when it is being exposed to direct sunlight.

In the near polar regions the amount of twangs appears to decrease in general as can be seen in any image displayed so far concerning the geographical twang distributions, but is especially obvious in the left image of figure 12.6 and in the following figure 12.7. In the polar regions,

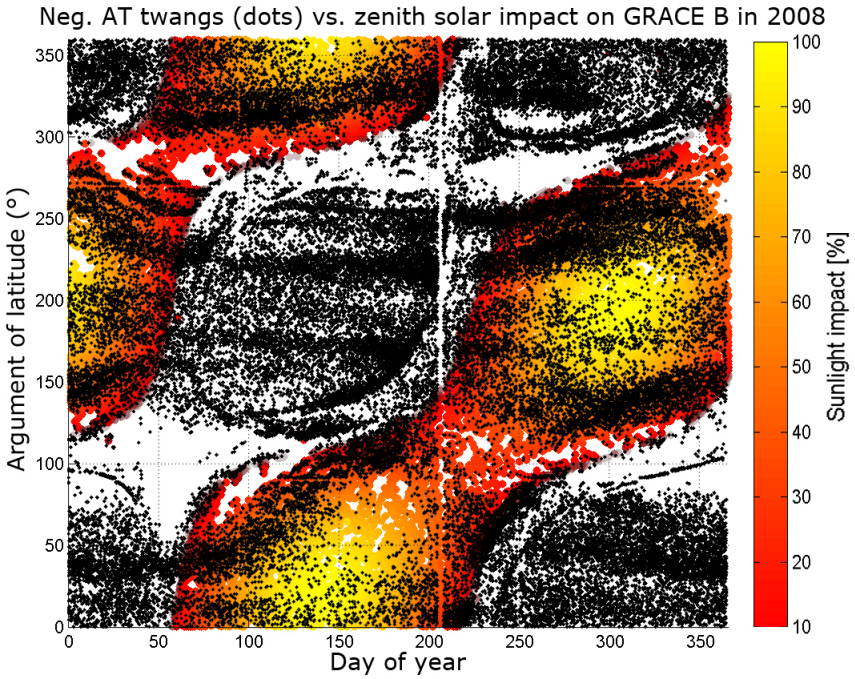

Figure 12.7: Negative twangs in along-track component of ACC1A data of GRACE B compared to the solar impact onto the zenith surface of the spacecraft. Each black dot represents a twang. Only solar impacted arcs of the orbit were taken into account in this picture.

including a 10 to 20 degree band surrounding the pole at 90° and 270° only a very limited amount of twangs can be observed. This is especially observable for the negative twangs of the along-track component of 2008 in figure 12.7, where nearly no twangs can be seen in the corresponding areas. This behavior is typical for any axis and any orientation of twangs. From this we can draw the conclusion that a sharp angle of 30 degrees between the orientation of the satellite and the sun results in fewer twangs than at other regions.

Furthermore, a slight correlation between a solar impact onto the zenith surface of the spacecraft and the distribution of negative twangs according to the along-track component of ACC1A data can be observed in figure 12.7. Here we compare the mentioned two scenarios. Wherever the solar impact onto the zenith surface of the GRACE spacecraft exceeds an approximate value of 80 per cent, which corresponds to an angle of 72 degrees, the amount of twangs in the corresponding area appears to get significantly fewer. This correlation is indeed less obvious than the impact that the solar impacted nadir surface has on the distribution of the twangs, and it can only be found in the negative twangs of the along-track component.

These are just examples for how the solar impact onto the satellite may affect the distribution and behavior of the twangs in the ACC1A data. However, this only gives evidence for a correlation between the solar impact and the twangs. So far, this cannot be considered as evidence that the solar impact is influencing the accelerometer measurements directly.

12.3 Group 3 - Annual impact

In this chapter we will address the question whether not only the direct solar light may have an effect onto the distribution and possibly also the behavior of the twangs in the GRACE accelerometer data, but also the season. An annual, i.e. seasonal, influence may be due to the

atmospheric behavior, which is greatly influenced by the sun, but also sunlight reflected from the Earth, known as terrestrial albedo and terrestrial emitted long wavelength, i.e. infrared. These sources may influence the parameters and the geographical patterns of the twangs and yield annual distributions of twangs, which will be referred to as group 3.

In figures 12.2 and 12.3 a sinusoidal shaped pattern of twangs is visible between degrees approximately 150 to 200. This pattern is visible throughout the whole displayed time-span and the individual bands are distinct from one another. The period of these bands is an annual period and is not correlated to the β_{prime}-cycle of the GRACE spacecraft.

12.4 Group 4 - Increasing number of twangs

As may be observed in the figure 12.3 in the previous chapter the overall number of twangs concerning the equatorial area appears to be increasing with progressing time. This is indeed not a distinct pattern itself. However, only very few patterns appear to be influenced by it, such as the sinusoidal shaped pattern introduced in the previous chapter. Therefore, this behavior shall be referred to as group 4 for further investigations. This also applies for the twang structures in the polar regions as observable in figure 12.2, especially concerning the southern pole area. Here, the number of twangs appears to be significantly increasing as the time past launch of the GRACE mission progresses.

In chapter 8.3.2 we could state that the mean amount of twangs per day has been steadily increasing since the launch of mission. This may contribute to this observation.

Interim Résumé

At this point we give a quick summary in order to emphasize the milestones that we have presented in this work so far and to guide the reader towards the hypothesis.

After preparing the ACC1A data of both GRACE spacecraft we were able to detect twangs within the data by comparing to succeeding 1-second intervals to each other by means of RMS values. Then we reconstructed the 10 Hz ACC1A data to 100 Hz as well as a reference twang by means of the Gaussian reconstruction filter, in order to determine twangs in ACC1A of similar shape and duration. For this we made use of a normalized cross-correlation as it also regards the differences, i.e. ratio, of the amplitudes of the two main peaks of the twang. Twangs may be separated into two main types of twang, negative or positive, depending on the orientation of the first peak. A twang can be modeled by means of a set of parameters which are based on the derivative of the Gaussian curve for the first two peaks and a double damped oscillation for the oscillating decay ending of a twang. These two parts are connected by a third degree polynomial in order to keep the structure continuously differentiable. All parts and parameters of the model ought to be adjusted by means of least square adjustment in order to keep the residuals as small as possible. By this approach most twangs in ACC1A data can be represented by the parameter based model, and a time-series with the length and sampling of the actual ACC1A only consisting of modeled twangs can be derived. With this, the influence of twangs can be determined and ACC1A data may be reduced. A possible impact onto the gravity field mapped by GRACE is found when the PSDs of the model time-series is compared to the accuracy models of the specific accelerometer axes. Reduced ACC1A data has been processed to ACC1B and differences where found, however not as accurately as needed. Yet, a possible influence onto the gravity field appears reasonable.

The overall daily amount of twangs has been steadily increasing since the launch of GRACE in 2002, whereas the mean daily amplitude appears to be decreasing. This applies for both negative and positive twangs. The amount of twangs is subjected to a periodicity, which might represent either an annual influence or an influence due to the β_{prime}-angle cycle.

When plotted geographically, twangs show to be distributed strongly correlated to geography. The patterns formed by twangs are the same for both spacecraft, but the orientation of the twangs may differ. Furthermore, the formation of twangs in terms of geography, season and time is strongly correlated to the parameters that were derived in the modeling process. The asymmetry of a twang, i.e. imbalance of the peak amplitudes, appears to be very sensitive to solar impact. Furthermore, a time deviation concerning the occurrence of twangs in the different axes, that appears to be random in the time domain, is strongly correlated to the surrounding environment of the spacecraft as well. A seasonal dependency as well as an impact of the local time or sun was detected for both the distribution of twangs in terms of geography as well as the behavior of the parameters of the twangs.

We introduced four different groups of twangs according to their geographical location and to the expected origin in order to guide the reader towards the hypotheses in the following chapter. In the following we want to address the sources that may be the cause for the development of twangs as well as the reason behind the distributions of twangs and what factors may be influencing the shape of twangs.

Part V
Hypotheses and satellite environment

So far we investigated the appearance, temporal behavior and shape of the twangs in the data itself. Furthermore, we investigated possible correlations with the geography, time, β_{prime} and season. However, so far we mainly stated observations and thus were able to give evidence that there indeed is a correlation between the twangs observed in the ACC1A data and the spacecraft environment. Due to the high frequent nature of the twangs they are considered not to be caused by the drag due to the residual atmosphere in GRACE altitudes or solar and albedo radiation pressure. Therefore, in this part of the thesis we want to address the question what exactly in the satellite's environment or which parts of the spacecraft itself can be identified as a cause for the twangs in the ACC1A data.

In this section we will present earlier hypotheses and investigations on the cause and nature of the twangs (cf. chapter 13). Then we will state our hypothesis, which is not in accordance with any previously stated hypothesis. In order to give support for our hypothesis we then will describe the environment of the GRACE satellites, i.e. ionosphere and thermosphere. Also, we will have a deeper look into the behavior of the used materials of the outer satellite surfaces as we expect them to play a significant role according to our hypothesis. In the end of this chapter we will discuss how this affects the accelerometer and how this might cause twangs to appear in ACC1A data. Twangs which cannot be directly linked to either of the hypotheses, but appear to have a more clear and obvious source, are stated prior to the hypothesis chapter.

13 Introduction and earlier hypotheses

Stating a hypothesis concerning the nature of a short, rapid and also prior to launch unexpected signal in one of the sensors data is not a trivial task. In case of twangs the source is up to date a speculative one. In this chapter the already existing prominent hypothesis according to this issue shall briefly be introduced. Furthermore, we will state our new hypothesis and briefly explain why we disagree with the former hypotheses and found the need to establish a new one. Further evidence will be given in chapter 17 if not already stated within this chapter. The explanations of the spacecraft environment and interactions of a spacecraft in a low Earth orbit (LEO) in the following chapter shall lead the reader towards our hypothesis.

13.1 Vibrations of the nadir mounted insulating foil

The phenomenon known as twang is being observed since the early mission phase of GRACE, and our studies reveal, that twangs can be found within ACC1A throughout the whole mission time until now. However, very few studies address this problem and even less hypotheses as to their occurrence were stated. Prior to our work only one hypothesis could be found, which was referenced by any following authors contributing their efforts to the complex task of the investigation of twangs. Yet, no actual publication associated with this hypothesis could be found, and most sources cite this hypothesis rather vaguely. Hudson (2003) describes the twangs as the result of vibrations of the nadir mounted insulating foil. According to this idea, the insulating foil expands inhomogeneously due to thermal effects. This insulating foil is made of Teflon and has a thickness of roughly 0.1 mm. This hypothesis is somewhat supported by correlating the amount of twangs to the temperatures detected by the CESS sensors on the GRACE spacecraft (cf. fig.

7.10 on page 60). Frommknecht (2007) tried to validate this rather speculative hypothesis by correlating the long wavelength albedo contribution heating the nadir side on the satellite and did indeed find vague hints, but no clear evidence. Up to this point, it was only known that for some twangs the solar impact, and hence the believed thermal impact, plays a significant role for the appearance of twangs. This hypothesis was originally established by Ab Davis and was confirmed in a personal communication (Davis (2013)).

Flury (2011) contradicts this hypothesis. He computed the possible impact of a slight vibration of such a thin and very light foil and found that the signal in the ACC1A is too large by several orders of magnitudes to be caused by vibrations of the insulating foil.

13.2 Solar array current impact

A solar array converts the energy of the light in the short wavelength spectrum directly into electricity making use of the photovoltaic effect. This results in electric currents from the solar arrays to the battery when one or more solar arrays of the GRACE spacecraft are exposed to sunlight. These currents can charge the battery if needed. As we could observe signals clearly above the noise level due to heater activations and de-activations as well as for current changes for the magnetic torquers in the milli-Ampere range it is valid to expect an impact onto the accelerometer due to starting or ending electrical currents from the solar arrays or current changes of this electrical current.

There are two main blocks of solar arrays mounted aboard the GRACE satellites, where solar array 1 consists of the solar arrays mounted on the inclined port and starboard sides of the GRACE spacecraft and solar array 2 consists of the two solar array panels mounted on the zenith surface of the satellites, one in front of and one behind the GPS antenna. Each of these two solar array blocks is connected to the battery of the spacecraft by two cable-strings mounted to either side of the spacecraft's body in order to avoid high magnetic fields.

A changing electrical current might be the cause for a significant amount of twangs that we observed and introduced in the previous chapters. Patterns of twangs, that correlate to the behavior of the electrical currents of the two solar arrays were introduced in chapter 12.1.

13.3 Charge and Discharge events of the spacecraft

Despite the fact that Flury (2011) found evidence that the nadir mounted Teflon foil is indeed too light in order to cause the signals known as twangs in the ACC1A data, our observation of the behavior and spatial distribution of twangs encouraged us to state an alternative hypothesis, that we believe to be more promising in explaining the nature of twangs. In chapter 8.1 we showed a figure that strongly suggests that twangs are not of random or unreproducible nature and they can be superimposed if the corresponding ACC1A data is referenced to the point of maximum cross-correlation in time. Such a superimposition is only possible if the signal is stable with respect to its length and duration. If mechanical vibrations were the source of the twangs, the expectation would be to find more variations of the periods and lengths of the twangs than those two types (negative and positive) that we found was the foundation of the majority of twangs.

Such a repetitive nature of a signal within ACC1A data hints at an electric origin of the twangs, as also the heater switching events (cf. chapter 7.2.3) and the electrical current changes within the magnetic torquer rods (MTQ, cf. chapter 7.2.4) lead to repetitive spikes within the ACC1A regarding to period and duration. Furthermore, figure 13.1 reveals that heater switching events,

MTQ current changes as well as twangs appear to have the very same period for the first two peaks of the signal. This hints at an influence of the transfer function (cf. chapter 5.2.2), which will transfer a short and rapid pulse into a signal as observed for these events in the ACC1A data. Heater switching events and electrical current changes of the MTQ are to couple into the accelerometer by electrical means and are visible as the spikes presented in the ACC1A data and are indeed based on electrical impulses of a very short and rapid nature. This strongly suggests that the source of twangs has an electronic origin as well. Figure 13.1 is indeed no contradiction to the statement made in section 13.2 as both twangs due to electrical current changes in the solar arrays and due to discharging events, are of electrical nature and thus are expected of the same short and rapid nature, that deviate only by means of amplitude and energy.

This leads us to our hypothesis. The global distribution of twangs with respect to their shape and amplitude hints at external sources (cf. chapter 17). There may be more than one cause for the existence and shape of a twang. The patterns observed hint at a direct solar impact, the ionosphere and albedo. As the cause seems to be of electrical nature, a charging and discharging event of the surfaces of the spacecraft may be the origin and source of twangs. Such charging and discharging phenomena are well known and described, and may lead to anomalies and malfunctions of the satellite's payload and will occur for any satellite at most orbits (cf. chapter 16). Also, the fact that the twangs have a slightly different deviation in time in different axes with respect to geographical occurrence contradicts the vibration hypothesis as this offset in time ought to be the same for any twang regardless of the spacecraft's position in case of a mechanical cause (cf. chapter 11.6). We believe that the discharging events of charged satellite surfaces of the GRACE satellites lead to the observed twangs in the ACC1A. The charging will occur due to the plasma along the GRACE orbit, which may be due to the ionized atmosphere, i.e. ionosphere, and due to the precipitation of electrons with a high energy content in the auroral regions (cf. chapter 15).

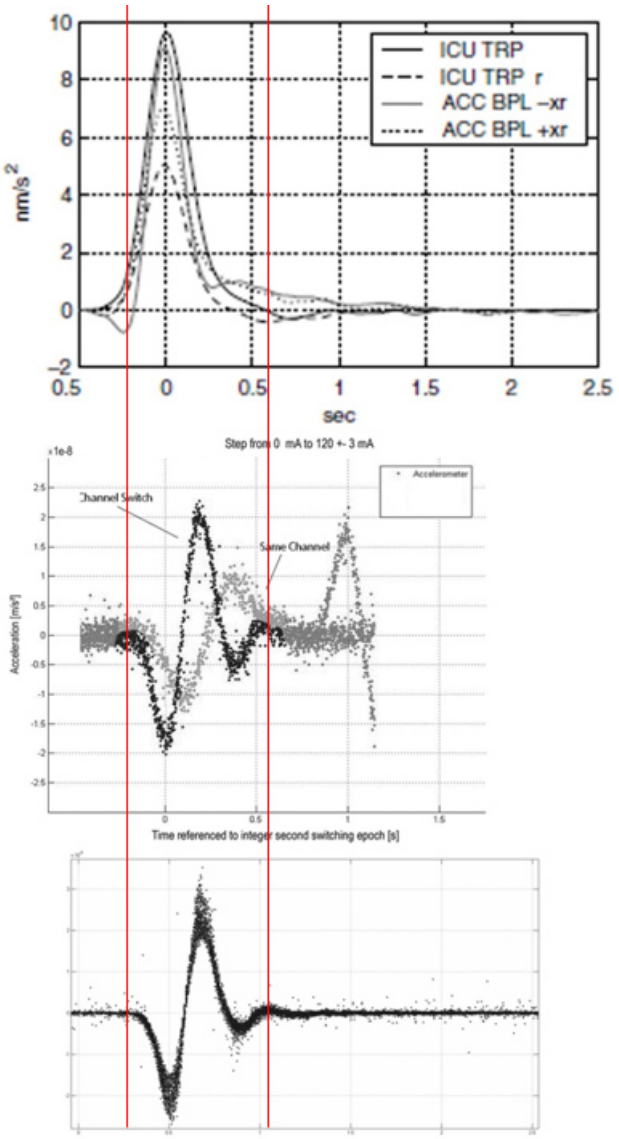

Figure 13.1: Heater switching event spikes (upper image), magnetic torquer current change spikes (center image) and twangs (lower image) in ACC1A data appear to have the same duration (cf. also Peterseim et al. (2012); Flury et al. (2008).

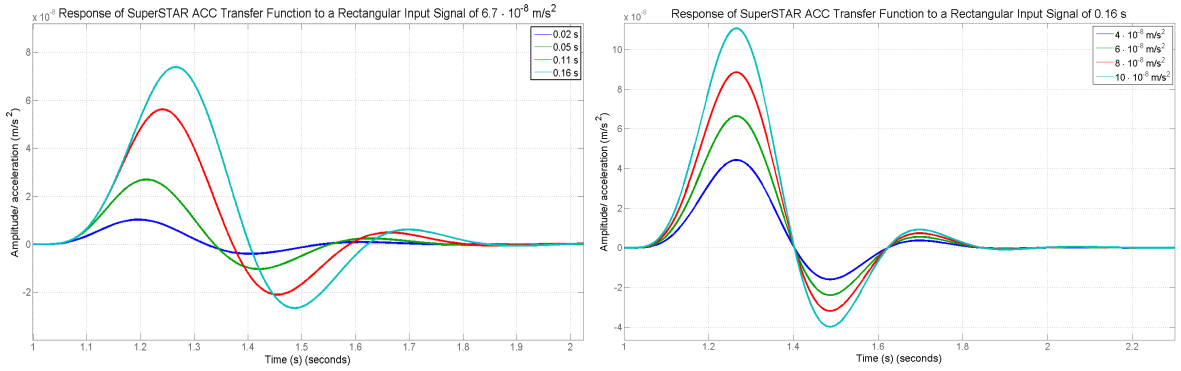

Figure 14.1: Responses of the SuperSTAR accelerometer transfer functions to different rectangular input pulses with varying duration (left) and amplitude (right).

14 Responses of the SuperSTAR accelerometer

In this chapter we want to discuss how twangs may couple into the SuperSTAR accelerometer of the GRACE spacecraft. In the previous chapters we introduced a model, with which the twangs in ACC1A data can be modeled, and how the twangs and their parameters behave with respect to time and location along the orbit.

In the previous section we showed in figure 13.1 (p.118) that the signals in ACC1A due to the heater activation and de-activation, electric current changes for the magnetic torquers and the twangs have the same duration for the main peaks. This fact hints at a process that may be strongly associated with the transfer function of the accelerometer, which is responsible for the shape of a signal as we can observe it in the ACC1A data. Furthermore, it may be regarded as a hint, that these signals may have the accelerometer as a common denominator in terms of source, but not of external origin.

We introduced the transfer function of the SuperSTAR accelerometer in chapter 5.2.2. A short and rapid signal in the order of a small fraction of a second cannot be resolved and displayed as such in the ACC1A. The shorter an impulse is, the smaller the amplitude will be in the ACC1A data. However, there will be a minimum duration of the signal within the ACC1A data with only little deviation. This is displayed in figure (14.1) (left) where the response of the SuperSTAR transfer function to a rectangular input pulse with an amplitude of $6.7 \cdot 10^{-8}$ m/s^2 is displayed. There are four scenarios, and for each scenario the length of the impulse is varying from 0.02 to 0.16 seconds. It is observable that the duration of the first two peaks is within limited boundaries and almost of the same length if the relatively short length of the input signal is considered. The average length of the response signal is approximately 0.6 seconds. Such a signal length is indeed in the same range as the mentioned signals above. A limitation of the width of the input pulse yields a limitation of the response width. In figure (14.1), right side, the input length is the same with 0.16 seconds, but the amplitude of the input signal ranges from $4 - 10 \cdot 10^{-8}$ m/s^2.

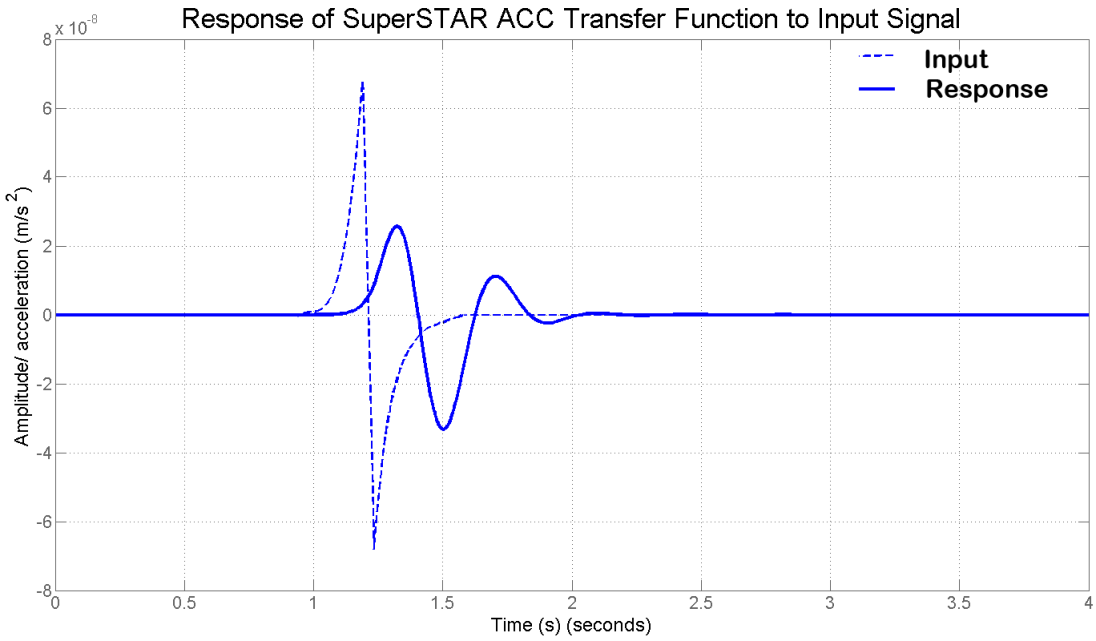

Figure 14.2: Response of the SuperSTAR transfer function to an input impulse. The response resembles the shape of a twang by means of duration, asymmetry and to some degree the oscillation.

This results in alternating amplitudes of the response. In these scenarios, however, the duration of the peaks always remain constant and can be used for superposition. As twangs can be clearly resolved for superposition, and show strong variation in the amplitude, but no variations in the duration, we can conclude that the source of twangs is probably due to an input impulse with a varying amplitude but a relatively stable duration (cf. figure (8.2), page 62). However, in chapter (8.3.2) we showed that the width of the Gaussian derivative part of the model changes in accordance to the amplitude. In these cases we assume that the width in ACC1A data can be detected with a better accuracy if the amplitude is great as the signal is better distinguishable from the sensor noise.

A promising approach in order to determine the nature and the appearance of the original input signal would be to use an inverse transfer function in order to obtain the signal by one of our twang models. However, an inverse transfer function was not available to us and could not be derived in this case. Another, but rather speculative way to address this issue is to construct an input impulse that yields a response of the transfer function, which resembles a twang, as good as possible. Such a scenario is shown in figure (14.2). In order to evoke a response signal, which resembles a twang the input signal needs to consist of two peaks of two different orientations. This results in an asymmetry of the response signal in the same order as we could observe it in the case of twangs. Furthermore, a better observable oscillation can be obtained by avoiding a rectangular signal, but rather using a triangular shaped input pulse, where the inclining and declining flanks are described by exponential functions.

Yet, there may be a range of differently shaped input impulses that may yield responses, that also resembles a twang-like shape. Therefore, our approach is merely of speculative nature and cannot securely be regarded as the original signal that results in the twangs in the ACC1A data of the GRACE satellite mission. However, we can conclude that the range of the duration of the input impulse only allows a very small tolerance in order to create a twang-like structure that is feasible for a superposition. Furthermore, the input signal needs to be of a shape where

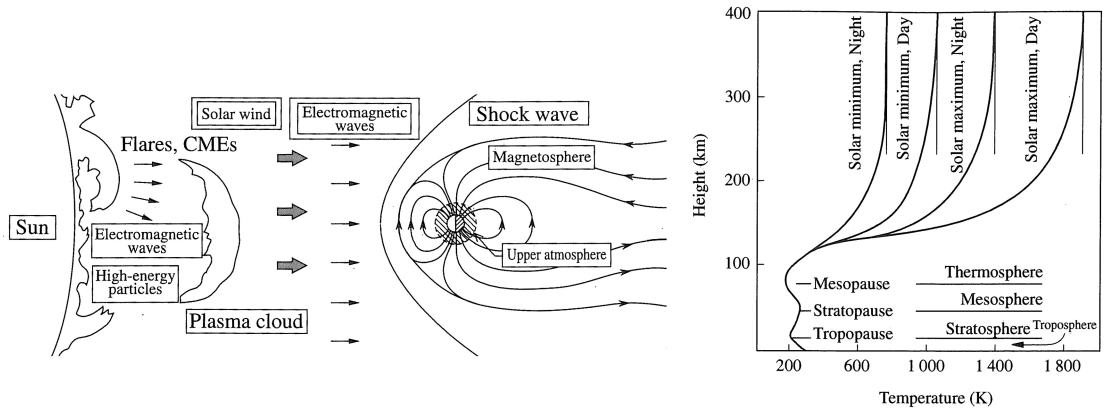

Figure 15.1: Left figure: Schematic view of the processes that shape the Earth's magnetosphere and influence the atmosphere (Ondoh and Marubashi (2001)); right figure: Atmospheric structure buildup as a function of altitude and temperature (Ondoh and Marubashi (2001)).

at least two peaks have a different orientation in order to evoke a response that resembles the asymmetry of a twang. Another constraint would be the net-zero acceleration fact of the twangs. Any input signal shorter than 1 millisecond will be displayed with the same length in the output signal as the polarization voltage V_p of the accelerometer has a frequency of 100 Hz and input signals with a shorter duration cannot be resolved according to their length.

15 Spacecraft environment

In order to understand how twangs may occur according to our hypothesis it is necessary to understand how a spacecraft at GRACE altitude is interacting with its surrounding environment, and thus an understanding of the ionosphere is inevitable. Therefore, this chapter is dedicated to the atmosphere at the height of the GRACE mission, the occurring electron and ion densities, the wind and currents at orbit as well as the temperature. The description in the following section is mainly based on Ondoh and Marubashi (2001) if not stated otherwise.

15.1 Fundamentals

At any time the sun emits an enormous amount of energy in terms of radiation and particles into space. This radiation consists of visible, ultraviolet and infra-red light, and has the form of electromagnetic waves. This solar energy greatly influences the Earth's atmosphere, and more precisely, it contributes greatly to the shape of the Earth's ionosphere. In addition to this emitted energy, the temperature near the sun ionizes the solar atmosphere, resulting in the creation of plasma, which is all around the sun and flows out into space. Plasma derives in fact from neutral gas by means of high temperature, high voltage or high radiation. As a result, plasma consists of highly energetic particles, ions and electrons. This flow of plasma from the sun is known as solar wind, which has a great impact onto the Earth's magnetic field. Most of the energy of the solar wind is guided around the Earth by the magnetic field. However, some of the energy is caught by the Earth's magnetosphere, and can for example be seen in the form of the aurora lights. The left image in fig. 15.1 gives a schematic overview of these processes.

The Earth's atmosphere begins at ground level, and stretches out into space, decaying with an increasing distance from Earth. It can be divided into different regions depending on the altitude. Each of these regions has different and unique characteristics, as the atmosphere absorbs different wavelengths of the solar radiation, depending on the altitude. Near the surface of the Earth the atmosphere consists of the air we know and breath, which is a mixture of nitrogen (N), oxygen (O_2), carbon dioxide (CO_2), water vapor (H_2O) and argon (Ar). However, the composition, density and pressure of the atmosphere depends exponentially on the altitude, and the amount of each gas may vary considerably. To a smaller amount the composition may also be time-dependent, but shall be neglected in this chapter. In most cases, the atmosphere is divided into regions based on a vertical temperature profile, as one of the main characteristics of the atmosphere, the temperature, is strongly depending on the altitude. The lowest layer, i.e. region, of the atmosphere is called troposphere and starts at the surface of the Earth. The upper boundary of the troposphere is called tropopause, which is about 10 to 17 km high, depending on the latitude. On top of the troposphere a layer called stratosphere is found, which extends to an altitude of approximately 50 km. While in the tropopause the temperature is lowest, it rises again in the stratosphere with increasing altitude. One of the main characteristics the stratosphere is known for is the ozone layer at heights of 20 to 40 km, which absorbs a great amount of the UV radiation emitted by the sun. This UV absorption is the reason why the atmospheric temperature is increasing in this layer. The upper boundary of the stratosphere is named stratopause, on top of which the mesosphere starts. This layer stretches from 50 to 80 km in altitude, and the temperature is decreasing again by 3.5 Kelvin per kilometer. Also in the mesosphere UV radiation is absorbed, however to a lower extent than in the stratosphere due to the smaller amount of molecular oxygen that is found in the mesosphere. The carbon dioxide amount, however, is increasing with respect to the amount of oxygen molecules and has a cooling effect onto the atmosphere in these altitudes. Analogous to the layers below, the upper boundary is named mesopause. On top of the mesosphere, the thermosphere is located, which is the last layer before the exosphere, where the atmosphere turns into space. The thermosphere extends up to 500 to 1000 km and the boundaries between thermosphere and exosphere are fluent. Due to absorption of the very high energetic solar radiation, the temperature within the thermosphere can rise to up to $2,500°C$ in sunlight. Furthermore, this radiation causes the particles in the thermosphere to become electrically charged, so that a great amount of the neutral gas in the thermosphere is excited into the state of plasma, which describes the ionosphere (described in the following chapter). Yet, the temperature stated above may be misleading as the plasma, i.e. gas, density is generally low, so that a thermometer as it is used on Earth would not detect this temperature but would read below freezing point as the impact rate between molecular particles and the actual object, i.e. thermometer, is too low. The correlation of temperature with the atmospheric layers introduced is displayed in the right image of figure 15.1.

15.2 The ionosphere

In this chapter we will introduce the ionosphere, which is part of the upper atmosphere, stretching from the upper part of the mesospheric layer at approximately 70 km height above Earth's surface extending to roughly 1000 km altitude, where it is replaced by the plasmasphere. In the ionosphere the plasma concentrations are sufficiently high, so that high frequent radio waves are reflected because of the high electron plasma frequencies. At an altitude of approximately 300 km the electron density reaches its maximum, which is monotonously decreasing with further increasing altitude. Below this altitude geographically correlated local densities with a higher or lower magnitude may occur, forming bumps or bulges in the electron density profile.

Hence, the ionosphere is divided into different regions, according to altitude. These regions are primarily determined by the electron concentration and the chemical equilibrium between the production of ions and electrons through ionization of the surrounding ambient neutral gas, and the loss due to recombination with the neutral gas. A chemical equilibrium describes the state in which the reactants as well as the products in their present concentrations have no further tendency to change with time if no other external force or reactant is applied. The regions of the ionosphere are displayed in figure 15.2. The lowest region is the D region, which starts in the mesosphere at 70 km and extends into the thermosphere to an altitude of 100 km. Above this is the E region (100 to 150 km), followed by the F_1 region (150 - 200 km) and the F_2 region (above 200 km). Between the D and F_1 regions the electron concentrations are mainly at chemical equilibrium, but each region has its own unique structural characteristics, as the spectrum of the UV reaching each region depends on the altitude. Because the ambient neutral gas decreases the diffusive equilibrium is found above the chemical equilibrium, as the ionization-recombination mechanism is no longer effective. The diffusion describes the thermal motion of the particles found in this area. This results in a state of hydrostatic equilibrium as the diffusion process becomes effective. This transition of chemical to diffusive equilibrium of the distribution of ions and electrons is found at about 300 km, at which we see the peak of the electron density in the F_2 region. Any region above this peak is also referred to as the topside ionosphere.

The formation and geographical distribution of the ionosphere may vary considerably depending on location and altitude. As the GRACE spacecraft is located within the F_2 region, we will refer to this region mainly and discuss the other regions only briefly for a better comprehension. In order to understand the formation of the ionosphere it is necessary to understand how plasma arises from the ambient neutral gas, how it returns back to this state, and how this process may be affected by the altitude and location. The behavior of the plasma is governed by gravity, pressure gradients, electromagnetic forces and collisions with the particles of the neutral gas. Plasma is considered to have an equal number of electrons and ions and thus is net neutral. The plasma density for ions is expressed by the continuity equation which is equally valid for electrons analogously:

$$\frac{\partial n_i}{\partial t} + \nabla \cdot (n_i v_i) = P_i - L_i. \tag{15.1}$$

In this equation n_i is the ith ion species, which are O^+, NO^+, O_2^+, and N_2^+ in case of the F region. v_i is the velocity vector of the ion, P_i and L_i represent the production and loss of the ionization, expressed as values of the solar energy and ionic recombination reaction. The largest contributor to the ionization of the neutral gas is the ultraviolet radiation of the sun, and nearly all particles in the extreme ultraviolet spectrum (EUV, $\lambda \leq 102.5$ nm) are absorbed. Retrieving the ionization rates of the ionosphere can be rather complex and is strongly depending on the gaseous species. For our purposes it is sufficient to present a simplified form which only considers one species and only one wavelength within the EUV spectrum. The simplified equation for the ionization rate reads as follows:

$$q = \Phi_\infty \sigma_i N_0 \exp\left[-\frac{h}{H} - \sec\chi\sigma_a H N_0 e^{-\frac{h}{H}}\right], \tag{15.2}$$

where q is the ionization rate, Φ is the EUV flux, $N_0 \exp(-\frac{h}{H})$ is the approximated height profile of the neutral particle density, with h the altitude and H the scale height, which is one of the means of measuring differences between ionospheric layers. The scale height is a value that determines the change of density regarding atmospheric molecules, i.e. atoms, with respect to altitude. Furthermore, it may be a rough reference for the distance between particles at the

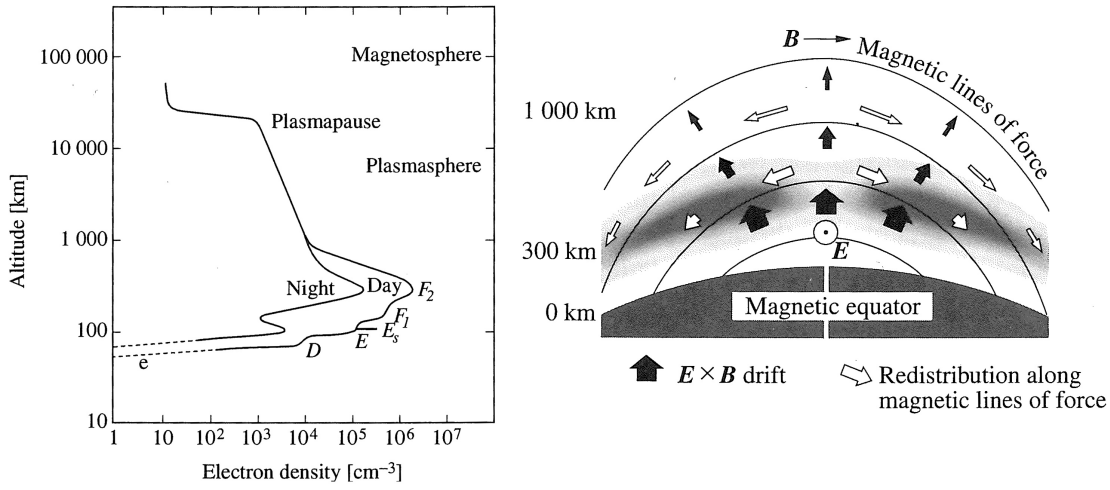

Figure 15.2: Left figure: Regions of the ionosphere (Ondoh and Marubashi (2001)); right figure: Plasma flow forming the equatorial anomaly (Ondoh and Marubashi (2001)).

corresponding height. σ_i is the ionization cross-section and σ_a the absorption cross-section. χ is the direction of the sun measured from the zenith at each point on the ray path. According to this equation, q has a maximum depending on an altitude h_m, which can be computed as

$$h_m = H \cdot \ln(\sigma_a H N). \tag{15.3}$$

The transition altitude differs depending on time, and is higher during the day than at night. The F_1 region has a dominant molecular ion population and is appearing during daytime. At night the F_1 region disappears, a solid F region and a dip between the E and the F region are formed.

The charged particles in the F region of the ionosphere are exposed to forces and thus experience a motion. These forces include gravitational force, pressure gradient force, Lorentz force, and the forces due to collisions with particles of other gaseous species.

Geographical Distribution and Variations

So far we have discussed the vertical structure of the ionosphere in terms of altitude and density. Apart from that, the ionosphere is bound to variations in terms of geography and seasons. Figure 15.3 shows the geographical distribution of the ionospheric density at midnight local time at Greenwich time ±1 hour. The image is based on observations of the ionosonde on-board of the ISS-b satellite, displaying $f_0F_2$values, which is one of the most measured parameters of the ionosphere and describes the critical frequency. The relationship between f_0F_2 and the maximum electron density $n_{max}(\mathrm{m}^{-3})$ is as follows:

$$f_0F_2 \backsimeq 8.98 \times \sqrt{n_{max}} \ \ (\mathrm{Hz}). \tag{15.4}$$

In this figure, noon is approximately at longitude 180°. This is being reflected by the high values in these corresponding longitudes and the lower values at other longitudes. At latitudes higher than 45° and lower than 70° the values are quite low at night time, with a minimum at about

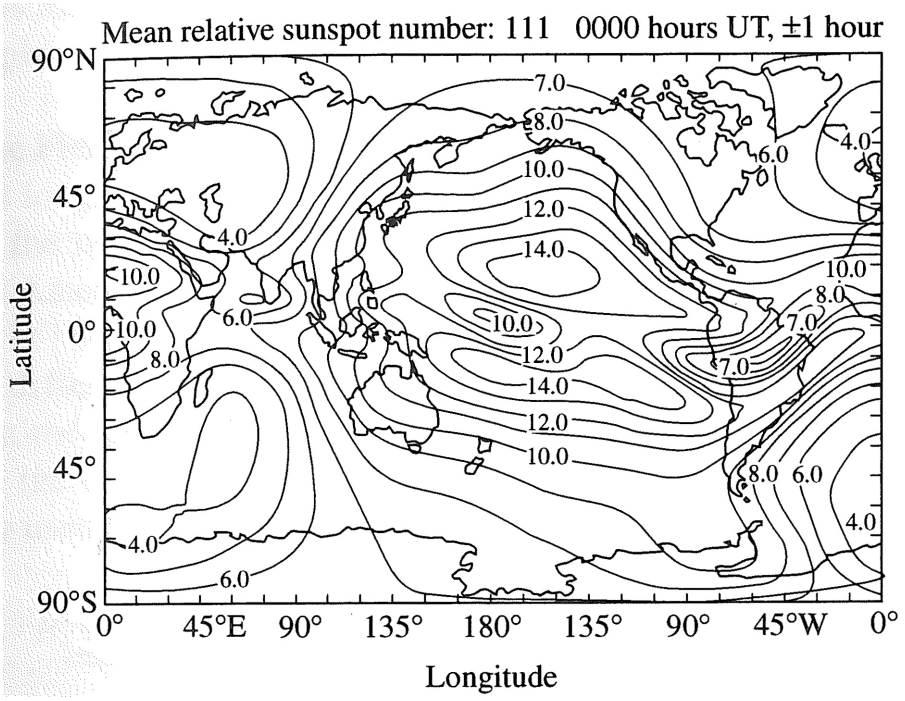

Figure 15.3: f_0F_2 global distribution at UT ±1 hour (Ondoh and Marubashi (2001)).

local time 4 hours. Considering the fact, that the ionosphere is formed by the energy radiated by the sun, it is easily understood, that values in latitudinal areas near the equator and during day are higher than at other regions. The structure of the ionosphere is rather complex near the equator, where two belts approximately 10° north and south of the equator are found, stretching in east-west direction. These belts are stretching along the magnetic latitude (cf. fig 15.3). This is due to the fact that the flow of plasma has components parallel and perpendicular to the magnetic lines of force. As we encounter two separate structures with high density values in this region, with lower density values in the middle, this structure is called the equatorial anomaly. The dip of lower density values in between these two structures follows the magnetic equator. This complex structure is formed due to the upward E x B drift of charged particles and the subsequent downward diffusion along the magnetic lines of force. E is the electrical field and B the magnetic field of Earth. As the electric field is very strong during day due to the ionization, and as it points eastward during the day and westward during the night, the electrons of the plasma experience an upward motion during the day. As the altitude of the plasma increases, the equilibrium breaks, and the electrons travel along the magnetic field lines either north or south, and descend along the field lines of force (cf. fig 15.2, right image). As a result, the density of plasma drops at the magnetic equator and reaches a maximum at latitudes between 10 and 15°. This structure arises with the beginning of ionization due to the beginning solar illumination at dawn, but will prevail several hours past sunset, even as the electric field reverses and is pointing westward.

The mentioned electric field arises due to the ionization. Electrons of the plasma travel along the magnetic field lines, but ions do not. Ions experience a motion across the field lines and are influenced by the winds of the neutral atmosphere of the thermosphere. The neutral wind is blowing across the field lines, westward in the evening hours and eastward in the morning hours. Due to this separation of electrons and ions a polarization electric field develops, whose strength

is strictly correlated with the rate of the ionization of the atmosphere. This effect is referred to as the ionospheric dynamo.

Apart from this geographical distribution of the plasma density, the distribution is also depending on local time and season. During summer season, the plasma density is lower than in any other seasons. Despite the fact, that the sun is more directly above the corresponding latitudes, the oxygen density level is lower in these seasons, and as a result of this effect the ionization rate decreases. Furthermore, the N_2 density is slightly increasing in the summer season which yields an increasing electron loss coefficient. This coefficient is the value of the recombination of free electrons with the surrounding ambient gas. A maximum of plasma density is found near the spring and autumn equinoxes.

The daily distribution of the plasma density depends on the local time of day, and thus the position of the sun as seen from the ionosphere. The plasma density will increase dramatically with sunset, but will prevail on a high level past sunset. One reason for this phenomenon may be attributed to the neutral atmospheric winds in the meridional plane. At mid-latitudes the wind generally blows towards the poles during day, and towards the equator during night. This results in collisions among the particles of the neutral gas and ions, which produces an upward force on the plasma along the inclined magnetic field lines, yielding a maintenance of the ionospheric plasma at high altitudes in the F region.

15.3 Auroral Oval

In order to understand the mechanisms behind the formation and content of the phenomena known as the Aurorae, i.e. Auroral Oval, we first need to introduce the Earth's magnetosphere. The magnetosphere of the Earth is the area in which charged particles are controlled by the Earth's magnetic field. This magnetic field stands as a protective barrier against the solar wind. The side of the magnetic field which is facing the sun, respectively the dayside, is being compressed by the flow of plasma from the sun and has a near spherical shape (cf. fig 15.4). The solar wind, approaching the geomagnetic field at a high speed, is being halted abruptly and is being impounded. This impound is referred to as the bow shock. Most of the plasma of the solar wind is then led around Earth by the magnetosphere. This part of the solar wind is known as the magnetosheath. The area, where the pressure of the geomagnetic field and the pressure of the solar wind are at balance, is called magnetopause. Due to the particle flux around the Earth the magnetosphere extends far beyond the Earth, and this formation is called magnetotail. This tail, which resembles the tail of a comet, is nearly empty of plasma and separated by a plasma sheath into two lobes (northern and southern lobe). This is also stretched to a considerable length as the pressure of the solar wind upon the magnetic field is relatively low at this point. The plasma sheath itself is an area with a rather dense plasma content and its boundaries are distinct.

As Earth is facing sun approximately with its equatorial side, the poles are, if the Earth's ecliptic is neglected, perpendicular to the Sun-Earth plane. As the magnetic poles are located relatively near the geographical poles, the magnetic lines of force enter Earth near this area. Due to this situation, the magnetosphere is consisting of two cusp regions, one for each pole. Not all plasma from the solar wind is being led around Earth, but some intrudes the plasmasphere of the Earth and is led towards the polar cusps by the magnetic field lines of force, which are open at the polar caps. This highly energetic electrons and protons of the solar wind will then descend gyroscoping due to the Lorentz force around the magnetic lines of force into the ionosphere, forming a downward current (cf. fig 15.4). These particles are moving more or less collisionless in the upper atmosphere until they are being reflected upon approach of the magnetic pole, which will reverse the velocity vector resulting in an upward current. The currents are referred

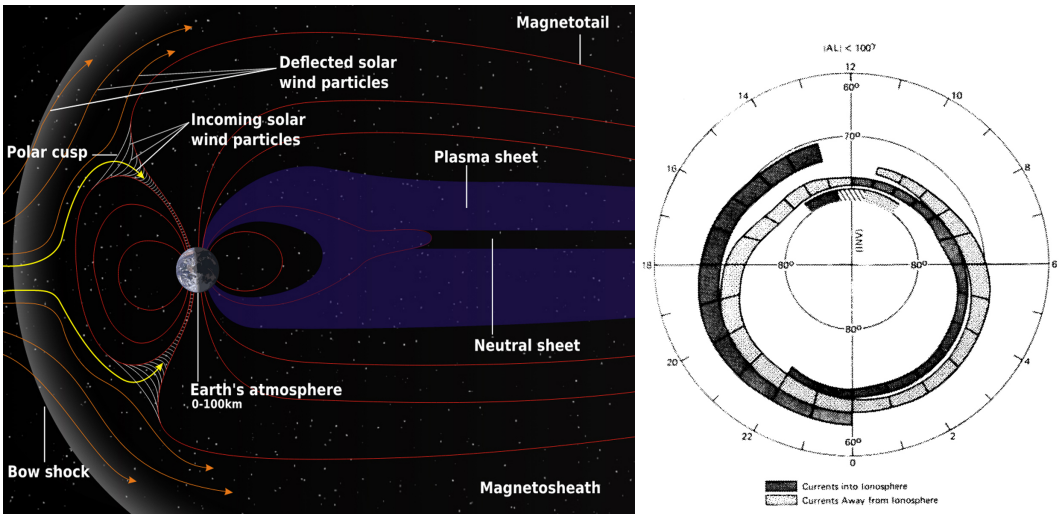

Figure 15.4: Left figure: Schematic over the Earth magnetosphere; Right image: Birkeland currents of the northern hemisphere with respect to magnetic local time (MLT) (Iijima and Potemra (1976)).

to as Birkeland current. While traveling along the magnetic lines of force they interact with the molecules of the ionosphere, resulting in an ionization which is visible as polar lights. The electrons will travel between the poles until they are released into open space, the plasma sheath, again. The recombination of the ionized molecules by the solar wind with the gas in the polar regions will lead to an emission of photons, and hence polar lights. This event is limited to a 3 to 6 degree wide formation situated about 20 degrees off the magnetic poles in latitude. This formation is then being referred to as the Auroral Oval and may be visible at night on Earth in the specific latitudes, which are 75 degrees during daytime and descending down to 65 degrees latitude at nighttime. During solar storms or times of an increased solar activity these Auroral Oval may descend to lower latitudes.

The Birkeland currents at the poles due to solar electrons captured by the Earth's magnetic lines are bound to specific latitudes, which vary with respect to the magnetic local time (MLT). According to Iijima and Potemra (1976) these currents can be most often observed in the dayside sector between 9:30 and 14:30 MLT. The inward current is generally strong in the afternoon and the outward current in the forenoon. In fig 15.4 (right) the distribution of the inward and outward Birkeland currents is displayed with respect to MLT and latitude in the northern hemisphere.

15.4 Terrestrial radiation

In this section we want to introduce the indirect solar radiation upon the GRACE spacecraft. Solar radiation can be divided into the direct solar impact, which has been introduced in chapter 12.2, and the indirect solar impact. In the previous chapters we learned that solar radiation has the power to shape Earth's atmosphere and the magnetosphere. Now we want to emphasize the indirect solar radiation in orbit by means of the visible and infrared light spectrum. This indirect radiation is mainly due to solar energy reflected by Earth's surface which may happen immediately in terms of visible light or with a latency in case of long wave radiation. Reflected solar radiation due to Earth's surface is know as albedo.

The term albedo describes generally the reflection coefficient, i.e. the ratio of reflected radiation from the surface to an incident radiation. In these terms, the albedo is dimensionless and is usually expressed as a percentage or a value ranging from 0 to 1, where 1 is the total reflection

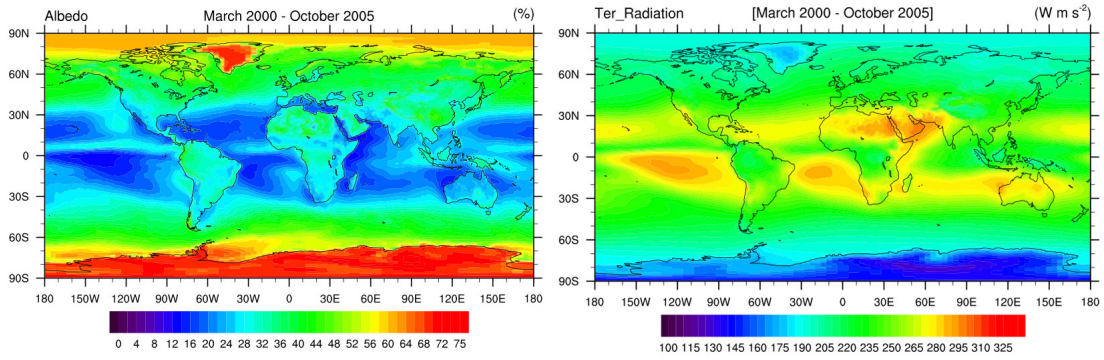

Figure 15.5: Mean terrestrial annual energy content of the albedo in the visible light spectrum (left image) and the emitted terrestrial radiance (i.e. infra-red, right image) (Lubis (2013)).

on a homogeneous white surface. In terms of the Earth, only the currently illuminated area due to sunlight of the Earth can contribute to the terrestrial albedo, being the sum of all visible light radiation emitted from the sun impacting Earth. In fact, only a fraction of the solar energy is being reflected from Earth back into space. Most land areas reflect more energy as they are usually to a larger extent covered by clouds than oceans and clouds have a higher reflection ratio. The average albedo coefficient of the Earth is approximately 0.3 (Goode et al. (2001)), which is mainly due to the Earth being covered by clouds. The highest albedo coefficient is observed over the ice-sheets. In our work we used the algorithms applied in the program developed by Rodríguez-Solano (2009) in order to estimate the amount of energy of the albedo at GRACE orbit altitude. For this, the albedo is not provided in terms of the dimensionless ratio of the overall reflected radiation of the sun, but as energy in terms of Watts per squaremeter ($\frac{W}{m^2}$). With these number we can correlate the intensity of the albedo at certain parts of the orbit with the distribution and possibly the behavior of twangs.

We divide the albedo into two components. The first one describes all wavelengths of the reflected radiation which is within the visible light spectrum. This is the part of the reflected solar energy which is generally referred to when speaking of the albedo. The other component contains wavelengths in the infra-red spectral domain, also known as the terrestrial emitted radiance. The difference between those two is, that the visible light can only be reflected by Earth at the time of impact, but cannot be stored and emitted from Earth with a delay in time. This makes the visible albedo strongly depending on the season and local time. Infra-red, however, is changing slowly with the seasons, as the terrestrial radiance is indeed emitted by Earth itself. This is due to the fact that the Earth is able to store some of the energy from the sun as heat which is released with a delay in time and can hence also be detected when Earth is eclipsed, i.e. at night. In figure 15.5 we display these two cases for a typical clouded sky, with albedo, the visible light spectral domain, on the left hand side, and the terrestrial radiance on the right hand side. In case of a clear sky, the energy content is significantly higher in case of the infra-red spectrum, and much lower in case of the visible light albedo. The figure displays the mean annual energy content, for these two mentioned components.

16 Interactions of spacecraft with environment

In the previous chapter we described the space environment at spacecraft orbital heights in terms of several aspects. It became clear that the space environment is indeed having a rather complex structure and consists of neutral ambient gas, plasma, and charged particles, which

may be emitted from various sources. As a result also electric and magnetic fields exist. These interact with any spacecraft orbiting in this height and have a potential of causing damage to it and possibly affecting its performance or lifetime. For instance, the US Air Force Defense Space System Communication Satellite (DSCD) 9431 experienced a discharge due to charging effects and suffered from a loss of power in the spacecraft's communication system as a result, causing the whole satellite to fail. In conclusion, the NASA and Air Force increased their efforts in investigating the space environment and possible impacts upon spacecraft.

As the spacecraft is orbiting Earth its outer surfaces will come into direct contact with the neutral ambient gas and the plasma in the residual atmosphere of Earth. Due to these interactions with the plasma the spacecraft surfaces may possibly be charged. It is obvious that the rate of charging is, among others, thus strongly depending on the orbit height, and low Earth orbit (LEO) spacecraft experience a different space environment than for example geosynchronous orbits (GEO). Since we are focused upon the GRACE twin satellites in this study, we will emphasize the space environment and interactions with spacecraft for low Earth orbits.

In this chapter we will first introduce how a spacecraft may become charged on the out- or inside relative to the space environment, and consequently how discharges of the space system may occur. This part will be kept rather general and is meant to give an overview about charging and discharging mechanisms. Furthermore, we will state some facts that will contribute to the hazards that spacecraft discharges have upon the on-board electronic systems of satellites. In the next section we will review the characteristics of the materials used for the GRACE spacecraft outer surfaces, as these are the ones mainly interacting with the space environment at mission height. We will reflect how the rather dielectric material may gain a state of conductivity under certain circumstances that can be found within the given space environment. In the last part of this chapter we will attempt to link twangs to charge and discharge events that are believed to occur on the GRACE satellites based on a set of examples.

16.1 Spacecraft Charging

According to Mikaelian (2001) the charge of a satellite is defined as the build-up of a charge on the satellite's surfaces or the spacecraft interior. Spacecraft charging alters the space systems potential with respect to the surrounding space environment, and it may also result in different potentials between different parts of the satellite itself, which is referred to as differential charging. In this section we will discuss the different sources of how the satellite surfaces may be charged by the space environment. A more detailed overview can be found in Mikaelian (2001). These sources are mainly plasma, high energy electrons, solar radiation and magnetic fields. Furthermore we will introduce how the surfaces of the satellite may be charged, and also give a brief overview about possible internal charges, for the state of completeness. An overview by means of table 17.1 is given on page 150.

16.1.1 Charging environments

Plasma

We already stated, that the plasma environment and density are correlated to the altitude and also to the latitude (cf. section 15). The orbital heights that are relevant to plasma charging effects are LEO and GEO, and of special interest is the polar Earth orbits (PEO), which are interesting due to its inclination. For our study, especially the LEO and PEO are of special interest. LEO will face a higher plasma density (10^2 to 10^6 cm^{-3}) than GEO, but a significantly lower energy (0.1 to 0.3 eV, Mikaelian (2001)). However, at PEO a spacecraft will experience the

precipitation of electrons due to the introduced Birkeland currents (cf. 15.3). Here, the energy can be as high as 1 to 100 keV, but the density will be lower, with 1 to 10 cm^{-3}. The plasma in the ionosphere (LEO height) is overall rather neutral, which means that ion and electron quantities are in equilibrium. The plasma induces charges upon the spacecraft due to the flux of electrons and positive ions. In addition, the motion of the spacecraft may contribute to a local rise of the plasma and may enhance the charging effect. This is due to the fact that the spacecraft usually travel with a velocity which is below the velocity of electrons, but slightly higher than the velocity of ions.

High energy electrons
High energy electrons are especially of concern in very high orbits such as GEO, and at polar orbits. If the sun has no impact onto the spacecraft the charging of the spacecraft is directly proportional to the electron temperature. In such case the overall potential of the spacecraft may vary between 1 and 20 keV, relative to the satellite environment. Electrons in these regions may have a high energy, mostly between 1 and 100 keV, where an electron with an energy larger than 10 keV has a potential of penetrating the surface material. Very few electrons even exceed the energy of 100 keV, which is harmful to most kinds of material.

Solar radiation
Solar radiation has the ability of neutralizing a negatively charged surface of a spacecraft. This neutralization, however, is strongly depending on the material used on spacecraft. Furthermore, a stronger solar activity can lead to a higher neutralization rate. The higher incidence angle between the satellite's surface and the sun may contribute to a better neutralization, as well as the overall spacecraft's potential. Solar radiation plays a significant role especially at GEO height. However, our studies suggest that an effect can also be observed in LEO altitudes, which may in its way differ from those known at GEO height (chapter 17).

Magnetic Fields
The Earth's magnetic field has a great influence upon the distribution of plasma in the ionosphere and hence it determines the region in space, where spacecraft charging can occur and where it will have a higher impact rate than at other places. Furthermore, the magnetic field can have an effect on the escape of electrons which are stuck to the surfaces of the spacecraft. When the magnetic lines of force are perpendicular to the given surface of the spacecraft, they can yield an escape of the electron, helping to reduce the overall negative charge. However, for other incidence angles of the magnetic field lines with respect to the surface they can actually redirect the electrons back to the surface. Also, the magnetic field can induce a potential on the spacecraft due to the spacecraft's motion in altitudes of the LEO.

16.1.2 Charging characteristics

Mechanism
The charging of a spacecraft is linked to the interactions of the spacecraft with its surrounding plasma environment and other charging sources that have been introduced above. If the surface of the spacecraft is made of conductive materials, the satellite's overall charge will be at global equilibrium with its surrounding plasma. If the surfaces consist of dielectric materials, the equilibrium with the surrounding plasma can only be obtained on a point-to-point basis. For any charging mechanism, magnetic field lines need to be taken into account whenever appropriate.

The total current between spacecraft and space can be described by the following equation (Mikaelian (2001)):

$$I_{NET}(V) = I_E(V) - [I_I(V) + I_{SE}(V) + I_{SI}(V) + I_{BSE}(V) + I_{PH}(V)]\,. \tag{16.1}$$

In this equation V is the surface potential relative to the plasma surrounding the spacecraft. I_{NET} is the total current from the space to the surface, which can be both positive or negative. I_E is the incident environmental electron current and I_I the corresponding positive ion current. I_{SE} and I_{SI} describe the secondary emitted electron currents due to I_E and I_I, respectively. I_{BSE} is the back-scattered electron current due to I_E, and I_{PH} is the solar photoelectron current. The spacecraft's charge is at equilibrium with its surrounding plasma if the following constraint is satisfied:

$$I_{NET}(V) = 0. \tag{16.2}$$

This means, that there is no current between the spacecraft and the surround space, and the charging of the spacecraft has come to a halt. This charging level is referred to as the "floating potential".

Absolute and differential charging of a spacecraft

Absolute charging describes the situation where the charging influences the whole spacecraft to a net potential relative to the surrounding space plasma. In case that all spacecraft surfaces are made from a conducting material, the charge will distribute uniformly over the whole spacecraft.

Differential charges occur when the surfaces of the spacecraft are made from dielectric, i.e. non-conducting, materials. This yields different magnitudes of the spacecraft charge to different "floating" potentials. A great impact for this may be due to solar radiation and magnetic field lines. In case of sunlit surfaces, the negative charge on the shaded surfaces is greater than on those which are sunlit. These strongly negative charged surfaces can prevent the emission of photoelectrons from the sunlit surfaces. As a result, the whole satellite's charge will become negative. This effect gives rise to differential charge up to several kV across the different parts of the surfaces. Differential charging is generally more dangerous to the overall performance of the spacecraft as it can lead to surface arcing or electrostatic discharge, that may affect the performance of the operation, cause various anomalies in the electrical system or lead to material degradation or destruction. Ultimately, a whole spacecraft mission could fail due to strong arcing or discharging events.

In LEO height a significant charging in low latitudes is not to be expected, as the plasma is rather cold compared to greater heights. At low latitudes the velocity of the spacecraft is mesothermal, which means that the spacecraft is faster than positive ions (v_I =1 km/s) but significantly slower than electrons (v_E =150 km/s). The typical speed for a spacecraft in LEO is 7.5-8 km/s (Mikaelian (2001)). Compared to the sound speed of ions v_S, which is in low latitudes the same as the thermal speed v_I, the spacecraft travels with supersonic, i.e. hypersonic, speed. This results in a relatively large amount of disturbed plasma as the spacecraft moves along the orbit, which means that there will be a region of depleted ions behind the spacecraft, near the wake region (cf. figure 16.1). In contrast, there will be a shock or ram wave of ions in front of and also to the sides of the spacecraft. This means, that ions are impacting the spacecraft only at the ram, while the much faster and hotter electrons can strike the spacecraft at all sides.

Also, at LEO there is a high density of plasma which keeps most of the photoelectron emission by the solar ultra-violet and extreme ultra-violet from descending as low as the LEO. Hence,

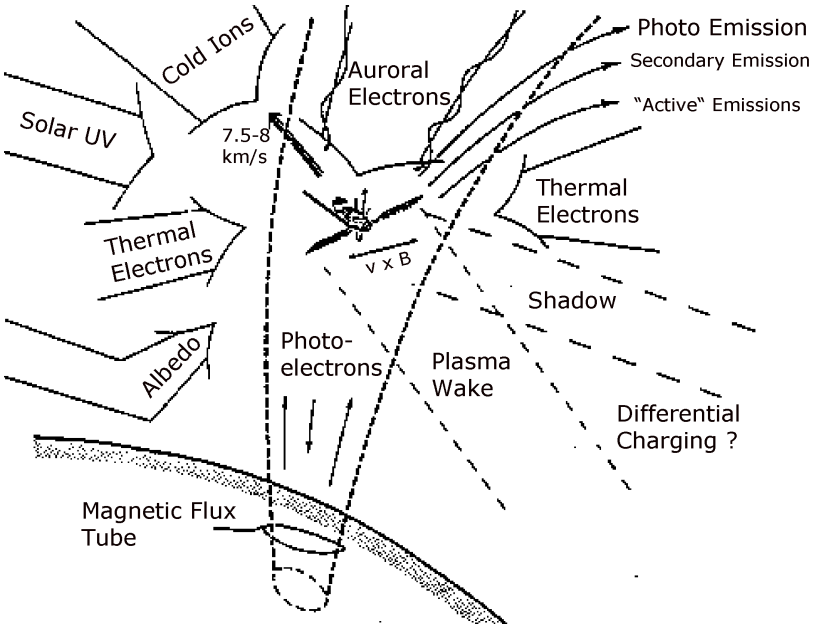

Figure 16.1: Plasma interactions with a spacecraft in polar orbit (Mikaelian (2001); Martin (1991))

most of the solar radiation impacts may be negligible, according to Mikaelian (2001). However, due to the rather high density of plasma, a slight charging is expected on the spacecraft, that should not be ignored.

This is different if the LEO is highly inclined and thus in a polar orbit. Here, the surface charging can be considered rather significant at high latitudes in the auroral ovals. The amount of charge is depending on the potentials of the spacecraft, orbit position and auroral activity. However, the rather perpendicular magnetic lines of force upon the nadir and zenith surfaces of the spacecraft can help electrons to escape (cf. figure 16.1). In auroral regions a spacecraft moving along its orbit could suddenly experience a transition from a situation with a spacecraft charging voltage no more than one volt, to a case where it is intercepting a high energy stream of electrons. If this occurs in darkness, where photoemission is suppressed, and the electrons impinge on surfaces facing the wake of the spacecraft where ions are excluded by the spacecraft motion, the potential for charging is high (ESA/ SPENVIS (2013)).

Internal charging of a spacecraft

This type of charging describes the penetration of highly charged particles into the surfaces of the satellites body. This may occur whenever an electron has an energy of 10 keV or more, and is also depending on the characteristics of the material. These electrons then are trapped within the material and may accumulate to a great charge. If the charge increases more and more it may be large enough to exceed the breakdown strength of the dielectric material used on the surface. This event may lead to an arc discharge and a dielectric breakdown. A fast transfer of great charges is the result of this event, and transient currents inside the spacecraft may occur. In case of a dielectric breakdown the typical voltage can actually be as high as -10 kV. Such a high voltage and the accompanying transient currents can lead to serious hazards to the on-board electronic systems, which may result in a damage or failure of these systems.

16.1.3 Spacecraft Discharging

One of the main effects that may occur due to spacecraft charging is the electrostatic discharge (ESD). Such an ESD may be a surface discharge or bulk discharge. Surface discharge is occurring whenever the surface voltage exceeds the breakdown voltage of the dielectric material applied. Such a discharging current may have a magnitude of several hundred Ampere. A special case of the surface discharge is the dielectric discharge, which occurs when the dielectric materials are exposed to any sort of space radiation. Bulk discharges are rather small in amplitudes compared to the surface discharges, but they are nevertheless hazardous to any on-board electrical system. This is due to the fact that a large amount of charge is released within a very short period of time, typically lasting only a few microseconds (Mikaelian (2001)).

If the discharge occurs in form of an arc discharge it may lead to anomalies and can result in a degradation of sensors and solar arrays, which would be harmful to the power supply of the spacecraft. Arc discharges are mainly due to differential charges or internal charges. Arc discharges in general can cause serious physical damage to surfaces, from loss of dielectric property, localized heating or ultimately material loss. The latter may cause a structural damage to the whole spacecraft. In addition, the penetration of highly energetic electrons into the surface and the resulting discharge lead to an alteration of the material and may degrade its dielectric properties.

There are three main types of discharges. These are:

- "Flashover": This type of discharge is a discharge that occurs from one charged surface to a surface with a different amount of charge and is thus only occurring in case of differential charging.
- "Punch-Through": This is a discharge from the interior structure of the satellite through its surface. It may cause serious damage and alteration to the surface material.
- "Discharge to space": This discharge describes a current from spacecraft to the surrounding plasma (also cf. equation 16.1).

Discharges can couple into electronic devices and disrupt their proper operation. Depending on the severity of the event they can cause transients or permanent damages by single events.

16.2 Material parameters

In the previous chapters we introduced the space environment at orbital heights and the characteristics of the corresponding layers of the atmosphere. Furthermore, we explained how a spacecraft may interact with its surrounding environment and what the effects and potential dangers are with respect to the spacecraft. Now we will give an overview of the characteristics of the surface materials used for the GRACE twin satellites. An overview about the shape and design of the GRACE spacecraft can be found in chapter 3. This overview is written under consideration of the previous sections and hence reflect upon the possible threats that the charging and discharging in combination with the individual material have on the GRACE space mission.

16.2.1 Teflon

Teflon is a synthetic flouropolymer of tetraflouroethylene, which runs under the scientific name polytetraflouroethylene or short PTFE. Teflon is the registered trademark name by the DuPont

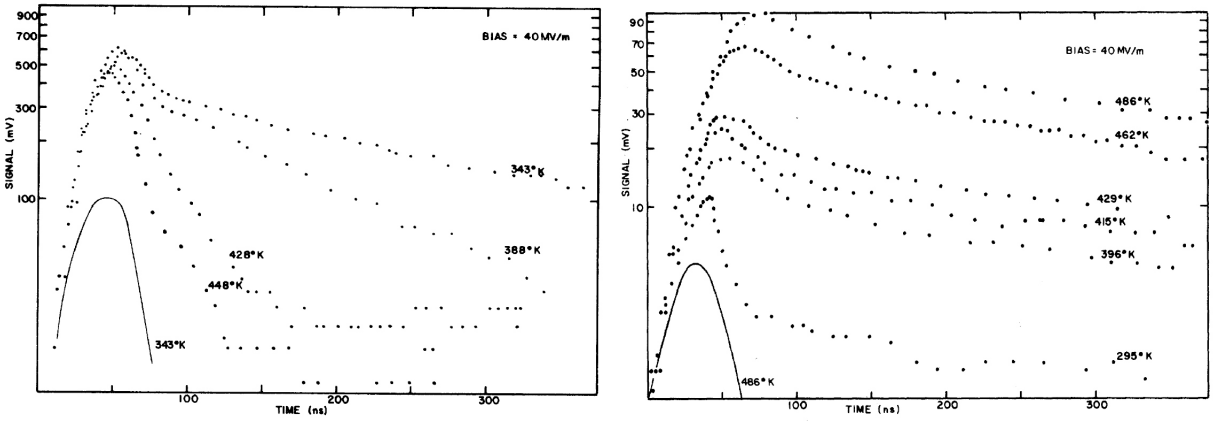

Figure 16.2: Left figure: Conductivity response with respect to time and signal of Teflon if an energy (solid line) exerted upon Teflon. Right figure: Analogue to the left figure for the material Kapton (Barlett et al. (1975)).

Company, but we will be referring to this material as Teflon due to the widespread term and the length of the scientific name. According to the DuPont company the melting point is at 327° C, and it is very strong and stable at average and low temperatures (DuPont (2013)). Teflon has great dielectric properties which makes this material suitable as an insulator. It is especially great as an insulator to microwave or high radio frequencies. In combination with its thermal stability and its rather low cost, Teflon may be the desired material applicable for insulating certain parts of space vehicles, and is hence widely used within spacecraft design. The dielectric strength of Teflon varies with temperature and the layer thickness, but is typically between 60-173 kV/mm, with a mean value of 118 kV/mm (DuPont (2013); Berger (2000)). The dielectric strength defines the maximum electric field that a pure material can withstand under ideal conditions without breaking down or without experiencing failure of its insulating properties.

Despite its well-known dielectric characteristics, Teflon may gain a state of conductivity under certain circumstances as most dielectric material. Barlett et al. (1975) investigated the photo-conductivity properties of Teflon and found, that if Teflon is exposed to a strong X-ray signal it may become photoconductive. Teflon reveals, that this gain of conductivity is rather invariant to the temperature applied to the material at the time of exposure. The delay in time remains stable for all situations applied for the same X-ray signal, only the decay of the conductivity after loss of the X-ray signal is depending on the temperature applied (cf. fig 16.2). However, the photoconductivity of Teflon is not a permanent or persistent conductivity, but merely a point-to-point based conductivity where electrons are free to jump from one place to another for a very brief period (also cf. chapter 16.2.5).

Coffey and Nanevicz (1975) showed in their work that Teflon shows overall great insulation characteristics, but this is only the case if the insulating layer of the applied Teflon has a certain thickness. If the layer is too thin, however, the properties are poor and may actually vary from sample to sample. Furthermore, the resistivity of Teflon under illumination is decreased.

These two studies reveal that Teflon may gain conductivity if the surfaces made of Teflon are sunlit. In case of the GRACE mission the nadir surface is made of Teflon and is approximately 0.1 mm thick. This means that only for short times this surface can actually be sunlit. This happens whenever the spacecraft are just leaving Earth's shadow zone or are about to enter it. Furthermore, the spacecraft may be exposed to a weaker source of light due to the Earth's albedo.

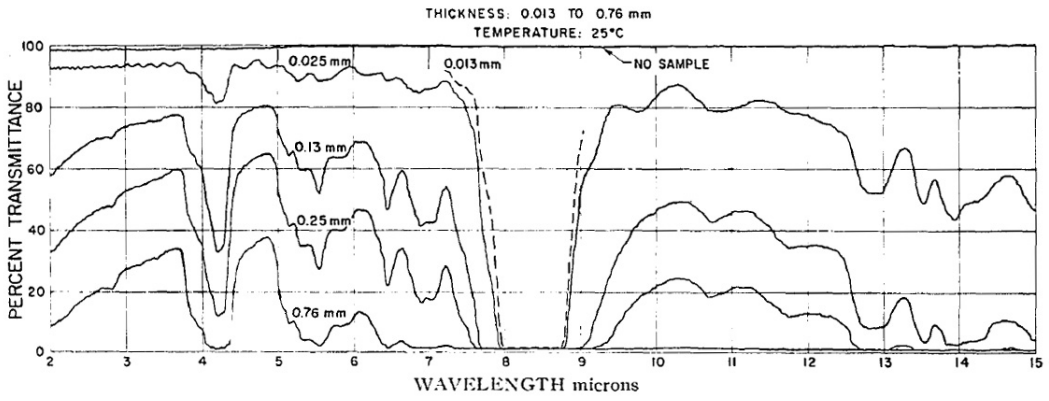

Figure 16.3: Infrared transmittance of Teflon (room temperature). The 0.025 mm sample was cast film and transparent in the visible; the thicker samples were skived (shaved) from bulk milk-white stock and opaque in the visible (Wentink and Planet (1961)).

While Teflon absorbs light in the visible as well as the UV and EUV spectrum, it is transparent to light in the infrared spectrum. This means that any material applied inside the satellite, i.e. behind the Teflon foil, may be exposed to infrared radiation whenever the nadir mounted Teflon foil is exposed to infrared radiation (Optris (2013)). The transmittance of Teflon-layers with a various thickness is displayed in figure 16.3.

16.2.2 Kapton

Kapton is just like Teflon the trademark of the DuPont company and describes polyimide film. We will refer to the term Kapton for a better understanding. Kapton is widely used as an insulator in avionics and astronautics. This material is known for rather good dielectric properties, and it is possible to produce it as very thin and light layers. Also, it has a very low outgasing rate which makes it a preferable material to be used in space environments.

Referring again to the studies by Barlett et al. (1975), Kapton shows a greater photoconductivity if exposed to X-ray than Teflon and is more dependent on the temperature applied during the different tests (cf. fig 16.2). The dielectric strength of Kapton is comparable with the values given for Teflon (Berger (2000)). Furthermore, Kurek et al. (2008) show that under Earth-bound conditions Kapton is aging fast and the insulating property is decaying. This is in accordance with the publication by Schwartz (2005), who reveals that Kapton was applied on the space shuttle missions as wire coating insulator, which tended to age quickly over time, resulting in short circuits, potentials and fires. In contrast to Teflon, however, the damage rate due to radiation is very low.

Kapton is used on the GRACE spacecraft as an insulating foil on the smaller front and back panels. The forward, trajectory facing panel will be exposed to a large amount of ions due to the plasma ram in front of the satellite, and the rear panel will be exposed to fast striking electrons. Both sides may be sunlit from time to time.

16.2.3 Fused quartz

Fused quartz is a glass that differs from regular, traditional glass in the fact, that no other ingredients are added in order to lower the melting temperature. This makes fused quartz superior in terms of thermal and optical properties to other types of glass, as it has a good

ultraviolet transmission. Therefore, it is applicable for covering solar arrays. Fused quartz furthermore has an extremely low coefficient of thermal expansion, which makes it resistant to damages due to thermal shocks. With 25-40 kV/mm at 20° C, the dielectric strength is lower than that of Teflon and Kapton, but nonetheless fused quartz may be considered to be a rather non-conductive material (Berger (2000)). But also a temperature dependency of quartz with respect to its electrical conductivity properties exists.

According to Sharma (1968) the charge collected by fused quartz due to a photon flux is higher than for regular glass or quartz crystal, where the charge collected is linear to the time of exposure to the photon flux. The yield of the photoconductivity for glass-like materials is strongly depending on the atomic composition of the material. The less Natrium (Na) the glass or quartz is consisting off, the more photoconductive it may become, as the electrons will be easier to excite into the conduction band.

In case of the GRACE spacecraft, fused quartz is mounted upon the solar array panels on the long slightly inclined side panels and on the zenith panel of the satellites.

16.2.4 Carbon-fiber-reinforced polymer

Carbon-fiber-reinforced polymer (CFRP) is a polymer that has been made extremely stable, strong and light by reinforcing it with carbon fibers. These properties are the reasons why CFRP is getting more and more important as a strong light-weight material within aerospace engineering. CFRP consists of two very distinct elements, a matrix, which is usually a polymer resin such as epoxy, and a reinforcement, which is mainly carbon fibers. Due to these structures, the behavior of CFRP is strongly depending on the properties of those two basic elements. It is indeed the reinforcement, as the term suggests, that provides the material with strength and rigidity. Due to the matrix and reinforcement binding structure, CFRP is not an isotropic material such as steel, but has directional strength properties, depending on the layout of the reinforcements applied relative to the matrix polymer resin. If no conductive fillers are added to the polymer design, the electrical resistivity is generally very good, and hence CFRP may be regarded as an insulator for such composites (Tipirneni (2008)). However, the mean dielectric strength of a common CFRP varies between 15-23 kV/mm and is hence below the other materials introduced so far (Berger (2000)).

In case of GRACE satellites, the front and aft panels of the satellites are made of CFRP and are covered to the outside by a thin Kapton foil. Both panels can be exposed to direct sunlight. The forward, trajectory facing panel will be exposed to a large amount of ions due to the plasma ram in front of the satellite, and the rear panel will be exposed to fast striking electrons.

16.2.5 Material discussion and gain of conductivity

All applied materials facing to space on the GRACE spacecraft are considered to be rather insulating, i.e. non-conducting or dielectric, materials. Teflon and Kapton show the greatest dielectric strengths and CFRP the poorest, whereas CFRP is due to the coverage by the Kapton foil not directly exposed to the outside. Dielectric strengths can be lowered under certain circumstances. No dielectric material is able to resist an infinitely high voltage, and the breakdown voltage necessary to turn a non-conducting material into a conducting one is depending on the material characteristics as introduced above as well as on the environment. Temperature, X-rays and photons may lower the dielectric properties of any material. However, each material responds differently to exposure to those three aspects.

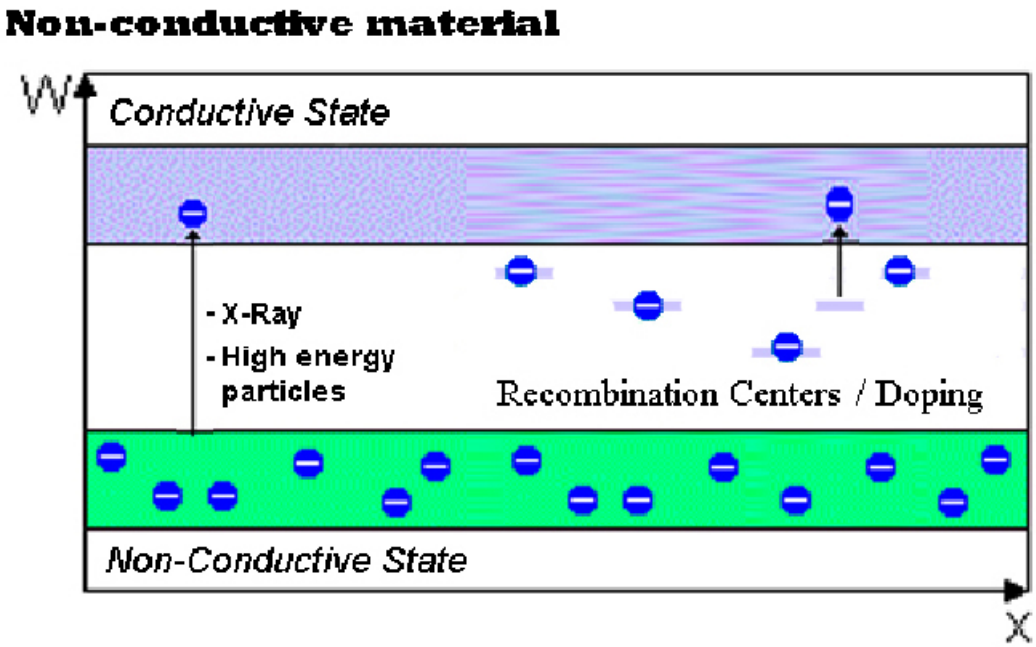

Figure 16.4: Schematic view of the electric conductivity of a dielectric material. If a sufficient number of electrons is elevated into the conductive state, the material will be conductive. Energy needs to be applied in order to elevate the electrons into the conductive state from the green non-conductive state (i.e. valence band).

In order to make a material conductive the electrons of a material need to be excited into the conduction band. This excitement can only occur if an external energy source is applied to the material that is able to bridge the energy gap between the valence and the conduction band. This is depicted in the schematic view in figure 16.4. The larger the gap between the valence band, i.e. non-conductive state, and the conductive state is, the more energy is necessary to excite electrons of the material into a conductive state. If the gap exceeds a material specific arbitrary threshold, the material may be considered dielectric. If a sufficient number of electrons are excited into the conductive state by means of additional energy, the material is becoming conductive. However, this is only a temporary situation. The electrons will fall back into the valence band as soon as the extra energy is no longer available. Depending on the material qualities, degradation of the material may occur and electrons may be trapped in so-called recombination centers somewhere between the actual valence band and the conductive state. From this recombination center it needs less energy to re-excite the electron back into the conductive state, as from the point of the recombination center to the conductive state the gap is significantly smaller now, depending on the degradation of the specific material. Each recombination center may occur randomly at a different place. The older the material becomes, the more degraded it will be, which will result in a decrease of the initial dielectric strength of the material over time. If the material is not replaced or repaired, this will ultimately result in a loss of the dielectric properties.

Taking chapter 16.1 and the material properties discussed above into account we can state, that the GRACE satellite is exposed to all introduced charging possibilities in LEO and hence will undergo charging. Furthermore, dielectric breakdowns of the materials applied, and consequently material degradation, will eventually occur. The extent of the latter at the present point (04/2014) is not known, however.

17 Twangs and their causes

Among other, we presented the behavior of twangs with respect to time and geographical behavior up to this point. We showed that the different parameters of twangs may behave differently according to time and their location. Based on this we separated the twangs into four different groups in chapter 12 according to their behavior. Furthermore, we introduced the reader to the different hypotheses regarding the source of twangs. In this chapter we want to connect the stated observation with the hypotheses by means of an overview, of how the different aspects and groups correspond and may support the hypotheses. We will refer to our observations in chapters 8.3.2 and 12, as well as part IV.

17.1 Reversed twangs in radial component of GRACE A and B

The first hint at either hypotheses is the fact that both GRACE spacecraft show the same distribution of twangs with respect to the geographic location (cf. chapter 9). This behavior excludes a randomly appearing process and is evidence for a process that has its origin in the exterior satellite environment. Furthermore, some patterns formed of twangs show an opposed sign regarding the two spacecraft.

A simple explanation could be, that the leading satellite is yawed by 180° and the input signal is exerted upon the spacecraft with the same vector as seen from space. As the accelerometer is mounted aboard the spacecraft in accordance with the satellite reference frame (SRF), the signal in ACC1A would be reversed for either the two satellites. In case of the micro-vibrations this could hint at a vibration at the same location of the two spacecraft relative to the velocity vector, but in opposite directions to the SRF center. However, we observe the reversed sign especially in the radial component which should be invariant to the yaw degree of the spacecraft.

Regarding the discharging hypothesis this could be due to different charging mechanisms. If the twangs of the same corresponding pattern of the two spacecraft are due to the same outer surface, the potential could be evoked by a positive charging on the one satellite and by a negative charging on the other satellite. This is due to the fact, that the surface of the one satellite will be in the ram region, exposed to slower ions, and the other will be in or near the wake regions, mainly free from ions and can mainly be struck by electrons. A discharge due to opposed potentials could lead to different discharging directions and may hence yield a reversed sign of twangs in the ACC1A data. This can also contribute to the fact that there are more twangs in ACC1A data in one of the satellites as the potential strengths would differ significantly.

In equatorial latitudes the sign of twangs is the same for both spacecraft in the patterns that are believed to be due to the infrared impacts. However, the twangs that are presumably due to infrared in the polar areas show to have reversed signs in the two spacecraft.

17.2 Solar impact/ incidence angle

The next observation that we want to discuss is the impact of the solar incidence onto the outer surfaces on the behavior of twangs, which we introduced as group 2 in chapter 12.2. In chapter 11.5 we show that the twangs become less energetic when the nadir surface is directly in sunlight. This is also once more displayed in figure 17.1. Furthermore, in chapter 12.2 we show that the overall number of twangs appears to be decreasing when the zenith surface of the spacecraft is sunlit. This hints at a direct correlation between sunlight and the occurrence of twangs. The lower image of figure 17.1 suggests that there are rather negative twangs to be found in the corresponding areas where the nadir surface is directly impacted by the sunlight, which are the

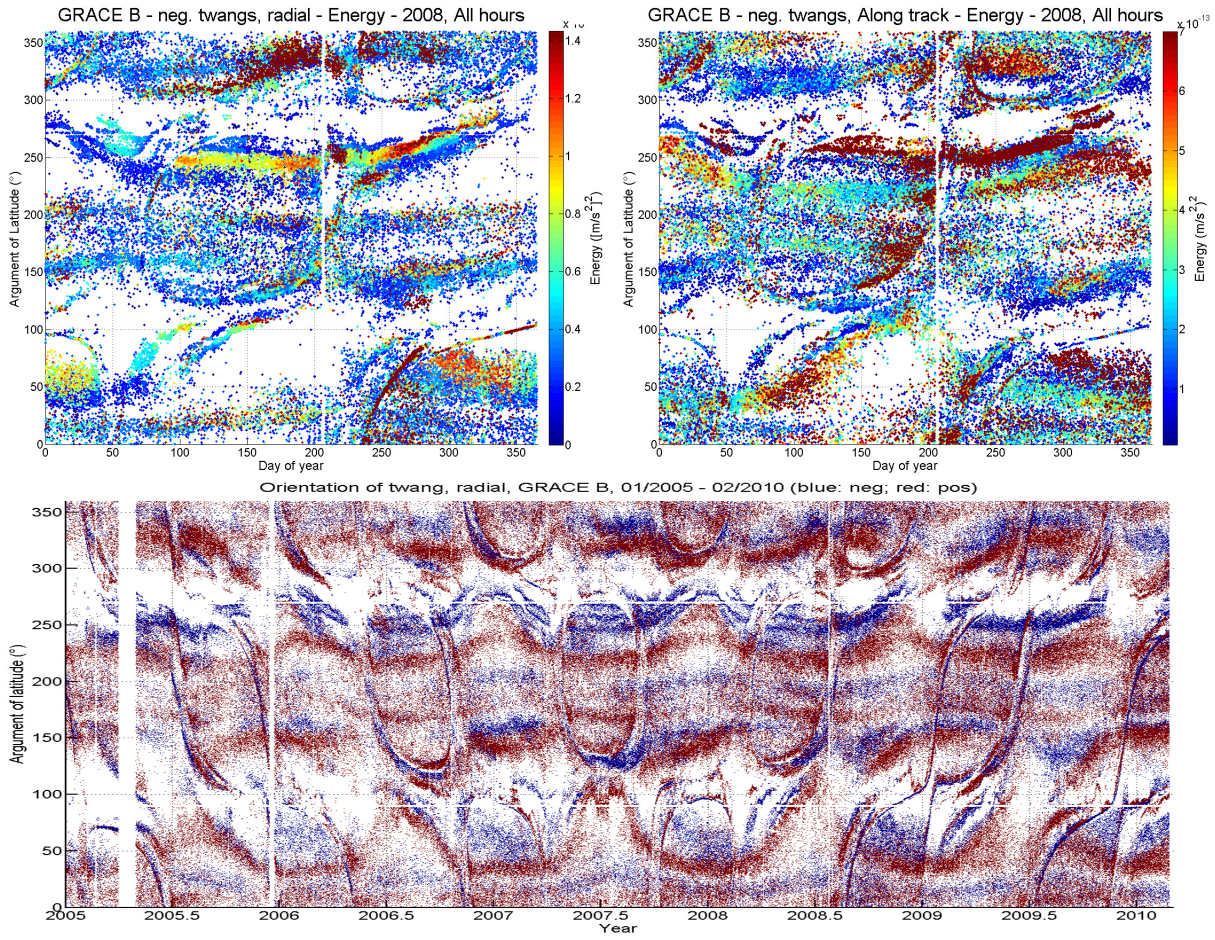

Figure 17.1: Examples for influence onto twang behavior due to solar impact onto assumed surface charges of the GRACE spacecraft. A twang is assumed to be a discharge event of the surface charge. All three images are from GRACE B ACC1A data (2008 for the upper images), argument of latitude on the y-axis, and day of year on the x-axis, i.e. the year. Upper left: Radial axis, energy; upper right: along-track axis, energy; bottom: Orientation of twangs in radial component covering twangs from 2005 to 2010.

oval shaped patterns between degree 120 and 270. The patterns formed by positive twangs appear to be disrupted or at least significantly reduced for the time of nadir illumination. This can be observed for both GRACE spacecraft.

In terms of the micro-vibration hypothesis the expectation is that the material of the surfaces is expanding due to the warming effect of the sunlight. The expanding coefficients are different for each material used and therefore a slightly different behavior of the nadir and zenith illuminated surfaces may be observable. However, the expectation would also be, that there is an increase of the number of twangs or amplitude due to the expansion.

Sunlight can lead to a lower dielectric strength of the material due to the photoconductivity characteristics of the materials as discussed in chapter 16.2. A dielectric breakdown of the material can be reached sooner with degradation of the material as we discuss in chapter 17.5, and it may become more prone to gain temporal conductive state due to photoconductivity. Furthermore, the energy of the solar wind is positive and has hence the ability of lowering a negative charge of the outer surface of the material, which may itself result in fewer twangs or twangs with a smaller energy. Furthermore, we observed a majority of negative twangs in the

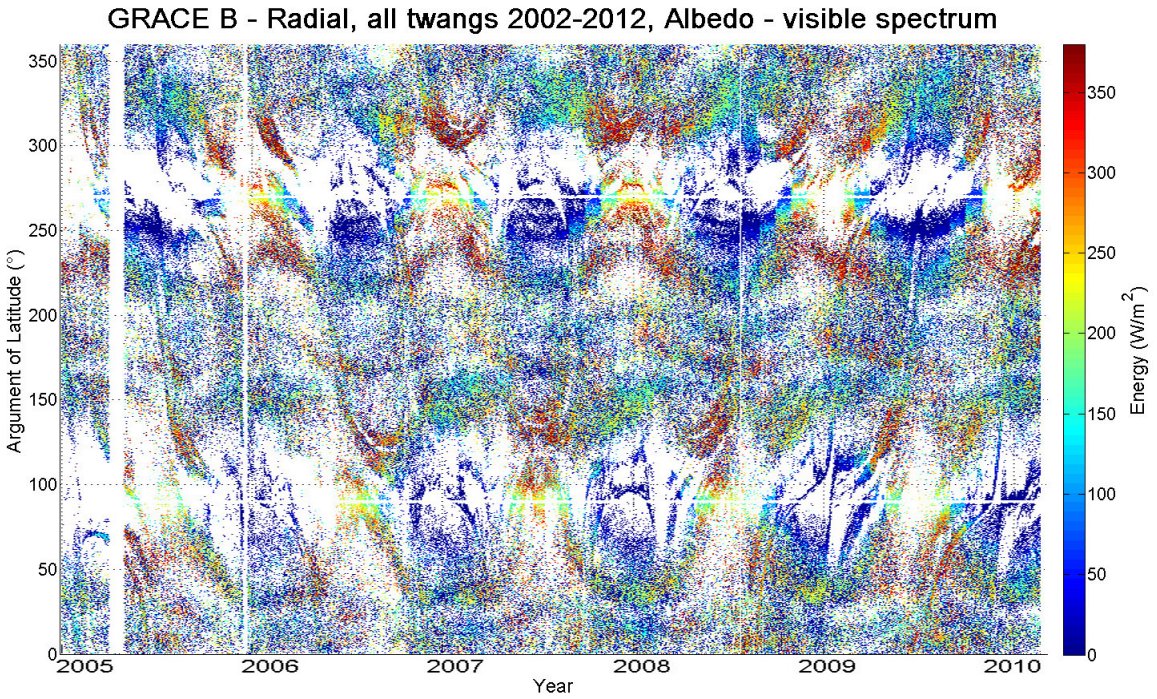

Figure 17.2: Both types of twangs in the radial component of ACC1A data of GRACE B. The color represents the energy content of the visible light spectrum of the terrestrial albedo at GRACE altitude at the time of the occurrence of the corresponding twang.

corresponding areas and only very few positive twangs. This could hint at a mechanism that influences the accelerometer from one side only while the other side, presumably from the nadir side, is diminished.

Furthermore, the solar impact greatly affects the input current of the solar arrays. The more perpendicular the solar rays impact the solar array the more efficient the photovoltaic effect of the solar cell can work. Therefore, the behavior of the solar arrays is strongly depending on the position and attitude of the satellite with respect to the sun and Earth's shadow. This is assumed to have a great impact onto the distribution of twangs.

17.2.1 Albedo, i.e. visible light

Beyond the direct solar impact onto the surfaces of GRACE, the visible albedo spectrum can be regarded as a direct impact of light onto the surfaces of GRACE. Especially the nadir surface is subject to be impacted by Earth's albedo. In figure 17.2 we display all twangs for all ACC1A data available since 2005 of the GRACE B spacecraft and colored them regarding to the energy of the visible light spectrum of the albedo at the height and time of the GRACE orbit. This is an integral over the visible and illuminated part of the Earth's surface. The seasons of the Earth are clearly visible due to the energy being zero at the poles at the corresponding winters, as they are within the polar circle and cannot reflect any visible light as they are being eclipsed. In contrast, in their corresponding summertime, the reflected energy in the visible light spectrum at GRACE orbit is about 220-250 W/m^2.

Caused by the intensity of energy in the visible light spectral domain of the terrestrial albedo, a clear distribution pattern in a geographical sense cannot be observed. If we compare figure 17.2 to figure 11.8 (p. 103), where we display all twangs with their energy (cf. chapter 11.5), it is

notable, that those areas with an energy of the twang higher than 2.5 m^2/s^4 also are subject to a rather high energy of the albedo in the visible light spectrum of at least 180 W/m^2. This may be a light indicator that the visible light spectrum of the albedo may have an influence onto the behavior of the twangs, mainly influencing the symmetry and hence the oscillation of the twang, but not the distribution itself. Despite this, no other obvious correlations could be observed.

17.2.2 Solar Array

Group 2 may directly be correlated to the behavior of the solar arrays of the GRACE satellites. The upper figure 17.3 shows the current changes of the solar arrays in 2008 of GRACE B of solar array 2. This solar array is mounted on the zenith surface of the satellite and only positions with an actual electrical current change have been plotted. In the lower row of figure 17.3 the orientation of the twangs of GRACE B is displayed, where blue are negative twangs and red are positive twangs. A series of patterns of twangs with a high energy content for positive twangs could be observed in northern latitudes (i.e. corresponding argument of latitude between 120 and 160 degrees) for a descending orbit, which are encircled in blue in the corresponding figure. These pattern correlate with a positive current change of the solar array 2, which are encircled in the upper image in light blue. From the lower figure it can be seen that these patterns are changing according to the shifting β_{prime}-cycle and therefore must be correlated to the solar activity rather than the season and is thus a further hint for the influence of the solar array.

The counterpart to this pattern is encircled in red in the lower image, which can be found in southern latitudes (i.e. argument of latitude between 210 and 250 degrees), which are correlating with a negative electric current change of the solar array 2, which is encircled in magenta in the upper right figure. This pattern is also changing according to the β_{prime}-cycle. These two patterns give evidence for a sensitive response of the accelerometer to very small current changes within the solar array input currents to the on-board battery.

However, the upper image of figure 17.3 displays current changes which are by magnitudes larger than the ones to which the twangs could be referenced (also cf. figure D.16 on page 199).

A correlation to the input currents of the zenith solar panels cannot be explained by means of the micro-vibration hypothesis of the nadir mounted Teflon foil.

17.3 Infrared impact

In contrast to the visible light spectrum of the albedo, a much clearer correlation between twangs detected in the ACC1A data of the GRACE satellites and the infra-red spectrum of the Earth's albedo can be observed. The long wavelengths of the terrestrial radiation, i.e. infrared, only changes slowly with respect to the terrestrial season and hence may be the responsible contributor to the previously introduced group 3 (cf. chapter 12.3). Figure 17.4, left side, displays all twangs of all data available for GRACE B with respect to their day of occurrence since 2005 and the argument of latitude. The color of the twang, where any dot represents a twang, is representing the energy of the infra-red spectrum of the emitted radiation from Earth. In this picture the near sinusoidal wave shape like patterns of the twangs near the equatorial latitudes correspond clearly to the energy of this spectrum which behaves in the same sinusoidal shape accordingly. This means that the emitted radiation in terms of the infra-red wavelength of the Earth is influencing the distribution of the twangs significantly. This is also valid for the times of the summer in the Arctic, where the icecap is being minimized and hence the energy in the infra-red spectrum is increased, which is clearly represented by the shape of the twangs and their colors.

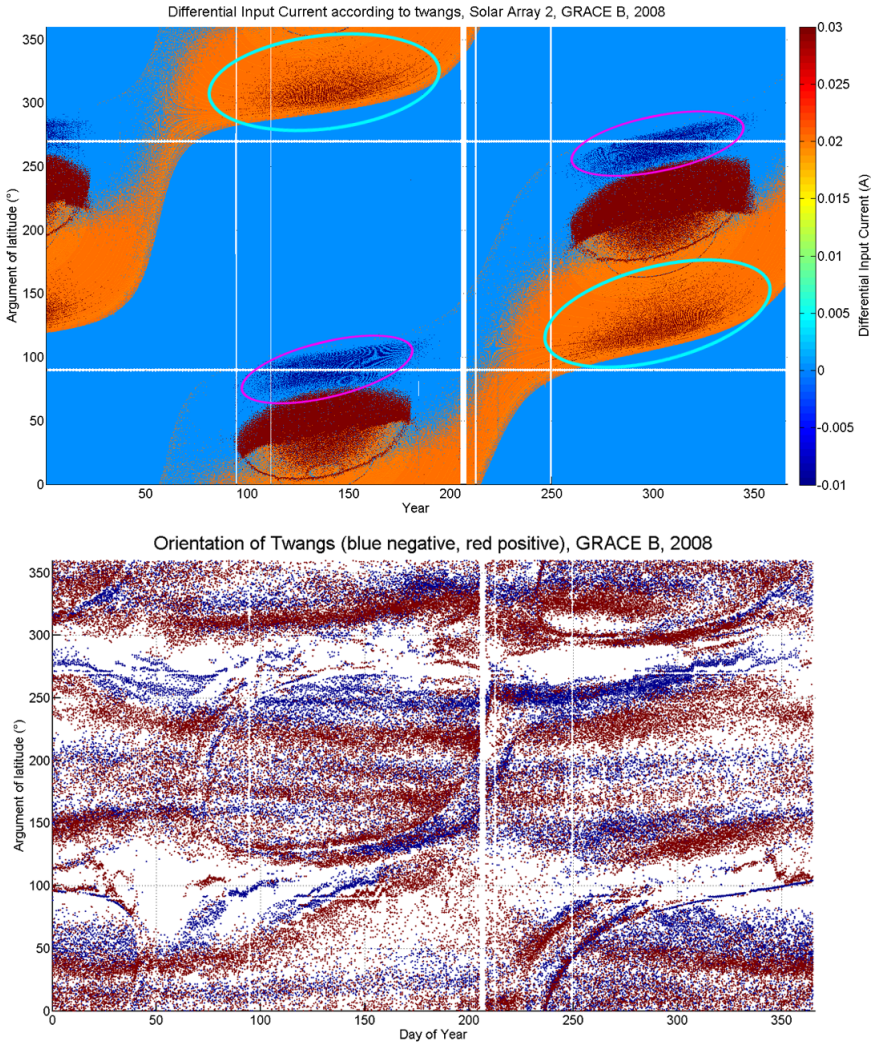

Figure 17.3: Upper : Small electric current changes of solar array 2 (zenith panel) of GRACE B of 2008; lower: Orientation of twangs in the radial component of ACC1A data of GRACE B 2008.

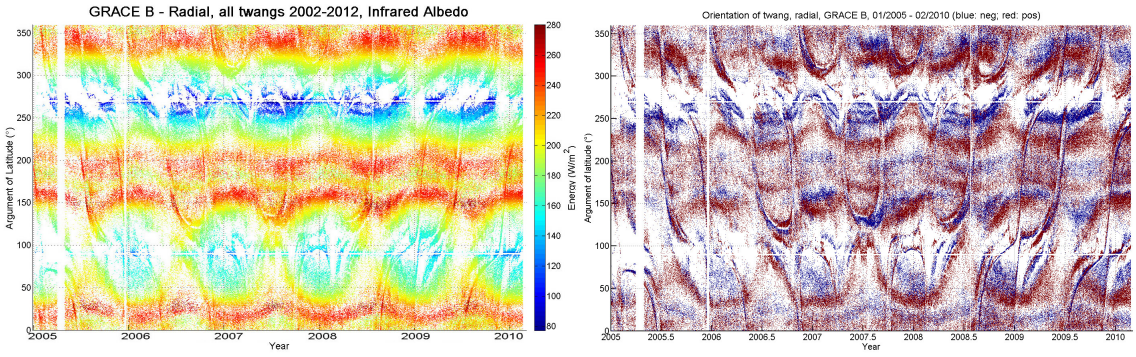

Figure 17.4: Left: Both types of twangs in the radial component of ACC1A data of GRACE B. The color represents the energy content of the infra-red spectrum of the terrestrial emitted radiance albedo at GRACE altitude at the time of the occurrence of the corresponding twang. Right: Orientation of twangs in the radial component of ACC1A data of GRACE B.

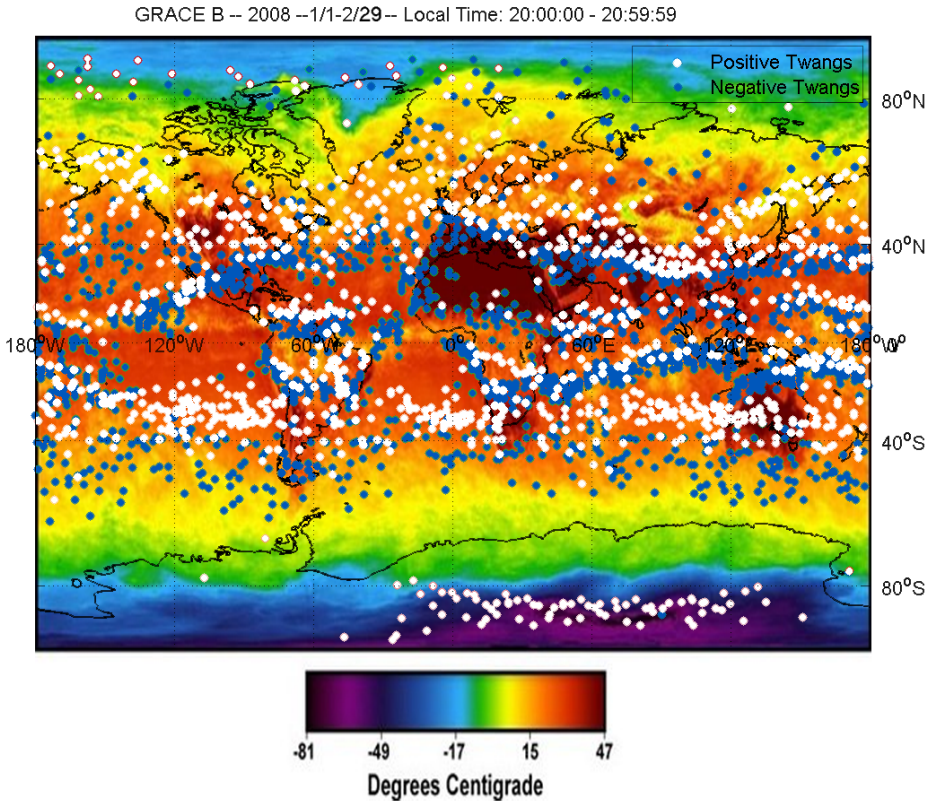

Figure 17.5: Geographical arrangement of twangs of ACC1A radial data component of GRACE B in January and February of 2008. White dots represent negative twangs and the blue dots positive twangs. Underlying color scheme represents the infrared radiation emitted by Earth, provided by NOAA, given in terms of Earth's surface temperature.

The sinusoidal shaped patterns furthermore correspond to the energy of the twangs in the radial component of both GRACE spacecraft as can be seen in the lower figures of figure 17.3. This is also valid for the along- and cross-track axes. Here, a lower infrared energy in the shadow regions of the orbit results in a twang with a higher energy. The infrared energy appears to affect also the amplitude, where the positive twangs show a smaller amplitude due to a higher infrared energy and the negative twangs show a greater amplitude when higher infrared energy is experienced by the satellite. Moreover, also the asymmetry is depending on the infrared, which is less obvious however. The twang show a more symmetric behavior when the infrared energy is becoming higher. Figures for the amplitudes and asymmetry can be found in Appendix C, where the shaded regions of the twangs should be regarded (according to figures 12.6 or D.1).

Furthermore, when we compare the right image of figure 15.5 to for example the figures 10.2 and 10.3 in chapter 10.1 or figures 10.4 and 10.5 in chapter 10.2 it is somewhat indicated that the patterns formed by the areas with a high energy content of 280 Wm/s^2 in figure 15.5 are represented by the patterns of twangs in the corresponding areas.

The orientation of the twangs show a behavior corresponding to the energy content of the infrared emitted radiation (cf. figure 17.4, right). Higher energy content (red in figure 17.4) appears to result in negative twangs, and lower (yellow) leads to positive twangs. The twangs that can be correlated to the sinusoidal shaped patterns near the equator shall be referred to as group 3a.

Figure 17.5 displays the geographical patterns of all twangs in the radial ACC1A data component of GRACE B in the first two months of the year 2008. The W-shaped pattern of positive twangs

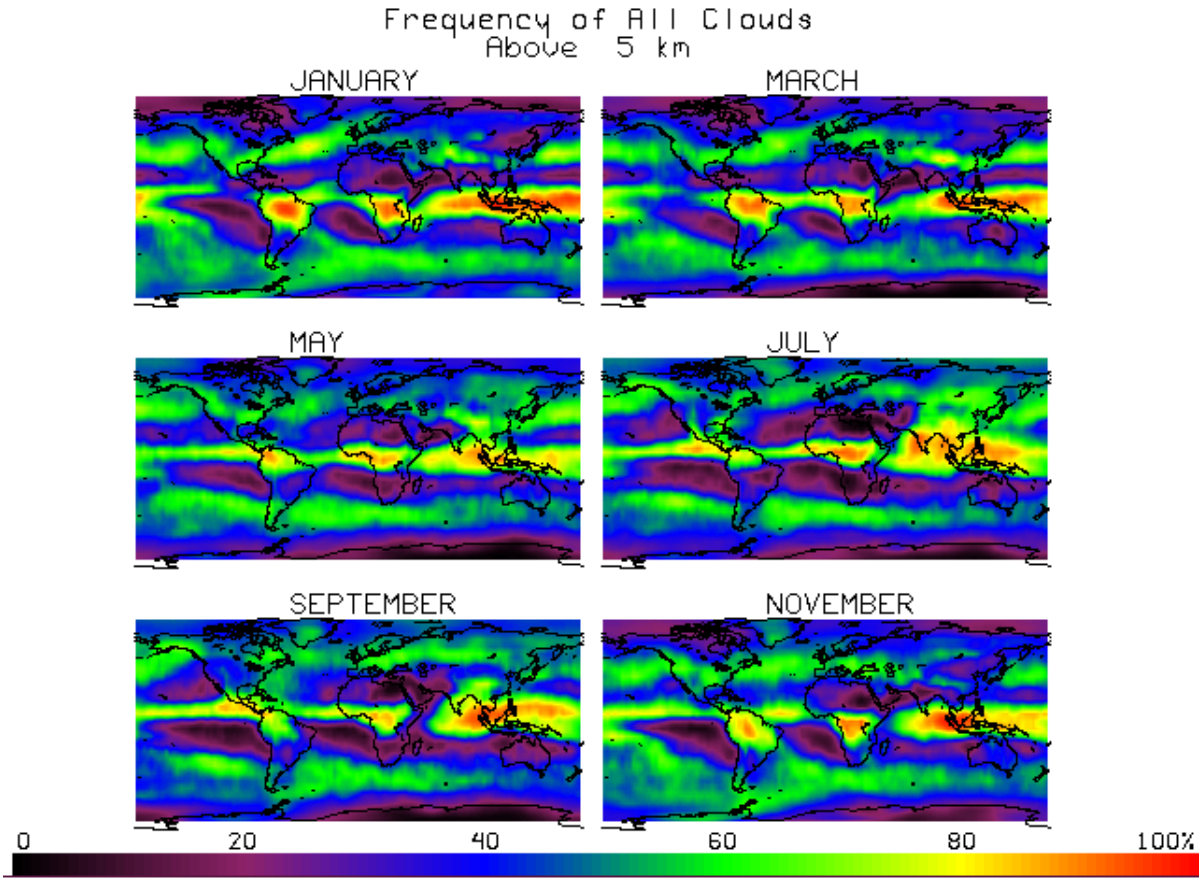

Figure 17.6: Geographical distribution of cirrus clouds in the summer and winter seasons (yellow and red regions indicate more frequent cloud occurrence). The months of December, January, and February were summarized for the boreal winter (austral summer) and the months of June, July, and August were used for the boreal summer (austral winter). The seasonal summaries were compiled using a uniformly spaced grid of 2 degree latitude by 3 degree longitude. Each grid box for each season has at least 500 observations (Wylie et al. (1994)).

in the north, as well as the pattern formed by positive twangs in the very south correspond to the behavior of the infrared radiation as emitted by Earth. This infrared emission varies according to season and can be a strong indicator as to why the patterns of twangs are strongly correlating with season. Such a correlation between the terrestrial infrared emission and the arrangement of the patterns in the polar-near regions can be found throughout the year. In contrast to the sinusoidal shaped patterns in the equatorial regions visible in figure 17.4, the polar-near patterns appear not to be an annual period but rather show a behavior correlated to the spacecraft's β_{prime}-cycle.

The majority of the observed twangs appears to be greatly influenced by the long wavelength radiation, i.e. infrared, from Earth. The distribution of twangs reflects the systematics of the emitted low frequency radiation from Earth in accordance with Earth's cirrus clouds. Cirrus clouds are thin clouds that consist mainly of small ice-particles and have the ability to reflect a great part of Earth's infrared radiation and thus may contribute to global warming. In case of the GRACE spacecraft this means, that less infrared radiation impacts the satellites whenever the satellite is above an area which is frequently covered by cirrus clouds. Figure 17.6 shows the mean annual distribution of cirrus clouds. The patterns that can be observed in this figure can

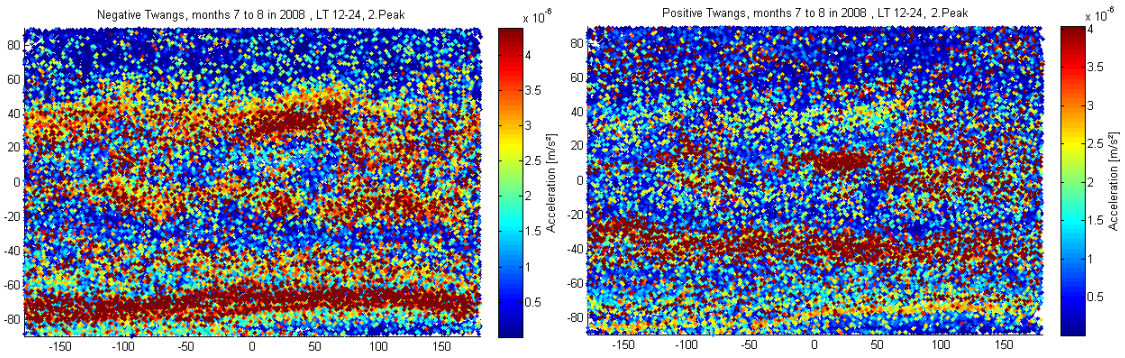

Figure 17.7: Distribution of negative (left) and positive (right) twangs of GRACE A in July and August of 2008 and the corresponding amplitude of the second peak. The patterns formed by infrared terrestrial radiation at equatorial and in the middle of the northern hemisphere, as well as latitudes around the sothern pole are clearly visible by the amplitudes of ≥ 2.5 m/s^2.

be also observed by the structures created by twangs (cf. figure 17.7 and the figures in Appendix A). The approximate wavelengths emitted from Earth that are presumed to impact GRACE are ranging between 9.6 µm to 11.5 µm and are thus indeed able to penetrate the Teflon foil (as introduced in chapter 16.2.1).

The infrared radiation emitted by Earth has a great impact onto the distribution of twangs along the orbit of GRACE (cf. chapter 12.3). The twangs appear to arrange according to the energy strength of the infrared radiation component (cf. figures 15.5 and 17.4 , and figure 17.7).

Infrared light has a longer wavelength and thus may yield to a warming of materials. This could potentially lead to an expansion of the material applied. However, the energy of the infrared radiation is relatively low compared to actual sunlight or albedo and can only be observed at night. Furthermore, the differences of the energy strength to the corresponding geographic location is very small compared to the energy difference between the infrared radiation as such and the sunlight. Therefore, we do not expect to see such clear correlations between the terrestrial infrared emission strengths and an expansion, and hence vibration, of the material.

In contrast to this, infrared radiation has just like the sunlight the ability of lowering a negative charge or yielding a lower dielectric strength of the material as discussed above in section 17.2. This may influence the distribution of twangs greatly. However, in figure 17.7 we observe twangs with a greater amplitude which contradicts the expectations that infrared impact onto the surfaces may have. Moreover, infrared would presumably only influence the nadir surface of the GRACE spacecraft, and thus the expectation would be that twangs may behave similar to the the observations made for the lower image of figure 17.1, where negative twangs are diminished.

In chapter 16.2.1 we introduced the fact that Teflon is highly permittive to infrared radiation. This could also yield a process of a payload within the satellite body which is highly sensitive to infrared radiation. This assumption in fact could result in twangs that are in fact having a larger amplitude than others at the corresponding equatorial latitudes and the latitudes in the polar regions as well. These patterns of twangs are easy to be observed in figure 17.7, where cloud-like patterns of twangs with a great amplitude in the equatorial latitudes as well as the bands near the southern pole are believed to be due to infrared impacts. Nonetheless, also infrared induced twangs are believed to be of electrical origin, as the twangs remain short, and rapid as well as superimposable.

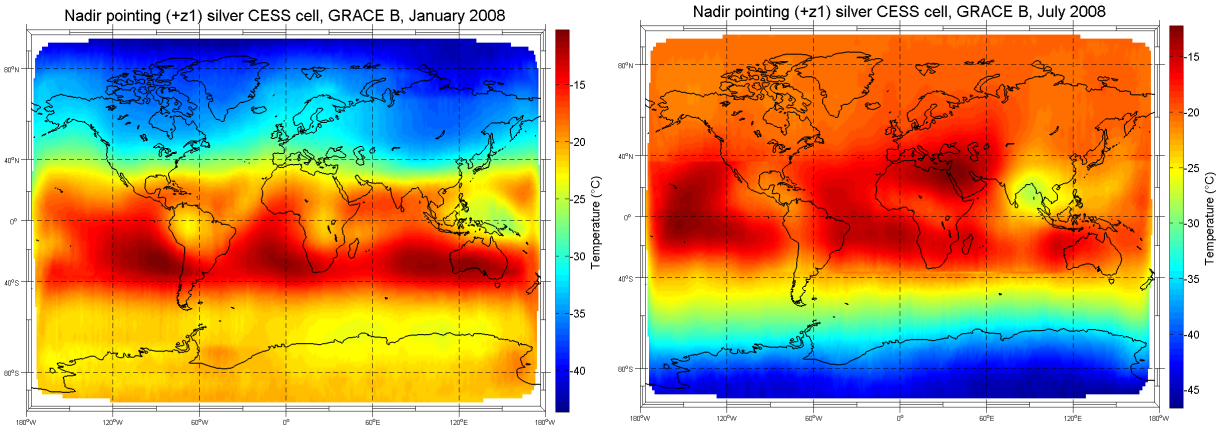

Figure 17.8: Mean temperatures detected by the nadir facing silver CESS panel (+z), resistance 1 of GRACE B for January 2008 (left) and July 2008 (right).

17.3.1 Correlation to CESS Sensors

The GRACE satellites are equipped with Coarse Earth and Sun Sensors (CESS), as stated in chapter 4.2. The silver panel of the nadir mounted CES sensor will reflect the visible light spectrum, but is able to absorb the infrared spectrum. Thus, the temperatures detected by this area of the CESS widely corresponds to the patterns formed by twangs. The temperatures for January and July detected by the nadir facing silver CESS panel are displayed in figure 17.8. However, this sensor only roughly detects the patterns formed by twangs. The structures of twangs in the corresponding northern hemisphere are visible in January in both the CESS detection as well as the twang formations, but the corresponding structures in the southern hemisphere in July can more distinctly be seen within the formation of twangs. The CESS shows a great difference in temperature, but does not reflect the same distinct curvature as the twangs.

The surface of the silver CESS panel is an Optical Solar Reflector (OSR), which consists of a top layer made from quartz, which is located over a reflecting layer made of metal. This results in a very low absorption coefficient, and the quartz is a good infrared emitter. This material may indeed have a slightly different behavior compared to the nadir mounted Teflon insulating foil and thus may detect long wavelength of the terrestrial radiation differently.

17.4 µ-Deviation in ACC1A axes

In figure 11.9 in chapter 11.6 we display the deviation of the time μ of the Gaussian derivative model. This deviation is strongly correlated with the geographical location and is in the order of milliseconds between the ACC1A data components. While there is no direct indicator that this observation may be regarded as a support for the discharging hypothesis, it may be regarded as a contradiction to the micro-vibration hypothesis. The expectation would be that the deviation, i.e. offset, in time between the axes of the accelerometer would be constant for a mechanical vibration. This would be valid for the two sensitive axes as they have the same transfer function. There is no valid explanation how the vibration of a material could affect the axes of the accelerometer in such a way, that there is a time-shift between the axes, which is furthermore depending on an external source.

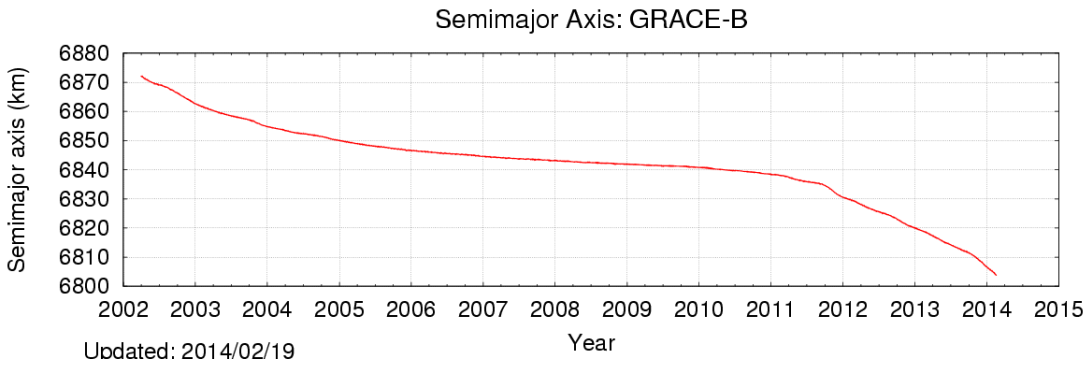

Figure 17.9: Decrease of the orbital height of the GRACE B spacecraft since mission launch (CSR/TSGC (2014)).

Also, signals in the ACC1A data due to heater activations and de-activations as well as electric current changes of the magnetic torquers show deviations with respect to time in the different axes. In these cases, however, this deviation is a constant offset for all cases and does not alter in a case to case scenario.

The deviation of μ also contradicts any hypothesis that twangs may be influenced by the gold wire that connects the proof mass of the accelerometer with its surrounding cage, as the gold wire is mounted at a very specific side of the proof mass relative to the cage and hence the deviation of μ should show systematics accordingly if the gold wire was influencing the behavior of twangs.

It may contribute to the hypothesis of discharges coupling into the accelerometer. The charging upon the satellites surfaces may occur at various areas of the panel, depending on the atmospheric condition and the position of the spacecraft. Hence, the discharge may occure at random locations of the satellite, leading to a slightly different coupling scenario for each discharge. As the charged area of the spacecraft may be correlated to the geolocation, we experience similar µ-deviations in certain geographic locations and season.

17.5 Temporal behavior

In chapter 8.3.2 we presented an increase of the overall mean number of twangs per day and stated a decrease of the mean daily amplitude. Such a behavior can be regarded as an aging process of the material used for GRACE. Furthermore, we introduced an increase of twangs with respect to different patterns with group 4 in chapter 12.4.

In terms of vibration, this could hint at a loss of elasticity, where the material expands easier due to warmth with less vibration. This observation could also support the discharge hypothesis as the dielectric strength of the material may be degraded due to the increasing formation of recombination centers in the material. As a result of the latter, the material may behave similar to what we described in section 17.2 for the solar incidence angle, i.e. the voltage needed to cause a dielectric breakdown may be significantly lowered. In figure 17.1 (p. 139) it is observable that the amount of twangs believed to be due to infrared radiation is increasing over the displayed years, supporting the hypothesis that the material is decaying as the overall strength of infrared did not increase over the displayed time-span.

Another possible explanation for the temporal behavior and increase of twangs could be the decrease of the orbit height of the GRACE spacecraft as shown in figure 17.9. The main contributor to the patterns of the twangs, the long wavelengths of the terrestrial radiation, may

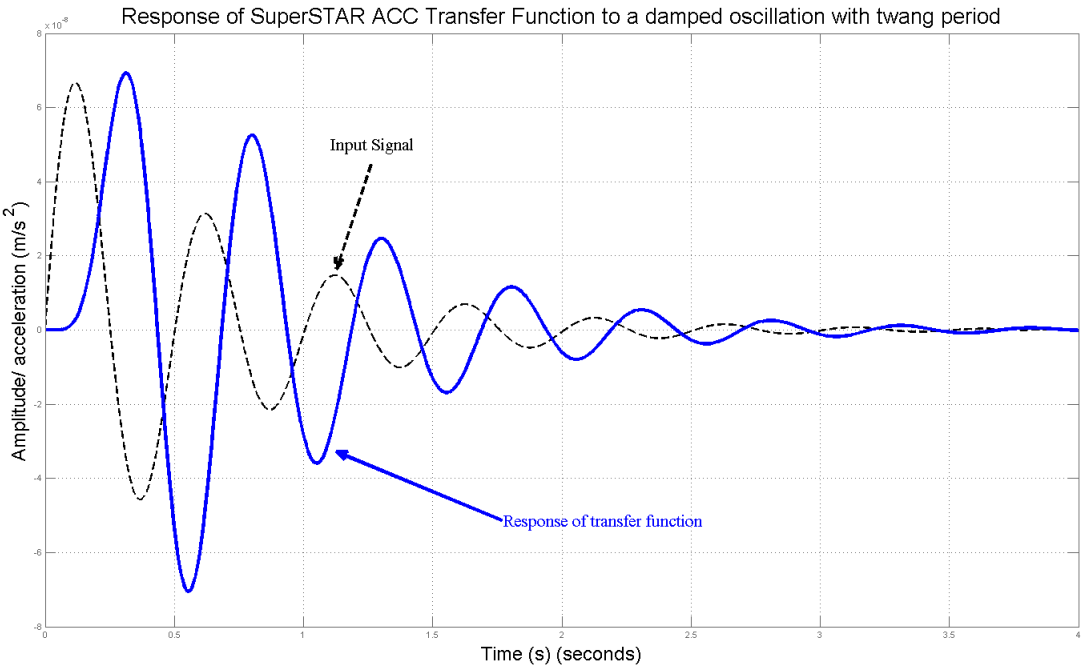

Figure 17.10: Response of the transfer function to a damped oscillation that may serve as a micro-vibration.

indeed be more energetic at a lower altitude and may hence yield more twangs as the outer surfaces are exposed to a stronger terrestrial radiation.

17.6 Role of transfer function

The last hint that the source of twang may be found within a discharge process of the surfaces can be found within the signal processing of the accelerometer by considering the transfer function. In chapter 14 we stated that there is very little tolerance of what the input signal may look like, regarding the signal length as well as the shape. In fact we expect a signal in the order of a few milliseconds only, where the length of the signal must remain in a very limited bandwidth in order to make twangs able to be superimposed.

Such a limited range of input signals cannot be expected for micro-vibrations, where a broader variety of input signals may be expected due to the vast possibilities that may result in a vibration of the materials used on-board of the GRACE spacecraft. An example for a response of the transfer function due to an input signal that may serve as a vibration in terms of an oscillation is displayed in figure 17.10. An input signal, as short and rapid as stated, which is rather strictly bound in terms of duration and only variable in terms of amplitude is a rather strong indicator for an electrical origin. Both detected sources of twangs, changing electrical input currents of the solar arrays as well a infrared radiation induced twangs, are believed to be electrical mechanisms.

17.7 Conclusion and overview of twang sources

In conclusion we can state, that the majority of the observations made with respect to twangs support the hypotheses which are based on an electrical origin. Only few observations correspond to the micro-vibration hypothesis, and some, such as the µ-deviation in the axes, even contradict the vibration hypothesis.

Table 17.1 provides a summary and overview of the observations and possible interactions of a spacecraft with its surrounding in orbit with regard to twangs. All observations may be related to the four groups of twangs as introduced in chapter 12 and the three hypotheses, which are current changes of the solar array (CC), discharging events (DE), and the micro-vibration (MV). The infrared impact onto the spacecraft is regarded to be a contributor to the discharging events in this overview.

Effect on GRACE	Observation/ Explanation	CC	DE	MV
Transfer Function Signal	Short rapid signal, in the order of msecond. Very little variation in duration. Indicator of an electrical signal.	✓ Group 1, 2	✓ Group 3, 4	✗ No group
GRACE A vs GRACE B	Same geographical distribution.	✓ All groups	✓ All groups	✓/✗ All groups
Solar impact/ incidence angle	Decrease or increase of number of twangs or their energy when surfaces are sunlit.	✓ Group 2	✗ No group	✓ Group 1, 2
Terrestrial infrared radiance	Geographic distribution of twangs correlated to the strength of infrared radiation.	✗ No group	✓ Group 3, 4	✗ No group
Earth's Albedo	Only speculative distributions observed, due to the dominating direct solar impact.	✓/✗ No Group	✗ No group	✓ No group
Seasonal impact	Some geographic distributions are strictly correlated to the seasons of the orbit.	✗ No Group	✓ Group 3	✓/✗ Group 3
β_{prime}-cycle	Some geographic distributions are strictly correlated to the β_{prime}-cycle of the orbit	✓ Group 1, 2	✓ Group 3 (polar)	✓/✗ Group 1, 2
μ-deviation of axes	Deviation of μ (time) in the axes in the order of msec. Geographically correlated.	✗ No group	✗ No group	✗ No group
Temporal behaviour of twangs	Increase of twangs over the data covered timespan, whereas the amplitude decreases.	✗ Group 4	✓ Group 4	✓ Group 4

Table 17.1: Overview about the processes that may result in a twang in ACC1A data. Comparison with the four groups of twangs that are presumed to have an electrical cause as a source and the micro-vibration hypotheses. The columns represent the hypotheses previously stated: CC = Current Changes of the solar array; DE = Discharge Events of the spacecraft surfaces; MV = Micro-Vibration of the insulation foil at nadir surface. Green check mark = Agrees with hypothesis; Red cross = Disagrees with hypothesis; Mix of green/red = partially explainable. The stated groups show, what group may be regarded to the hypothesis.

Part VI
Discussion and summary

18 Summary & Conclusions

In this work we introduced the GRACE satellite mission and the key instruments mounted aboard the two twin satellites. Moreover, we described the shape and design of the spacecraft. By the description of the instruments we put special emphasis onto the accelerometer which is the key sensor in our work.

We introduced the reader into the signals detected in the ACC1A data called twangs and how they are distributed in the ACC1A data as well as how they can be modeled by a set of parameters. Furthermore, we discussed the spatial and temporal distribution of twangs and the geographical behavior of individual parameters of the model. As a result of these two we were able to state a new hypothesis concerning the external aspect of the source of the twangs. However, it is yet unclear of how these effects couple into the accelerometer and ultimately are visible by means of twangs within the ACC1A data.

We could show that twangs typically consist of two main peaks, one negative followed by one positive or vice versa. If the amplitudes of these two peaks differed significantly, for a majority of twangs an oscillating decay after the twang could be detected, whereas almost no oscillation could be found if the ratio of the amplitudes of the two main peaks was close to 1. This results in the fact that a twang is usually significantly shorter than 1 second, but can extend to up to 5 or more seconds if it is followed by an oscillating decay.

Twangs occur simultaneously in all three axes, and can be detected if the amplitude exceeds the noise level of the specific axis. In the radial component this is usually the case and hence we oriented our detection techniques at the twangs observable in the radial component of the ACC1A data. The amplitudes in the along-track and cross-track axes are usually significantly smaller by several orders of magnitude. However, we could detect slight diversions concerning the time of occurrence in the axes. The offset of the time of occurrence among the axes is not stable and is subject to change case by case.

In the year 2010 we detected about 600 twangs per day in ACC1A, but at the beginning of the GRACE space mission this number was significantly lower, and was usually below 100 per day. This increase in the number of twangs appeared to be a continuous process over the whole GRACE lifetime for the data available to us. At the same time we found evidence that with an overall increasing number of twangs the mean amplitude of twangs appeared to decrease slightly.

The geographical distribution of twangs is in many cases strongly bound to certain bands and patterns and hence a correlation to an external source is evident. We found that these distributions can be correlated to the seasons and local time, and thus an impact due to the surrounding satellite environment is given. Furthermore, we were able to show that a direct solar impact onto the outer spacecraft's planes can significantly change the parameters of the twangs. Most striking is the fact that twangs will become more symmetric and less energetic whenever the nadir pointing plane of the satellite is being sunlit. Also, the deviation in the occurrence of a twang in time between the axes is strictly geographically or orbitally correlated and thus an external impact onto the spacecraft is more than likely.

A majority of the patterns can be traced back to an influence of the terrestrial infrared emission, whereas the energy of the long wave radiation may significantly influence the arrangements of

patterns as well as the amplitude of twangs. The structures shaped by twangs resemble the patterns of cirrus clouds above Earth which have the ability to block or reflect the terrestrial radiation to a certain amount and hence influence the formations.

Another source can be found in a changing electrical input current of the solar arrays of the spacecraft, where especially the zenith mounted solar array has an impact whenever the current changes in a certain range. Very narrow and distinct bands may be formed whenever the GRACE spacecraft are entering or leaving Earth's shadow.

Based on these observations, and especially the deviation of time, the prominent hypothesis, that twangs are caused by micro-vibrations of the nadir mounted insulation-foil needs to be reconsidered. A mechanical source can by no means evoke the twang to occur with deviations in time in different axes, and hence a different hypothesis was needed.

As the heater switch events as well as the electric current changes are of electrical nature, and the durations is the same for these two as well as for twangs, one could suggest that also the source of twangs may have an electrical reason. We stated the hypothesis, that twangs may be the response of the accelerometer to a discharging event of the satellite's surfaces. An outer surface of a spacecraft ultimately charges due to the surrounding plasma in orbit. The amount of charge is depending on the altitude, season, solar impact as well as the shape of the spacecraft. Our hypothesis is supported by the fact, that the number of twangs is increasing and the amplitudes are decreasing, which hints at a degradation of the applied dielectric material on the GRACE satellites. However, this feature could also be due to the decreasing orbit over the whole mission's lifetime. Furthermore, the distribution of twangs contribute to this hypothesis, as the alignment to the radial component of the magnetic field may enhance the charge of a surface, as well as the precipitation of highly energetic electrons in the polar regions. Also, the decrease of the energy of the number of twangs due to surfaces being illuminated by the sun may support this hypothesis, as sunlight can decrease the negative charge of a surface and also make the material of the surface more conductive, resulting in smaller energetic twangs. The same may be observed for terrestrial infrared emission.

We introduced the transfer function of the SuperSTAR accelerometer and showed how the response of the accelerometer is to different input pulses, such as rectangular pulses of different duration and amplitudes. Furthermore, we suggest what the original input of the twang might look like and could by these means support the discharge hypothesis, as the input signal allows very little variation by means of the input signal duration. This would be very unlikely in case of other hypotheses.

18.1 Impact onto the gravity field

In the frame of our investigation we developed an adhoc approach which allowed us to give a rough estimation whether changes within the ACC1A by reduction of twangs may affect the gravity field as determined by the GRACE satellite mission. We introduce this fact in this chapter of the thesis, as this approach is far from complete and is not meant to give detailed overview about analysis nor to give a finite answer about whether a real impact is seen. In this approach we reduced the signals due to magnetic torquer and heater activations and de-activations from ACC1A data as described in chapter 7.2.3 and 7.2.4, and reduced the twangs to the mean value of the corresponding time, i.e. flattened the signal, obtaining ACC1A-TR data. From these ACC1A-TR we derived ACR1B data, which we forwarded to GFZ. With these data GFZ computed a monthly solution which was then compared to the monthly solution where the official ACC1B data was used. The differences of the obtained monthly solution is displayed in figure 18.1 (left).

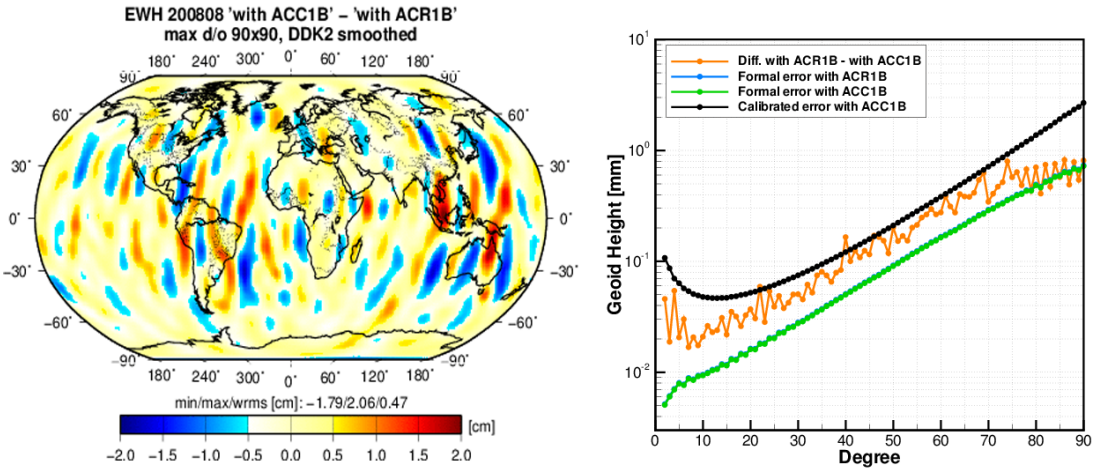

Figure 18.1: Left: Impact of the reduction of magnetic torquer, heater activation and de-activation as well as flattened twangs to the underlying mean acceleration value (ACR1B) onto the gravity field determined by GRACE by GFZ. Comparison of ACR1B to ACC1B in equivalent waterheight of the geoid. Right: Formal error of the ACR1B and ACC1B data, computed by GFZ.

There are some differences visible, especially contributing to the striping of the GRACE monthly solution. The stripings appear to differ, but not vanish. However, in chapter 8.5 we stated that a reduction of signals yielding a non-net-zero acceleration results in major peaks within the ACR1B data which may enhance the actual gravity field with artifacts which may be not due to the twangs but to the incorrect reduction. What we can observe is that the gravity field undergoes some changed by the reductions made. However, we cannot state that there is an actual improvement made by these reductions yet, which may be due to the unsatisfying nature of the adhoc approach. This is supported by figure 18.1 (right) where the formal errors of the ACR1B and ACC1B errors are plotted. From this figure it is obvious that the formal error of the ACR1B data is slightly above the formal error of the ACC1B data. Therefore, the impact onto the gravity field by means of the adhoc approach of the ACR1B data has to be considered carefully. However, we wanted to give a rough estimation as to how the twangs might influence the gravity field.

19 Outlook & further investigations

This work is the most comprising work dedicated to twangs in the accelerometer data of the GRACE gravity field space mission. Although many parameters and the behavior of the twangs could be observed, analyzed and new hypotheses could be stated, many questions remain and should be addressed in the near future.

The most interesting field of work is indeed a successful reduction of twangs from the ACC1A, including the constraint that the acceleration needs to be of net-zero nature past the reduction in order to suppress rapid peaks with a high amplitude in the ACR1B data files which are needed in order to derive the gravity field. Furthermore, the behavior and importance of different parameters of twangs onto the Earth's gravity field can be determined by deriving different ACR1B files and comparing them against each other. This approach could either be carried out with help of the analysis centers such as GFZ or by means of a gravity field satellite simulator.

In this work we stated, that the satellites are flown with a slightly deviating pitch angle in order to establish the K-band ranging system successfully. Furthermore, we stated that the satellites

have a majority of slower ions in the ram region and mainly electrons in or near the wake region. It would be interesting to find out whether the spatial distribution of twangs as well as the behavior of twangs are influenced by a changing pitch angle of the spacecraft. If this is the case, this would be another very strong indicator supporting the discharging hypothesis stated in the frame of this work.

The time-span of data analyzed by us was from 2002 to 2010. During these years the solar activity was on an all-time minimum with close to no solar spots on the surface on the sun. This low solar activity enhanced the lifetime of GRACE as the overall plasma flux of the sun as well as the ionization rate of the Earth's atmosphere was very low, accordingly. However, as we expect a great solar influence onto the behavior of the twangs it would be worthwhile to assess whether a stronger solar activity would impact the accelerometer data significantly. Since 2010 the solar activity has been constantly rising until there has been solar storms and flares in 2013. It would be valuable if the corresponding ACC1A of that time will be investigated with respect to twangs.

Another approach to investigate the source of the twangs would be to test a SuperSTAR accelerometer under laboratory conditions. Here, one could determine how a discharge current, or any other electrical signal such as the magnetic torquer current changes or heater activations and de-activations may couple into the instrument. Furthermore, it would be valuable to use an inverse transfer function of the SuperSTAR accelerometer in order to estimate what the actual original signal of a twang may look like, which would be a great step towards the investigation of the source of the twangs. This could validate a hypothesis.

Few investigations were carried out concerning the impact of the long wavelengths of the terrestrial radiation upon satellites (e.g. Knocke et al. (1988)). The outcome of our researches indicated a significant impact of the long wavelengths of the terrestrial radiation pressure upon the accelerometer data of GRACE. This effect deserves a broader attention and may also be observed upon other spacecraft in similar height which carry outer surface material with the same or similar parameters as mounted on the GRACE satellites. It may be worthwhile to gain more understanding of how the terrestrial infrared emission may affect the sensor output of space missions.

There is very little knowledge of the degree of degradation of the materials mounted aboard the GRACE spacecraft. It is known for a fact that any material that is exposed to the spacecraft environment will ultimately undergo alterations that will change the characteristics and qualities of the material, such as the dielectric strengths. However, it is unknown to what impact for example dust upon the solar arrays may affect the twangs, or to what degree the dielectric qualities is influenced. Furthermore, it is yet uncertain what panels exactly may contribute to which pattern of twangs. So far, only a direct association to the nadir surface as well as the zenith surface could be determined.

It would be of interest to estimate whether twangs are occurring on other gravity field space missions. The accelerometer data of the CHAMP gravity field mission had a low sampling of 1 Hz and the accelerometer was less sensitive than the one mounted aboard the GRACE satellites and thus a twang investigation concerning the CHAMP satellite mission is difficult if not impossible. However, the GOCE gradiometer consists of six highly sensitive accelerometers and the accelerometer data of the drag-free mode are available as 10 Hz. Especially the different design and shape of the GOCE satellite makes GOCE an interesting object to find out whether the satellite experiences discharges of the surfaces and whether these signals may couple into the accelerometers.

In the end it may be important to consider the results of this work for the recently planned GRACE Follow-On (FO) mission as this mission will again consist of two identical twin satellites, which are very similar in their conception to the original GRACE mission. Few changes are

planned in the GRACE-FO mission, for example a more subtle change of the electric current as used for the heater activations, a different mounting foil on the nadir side and a slightly different design (Astrium (2011)). According to our investigations concerning the accelerometer transfer function a longer slope of the input signal may lead to a longer signal in the accelerometer data, however, with a greater oscillation. Although the more steady slope in the electric current of the hearters and magnetorquer is meant to avoid an impact onto the accelerometer and possibly other instruments it may actually enhance the data to a larger degree, as the signals then will not be of high-frequency nature only. Furthermore, it is planned to use a nadir insulating foil with a greater stiffness than it has been used for the original GRACE mission (Astrium (2011)). This may not be necessary if the origin of the twangs is indeed a discharging effect instead of micro-vibrations. In such case, it would be more useful to use a material with a greater dielectric strength or implement a mechanism that allows controlled discharges. Furthermore, the material should not age before the end of the mission.

References

Asmar, S.W. (1997). Characteristic Trends of Ultrastable Oscillators for Radio Science Experiments. TDA Progress Report 42-129.

Astrium, EADS (2011). Personal Communication.

Barlett, R.H.; Fulk, G.A.; Lee, R.S.; Weingart, R.C. (1975). Temperature Dependence of X-Ray-Induced Photoconductivity in Kapton and Teflon. IEEE Transactions on Nuclear Science, Vol. 22, No. 6. Dec 1975.

Berger, L.I. (2000). Dielectric Strength of Insulating Materials. CRC Handbook of Chemistry & Physics. CRC PRESS LLC, ISBN 1439880492, 2000.

Bertin, P.-Y.; Foulon, B.; Le Clerc, G.-M.; Rodrigues, M. (2000). SuperSTAR Accelerometer for the Gravity Recovery And Climate Experiment - Specification Document. ONERA, GRACE-327-520, Technical Report.

Bertin, P.-Y. (2000). GRACE: SuperSTAR accelerometer Transfer fucntion. Internal Report, 11/05/00, ONERA.

Bettadpur, S. (2000). Brief note on the ACC transfer function & its application to simulated drag time series. Note, Center for Space Research, University of Texas at Austin, 2000/05/11.

Bettadpur, S. (2007). Gravity Recovery and Climate Experiment - Product Specification Document, Rev 4.5. Center for Space Research, The University of Texas at Austin, GRACE 327-720, CSR-GR-03-02.

Bindel, D. (2009). Angular Acceleration from Magnetic Torquer Current. Internal Report, ZARM, Universität Bremen.

Coffey, H.T.; Nanevicz, J.E. (1975). Photoconductivity of High-Voltage Space Insulating Materials - Measurements with Metal Electrodes. Interim Technical Report 1, NASA, NASA-CR-152839. Apr 1975.

CSR, TSGC. GRACE Orbital Configuration (plots updated daily). Center for Space Research, The University of Texas at Austin. Texas Space Grant Consortium. http://www.csr.utexas.edu/grace/operations/configuration.html, last access: 02/20/2014.

Davis, A. (2013). Personal Communication, at GRACE Science Team Meeting 2013 in Austin, Texas.

Doornbos, E. (2011). Thermospheric Density and Wind Determination from Satellite Dynamics. Dissertation, Technische Universiteit Delft, The Netherlands.

Doornbos, E. (2012). Personal Communication, TU Delft.

DuPont Co. (2013). Flouroplastic Comparison - Typical Properties. DuPont Company, Website http://www2.dupont.com/Teflon_Industrial/en_US/tech_info/techinfo_compare.html, last access 18/10/2013.

European Space Agency (2013). Models of spacecraft charging. SPENVIS, ESA, Belgian Institute for Space Aeronomy. http://www.spenvis.oma.be/help/background/charging/charging.html; last access: 16/10/2013.

Fackler, U. (2005). GRACE - Analyse von Beschleunigungsmessung. Diploma thesis, TU München.

Forsberg, R.; Skourup, H. (2005). Arctic Ocean gravity, geoid and sea-ice freeboard heights from ICE Sat and GRACE. Geophys. Res. Letters Vol 32, L21502, doi: 10.1029/2005GL023711.

Flury, J.; Bettadpur, S.; Tapley, B. D. (2008). Precise accelerometry onboard the GRACE gravity field satellite mission. Adv. in Space Research 42 (2008) 1414-1423.

Flury, J. (2011). Personal Communication, Leibniz Universität Hannover, 2011.

Frommknecht, B. (2007). Integrated Sensor Analysis of the GRACE Mission. Dissertation, Verlag der Bayerischen Akademie der Wissenschaften in Kommission beim Verlag C.H. Beck. ISBN 3 7696 5056 5.

Helmholtz-Zentrum GFZ Potsdam (2013). GFZ German Research Centre for Geosciences - The CHAMP Mission. Internet information websites dedicated to the CHAMP Mission, GFZ Potsdam. http://op.gfz-potsdam.de/champ/ - last access: 2013/07/16.

Goode, P.R.; Qiu, J.; Yurchychyn, V.; Hickey, J.; Chu, M.-C.; Kolbe, E.; Brown, C.T.; Koonin, S.E. (2001). Earthshine observations of the Earth's reflectance. Geophys. Res. Letters (Vol 28, Issue 9), 1671-1674. doi: 10.1029/2000GL012580.

Grunwaldt, L.; Bock, R. (2000). Heater Switching Procedure and Test Results. GFZ Potsdam, Technical Report CH-GFZ-TR-2201.

Herman, J.; Presti, D.; Codazzi, A.; Belle, C. (2004). Attitude Control for GRACE - The first Low-Flying Satellite Formation. European Space Agency, provided by the NASA Astrophysics Data System, 2004ESASP.548...27H.

Hudson, D. (2003). In-Flight Characterization and Calibration of the SuperSTAR Accelerometer. Master Thesis, Center for Space Research, The University of Texas at Austin.

Japan Aerospace Exploration Agency (2012). Design Standard - Spacecraft Charging and Discharging. JAXA, JERG-2-211A, Revision A. May 10, 2012.

Jørgensen J.L. (2000). In Orbit Performance of a fully Autonomous Star Tracker. Proceedings 4th ESA International Conference on Spacecraft Guidance, Navigation and Control Systems, ESTEC, 18-21 October 1999. ESA SP-425, Feb 2000.

Josselin, V.; Touboul, P.; Kielbasa, R. (1999). Capacitive detection scheme for space accelerometer applications. Sensors and Actuators 78 (1999) 92-98, Elsevier.

JPL (2002). GRACE Science & Mission Requirements Document. JPL CalTech Pasadena, Rept D-15928, Revision C, 2002.

Iijima, T.; Potemra, T.A. (1976). Field-Aligned Currents in the Dayside Cusp Observed by Triad. J. Geophys. Res., Vol. 81, No. 34, 5971-5979, Dec 1976.

JPL (2006). GRACE input/ output library file (GRACEiolib.h). JPL, version 1.78, 03/06/06.

Karslioglu, M. O. (2000). Probleme der Mess- und Regeltechnik bei der geodätischen Nutzung künstlicher Erdsatelliten. Dissertation, GFZ Potsdam, Scientific Technical Report STR00/06.

Kim, J. (2000). Simulation Study of a Low-Low Satellite-to-Satellite Tracking Mission. Dissertation, Center for Space Research, The University of Texas at Austin.

Knocke, P. C.; Ries, J. C.; Tapley, B. D. (1988). Earth Radiation Pressure Effects on Satellites. The American Institute of Aeronautics and Astronautics, 88-4292-CP, p. 577 ff., doi: 10.2514/6.1988-4292, 1988.

Kurek, J.; Bernstein, R.; Etheridge, M.; LaSalle, G.; McMahon, R.; Meiner, J.; Turner, N.; Walz, M.; Gomez, C. (2008). Aircraft Wiring Degradation Study. US Department of Transportation. Final Report, DOT/FAA/AR-08/2. Jan 2008.

Lubis, S. (2013). Mean Annual of Terrestrial Radiation (TAO) and Albedo. Personal Website, last access 06. September 2013, http://sandrolubis.wordpress.com/2012/04/29/mean-annual-of-global-outgoing-terrestrial-radiation-from-toa-clear-sky/

Marque, J.-P.; Christophe, B.; Liorzou, F.; Bodovillé, G.; Foulon, B.; Guérard, J.; Lebat, V. (2008). The Ultra Sensitive Accelerometers of the ESA GOCE Mission. IAC-08-B1.3.7.

Martin, A.R. (1991). Spacecraft/ Plasma Interactions and Electromagnetic Effects in LEO and Polar Orbits. Final Report for ESA/ESTEC Contract No. 7989/88/NL/PB(SC), Vol. 3, 1991.

Mazanek, D.; Kumar, R.; Qu, M.; Seywald, H. (2000). Aerothermal Analysis and Design of the Gravity Recovery and Climate Experiment (GRACE) Spacecraft. NASA Technical Memorandum, NASA/TM-2000-210095.

Meyer, M. (2000). Signalverarbeitung - Analoge und digitale Signale, Systeme und Filter. 2. Auflage, F. Vieweg & Sohn Verlagsgesellschaft mbH, Braunschweig/ Wiesbaden, 2000. ISBN 3-528-16955-9.

Mikaelian, T. (2001). Spacecraft Charging and Hazards to Electronics in Space. Physics of the Space Environment, York University, May 2001.

Morrison, J.; Wahr, J.; Kwok, R.; Peralta-Ferriz, C. (2007). Recent Trends in Arctic Ocean mass distribution revealed by GRACE. Geophys. Res. Letters Vol 34, L07602, doi: 10.1029/2006GL029016.

Ondoh, T.; Marubashi, K. (2001). Science of Space Environment. Ohmsha, Ltd., Japan; IOS Press. ISBN 4-427-90384-2 (Ohmsha), 2001.

ONERA (2013). Personal Communications with various staff members, Châtillon, France.

Optris GmbH (2013). Grundlagen der berührungslosen Temperaturmessung, Innovative Infrared Technology. IR-Broschüre-D2013-07-A, Optris GmbH, Berlin, Germany, 2013.

Perryman, M. A. C.; Lindegren, L.; Kovalevsky, J.; Hoeg, E.; Bastian, U.; Bernacca, P. L.; Crézé, M.; Donati, F.; Grenon, M.; Grewing, M.; van Leeuwen, F.; van der Marel, H.; Mignard, F.; Murray, C. A.; Le Poole, R. S.; Schrijver, H.; Turon, C.; Arenou, F.; Froeschlé, M.; Petersen, C. S. (1997). The HIPPARCOS Catalogue. Astronomy and Astrophysics 323, L49-L52, p. 620-633, 07/1997.

Peterseim, N. (2009). Bestimmung langperiodischer Massenvariationen aus GRACE Monatslösungen. Studienarbeit, Institut für Erdmessung, Leibniz Universität Hannover.

Peterseim, N. (2010). Acceleration Disturbances onboard of GRACE Satellites due to Magnetic Torquers. Diplomarbeit, Institut für Erdmessung, QUEST, Leibniz Universität Hannover.

Peterseim, N.; Flury, J.; Schlicht, A. (2012). Magnetic torquer induced disturbing signals within GRACE accelerometer data. Adv. in Space Research 49 (2012) No.9, 1388-1394, doi: 10.1016/j.asr.2012.02.013.

Ramillien, G.; Lombard, A.; Cazenave, A.; Ivins, E.R.; Llubes, M.; Remy, F.; Biancale, R. (2006). Interannual variations of the mass balance of the Antarctica and Greenland ice sheets from GRACE. Global and Planetary Change 53, 198-208, doi:10.1016/j.gloplacha.2006.06.003.

Reigber, C.; Lühr, H.; Grundwald, L.; Förste, C.; König, R.; Massmann, H.; Falck, C. (2006). CHAMP Mission 5 Years in Orbit. In Flury, J. et al., Observation of the Earth System from Space, Springer-Verlag Berlin Hamburg New York, ISBN 3-540-29520-8.

Rodríguez-Solano, C.J. (2009). Impact of Albedo Modelling on GPS Orbits. Master Thesis, Technische Universität München, November 2009.

Roesset, P. (2003). A simulation study of the use of accelerometer data in the GRACE mission. Dissertation, The University of Texas at Austin, December 2003.

Rummel, R.; Gruber, T. (2008). IMProved Acceleration modelling and Level 1 processing Alternative (IMPALA) - Long Time Series of Consistently Reprocessed High-Accuracy CHAMP/ GRACE Products (LOTSE-CHAMP/GRACE). Individual Proposal to "Erfassung des Systems Erde aus dem Weltraum" in the frame of the BMBF/DFG special Program "GEOTECHNOLOGIEN", IAPG, TU München, 2008.

Schwartz, J. (2005). High Tech in the 70's, Shuttles Feel Their Age. The New York Times, Science section, published July 25, 2005.

Seeber, G. (2003). Satellite Geodesy: Foundations, Methods, and Applications. de Gruyter, ISBN-10: 3110175495.

Sharma, B. S. (1968). Laser Induced Dielectric Breakdown and Mechanical Damage in Silicate Glass. Dissertation, Simon Fraser University, Sep 1968.

Space Systems/ Loral (1998). GRACE Attitude and Orbit Control System (AOCS) Specification and Description. Tecnical Report, Version 3.0, Draft, 327-440.

Stanton, R. (2000). Functional Specification of the Twin GRACE Satellites. JPL Technical Report, GRACE-327-220.

Steffen, H.; Müller, J.; Peterseim, N. (2009). Mass variations in the Siberian permafrost region from GRACE. U. J. (eds.) Geodesy for Planet Earth, IAG Symposia, Vol. 136, pp 597-603, Springer, ISBN (Print) 978-3-642-20337-4, doi:10.1007/978-3-642-20338-1_73.

Stoer, J. (2005). Numerische Mathematik. 9th Version, Springer-Verlag Berlin u.a., ISBN 3-540-21395-3, 2005.

Thomas, J.B. (1999). An Analysis of Gravity-Field Estimation Based on Intersatellite Dual-1-Way Biased Ranging. JPL Publication 98-15.

Tipirneni, R.R. (2008). Characterization of Thermal and Electrical Properties of Fiber Reinforced Polymer (FRP) Composites. Master Thesis, College of Engineering and Mineral Ressources, West Virginia University, 2008.

Touboul, P.; Foulon, B.; Willemenot, E. (1998). Electrostatic Space Accelerometers for present and future Mission. Acta Astronautica Vol. 45, No. 10, 605-617.

Touboul, P. (2001). Space Accelerometers: Present Status. In Lämmerzahl, C. et al. (2001). LNP 562, pp. 273-291, 2001. Springer-Verlag Berlin Heidelberg.

Velicogna, I.; Wahr, J. (2005). Greenland mass balance from GRACE. Geophys. Res. Letters Vol 32, L18505, doi: 10.1029/2005GL023955.

Wahr, J.; Swenson, S.; Velicogna, I. (2006). Accuracies of GRACE mass estimates. Geophys. Res. Letters Vol 33, L06401. doi: 10.1029/2005GL025305.

Wang, F. (2003). Study on Center of Mass Calibration and K-Band Ranging System Calibration of the GRACE Mission. Dissertation, Center for Space Research, The University of Texas at Austin.

Wang, H.; Wang, Z.; Yuan, X.; Wu, P.; Rangelova, E. (2007). Water storage changes in Three Gorges Water Systems are inferred from GRACE time-variable gravity data. Unpublished english translation.

Wentink, T.; Planet W. G. (1961). Infrared Transmittance and Emittance of Polytetraflouroethylene. Journal of the Optical Society of America, Vol. 51, No. 6, p. 601-602, June 1961.

Wertz, J.R. (1991). Spacecraft Attitude Determination and Control. Kluwer Academic Publishers, Dordrecht/ Boston/ London.

Willemenot, E.; Touboul, P. (2000). On-ground investigation of space accelerometers noise with an electrostatic torsion pendulum. Rev. Sci. Instrum. Vol 71, 302. doi: 10.1063/1.1150197.

Witkowski, M.; Massmann, F.-H. (2012). Status GRACE Mission Operations. Presentation at GRACE Science Team Meeting, September 17 2012 in Potsdam, Germany, last access 2013/01/29 on http://www.gfz-potsdam.de/portal/gfz/Neuestes/Veranstaltungen/
Tagungen+und+Konferenzen/2012/GRACE+Meeting/
GRACE+meeting_Startseite/proceedings.

Wu, S.-C.; Kruizinga, G.; Bertinger, W. (2006). Algorithm Theoretical Basis Document for GRACE Level-1B Data Processing V1.2. Tech. Rep. JPL D-27672, JPL.

Wylie, D. P.; Menzel, W. P.; Woolf, H. M.; Strabala, K. I. (1994). Four Years of Global Cirrus Cloud Statistics Using HIRS. Journal of Climate, Vol. 7, No. 12, p. 1972-1986, Dec 1994.

Zheng, W.; Hsu, H,; Zhong, M.; Yun M.-J.; Zhou, X.-H.; Peng, B.-B. (2009). Influence of the Adjusted Accuracy of Center of Mass between GRACE Satellite and SuperSTAR Accelerometer on the Accuracy of Earth's Gravitational Field. Chin. J. Geophys. Vol. 52, No. 3, 564-574.

Zumberge J.F.; Hajj, G.; Lichten, S.M.; Meehan, T.K. (2003). The NASA/JPL BlackJack GPS Receiver on CONAE's SAC-C Mission. JPL Presentation, November 2003, http://trs-new.jpl.nasa.gov/dspace/bitstream/2014/38598/1/03-3217.pdf (last access 2013/01/15).

List of abbreviations

ACC	Accelerometer
ACC ICU	Accelerometer Interface Control Unit
ACC SU	Accelerometer Sensor Unit
ACC1A	Level-1A Accelerometer Data
ACC1B	Level-1B Accelerometer Data
ACT	Time tag corrected accelerometer data by CSR
AF	Acceleration Frame
AHM	Attitude Hold Mode
AOCS	Attitude and Orbit Control System
ARF	Accelerometer Reference Frame
ASC	Advanced Stellar Compass
ASTRE	Accéléromètre Spatial TRiaxial Electrostatique
AT	Along Track
CACTUS	Capteur Accéléromètrique Capacitif Triaxial Ultra Sensible
CESS	Coarse Earth-Sun Sensor
CFRP	Carbon-fiber-reinforced polymer
CHAMP	Challenger Mini-Satellite Payload for Geophysical Research and Application
CLK	Clock correction data file
COM	Center of mass
CPM	Coars Pointing Mode
CRN	N self-convolutions of a rectangular time-domain window function
C/A	Coarse/ Acquisition (GPS Frequency Mode)
CFRP	Carbon-Fibre Reinforced Plastics
CHU	Camera Head Unit of the ASC
CSR	Center for Space Research, University of Texas at Austin
CT	Cross Track
d/o	Degree / Order
DC	Direct Current
DLR	Deutsches Zentrum für Luft- und Raumfahrt
DOY	Day of year
DPU	Data Processing Unit of the ASC
DTU	Technical University of Denmark (Danmarks Tekniske Universitet)
EEU	Electromagnetic Exiter Unit (Accelerometer)

EGM96	Earth Gravitational Model 1996
ESSP	Earth System Science Pathfinders
ESA	European Space Agency
FPM	Fine Pointing Mode
GEO	Geosynchronous Orbit
GFZ	Helmholtz Zentrum Potsdam, GeoForschungsZentrum Potsdam
GOCE	Gravity Field and Steady-State Ocean Circulation Explorer
GPS	Global Positioning System
GPS NAV	GPS Navigation Antenna
GPS BKUP	GPS BackUp Antenna
GPS OCC	GPS Occultation Antenna
GRACE	Gravity Recovery and Climate Experiment
HIPPARCOS	High Precision Parallax Collecting Satellite
ICRS	International Celestial Reference System
ICU	Interface Control Unit (Accelerometer)
IfE	Institut für Erdmessung (Institute of Geodesy), Leibniz Universität Hannover
IPU	Instrument processing unit
IRU	Inertial Reference Unit
ISDC	Integrated System Data Center
ITRF	Inertial Terrestrial Reference Frame
JPL	Jet Propulsion Laboratory, California Institute of Technology
KBR	K-Band-Ranging System
LEO	Low Earth Orbit Satellite
LoS	Line of sight
LT	Local Time
MAG	Magnetometer and magnetorquer data file
MESA	Miniature ElectroStatic Accelerometer
MLT	Magnetic Local Time
MTE	Center of Mass Trim assembly Electronics
MTM	Center of Mass Trim assembly Mechanism
MTQ	Magnetic Torquer
NASA	National Aeronautics and Space Administration
OARE	Orbital Acceleration Research Experiment
OBDH	OnBoard Data Handling
ONERA	Office National d'Études et de Recherches Aérospatiales (France)

P/Y	Precise/ encrypted (GPS Frequency Mode)
PCDU	Power Control and Distribution Unit
PEO	Polar Earth Orbit
PM	proof-mass of an accelerometer
PO.DAAC	Physical Oceanography Distributed Active Data Center
PSD	Power Spectral Density
QSAM	Quasi-Steady Acceleration Measurement
R	Radial
RFEA	Radio Frequency and Electronics Assembly
SCA	Star Camera Assembly sensor
SM	Science Mode
SMRD	GRACE Science Mission Requirements Document
SRF	Satellite Reference Frame
SSRF	Star Sensor Reference Fram
STAR	Space Three-Axis Accelerometer for Research
STS	Space Transportation System (Columbia Space Shuttle)
THR	Thruster data file
TUM	Technische Universität München
USO	Ultra Stable Oscillator
US	United States of America
UT	University of Texas
ZARM	Center of Applied Space Technology and Microgravity (Zentrum für angewandte Raumfahrttechnologie und Mikrogravitation)

Acknowledgements

First of all I would like to thank professor Roland Pail for his unconditional support and the helpful discussions. Whenever in doubt, he had an interesting idea or comment or simply a plain compliment that re-encouraged me to carry on with my work.

The next person I want to thank is Dr. Anja Schlicht, who has been my mentor throughout the years and is probably the person who helped me most to advance with my work. She is the person I always bugged first when I had a thought in mind I needed to discuss or simply (which is worse) when I had no thought at all and felt stuck.

Professor Srivinvas Bettadpur from the Center for Space Research at the University of Texas at Austin gave me the opportunity to carry out a great deal of my investigations at his facility and deserves special thanks. At CSR I could make use of a lot more GRACE data than I could ever dream of (and besides - I had a great time in Texas). In addition, I would like to thank the whole CSR staff - thanks to you this was a very smooth stay and time.

Thank you Pieter Visser from TU Delft, who agreed to be the second supervisor of my thesis and probably spent a lot of time finding logical errors in my work. In addition, professor Urs Hugentobler from FESG at TU Munich deserves many thanks, as he proof read a great part of the thesis in detail long before it was done and helped me to figure out weaknesses. Furthermore, thanks for being the third supervisor. Also from TU Delft, my warmest thanks go out to Dr. Eelco Doornbos, who helped me a lot with the model of the GRACE satellites and helped me out with a dataset that I could use in order to determine which surface was eclipsed at what time. You saved me an unfathomable amount of time!

A great deal of my skills can be traced back to my former mentor and professor Jakob Flury from IfE at the Leibniz Universtät Hannover, who trained me in days where I was working on my diploma thesis. Also, I had countless discussions with him in the frame of this thesis as well, and many of his ideas opened my eyes. I do not think that I could have come up with the hypothesis stated in this work without Jakob. The latter also applies for his former student Guy Apelbaum.

The staff of ONERA around Bernard Foulon helped me understand how the accelerometer works and tried to help me understand how signals might couple into the accelerometer. The GRACE group at Astrium arranged a few meetings, which worked like a think tank for me, and where we could exchange ideas.

Even if he does not know it, I probably need to thank Dr. Björn Frommknecht as I made use of his Level 1B processing software he developed at his time at IAPG. That did save a lot of time, and there is no need to reinvent the wheel.

Moreover, thanks to Frank Flechtner and Christoph Dahle from GFZ, with whom I worked together in the frame of the BMBF project, that had been the initial stimulus to carry out my investigations, and who were able to determine a possible impact of my findings on the gravity field (even if my findings where wrong at that time...).

Now, I would like to thank anyone I did not mention yet. There have been many people I met along the way that helped me progress with my work. Last but not least all my colleagues at IAPG here at TU München, who either helped me out with my problems or simply made me laugh and thus made my day. I sincerely did have a great time!

Thanks y'all!

Appendix

In the appendix we display a range of figures that may help to understand the conclusions drawn the work. In our work we only display chosen figures to illustrate the stated observation as good as possible. However, all statements made are based on a broader range of images. These figures are displayed by means of the year 2008 as most observations correspond to this year. Furthermore, all twangs are displayed by means of the radial component, except for section Appendix C, where we displayed all parameters also with respect to the axes.

In the following we make a distinction between seasonal impact and local time. However, it is not clearly possible to distinct between local time and season and only a chosen selection can be displayed. Furthermore, we try to display both GRACE A and B satellites.

In section Appendix C we display the distribution of twangs by means of the argument of latitude with respect to the day of year, either corresponding to the year 2008 or the whole range of available data from 2002 to 2010.

The last section displays the illuminated surfaces of the GRACE spacecraft corresponding to the investigated twangs.

Each series of figures in the sections of the appendix may be regarded as an observation concerning the orientation of twangs between the two GRACE spacecraft or the differing orientation of twangs between the different axes.

A Seasonal impact

A.1 Year 2008, Local time 0-1 hour

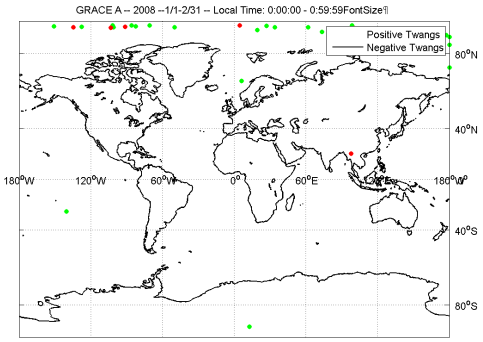

Figure A.1: Twangs, GRACE A, Jan-Feb 2008, LT 0-1h.

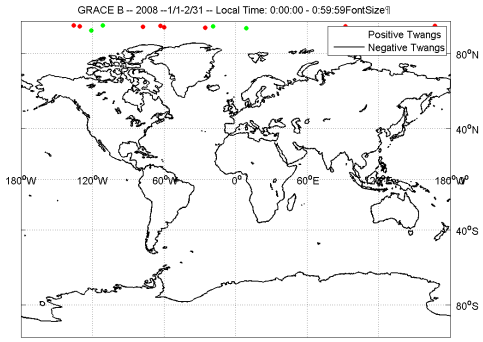

Figure A.2: Twangs, GRACE B, Jan-Feb 2008, LT 0-1h.

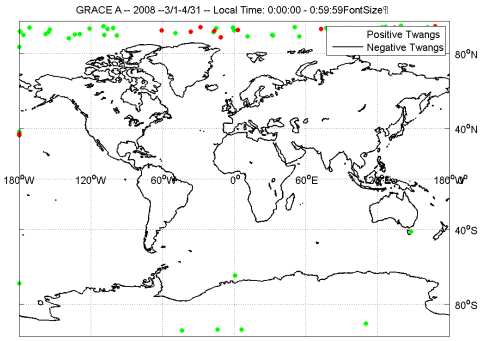

Figure A.3: Twangs, GRACE A, Mar-Apr 2008, LT 0-1h.

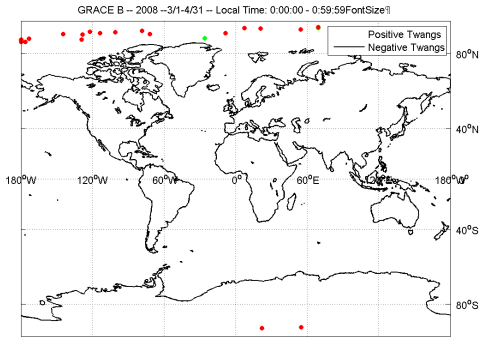

Figure A.4: Twangs, GRACE B, Mar-Apr 2008, LT 0-1h.

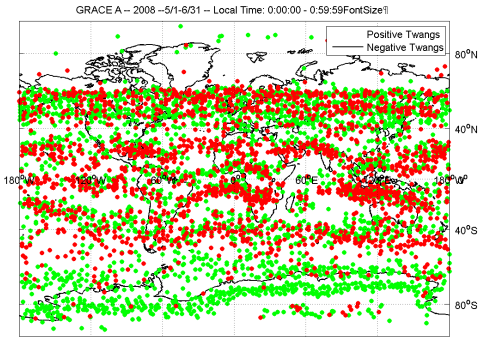

Figure A.5: Twangs, GRACE A, May-Jun 2008, LT 0-1h.

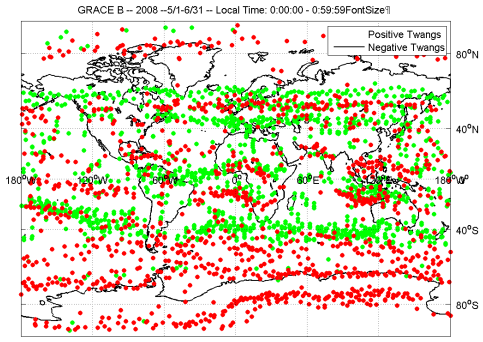

Figure A.6: Twangs, GRACE B, May-Jun 2008, LT 0-1h.

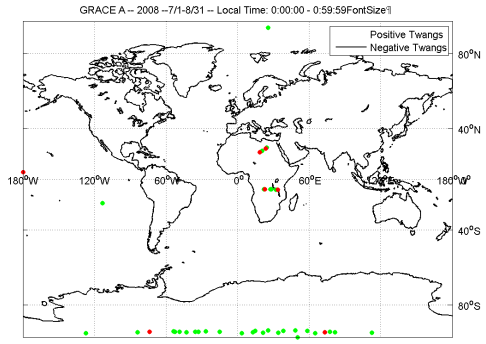

Figure A.7: Twangs, GRACE A, Jul-Aug 2008, LT 0-1h.

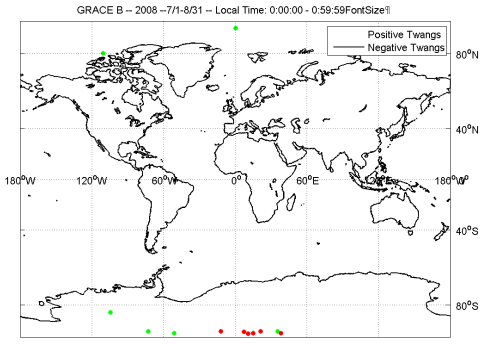

Figure A.8: Twangs, GRACE B, Jul-Aug 2008, LT 0-1h.

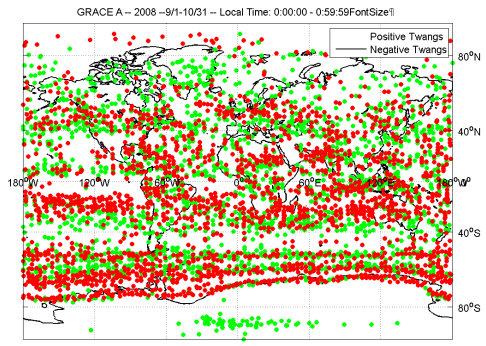

Figure A.9: Twangs, GRACE A, Sep-Oct 2008, LT 0-1h.

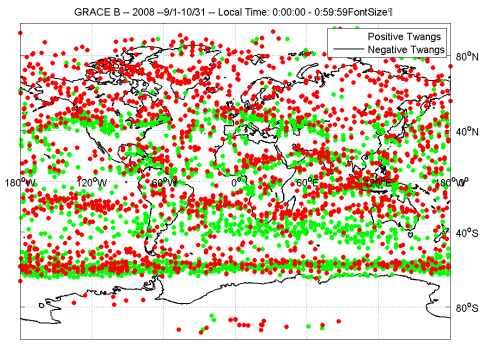

Figure A.10: Twangs, GRACE B, Sep-Oct 2008, LT 0-1h.

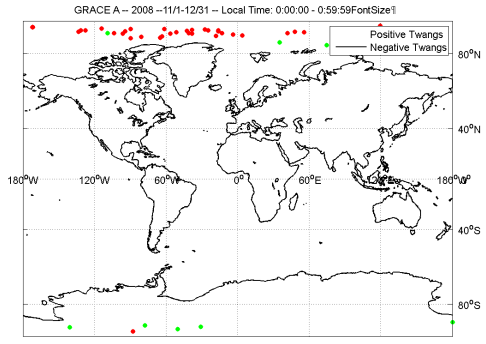

Figure A.11: Twangs, GRACE A, Nov-Dec 2008, LT 0-1h.

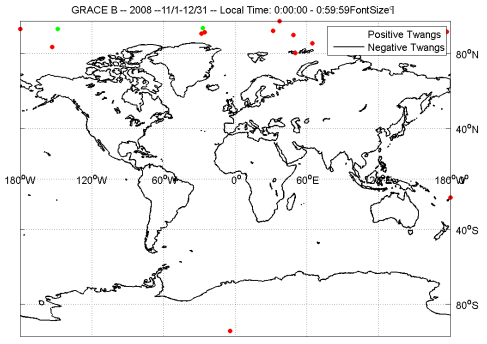

Figure A.12: Twangs, GRACE B, Nov-Dec 2008, LT 0-1h.

A.2 Year 2008, Local time 12-13 hour

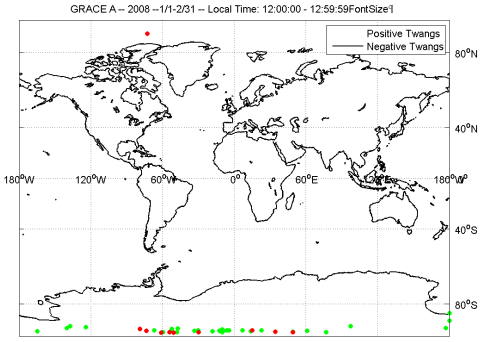

Figure A.13: Twangs, GRACE A, Jan-Feb 2008, LT 12-13h.

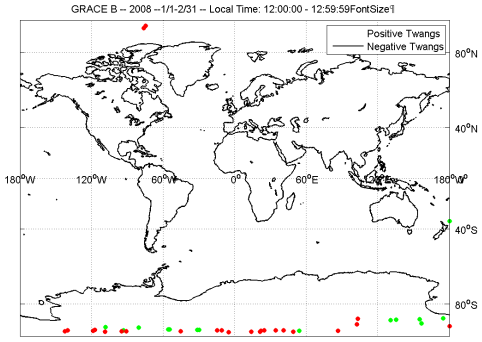

Figure A.14: Twangs, GRACE B, Jan-Feb 2008, LT 12-13h.

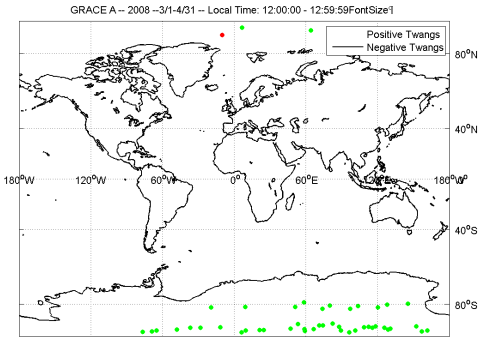

Figure A.15: Twangs, GRACE A, Mar-Apr 2008, LT 12-13h.

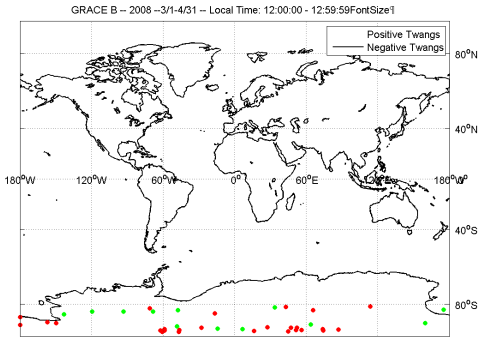

Figure A.16: Twangs, GRACE B, Mar-Apr 2008, LT 12-13h.

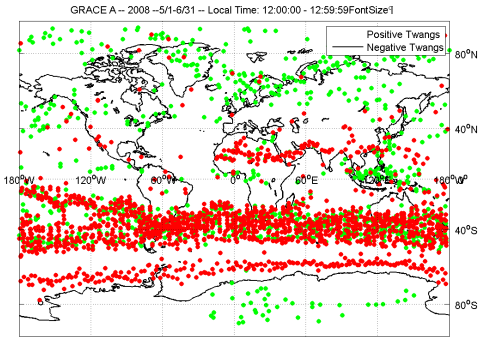

Figure A.17: Twangs, GRACE A, May-Jun 2008, LT 12-13h.

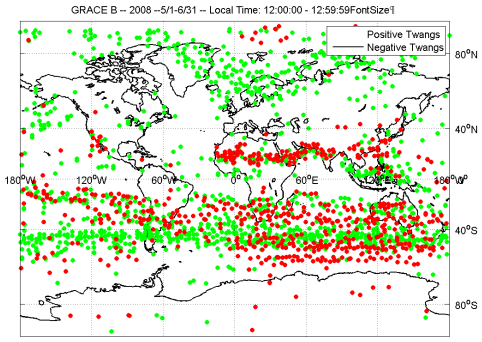

Figure A.18: Twangs, GRACE B, May-Jun 2008, LT 12-13h.

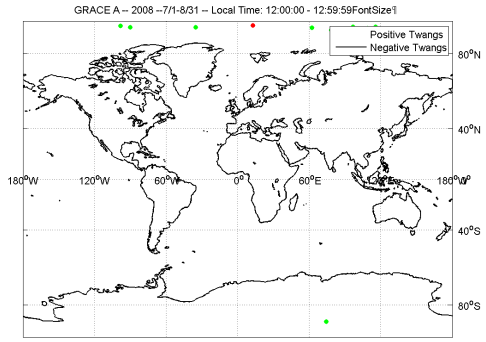

Figure A.19: Twangs, GRACE A, Jul-Aug 2008, LT 12-13h.

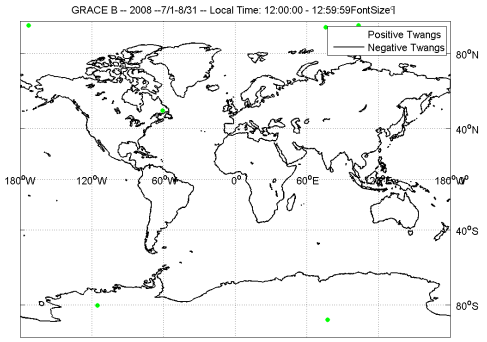

Figure A.20: Twangs, GRACE B, Jul-Aug 2008, LT 12-13h.

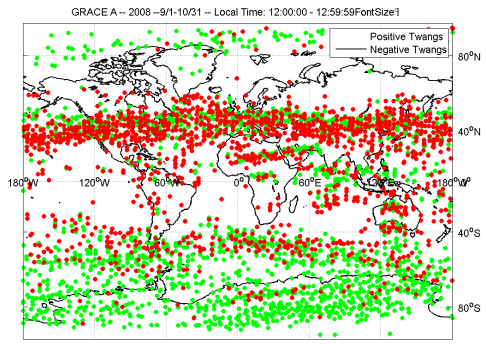

Figure A.21: Twangs, GRACE A, Sep-Oct 2008, LT 12-13h.

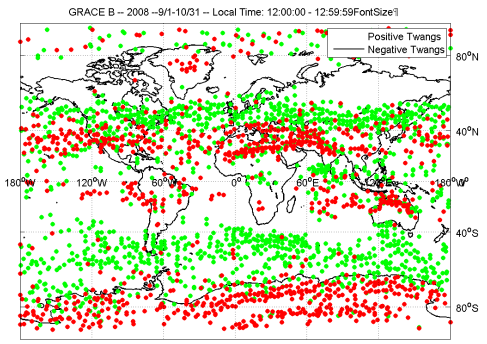

Figure A.22: Twangs, GRACE B, Sep-Oct 2008, LT 12-13h.

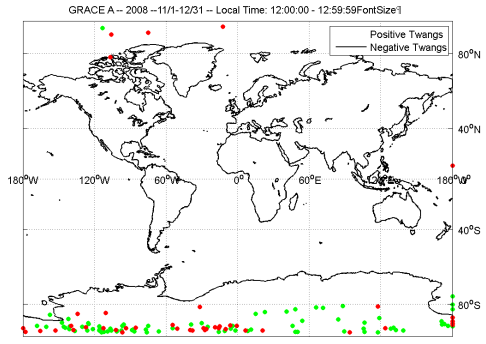

Figure A.23: Twangs, GRACE A, Nov-Dec 2008, LT 12-13h.

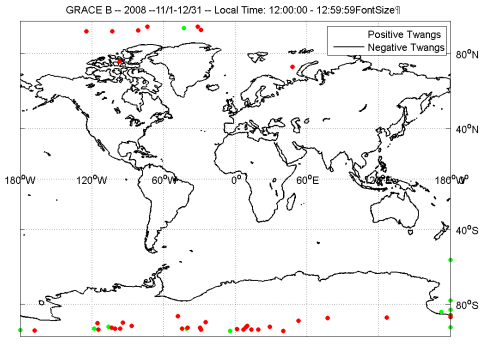

Figure A.24: Twangs, GRACE B, Nov-Dec 2008, LT 12-13h.

B Twang distribution due to local time

B.1 GRACE A, March to April 2008, Local time 0-23 h

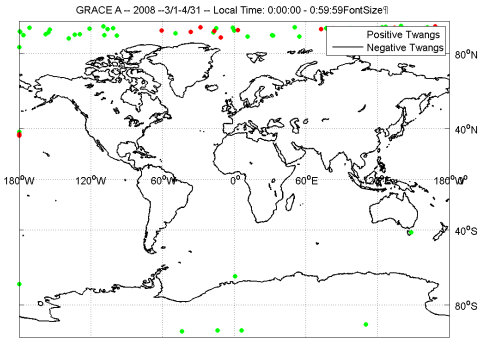

Figure B.1: Twangs, GRACE A, Mar-Apr 2008, LT 0-1h.

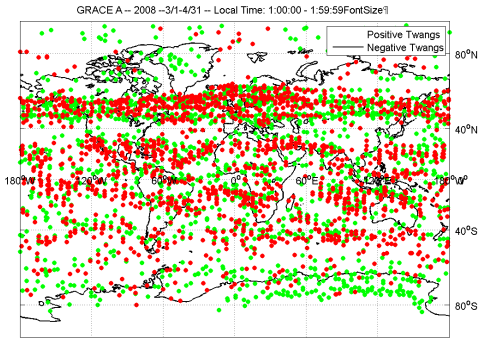

Figure B.2: Twangs, GRACE A, Mar-Apr 2008, LT 1-2h.

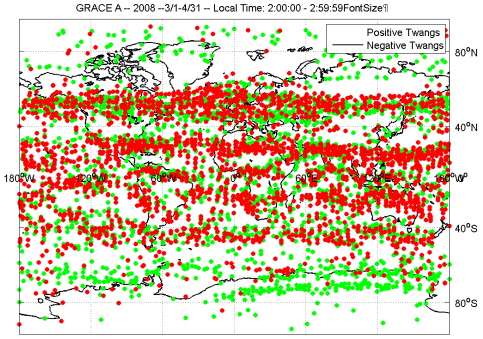

Figure B.3: Twangs, GRACE A, Mar-Apr 2008, LT 2-3h.

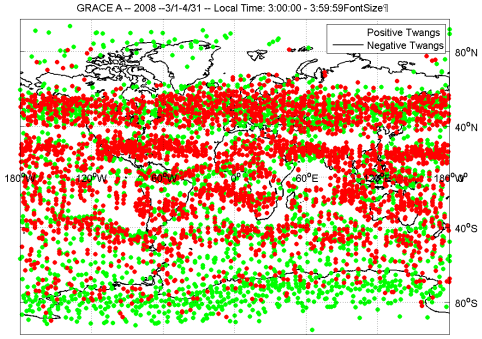

Figure B.4: Twangs, GRACE A, Mar-Apr 2008, LT 3-4h.

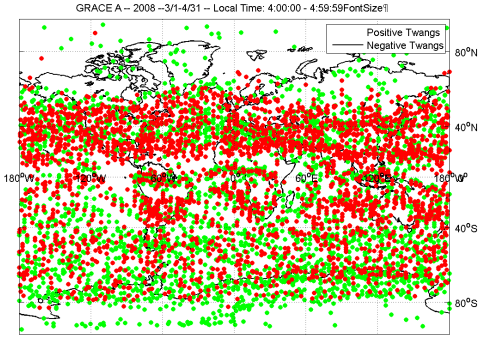

Figure B.5: Twangs, GRACE A, Mar-Apr 2008, LT 4-5h.

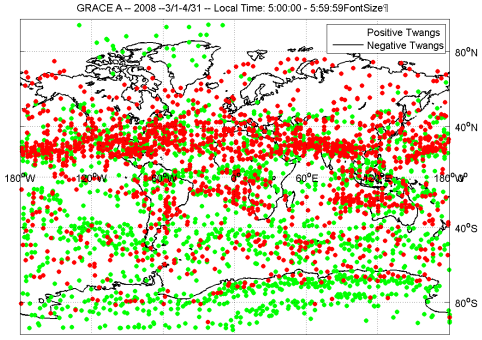

Figure B.6: Twangs, GRACE A, Mar-Apr 2008, LT 5-6h.

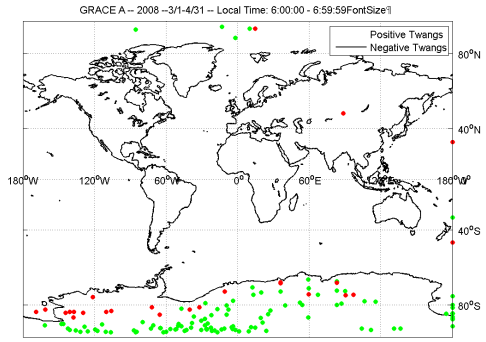

Figure B.7: Twangs, GRACE A, Mar-Apr 2008, LT 6-7h.

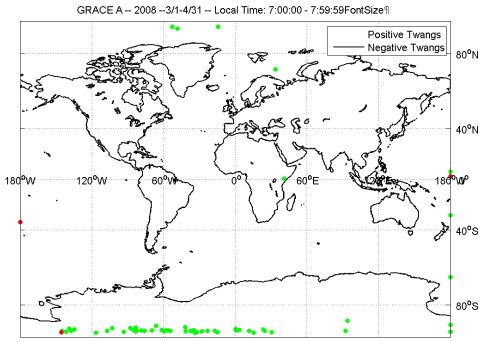

Figure B.8: Twangs, GRACE A, Mar-Apr 2008, LT 7-8h.

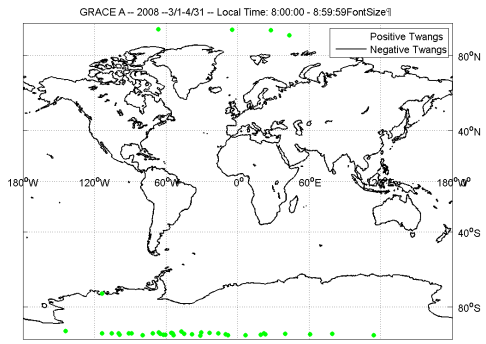

Figure B.9: Twangs, GRACE A, Mar-Apr 2008, LT 8-9h.

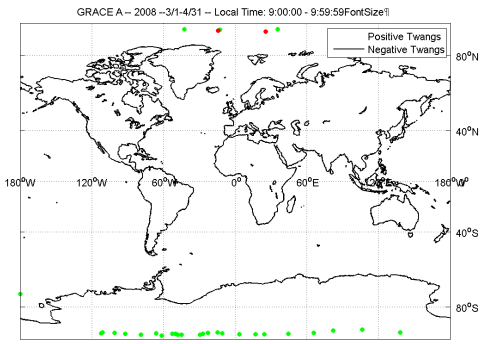

Figure B.10: Twangs, GRACE A, Mar-Apr 2008, LT 9-10h.

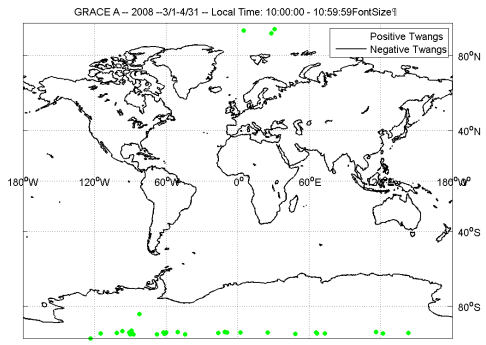

Figure B.11: Twangs, GRACE A, Mar-Apr 2008, LT 10-11h.

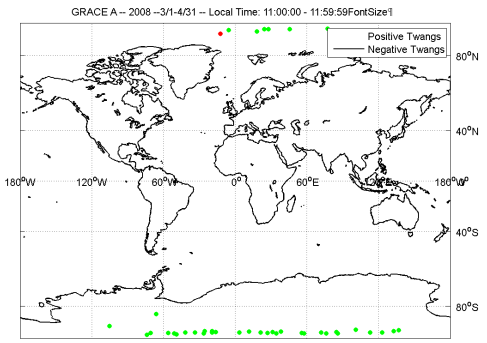

Figure B.12: Twangs, GRACE A, Mar-Apr 2008, LT 11-12h.

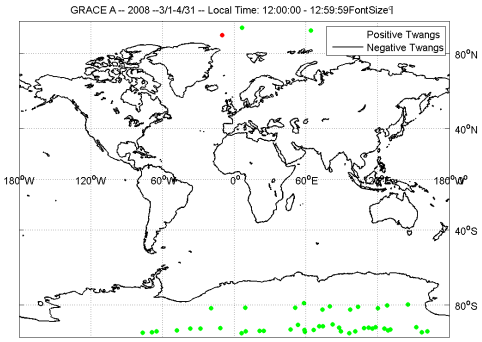

Figure B.13: Twangs, GRACE A, Mar-Apr 2008, LT 12-13h.

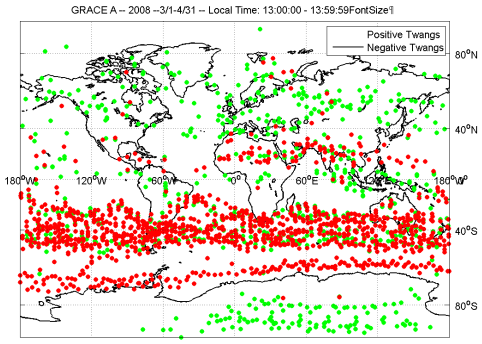

Figure B.14: Twangs, GRACE A, Mar-Apr 2008, LT 13-14h.

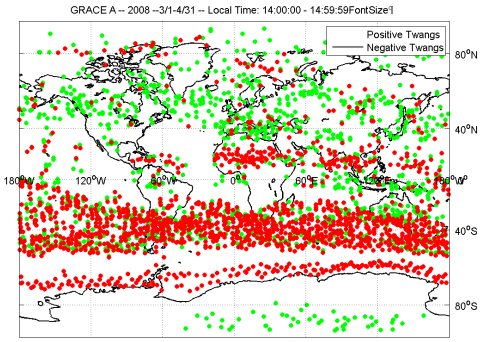

Figure B.15: Twangs, GRACE A, Mar-Apr 2008, LT 14-15h.

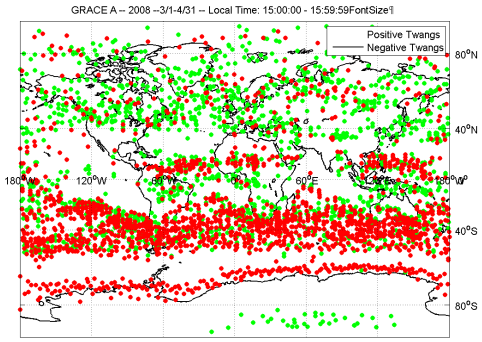

Figure B.16: Twangs, GRACE A, Mar-Apr 2008, LT 15-16h.

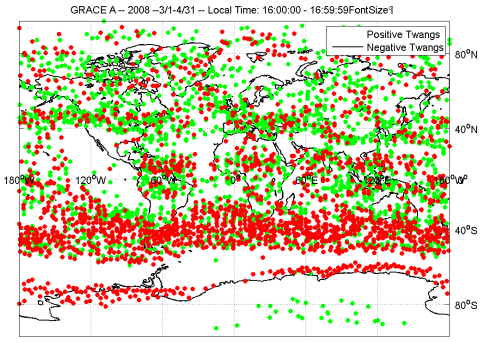

Figure B.17: Twangs, GRACE A, Mar-Apr 2008, LT 16-17h.

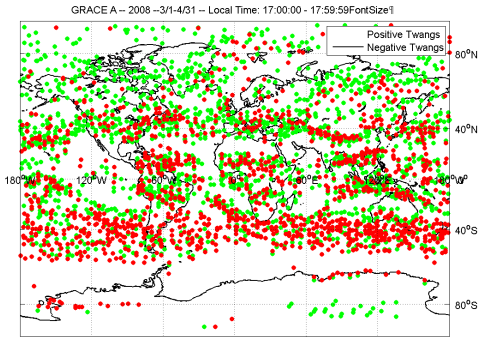

Figure B.18: Twangs, GRACE A, Mar-Apr 2008, LT 17-18h.

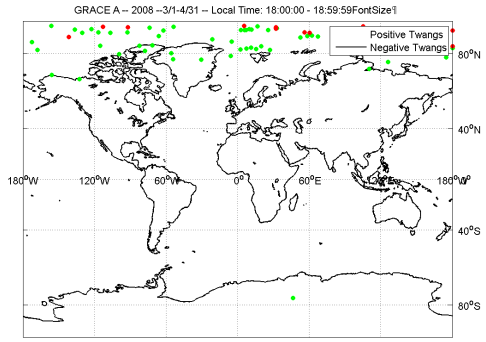

Figure B.19: Twangs, GRACE A, Mar-Apr 2008, LT 18-19h.

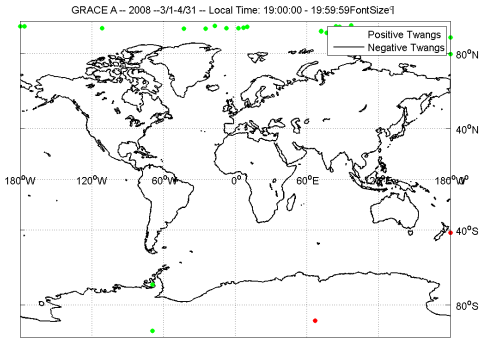

Figure B.20: Twangs, GRACE A, Mar-Apr 2008, LT 19-20h.

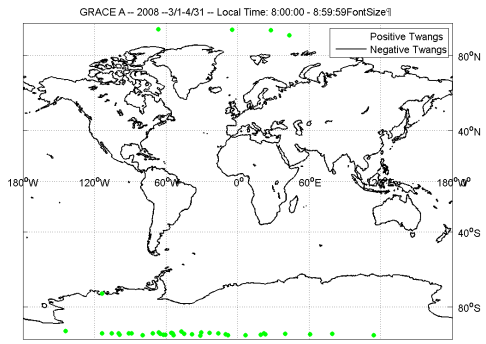

Figure B.21: Twangs, GRACE A, Mar-Apr 2008, LT 20-21h.

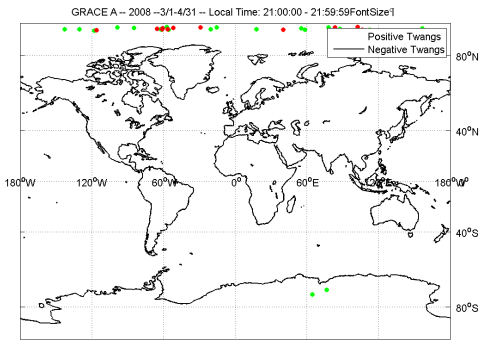

Figure B.22: Twangs, GRACE A, Mar-Apr 2008, LT 21-22h.

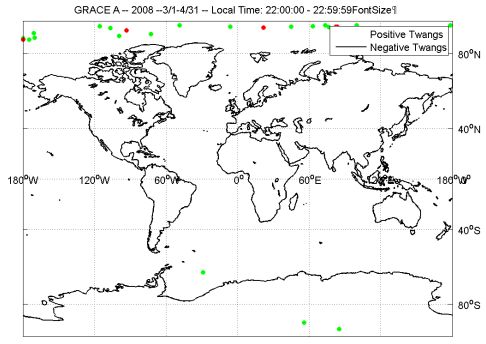

Figure B.23: Twangs, GRACE A, Mar-Apr 2008, LT 22-23h.

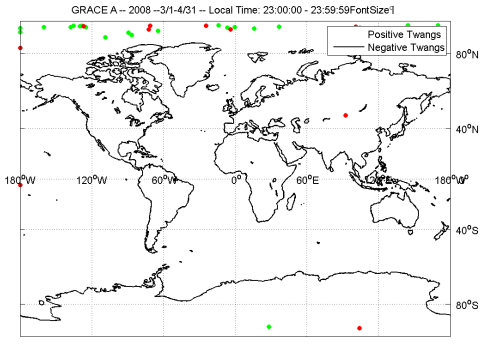

Figure B.24: Twangs, GRACE A, Mar-Apr 2008, LT 23-0h.

B.2 GRACE B, September to October 2008, Local time 0-23 h

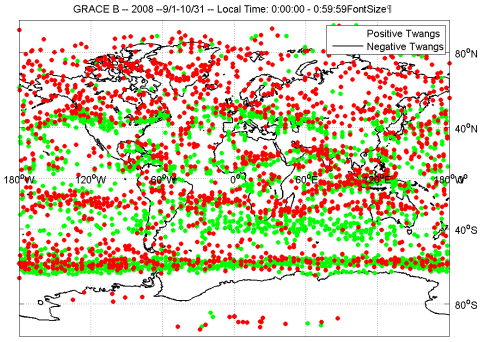

Figure B.25: Twangs, GRACE B, Sep-Oct 2008, LT 0-1h.

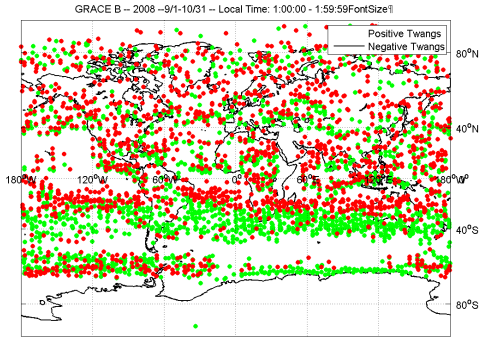

Figure B.26: Twangs, GRACE B, Sep-Oct 2008, LT 1-2h.

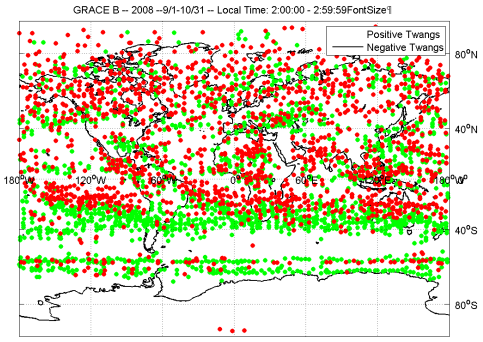

Figure B.27: Twangs, GRACE B, Sep-Oct 2008, LT 2-3h.

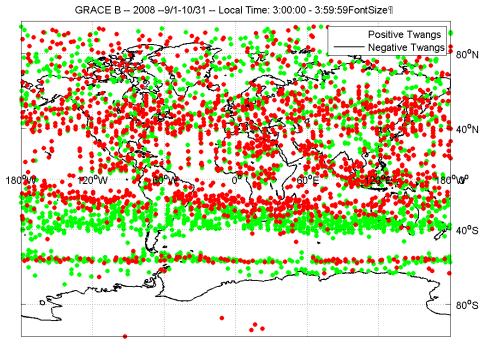

Figure B.28: Twangs, GRACE B, Sep-Oct 2008, LT 3-4h.

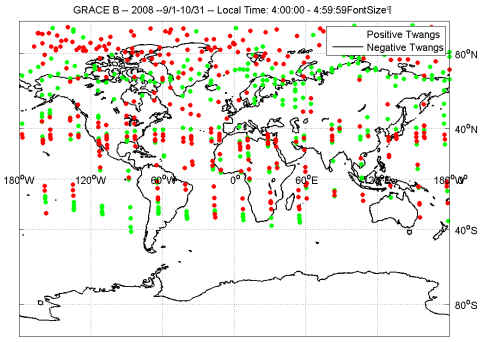

Figure B.29: Twangs, GRACE B, Sep-Oct 2008, LT 4-5h.

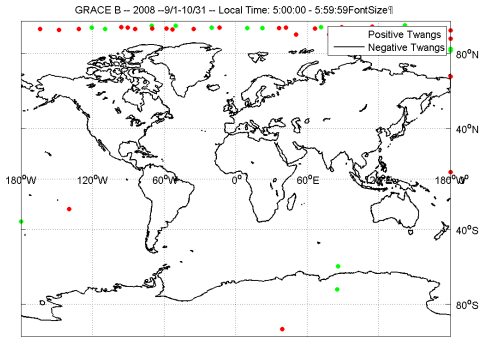

Figure B.30: Twangs, GRACE B, Sep-Oct 2008, LT 5-6h.

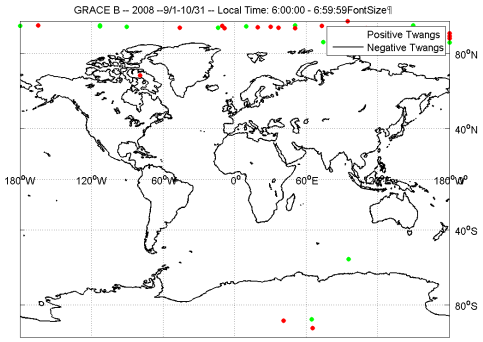

Figure B.31: Twangs, GRACE B, Sep-Oct 2008, LT 6-7h.

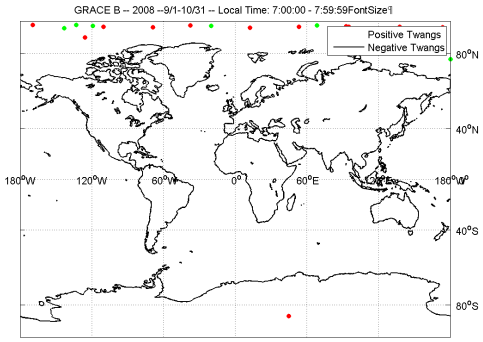

Figure B.32: Twangs, GRACE B, Sep-Oct 2008, LT 7-8h.

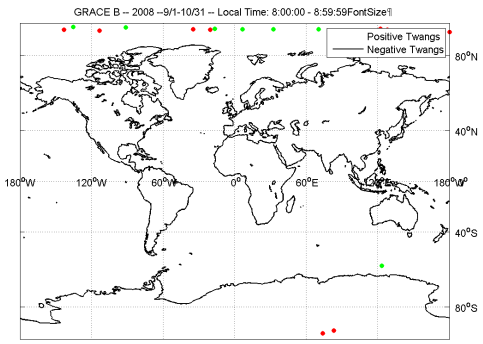

Figure B.33: Twangs, GRACE B, Sep-Oct 2008, LT 8-9h.

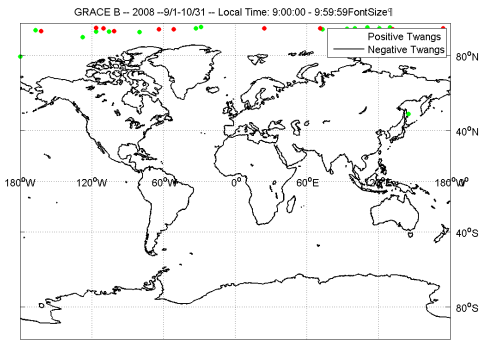

Figure B.34: Twangs, GRACE B, Sep-Oct 2008, LT 9-10h.

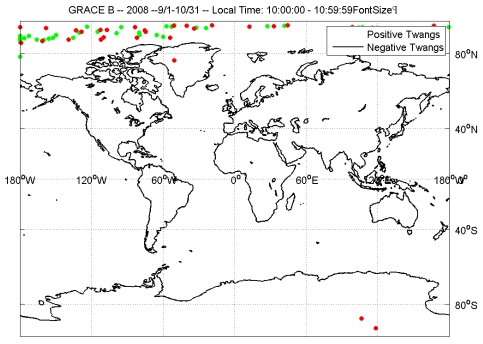

Figure B.35: Twangs, GRACE B, Sep-Oct 2008, LT 10-11h.

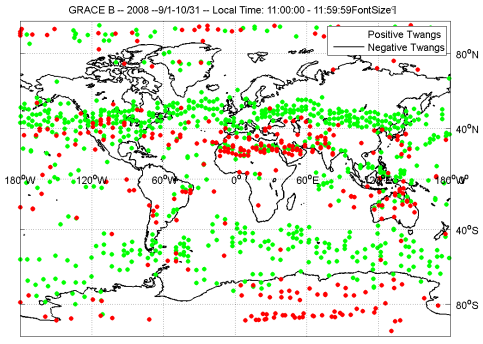

Figure B.36: Twangs, GRACE B, Sep-Oct 2008, LT 11-12h.

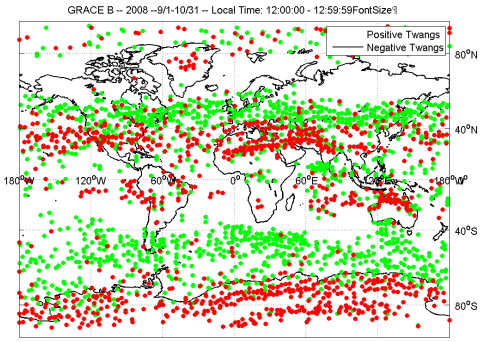

Figure B.37: Twangs, GRACE B, Sep-Oct 2008, LT 12-13h.

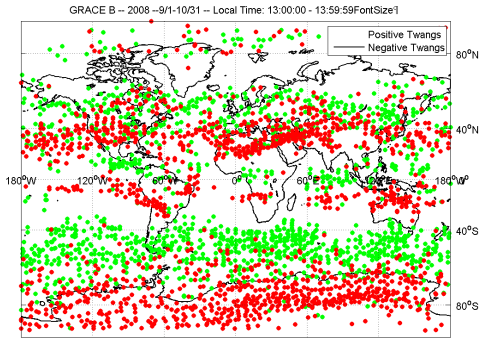

Figure B.38: Twangs, GRACE B, Sep-Oct 2008, LT 13-14h.

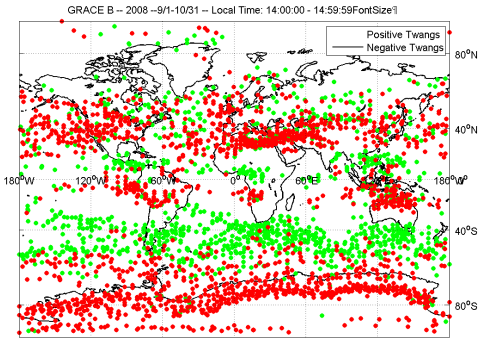

Figure B.39: Twangs, GRACE B, Sep-Oct 2008, LT 14-15h.

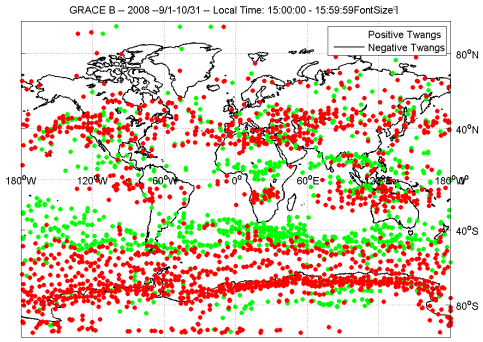

Figure B.40: Twangs, GRACE B, Sep-Oct 2008, LT 15-16h.

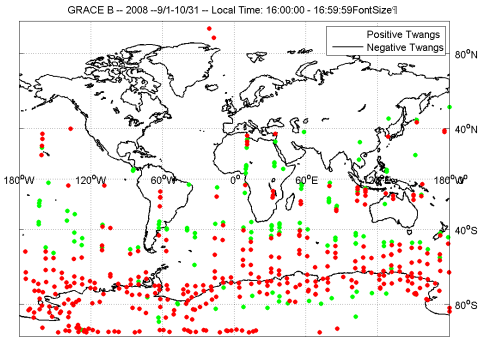

Figure B.41: Twangs, GRACE B, Sep-Oct 2008, LT 16-17h.

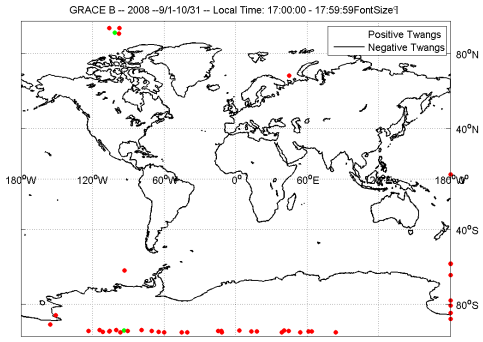

Figure B.42: Twangs, GRACE B, Sep-Oct 2008, LT 17-18h.

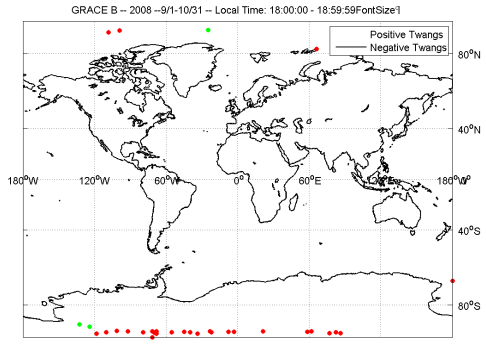

Figure B.43: Twangs, GRACE B, Sep-Oct 2008, LT 18-19h.

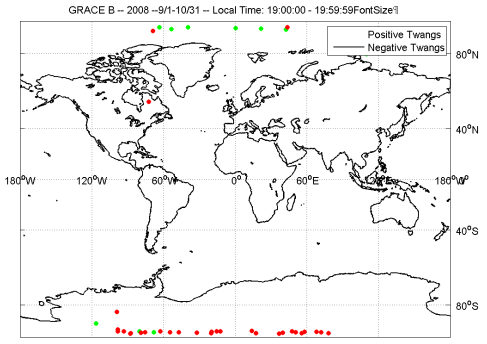

Figure B.44: Twangs, GRACE B, Sep-Oct 2008, LT 19-20h.

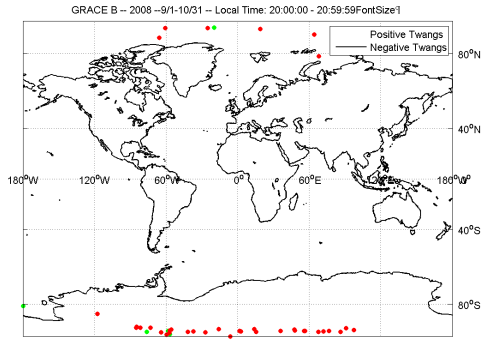

Figure B.45: Twangs, GRACE B, Sep-Oct 2008, LT 20-21h.

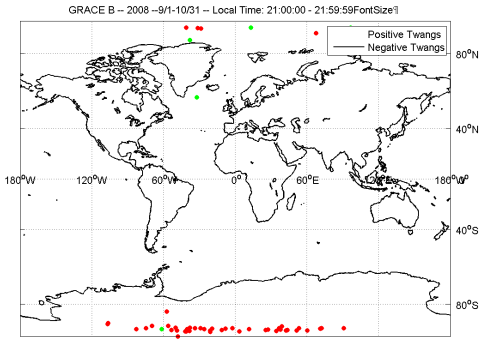

Figure B.46: Twangs, GRACE B, Sep-Oct 2008, LT 21-22h.

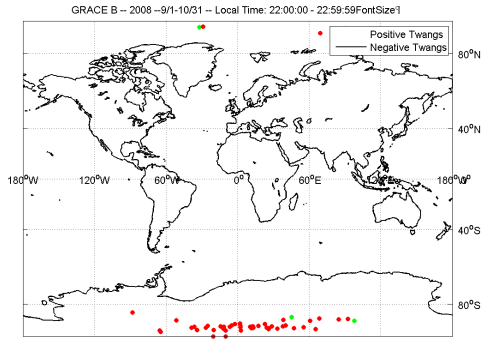

Figure B.47: Twangs, GRACE B, Sep-Oct 2008, LT 22-23h.

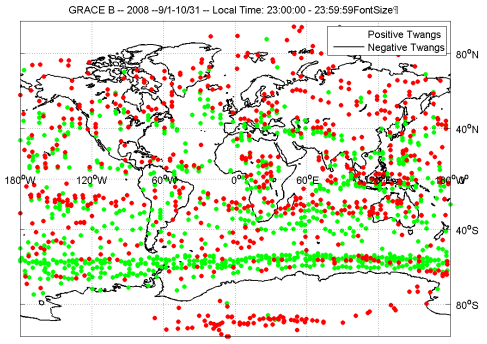

Figure B.48: Twangs, GRACE B, Sep-Oct 2008, LT 23-0h.

C Parameter behaviour - DOY vs. argument of latitude

This chapter of the appendix will display the behaviour of the parameters previously introduced and determined in chapter 8.3.

C.1 Local Time of Twangs

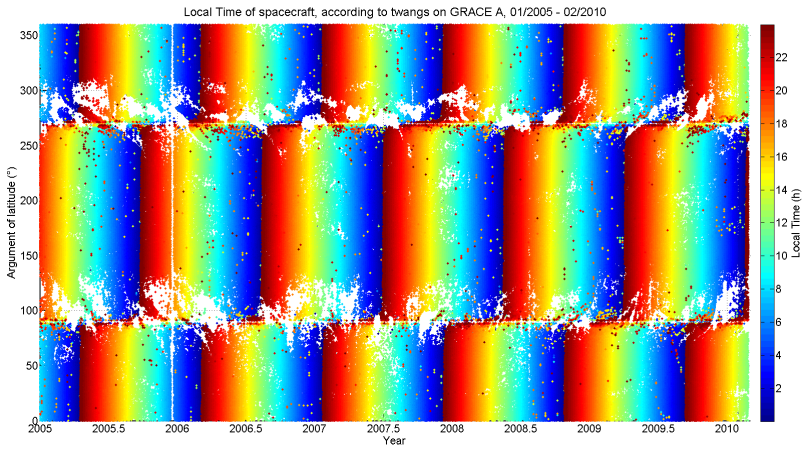

Figure C.1: Local time of twangs, according to twangs in radial component, GRACE A.

C.2 Orientation

C.2.1 GRACE A

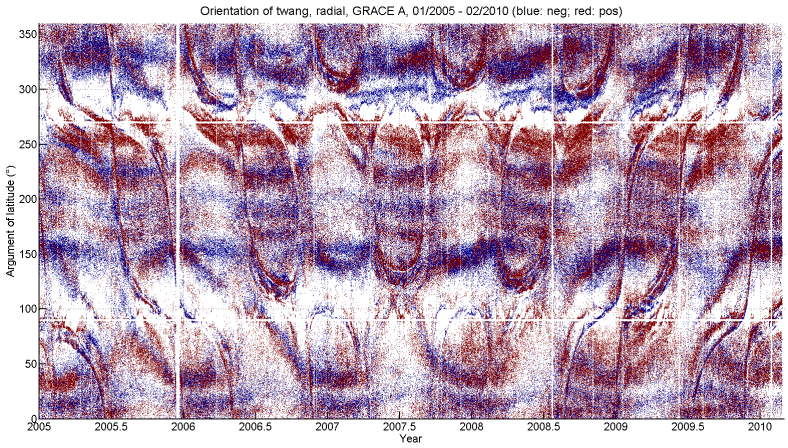

Figure C.2: Orientation of twangs, radial component, GRACE A.

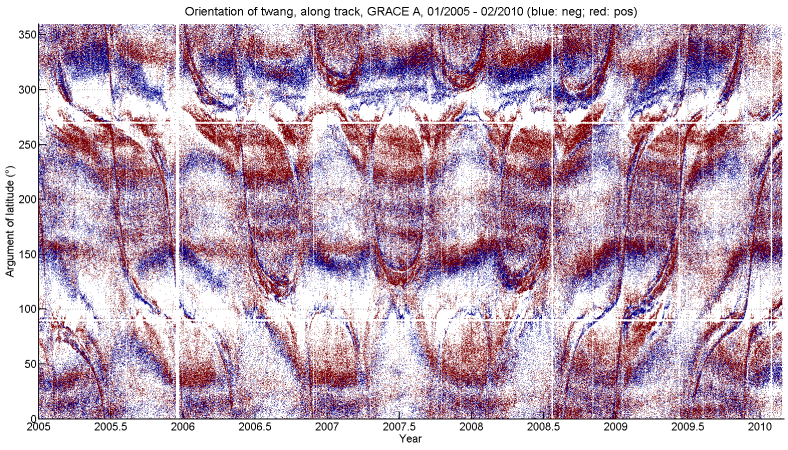

Figure C.3: Orientation of twangs, along track component, GRACE A.

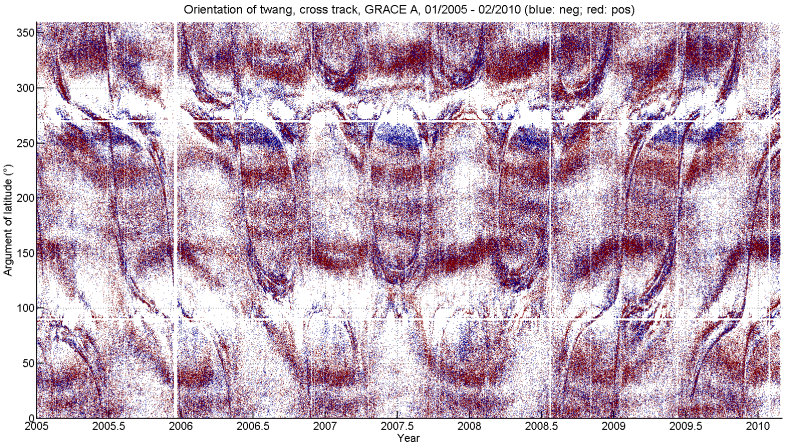

Figure C.4: Orientation of twangs, cross track component, GRACE A.

C.2.2 GRACE B

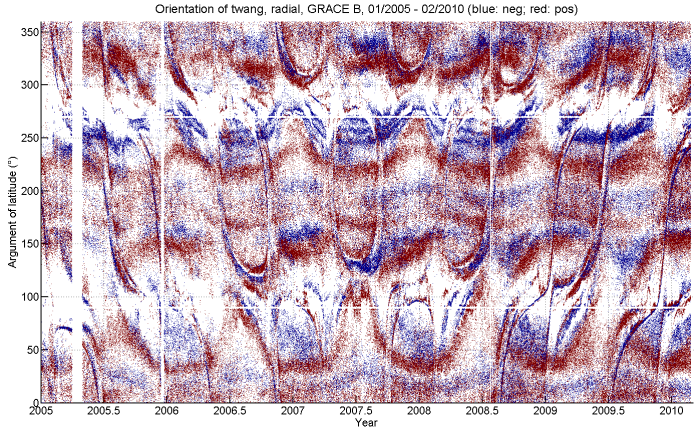

Figure C.5: Orientation of twangs, radial component, GRACE B.

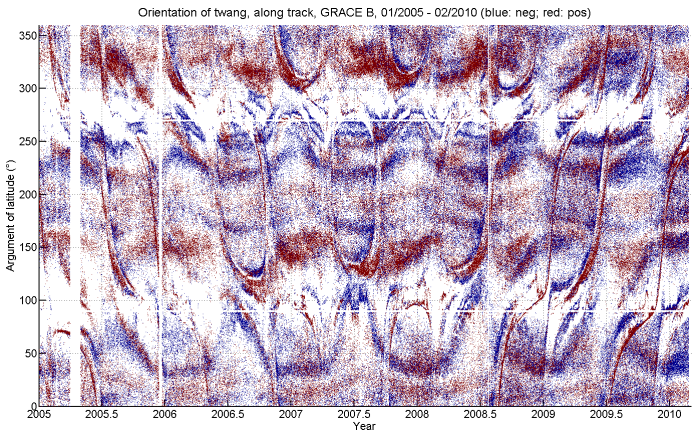

Figure C.6: Orientation of twangs, along track component, GRACE B.

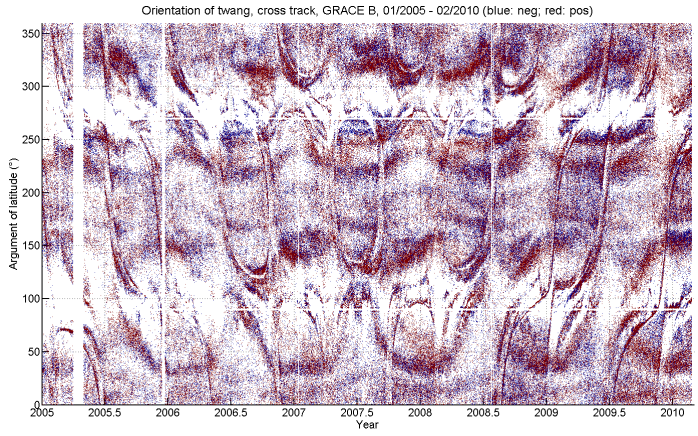

Figure C.7: Orientation of twangs, cross track component, GRACE B.

C.3 Amplitude

The pictures of the cross track axis were neglected at this point as the amplitude could not securely be determined due to the high noise level of the axis.

C.3.1 GRACE A

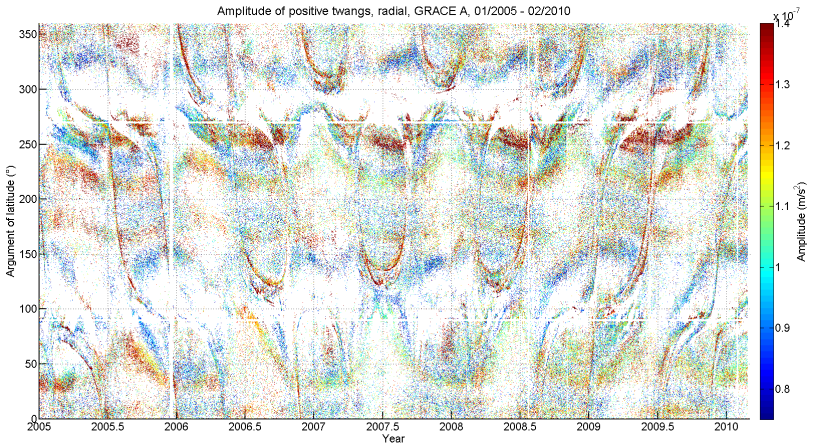

Figure C.8: Amplitude of positive twangs, radial component, GRACE A.

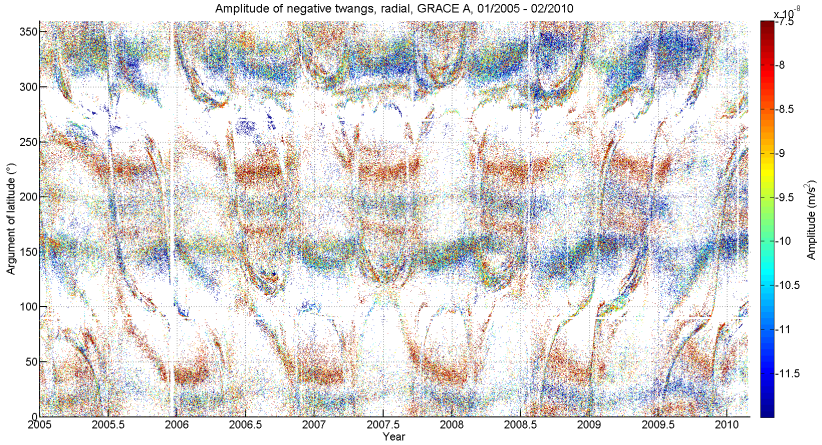

Figure C.9: Amplitude of negative twangs, radial component, GRACE A.

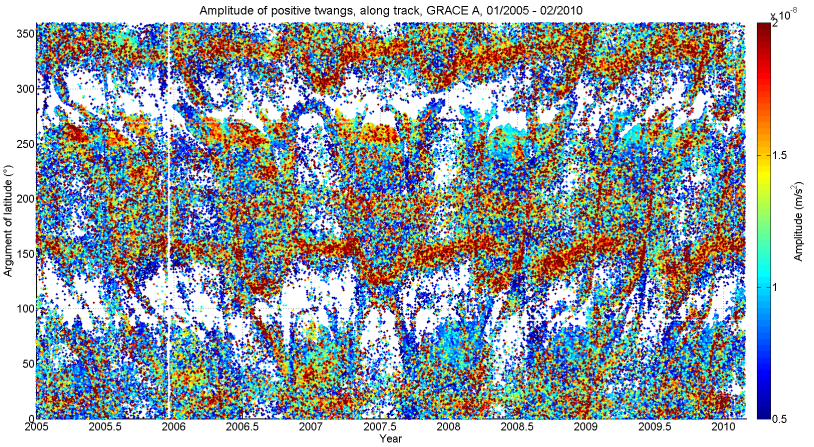

Figure C.10: Amplitude of positive twangs, along track component, GRACE A.

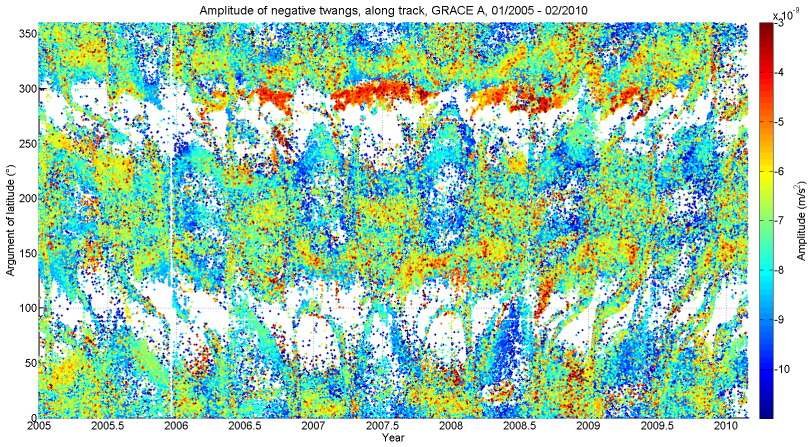

Figure C.11: Amplitude of negative twangs, along track component, GRACE A.

C.3.2 GRACE B

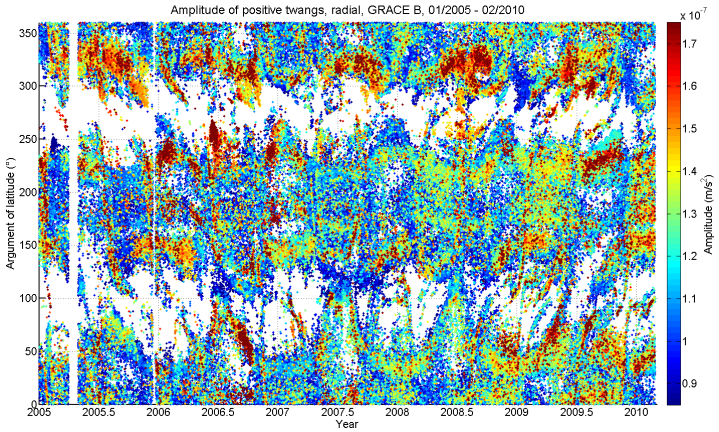

Figure C.12: Amplitude of positive twangs, radial component, GRACE B.

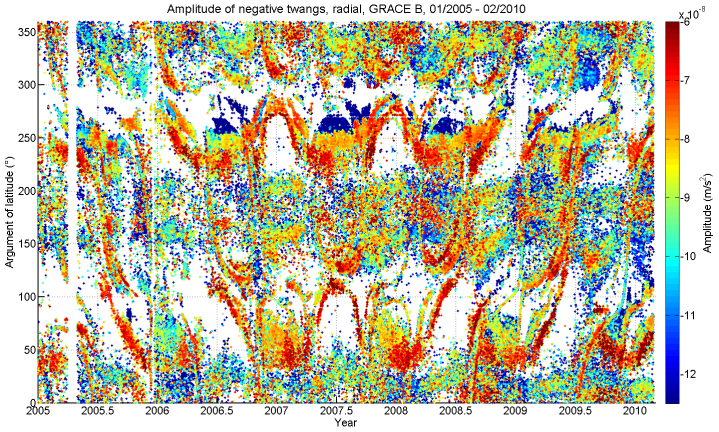

Figure C.13: Amplitude of negative twangs, radial component, GRACE B.

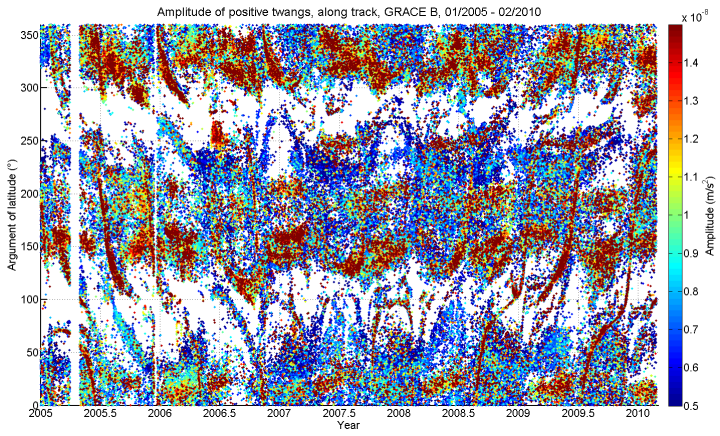

Figure C.14: Amplitude of positive twangs, along track component, GRACE B.

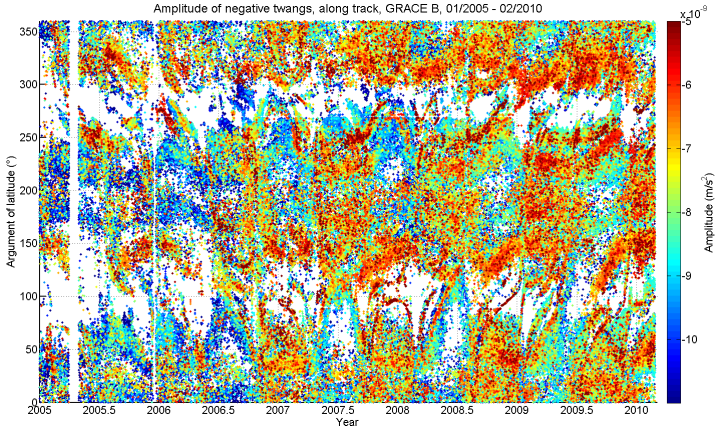

Figure C.15: Amplitude of negative twangs, along track component, GRACE B.

C.4 Asymmetry

C.4.1 GRACE A

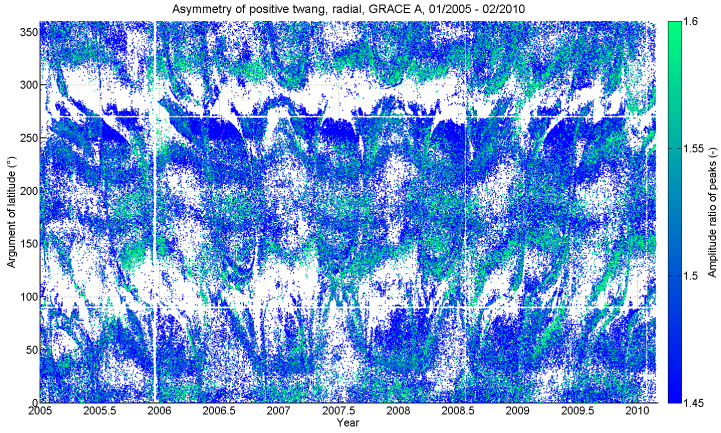

Figure C.16: Asymmetry of positive twangs, radial component, GRACE A.

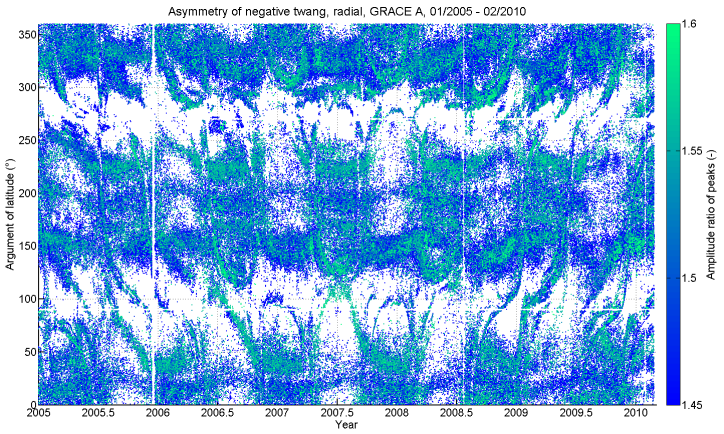

Figure C.17: Asymmetry of negative twangs, radial component, GRACE A.

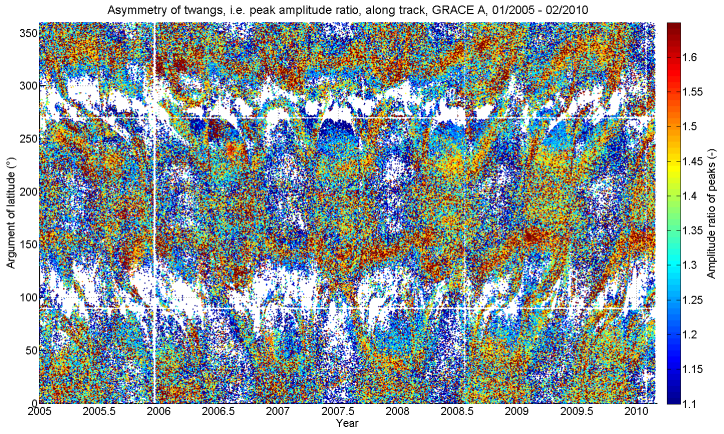

Figure C.18: Asymmetry of twangs, along track component, GRACE A.

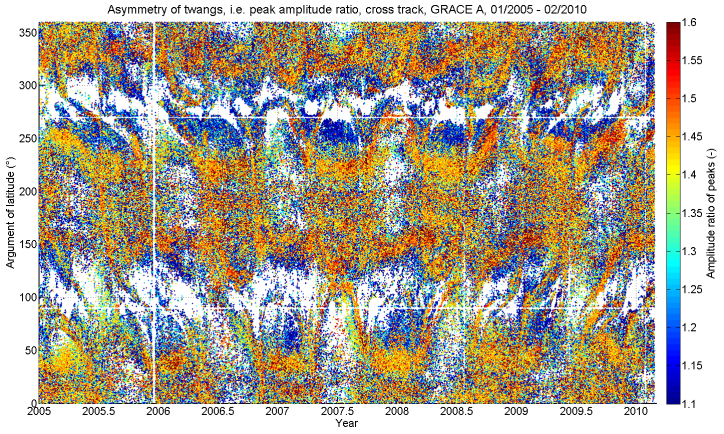

Figure C.19: Asymmetry of twangs, cross track component, GRACE A.

C.4.2 GRACE B

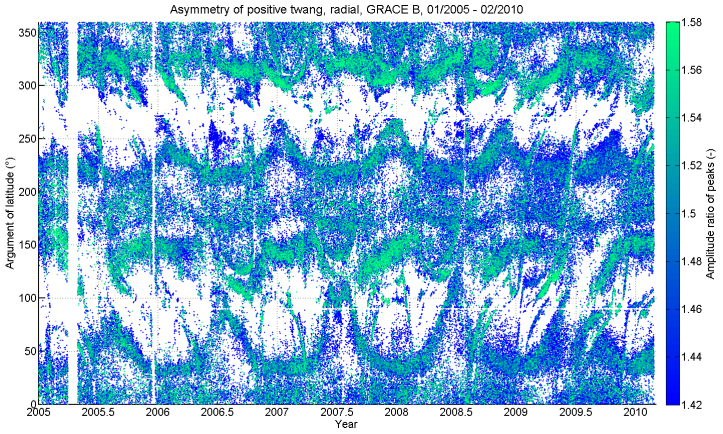

Figure C.20: Asymmetry of positive twangs, radial component, GRACE B.

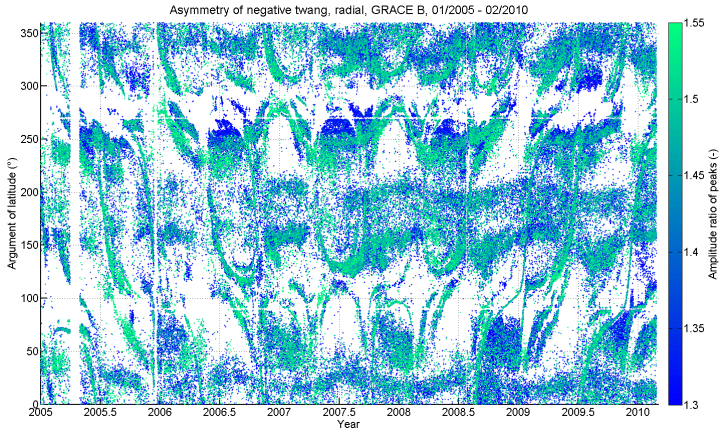

Figure C.21: Asymmetry of negative twangs, radial component, GRACE B.

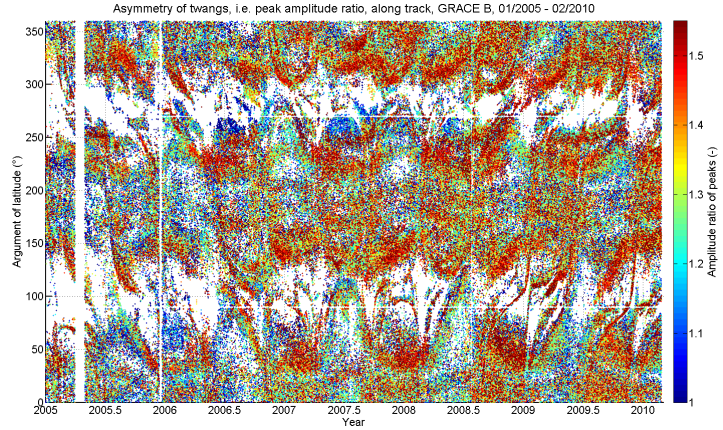

Figure C.22: Asymmetry of twangs, along track component, GRACE B.

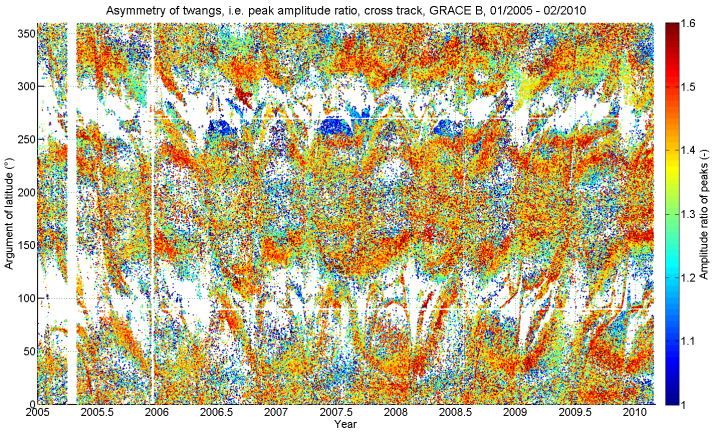

Figure C.23: Asymmetry of twangs, cross track component, GRACE B.

C.5 Width (σ)

C.5.1 GRACE A

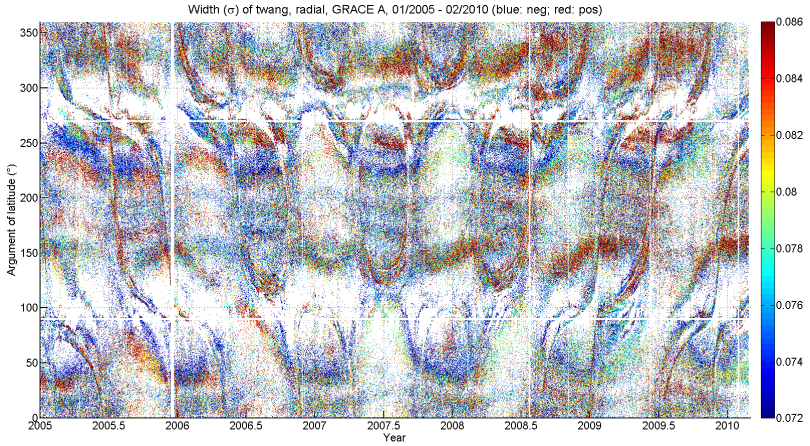

Figure C.24: Width (σ) of twangs, radial component, GRACE A.

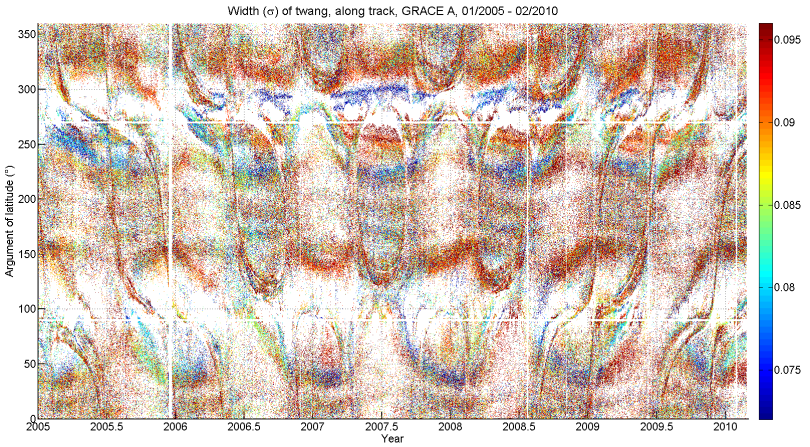

Figure C.25: Width (σ) of twangs, along track component, GRACE A.

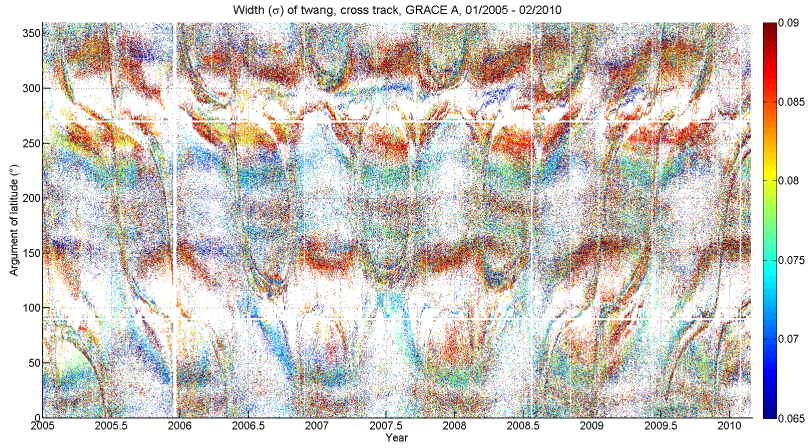

Figure C.26: Width (σ) of twangs, cross track component, GRACE A.

C.5.2 GRACE B

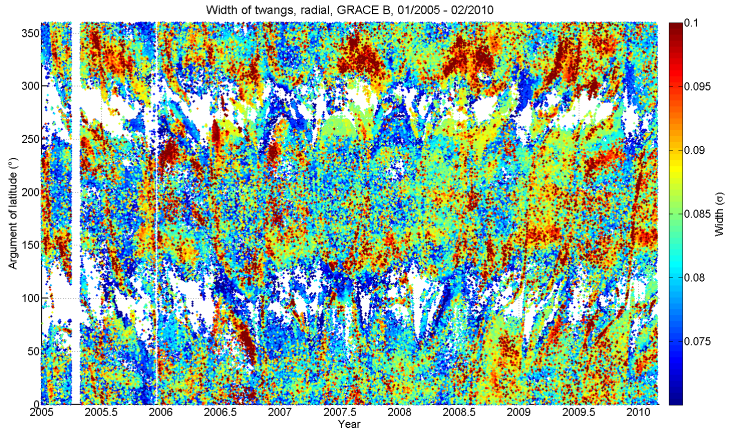

Figure C.27: Width (σ) of twangs, radial component, GRACE B.

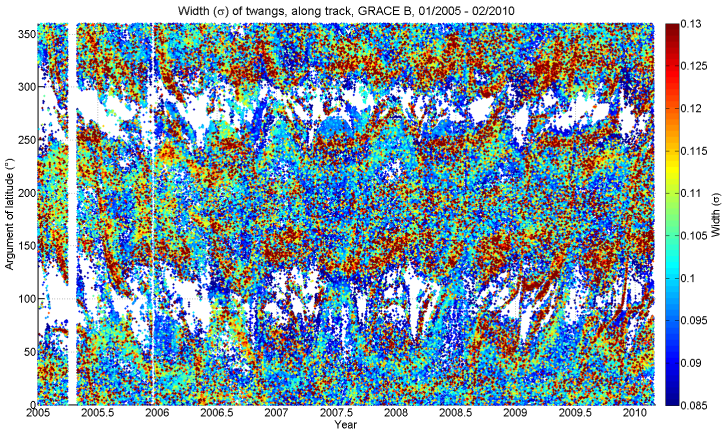

Figure C.28: Width (σ) of twaAsymmetryngs, along track component, GRACE B.

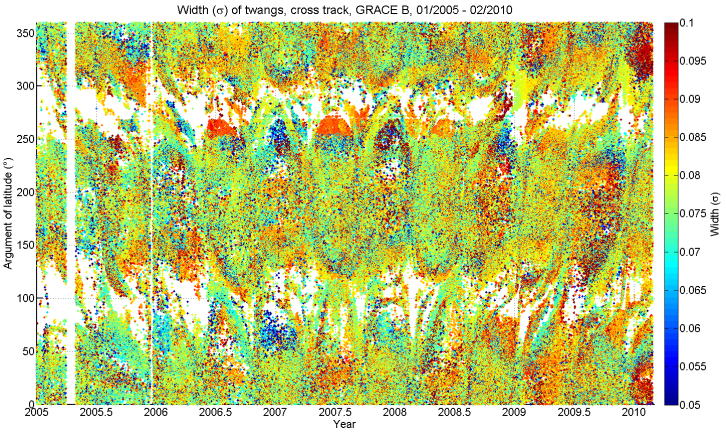

Figure C.29: Width (σ) of twangs, cross track component, GRACE B.

C.6 Oscillation period

The oscillation in the cross track component could not be determined due to the high noise level of this axis.

C.6.1 GRACE A

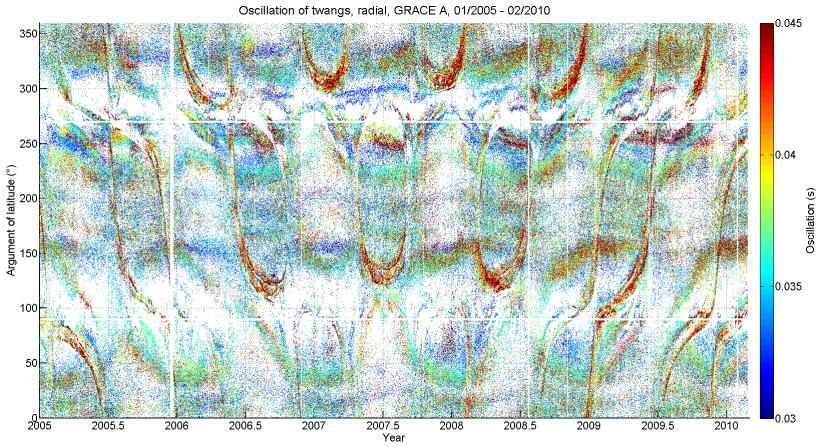

Figure C.30: Oscillation period of twangs, radial component, GRACE A.

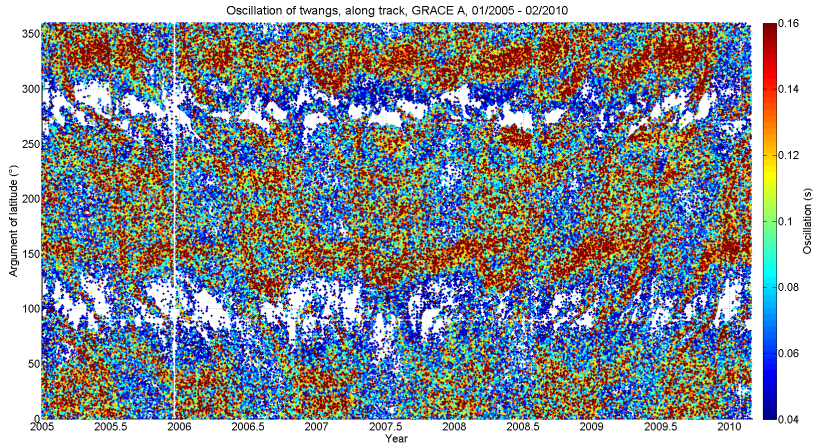

Figure C.31: Oscillation period of twangs, along track component, GRACE A.

C.6.2 GRACE B

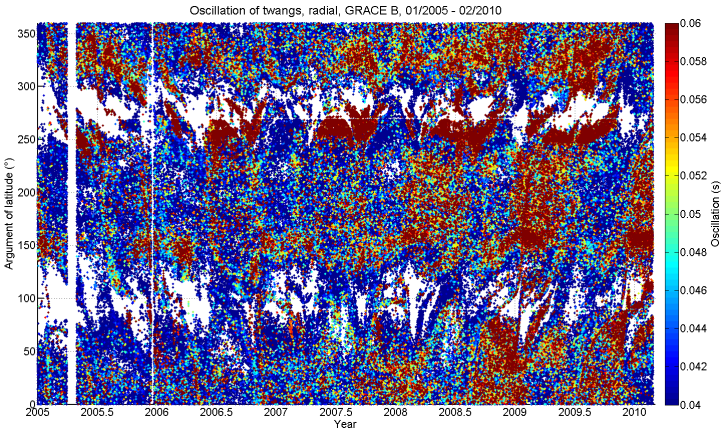

Figure C.32: Oscillation period of twangs, radial component, GRACE B.

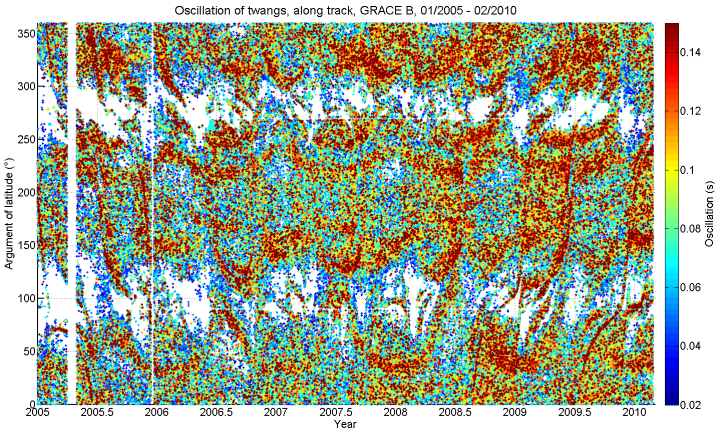

Figure C.33: Oscillation period of twangs, along track component, GRACE B.

C.7 Energy

C.7.1 GRACE A

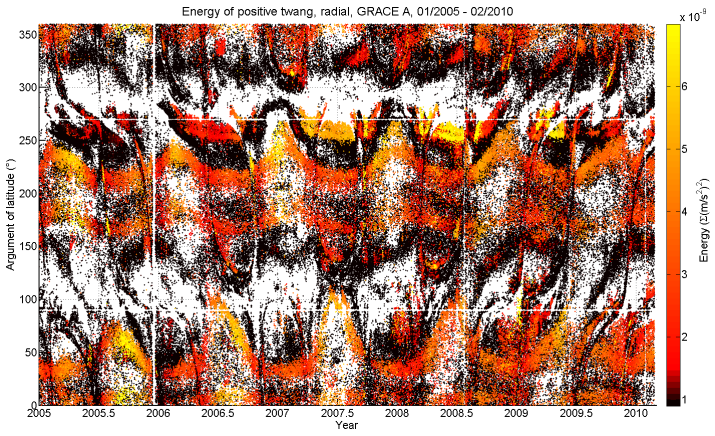

Figure C.34: Energy of positive twangs, radial component, GRACE A.

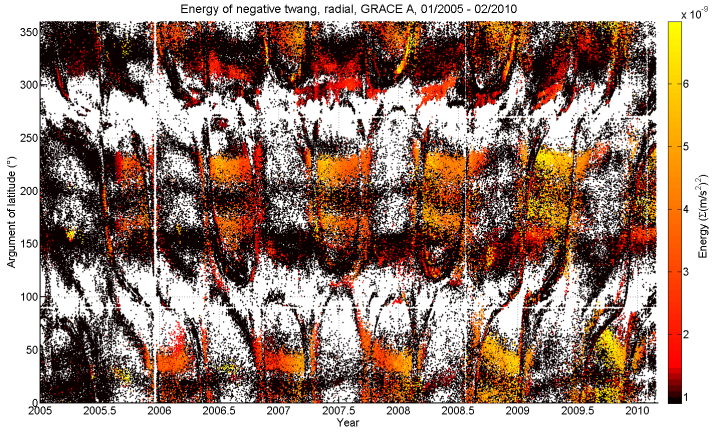

Figure C.35: Energy of negative twangs, radial component, GRACE A.

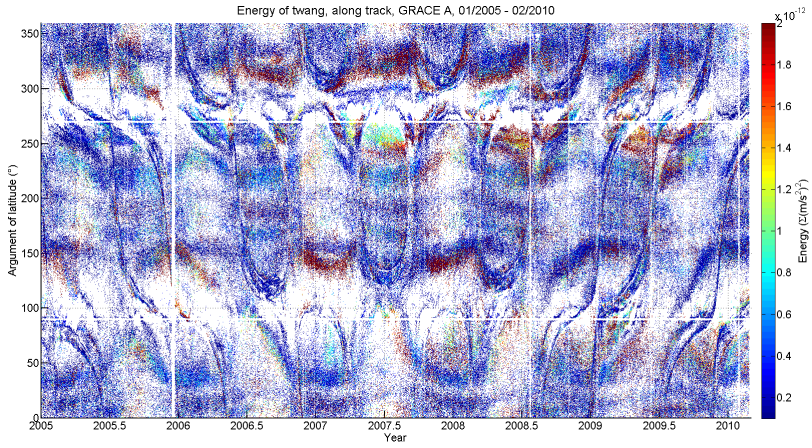

Figure C.36: Energy of twangs, along track component, GRACE A.

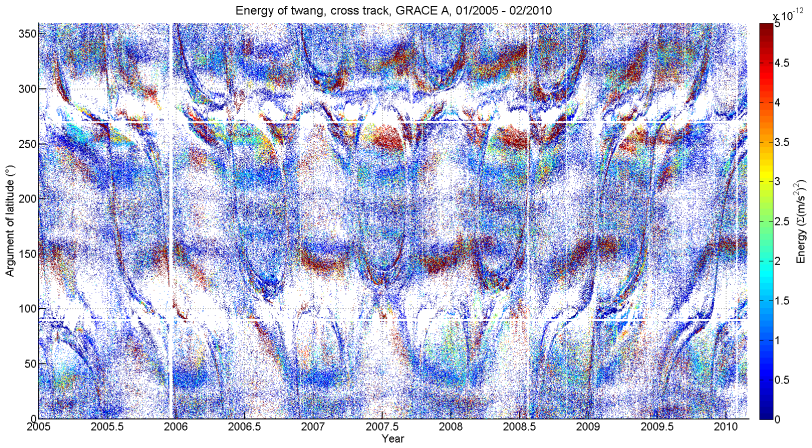

Figure C.37: Energy of twangs, cross track component, GRACE A.

C.7.2 GRACE B

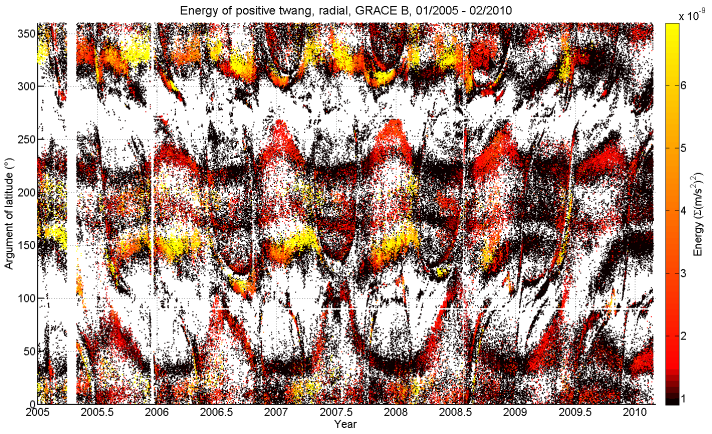

Figure C.38: Energy of positive twangs, radial component, GRACE B.

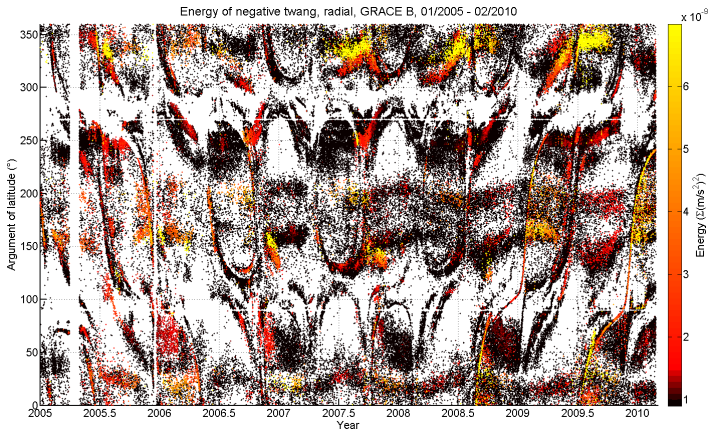

Figure C.39: Energy of negative twangs, radial component, GRACE B.

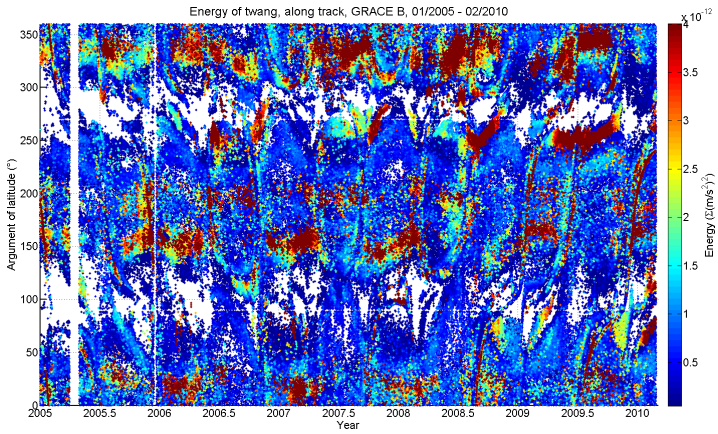

Figure C.40: Energy of twangs, along track component, GRACE B.

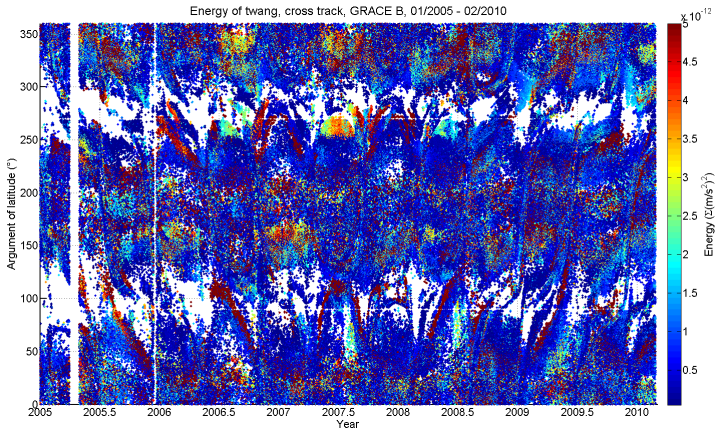

Figure C.41: Energy of twangs, cross track component, GRACE B.

D GRACE surfaces impacted by radiation

In this part of the appendix the illuminated areas in orbit for each outer surface of the GRACE spacecraft is displayed. Furthermore we display the figures for albedo and infrared impacts. For these images we considered the GRACE B spacecraft. The results for GRACE A are analogously. However, GRACE A is yawed by 180 degress relative to GRACE B, which means that the front and aft panels, as well as the port starboard panels are illuminated at opposed times (i.e. starboard of GRACE A is illuminated when port of GRACE B is illuminated). All figures are given by means of the twangs identified in this work.

D.1 Solar illuminated, according to twangs

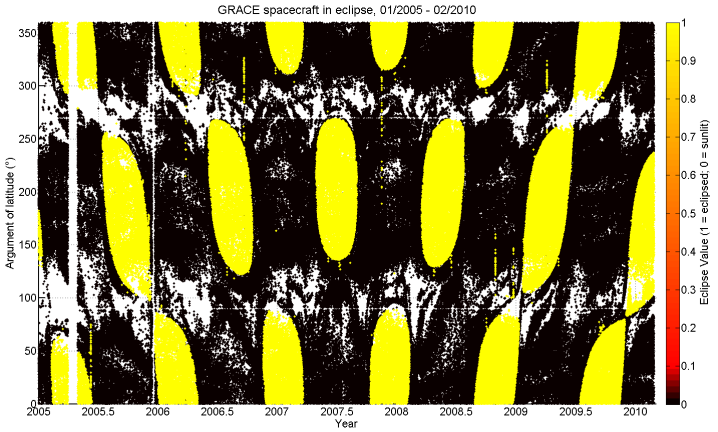

Figure D.1: Eclipsed phases of the GRACE spacecraft, according to twangs in radial component, GRACE B.

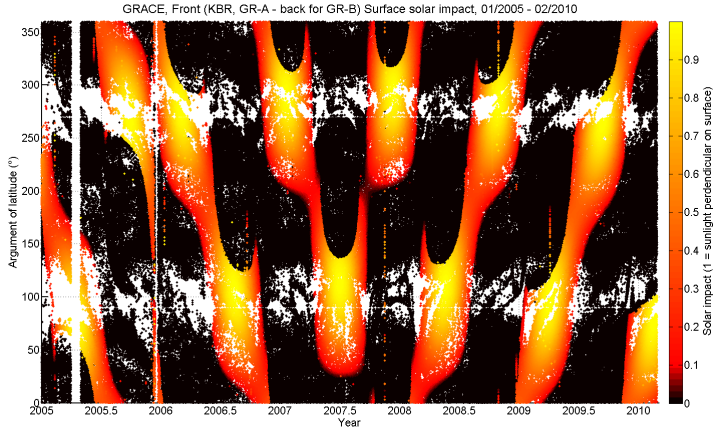

Figure D.2: Front surface illuminated, according to twangs in radial component, GRACE B.

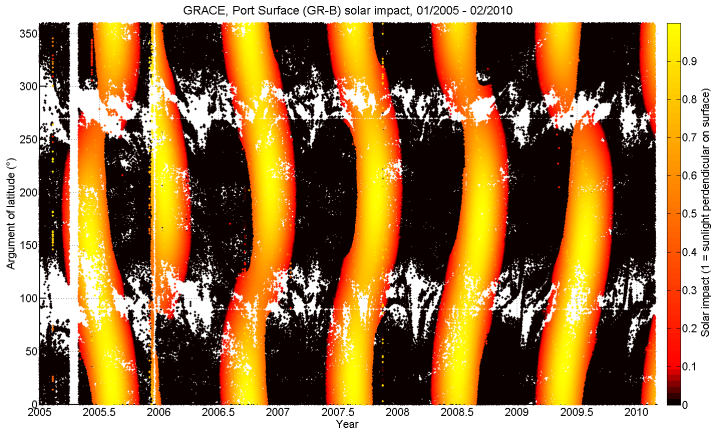

Figure D.3: Port surface illuminated, according to twangs in radial component, GRACE B.

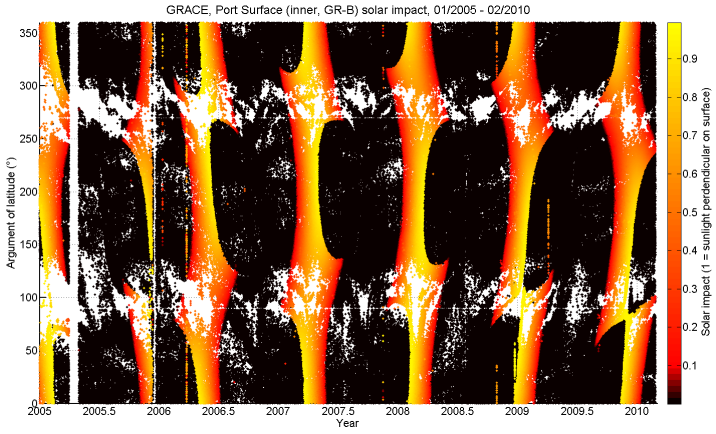

Figure D.4: Inner part of Port surface (at nadir surface) illuminated, according to twangs in radial component, GRACE B.

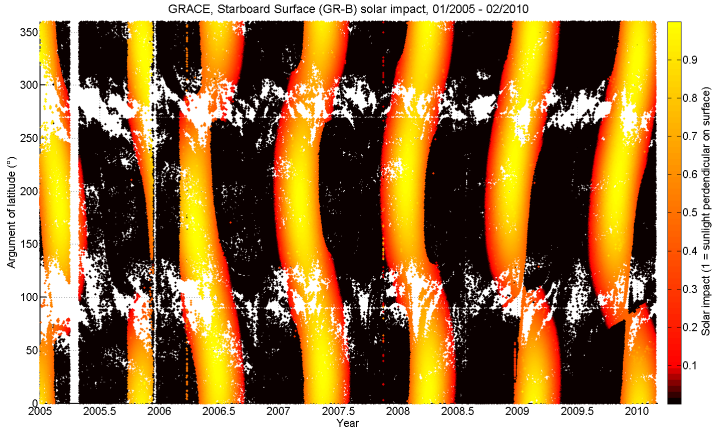

Figure D.5: Starboard surface illuminated, according to twangs in radial component, GRACE B.

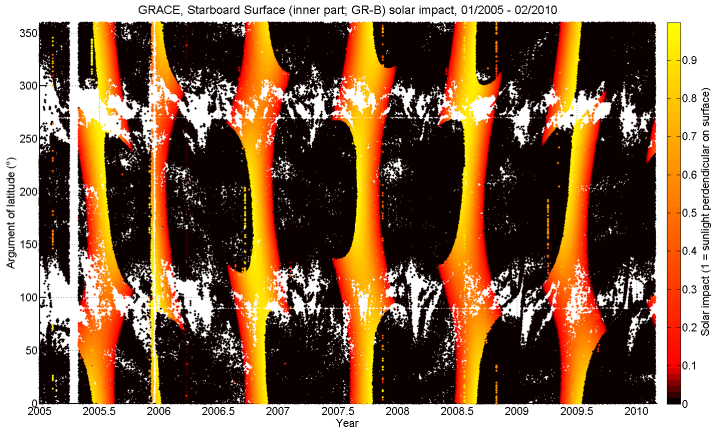

Figure D.6: Inner part of Starboard surface (at nadir surface) illuminated, according to twangs in radial component, GRACE B.

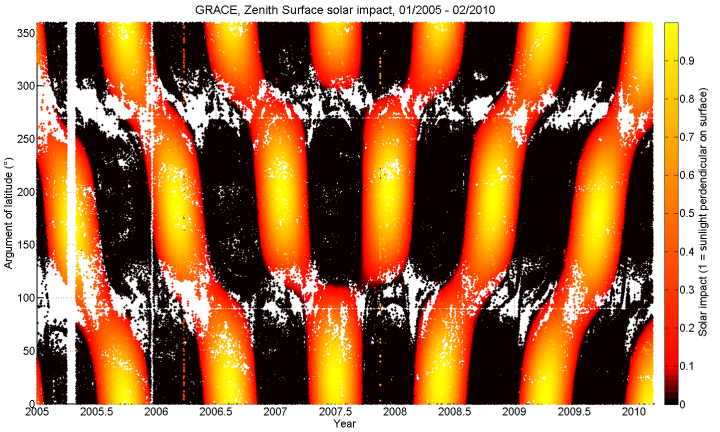

Figure D.7: Zenith surface illuminated, according to twangs in radial component, GRACE B.

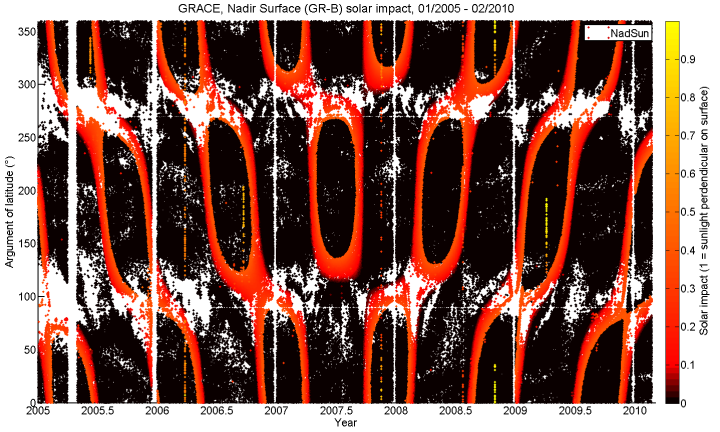

Figure D.8: Nadir surface illuminated, according to twangs in radial component, GRACE B.

D.2 Terrestrial radiation

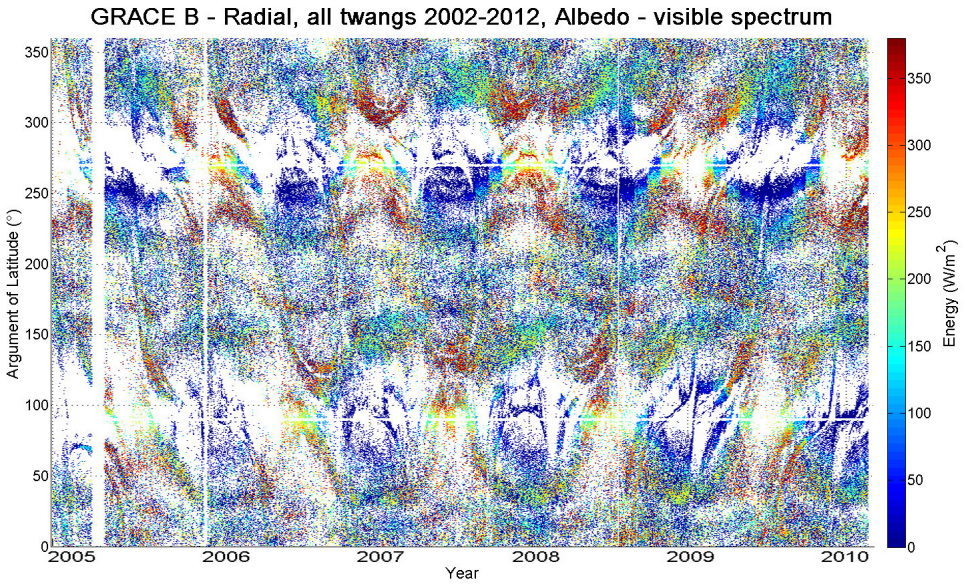

Figure D.9: Twangs coloured according to the albedo strength at GRACE position at time of twang occurrence, GRACE B.

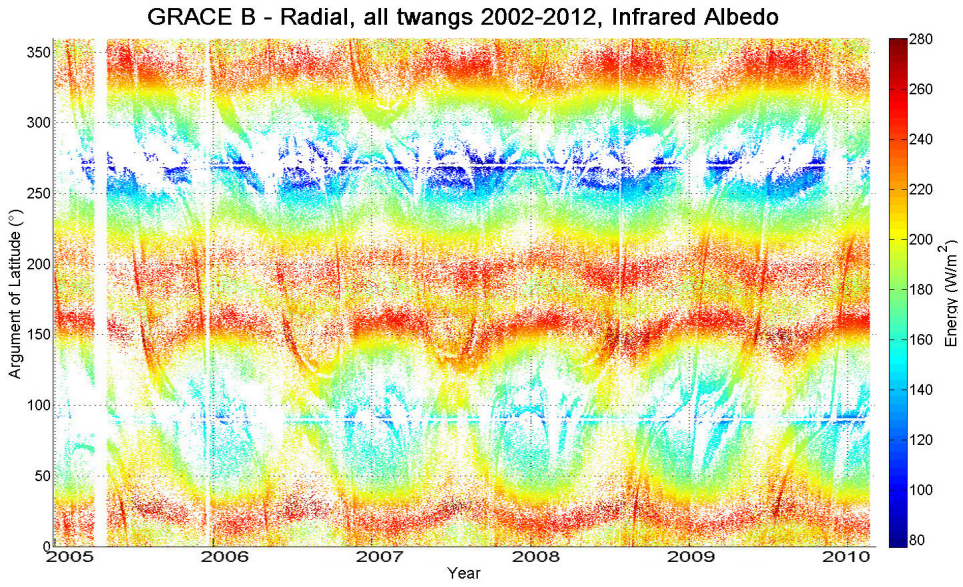

Figure D.10: Twangs coloured according to the terrestrial infrared radiation strength at GRACE position at time of twang occurrence, GRACE B.

D.3 Solar array input currents

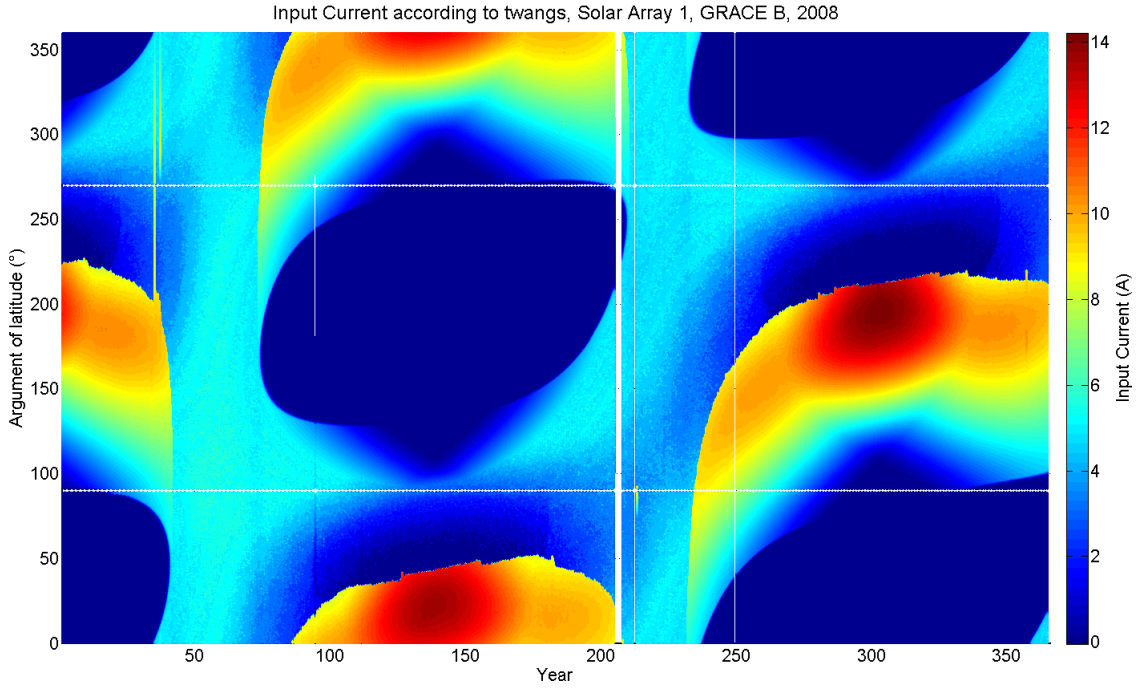

Figure D.11: Input Current of Solar Array 1, GRACE B, 2008.

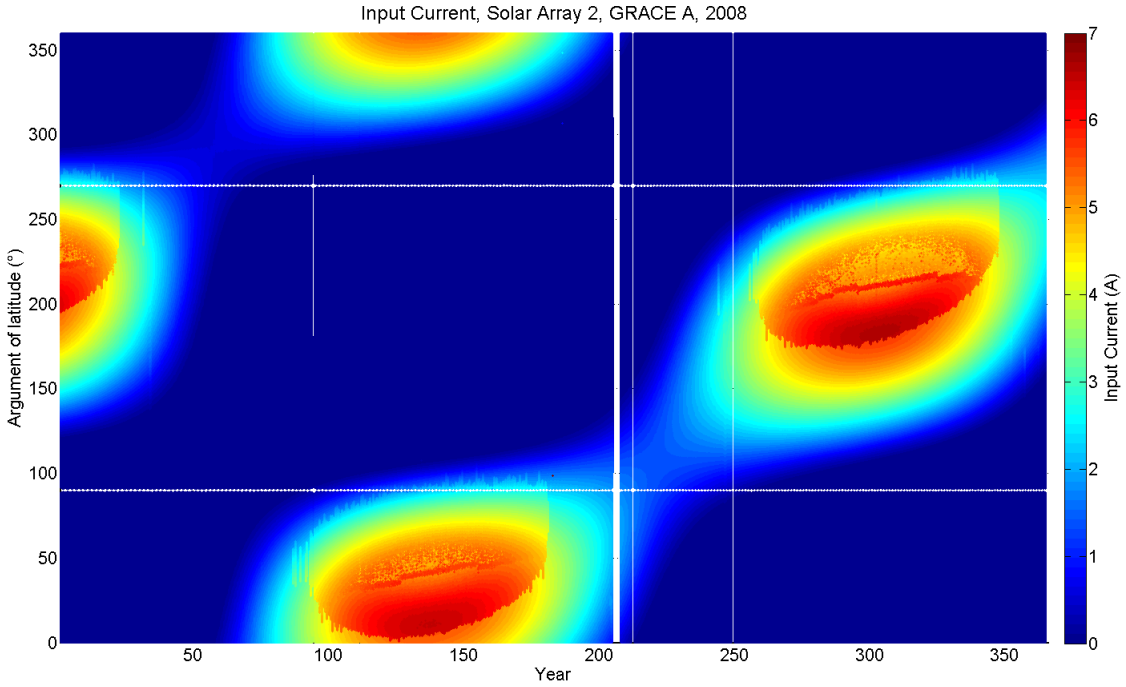

Figure D.12: Input Current of Solar Array 2, GRACE B, 2008.

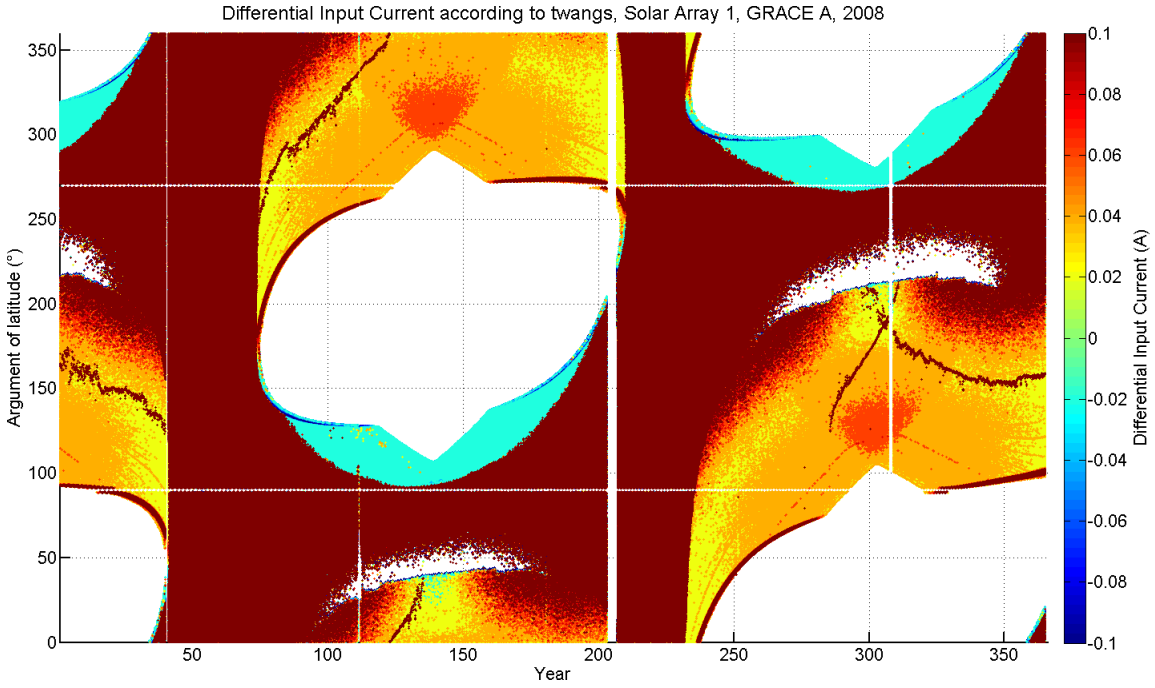

Figure D.13: Changing Input Current (from 0 Ampere or to 0 Ampere) of Solar Array 1, GRACE A, 2008.

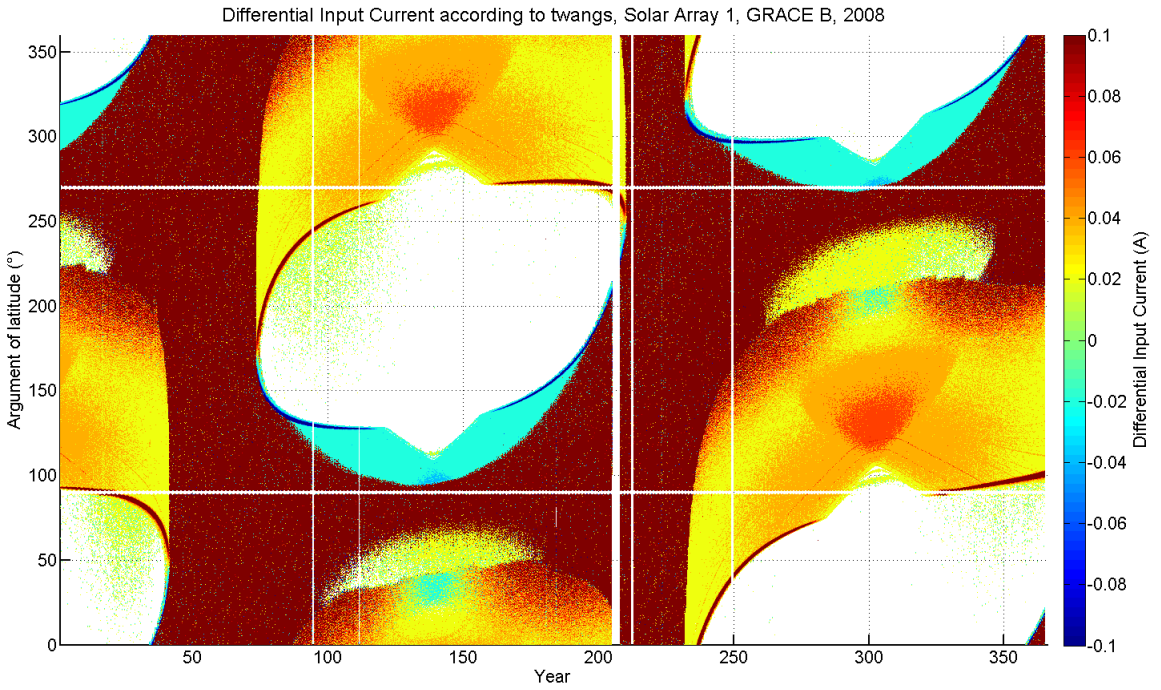

Figure D.14: Changing Input Current (from 0 Ampere or to 0 Ampere) of Solar Array 1, GRACE B, 2008.

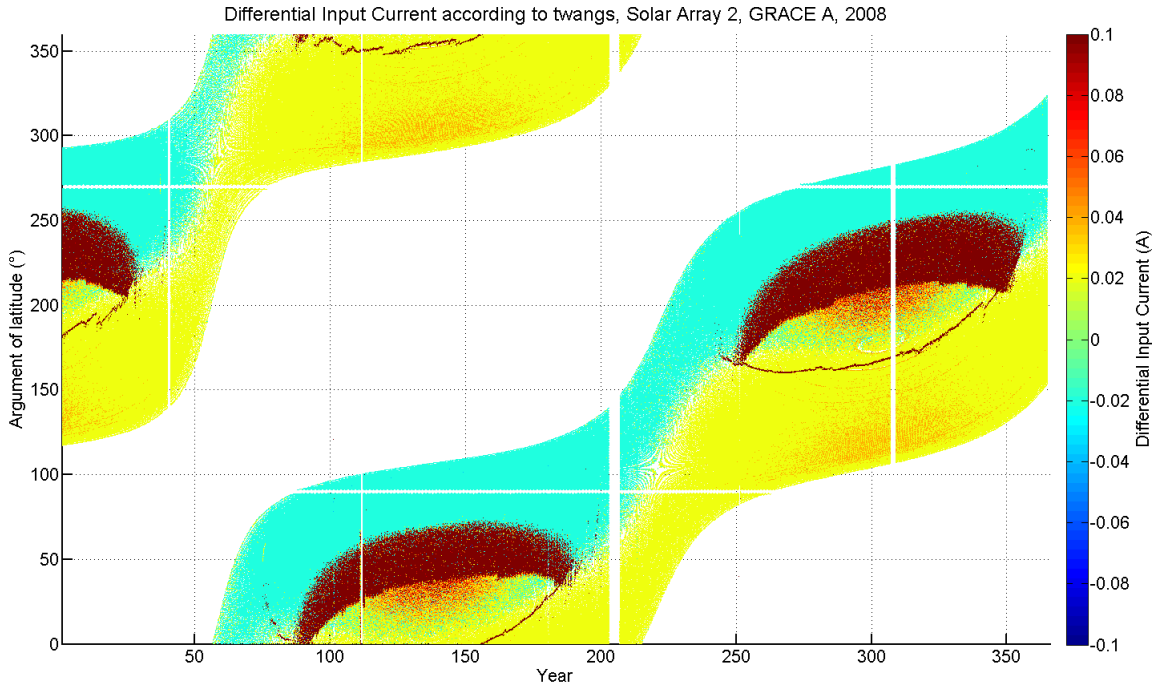

Figure D.15: Changing Input Current (from 0 Ampere or to 0 Ampere) of Solar Array 2, GRACE A, 2008.

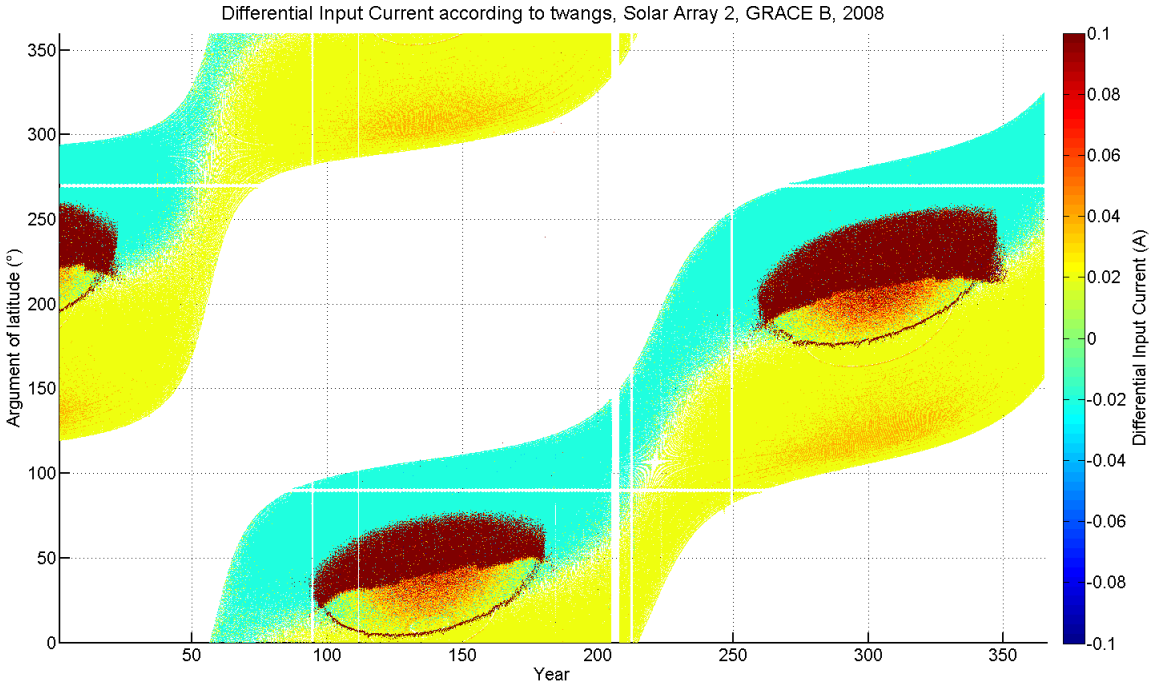

Figure D.16: Changing Input Current (from 0 Ampere or to 0 Ampere) of Solar Array 2, GRACE B, 2008.

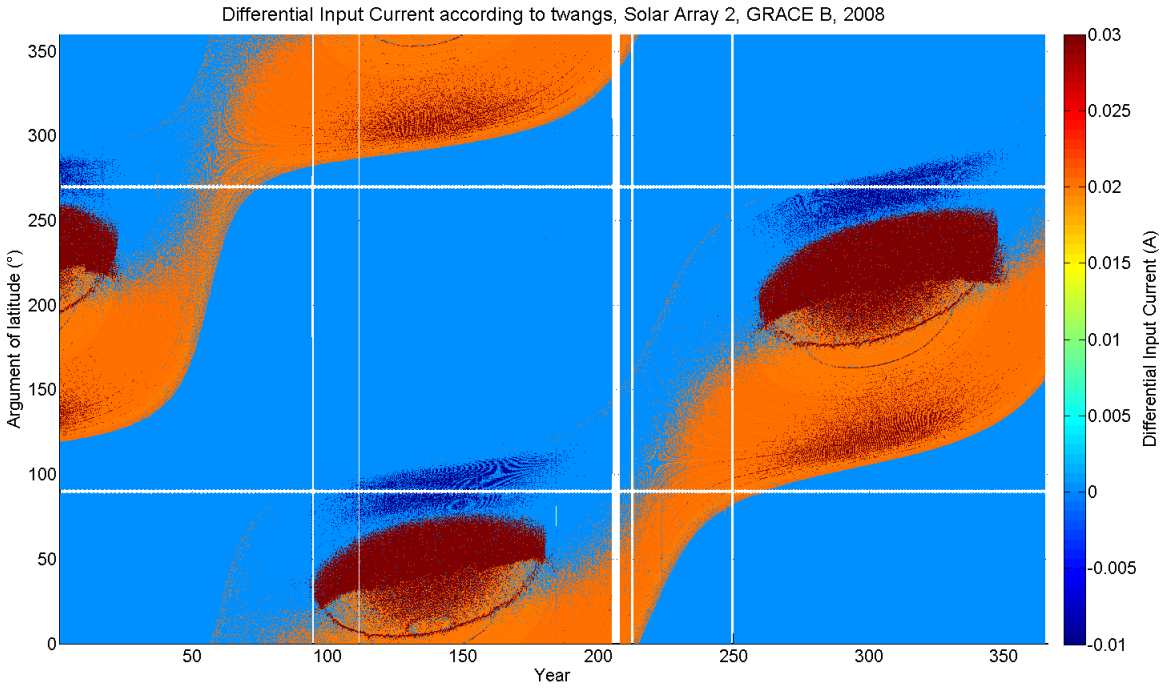

Figure D.17: Changing Input Current (from 0 Ampere or to 0 Ampere) of Solar Array 2, GRACE B, 2008. Different scale.